UNIVERSITY OF TRENTO

DOCTORAL THESIS

Correlated photon sources for quantum silicon photonics

Author:
Matteo SANNA

Supervisor:
Prof. Lorenzo PAVESI

A thesis submitted in fulfillment of the requirements for the degree of Doctor of Philosophy

in the

Nanoscience Laboratory
Department of Physics

July 4, 2024

Correlated photon sources for quantum silicon photonics

by

Matteo SANNA

A Thesis Submitted in Fulfilment
of the Requirements for the Degree of
Doctor of Philosophy

at

University of Trento
July 4, 2024

Supervisor: Prof. Lorenzo Pavesi
Reviewers: Prof. Matteo Galli and Prof. Alberto Politi

To my Family

Acknowledgements

Questo percorso è stato un viaggio fatto di incontri e di volti, ognuno dei quali ha lasciato un mattoncino fondamentale per costruire il mio cammino. Desidero quindi esprimere la mia sincera gratitudine a coloro che hanno incrociato la mia strada.

Innanzitutto, voglio ringraziare il Prof. Lorenzo Pavesi per avermi dato l'opportunità di far parte del gruppo NL e per la sua preziosa supervisione nel corso di questi anni. Il suo sostegno e la sua guida non sono mai mancati e sono stati fondamentali per il mio percorso.

Un ringraziamento speciale al Dr. Alessio Baldazzi per le collaborazioni fondamentali nei capitoli 3, 5 e 6. Siamo cresciuti insieme in questi anni tra allineamenti di obiettivi e panini con verdurine dell'orto del nostro amico. Mi hai insegnato piu di quanto pensi.

Dr. Nicolo Leone per la collaborazione mostrata nel capitolo 6. Per tutti i "prestiti" di attrezzatura e per avermi insegnato a fare le cose "CDC".

Dr. Stefano Signorini per i lavori mostrati nel capitolo 4. Per avermi insegnato l'arte del laboratorio (e non solo) e per avermi trasmesso la pazienza e la dinamicità nello stesso momento. Sei e sarai il mio sensei.

Dr. Massimo Borghi per i lavori mostrati nel capitolo 5. Per avermi insegnato e trasmesso un amore smisurato per la materia. Anche se solo per un anno ho imparato una passione e una costanza che non scorderò mai. Grazie

Il gruppo quantum composto dal Prof. Stefano Azzini, Dr. Riccardo Franchi, Chiara Michelini e Nicolo Broseghin. Per i loro continui feedback e consigli preziosi che hanno arricchito il mio lavoro e permesso di ottenere risultati.

Gioele Piccoli per la sua collaborazione nel capitolo 5, per le immagini SEM e del microscopio ottico, ma soprattutto per essere stato un compagno nelle varie avventure del percorso di dottorato. Per le pause caffe, i corsi condivisi, il tutorato, i pantaloni da sci prestati e tanto altro.

Dr. Mher Ghulinyan per la realizzazione dei chip del capitolo 4 e 5 e per le interazioni che hanno permesso di raggiungere il risultato comune del capitolo 5.

To the full Nanoscience group. For all the coffee, lunches and "loaned items." Now you can take them all back.

A tutti i coautori dei vari articoli i quali hanno contribuito alla ricerca e permesso la pubblicazione dei risultati ottenuti.

A Cerare M., Michele C., Giorgio C., Margherita M. e Elena F. per essere stati la famiglia di Trento.

A Gabriele T. e Chiara D. per le revisioni ed essere un punto oltremare che non si perde mai.

A Ele per essere la fonte di distrazione di cui ho bisogno. Per essere sempre qui al mio fianco.

Alla mia famiglia.

Matteo SANNA
University of Trento
July 4, 2024

List of Publications

JOURNALS:

[1] Signorini, S., **Sanna, M.**, Piccione, S., Ghulinyan, M., Tidemand-Lichtenberg, P., Pedersen, C., & Pavesi, L. (2021). A silicon source of heralded single photons at 2 μm. *APL Photonics*, 6(12).

[2] **Sanna, M.**, Rizzotti, D., Signorini, S., & Pavesi, L. (2022, March). An integrated entangled photons source for mid-infrared ghost spectroscopy. In *Quantum Sensing and Nano Electronics and Photonics XVIII* (Vol. 12009, pp. 143-151). SPIE.

[3] Piccoli, G., **Sanna, M**., Borghi, M., Pavesi, L., & Ghulinyan, M. (2022). Silicon oxynitride platform for linear and nonlinear photonics at NIR wavelengths. *Optical Materials Express*, 12(9), 3551-3562.

[4] Leone, N., Azzini, S., Mazzucchi, S., Moretti, V., **Sanna, M.**, Borghi, M., ... & Pavesi, L. (2023). Generation of quantum-certified random numbers using on-chip path-entangled single photons from an LED. *Photonics Research* 11, 1484-1499.

[5] **Sanna, M.**, Rizzotti, D., Signorini, S., & Pavesi, L. (2023). 2 µm Ghost Spectroscopy with an Integrated Silicon Quantum Photonics Source. *Advanced Quantum Technologies*, 2300159.

[6] Lee, J. M., Baldazzi, A., **Sanna, M.**, Azzini, S., Ahn, J. T., Lee, M. L., ... & Pavesi, L. (2023). Do different kinds of photon-pair sources have the same indistinguishability in quantum silicon photonics?. *Photonics Research*, 11(11), 1820-1837.

[7] **Sanna, M.**, Baldazzi, A., Piccoli, G., & Pavesi, L. (2024). SiN integrated photonic components in the Visible to Near-Infrared spectral region. *Optics Express*, 32(6), 9081-9094

[8] Baldazzi, A.,Leone, N.,**Sanna, M.**, Azzini, S. & Pavesi, L. (2024) A linear photonic swap test circuit for quantum kernel estimation. arXiv preprint arXiv:2402.17923.

[9] Lee J., Park J., Bang J., Sohn Y., Baldazzi, A.,**Sanna, M.**, SAzzini, S. & Pavesi, L. (2023). Versatile Quantum State Generation and Manipulation in a Programmable Silicon-Photonic 4-Qubit System with High-Fidelity and Purity. Submitted to APL Photonics.

[10] Ye, K., Keloth, A., Klaver, Y., Baldazzi, A., Piccoli, G., **Sanna, M.**, ... & Marpaung, D. (2024). Brillouin nonlinearity characterizations of a high-refractive index silicon oxynitride platform. arXiv preprint arXiv:2401.12651. Submitted to Optical Materials Express.

CONFERENCES:

[1] **A silicon source of quantum light for sensing beyond 2 µm**
European Quantum Technologies Conference (EQTC) 2021, Dublin, Ireland
Poster presentation

[2] **An integrated entangled photons source for mid-infrared ghost spectroscopy**
SPIE Photonics West (PW) 2022, San Francisco, California (USA)
Oral presentation

[3] **Mid-infrared Ghost spectroscopy application using an entangled photons source in silicon**
European Conference on Integrated Optics (ECIO) 2022, Milano, Italy
Oral presentation

[4] **An entangled photons source in the silicon platform for Mid-infrared Ghost spectroscopy**
Italian Conference on Optics and Photonics (ICOP) 2022, Trento, Italy
Oral presentation

[5] **On the indistinguishability of photon-pair sources: resonant or not resonant, that is the question**
Quantum Science Generation (QSG) 2023, Trento, Italy
Poster presentation

[6] **High-performance Silicon Nitride photonic devices for quantum Circuits at near visible wavelengths**
Quantum 2.0, Optica 2023, Denver, Colorado (USA)
Poster presentation

[7] **On the comparison of two integrated photon-pair sources through on-chip Hong-Ou-Mandel interference**
Quantum 2.0, Optica 2023, Denver, Colorado (USA)
Poster presentation

[8] **Silicon Nitride: A versatile platform for biphoton state generation and manipulation across the Visible to Near-Infrared Spectrum**
Italian Conference on Optics and Photonics (ICOP) 2024, Firenze, Italy
Oral presentation

Contents

List of Figures

List of Tables

List of Abbreviations

A

AP	**A**ll **P**ass
ADC	**A**symmetric **D**irectional **C**oupler
aMZI	**a**symmetric **M**ach-**Z**ehnder **I**nterferometer
ASE	**A**mplified **S**pontaneous **E**mission

B

BAL	**B**road-**A**rea diode **L**aser
BG	**B**ragg **G**rating
BPF	**B**and-**P**ass **F**ilter
BS	**B**eam-**S**plitter

C

CAR	**C**oincidence to **A**ccidental **R**atio
CARS	**C**oherent **A**nti-Stokes **R**aman **S**cattering
CMOS	**C**omplementary **M**etal **O**xide **S**emiconductor
CMT	**C**oupled **M**ode **T**heroy
CR	waveguide **CR**ossing
CW	**C**ontinuous-**W**ave

D

DC	**D**irectional **C**oupler
DFG	**D**ifference-**F**requency **G**eneration

E

ECDL	**E**xtended-**C**avity **D**iode **L**aser
EDFA	**E**rbium-**D**oped **F**iber **A**mplifier
EPIQUS	**E**lectronic-**P**hotonic **I**ntegrated **P**latform for **Q**uantum **S**imulator

F

FBK	**F**ondazione **B**runo **K**essler
FCA	**F**ree **C**arrier **D**ispersion
FCD	**F**ree **C**arrier **A**bsorption
FE	**F**ield **E**nhancement
FWHM	**F**ull **W**idth at **H**alf **M**aximum
FWM	**F**our **W**ave **M**ixing
FSR	**F**ree **S**pectral **R**ange

G

GACDC	**G**rating-**A**ssisted **C**ontra-**D**irectional **C**oupler
GI	**G**host **I**maging
GS	**G**host **S**pectroscopy
GVD	**G**roup **V**elocity **D**ispersion

H

HBT	**H**anbury **B**rown **T**wiss
HOM	**H**ong **O**u **M**andel

I

IC	**I**ntegrated **C**ircuit
IR	**I**nfrared **R**ange

J

JSA	**J**oint **S**pectral **A**mplitude
JSI	**J**oint **S**pectral **I**ntensity

L

LOQC	**L**inear **O**ptical **Q**uantum **C**omputation
LPCVD	**L**ow-**P**ressure **C**hemical **V**apor **D**eposition
LPF	**L**ong **P**ass **F**ilter

M

M	**M**irror
MIR	**M**id-**I**nfrared **R**ange
MMI	**M**ulti-**M**ode **I**nterferemeter
MFD	**M**ode **F**ield **D**iameter
MMWG	**M**ulti**M**ode **W**ave**G**uide
MPW	**M**ulti-**P**roject **W**afer
MZI	**M**ach-**Z**ehnder **I**nterferometer

N

NIR	**N**ear **I**nfrared **R**ange
NISQ	**N**oise **I**ntermediate-**S**cale **Q**uantum computing
NV	**N**itrogen-**V**acancy

O

OR	**O**ptical **R**ectification
OSA	**O**ptical **S**pectrum **A**nalyzer

P

PCB	**P**rinted **C**icuit **B**oard
PECVD	**P**lasma-**E**nhanced **C**hemical **V**apor **D**eposition
PIC	**P**hotonic **I**ntegrated **C**ircuit
PM	**P**hase **M**atching
POVM	**P**ositive **O**perator-**V**alued **M**easure
PPLN	**P**eriodically **P**oled **L**ithium **N**iobate
PS	**P**hase **S**hifter

Q

QC	**Q**uantum **C**omputing
QML	**Q**uantum **M**achine **L**earning
QS	**Q**uantum **S**imulation

S

SEM	**S**canning **E**lectron **M**icroscopy
(s)FWM	(**S**pontaneous) **F**our **W**ave **M**ixing
(S)FWM	(**S**timulated) **F**our **W**ave **M**ixing

SHG **S**econd **H**armonic **G**eneration
Si **Si**licon
SiN **Si**licon **N**itride
SiON **Si**licon **O**xy**N**itride
SM **S**ingle **M**ode
SNL **S**hot **N**oise **L**imit
SNR **S**ignal **N**oise **R**atio
SNSPD **S**uperconducting **N**anowire **S**ingle **P**hoton **D**etector
SOI **S**ilicon **O**n **I**nsulator
SPDC **S**pontaneous **P**arametric **D**own **C**onversion
SPAD **S**ingle **P**hoton **A**valanche **D**iode
SPD **S**ingle **P**hoton **D**etector
SPF **S**hort **P**ass **F**ilter
SPM **S**elf-**P**hase **M**odulator
SRS **S**timulated **R**aman **S**cattering
SVM **S**upport **V**ector **M**achine
SWT **Sw**ap **T**est

T

TCSPC **T**ime-**C**orrelated **S**ingle-**P**hoton **C**ounter
TE **T**ransverse **E**lectric
TEC **T**hermo **E**lectric **C**ooler
TM **T**ransverse **M**agnetic
TPA **T**wo **P**hoton **A**bsorption
THG **T**hird **H**armonic **G**eneration
TMM **T**ransfer **M**atrix **M**ethod

P

PD **P**hoto**D**iode
POVM **P**ositive **O**perator-**V**alued **M**easure.

V

VIS **VIS**ible
VQA **V**ariational **Q**uantum **A**lgorithm
VQE **V**ariational **Q**uantum **E**igensolver

W

WCS **W**eak **C**oherent **S**tate

X

XPM **Cross**-**P**hase **M**odulation
XTPA **Cross** **T**wo **P**hoton **A**bsorption

Introduction

Quantum mechanics constitutes the cornerstone supporting a multitude of scientific and technological innovations, exerting a profound influence on society and heralding a future full of transformative advancements across diverse sectors [1, 2]. This discipline has not merely redefined existing fields but has also paved the way for entirely new paradigms of innovation. Within this framework, numerous fields have reached substantial benefits. Quantum computing [3] stands on the cusp of revolutionizing data processing with its promised computational power: for example, quantum principles are advancing in medical diagnostics [4] and imaging modalities [5]. Quantum sensors increase accuracy in measurement science and environmental surveillance [6–8], and quantum cryptography reinforces the security of communication networks [9]. Furthermore, the insights obtained through quantum mechanics are catalyzing progress in materials science [10], fostering the emergence of materials with different characteristics.

Quantum light (or "non-classical" light) is central to these innovations [11]. It is an essential component for leveraging the benefits of quantum mechanics. Unlike classical light, quantum light exhibits distinct statistical properties, notably characterized by photon number distributions featuring variances (Δn) such that $n > \Delta n$ [12]. Here, n denotes the average number of photons, surpassing classical thresholds where $n \leq \Delta n$. This distinctive attribute provides detection mechanisms with lower noise levels than traditional classical light sources. In addition, quantum light behaves in ways that contradict classical interpretations. It demonstrates the superposition phenomenon [12] where particles can exist in multiple states simultaneously. It also involves entanglement [13], a concept initially described by Einstein as "spooky action at a distance". Entangled particles maintain a correlation despite vast separations, with one particle instantaneously influencing its counterpart.

Quantum light is also characterized by two main features: indistinguishability and coherence. The first feature is purely quantum, which means that each photon is an exact copy of another, having no differences in any aspect. The second characteristic is not purely quantum and refers to the consistent phase relationship among the electromagnetic wavefronts that make up the light. Coherence helps in creating pure states, which are different from mixed states that do not show interference. Some examples of non-classical light include squeezed states [14], photon-number (or Fock) states, and, in particular, single-photon states [15]. Furthermore, examples of classical light include thermal light from a blackbody source and coherent light from a laser.

Quantum light generation stands as a formidable challenge in the field of quantum physics. The search for a source of quantum light—capable of consistently emitting single photons or entangled photon pairs—has catalyzed substantial advancements in this domain. The key to achieving this goal lies in utilizing the unique emission characteristics of individual quantum systems, leading to sub-Poisson statistics. Single photons exhibit such statistics, which can be achieved by making sure that a quantum system's transition from an excited state precludes subsequent re-emission, guaranteeing the release of a solitary photon per instance. This "anti-bunching" phenomenon of photons is a pivotal element of quantum mechanics, highlighting the discrete nature of quantum emissions. The observation of anti-bunching was first made in resonance fluorescence experiments involving low-density sodium vapor, as chronicled by Hanbury Brown and Twiss in 1979 [16]. This discovery was later confirmed within single ion systems through the work of Mandel in 1979 [17].

The journey of single photons and quantum light has seen remarkable advancements over the past four decades, tracing its origins back to the early 20th century by Max Planck. The crucial moment occurred in 1977 when Kimble's work on the statistical properties of a single photon emerged [18]. Entering the new millennium, Knill's groundbreaking discovery showed that single-photon pulses could be exploited for optimal linear optical quantum computation (LOQC) [19], propelling multiple experimental efforts to develop a reliable single-photon source.
Based on a thorough examination of citations and patents, as depicted in Figure 1, it is evident that there has been significant progress in quantum light research. A review by Shahram MohammadNejad [20] highlights a surge of interest in important areas such as quantum communication, quantum computation, and quantum entanglement. This surge not only reflects the growing curiosity and potential in these fields, but it also confirms the robust and continuous advancement of research in quantum light. The

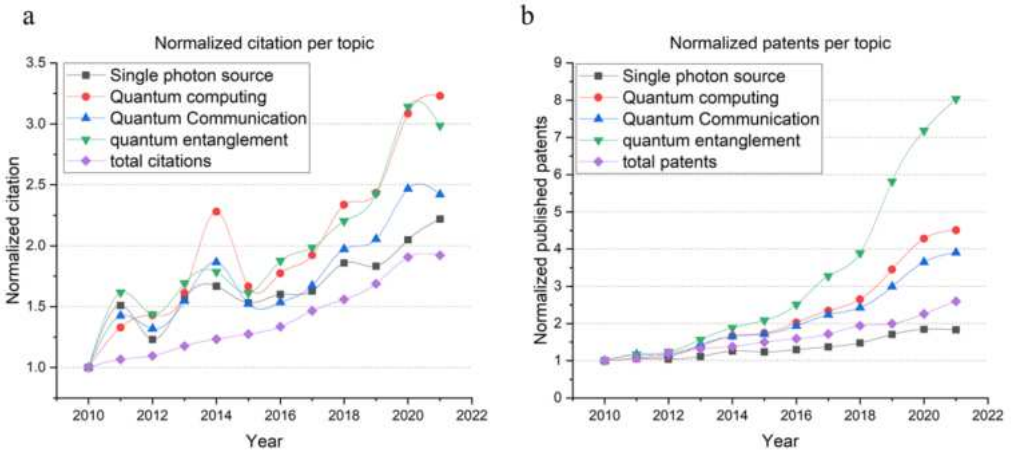

Figure 1: Trend of different quantum topics rates in both academic citations (a) and patents (b). The data are taken from a review authored by Shahram MohammadNejad [20]. Reproduced with permission from Springer Nature.

field of quantum light generation has seen significant expansion in recent years due to the development of various platforms and techniques. This has opened up new possibilities for exploration and applications in science and technology. Each method has unique features and potential advantages that require thorough examination. Let us focus on some of the most important techniques that have emerged.
Quantum dots [21], often referred to as "artificial atoms", offer a promising approach to creating predictable quantum light sources. These nanoscopic structures exhibit electron motion that is quantized in all three spatial dimensions, leading to an energy spectrum that mirrors that of natural atoms. Quantum dots provide a versatile platform for building quantum systems within robust semiconductor frameworks, allowing for emission properties to be tailored to specific needs.

Trapped ions [22] are becoming a leading technology in the field of quantum computing, with great potential as sources of quantum light. They are known for producing qubits with minimal noise, which makes them highly desirable for both quantum computing and communication. Additionally, trapped ions have prolonged coherence times, which helps to ensure consistent and stable quantum operations, further solidifying their essential role in advancing quantum technologies.

Diamond color centers [23], especially nitrogen-vacancy (NV) centers, are at the forefront of quantum technology research. These atomic-scale imperfections can be

engineered to emit single photons. Exhibiting unique quantum properties, these lattice defects in diamonds become efficient quantum emitters. NV centers, in particular, have attracted considerable interest due to their capacity to produce single photons of remarkable purity and coherence.

Cold atomic gases [24] offer a scalable and versatile approach to quantum light generation, with controlled interactions leading to the emission of single photons. Recent research has focused on the creation of quantum droplets and supersolid states in ultracold atomic gases, which present new opportunities for fundamental research and quantum sensing technologies. Additionally, the generation of nonclassical photon pairs with extensive bandwidth in hot atomic vapors highlights the potential of these systems as high-efficiency, broad-bandwidth quantum light sources.

Alternative approaches for the generation of entangled and single photon pairs are based on the principles of nonlinear optics, which are employed in various media such as crystals or integrated waveguides. These media facilitate two key processes: Spontaneous Parametric Down-Conversion (SPDC) [25, 26] and Spontaneous Four-Wave Mixing (sFWM) [27, 28]. These processes can simultaneously generate pairs of entangled photons and emit a single photon pair at a specific input power, with probabilistic generation events.

SPDC is a quantum optical process that occurs in nonlinear materials. In this process, a photon is converted into two photons, known as signal and idler photons. These photons are time-energy correlated and are generated from non-centrosymmetric materials, typically bulk crystals. This nonlinear process guarantees energy and momentum conservation. The entangled nature of the generated photon pairs makes SPDC an essential tool for conducting quantum communication and information experiments.

On the other hand, sFWM is another nonlinear optical process that can be used in integrated optical circuits. In sFWM, two photons interact in a nonlinear medium, creating two more photons that are time-energy correlated. As with SPDC, this process requires energy and momentum conservation. Integrated waveguides are particularly advantageous for sFWM due to their ability to confine light effectively, enhancing the nonlinear interaction and, thus, the efficiency of the process.

In the case of photon pair sources, the generation of single photons is achieved through the heralding technique. This method exploits the correlation between the photon pairs produced in either SPDC or sFWM. When one photon (the herald) is detected, it signals the presence of its counterpart, thereby indicating the generation of a single photon with a higher degree of certainty. By employing this method, the so-called Heralded photon attains sub-Poissonian statistics. This heralding process is crucial for applications that require a deterministic source of single photons, such as certain quantum computing protocols and quantum key distribution systems.

All these different methods give a variety of advantages and disadvantages crucial for their practical application. One significant challenge lies in the requirement for cryogenic temperatures, imperative for maintaining quantum coherence. However, this necessity entails substantial logistical and financial burdens.

Moreover, these platforms require protection from external perturbations to prevent decoherence. This requires advanced engineering solutions that may limit scalability. The complexity of their manufacturing processes adds an extra level of difficulty, often involving complicated techniques that can affect the coherence and consistency of photon sources.

Integrated nonlinear optics is a promising solution to the challenges faced in the field of quantum light. This approach allows for the utilization of nonlinear optical

effects within integrated circuits, making it easier to generate and manipulate quantum light. With this method, ultra-low temperatures are no longer necessary, as some operations can be performed at more manageable temperatures.

This approach enhances protection from environmental interference by integrating optical components onto a single chip. The manufacturing process is simplified and produces more coherent and scalable photon sources in micrometer sizes, taking advantage of well-established semiconductor fabrication methods.

Integrated nonlinear optics offers a more refined configuration compared to traditional bulky free-space optics. It can encapsulate not only the generation of quantum states but also their manipulation [29] and detection within a single compact platform [30]. This fusion of nonlinear optics and integrated photonics represents a significant step forward toward the practical realization of quantum light technologies. It paves the way for a future illuminated by the principles of quantum mechanics.

This thesis work is dedicated to the generation of quantum light, specifically biphoton states, through the nonlinear parametric process of sFWM on an integrated silicon photonics platform. These states, composed of entangled pairs of photons, have found various applications that exploit time-energy correlation. The thesis is structured into six chapters, each addressing specific aspects of my research:

Chapter 1: Entangled Photons. This chapter introduces the fundamental principles of quantum optics, with a focus on the parametric non-linear sFWM process. It elucidates critical parameters characterizing biphoton states, providing a comprehensive understanding of their generation and significance.

Chapter 2: Silicon Quantum Photonics. This chapter discusses the central role of silicon and silicon nitride materials in integrated optics. It covers the basics of integrated waveguides, integrated optical components, and the manifestation of sFWM within them.

Chapter 3: Comparison of sFWM Integrated Sources. This chapter presents a detailed comparison between various sFWM sources, highlighting the differences between two integrated sources of biphoton state, namely spiral sources and microring resonators. The comparison takes into consideration different quantum parameters that characterize the quantum light source. It covers analytical analyses, simulations, and experimental measurements to characterize the different aspects of integrated sources. Additionally, the text discusses the comparison of intramodal versus intermodal generation approaches. Here, I have performed the simulations and theoretical analyses reported.

Chapter 4: 2 µm Sensing. This chapter presents groundbreaking research on the generation of single photons in the mid-infrared range achieved through the intermodal sFWM process using infrared lasers in the C-band. The integrated sources, are thoroughly characterized based on various figures of merit. Finally, the chapter discusses the application of entangled photons silicon-based sources in Ghost spectroscopy under noisy conditions, demonstrating their superiority over conventional spectroscopic methods. Here I have conducted all the experimental measurements and theoretical analyses reported.

Chapter 5: Toward Quantum Simulator in a Monolithic Platform. As part of the EPIQUS project, this chapter focuses on the development of a quantum simulator on a single photonic platform. The chapter discusses the use of a silicon nitride-based platform that has been optimized for operation within the visible to near-infrared spectrum, along with its linear and nonlinear characterizations. The generation of biphoton states is described in detail, along with the study of different integrated structures

that are useful for enabling the selection of generated photons, the removal of residual pumps, the routing of the quantum state, and its manipulation. Here, I designed the different building blocks and performed linear and nonlinear measurements of the FBK-manufactured devices.

Chapter 6: SWAP Test Algorithm on a Linear Photonic Integrated Circuit. The final chapter explores the implementation of the quantum Swap Test algorithm on a silicon nitride platform, using path encoding for qudit representation. It investigates the potential of the Swap Test for efficient kernel function estimation, presenting a novel approach to quantum algorithms. Here, I contributed to the design and performed the experimental measurements.

The chapters end with a summary of the key findings and suggestions for future research. The appendices contain additional information that helps in understanding the concepts discussed in the main chapters. In the conclusion, I reflect on the implications and contributions of my research to the field of quantum light generation.

These chapters detail the primary research conducted throughout my doctoral years. Further work in which I have contributed without a leading role can be found in the list of my publications.

Chapter 1

Entangled photons

> "I would not call [entanglement] one but the characteristic trait of quantum mechanics, the one that enforces its entire departure from classical lines of thought."
>
> Erwin Schrödinger

The term "biphoton state" [12] refers to a fundamental quantum state in quantum optics that describes the behavior of two interacting photons. The traits and qualities of these two photons are inherently linked, resulting in a robust correlation. Entanglement [13, 31] characterizes this correlation that exists between these photons. In this scenario, the quantum states of the two photons are so entwined that it becomes impossible to describe the state of one photon without simultaneously describing the other's.

Biphoton states are relevant across a broad spectrum of quantum phenomena and application domains. They serve as indispensable tools for the fundamental exploration of quantum entanglement. They are crucial for advancing the field of quantum technologies, including quantum sensing [8], quantum cryptography, quantum computing [3], and various other quantum optical experiments [32–34].

Two approaches to generate biphoton states, spontaneous parametric down-conversion (SPDC) [26] and spontaneous four-wave mixing (sFWM) [28], assume prominence. The following chapter, after the introduction of foundational aspects of quantum optics, provides a detailed exposition of these processes. It includes an in-depth analysis of the characteristics exhibited by these entangled photons.

1.1 Quantum aspects

1.1.1 Quantum electric field: basic description

In this chapter, we explore the fundamental principles underlying the quantum perspective of the electric field, drawing inspiration from the work presented in the book by Gerry and Knight [12].

Quantized harmonic oscillator

The mathematical characterization of the quantum electric field is achieved through the framework of quantum field operators. These operators, responsible for both the creation and annihilation of photons, play a fundamental role in governing the interplay between charged particles and photons. The formulation of these field operators

is guided by quantization rules that ensure the internal consistency of the quantum theory.

The Hamiltonian describing the electromagnetic field is treated as a quantized harmonic oscillator, represented as:

$$\hat{\mathcal{H}} = \sum_j \hat{\mathcal{H}}_j = \sum_j \hbar\omega_j \left(\hat{a}_j^\dagger \hat{a}_j + \frac{1}{2}\right). \tag{1.1}$$

Here, $\hbar$ denotes the reduced Planck constant, $h/2\pi$, and ω_j is the frequency associated with the j-th mode. The operators $\hat{a}_j^\dagger$ and $\hat{a}_j$ are non-Hermitian boson creation and annihilation operators for excitations in mode j.

The operator product $\hat{a}^\dagger\hat{a}$ assumes particular significance, termed as the number operator or occupation number (representing the number of photons), denoted as $\hat{n}$.

By applying $\hat{a}^\dagger$, a set of normalized number states $|n_j\rangle$ is created, serving as eigenstates of the Hamiltonian $\hat{\mathcal{H}}_j$ for mode j. In the photons concept of view, $\hat{a}^\dagger$ adds a quantum energy, $\hbar\omega$, or a photon, to the j-th mode of the radiation field. Similarly, $\hat{a}$ subtracts a quantum energy.
The boson creation and annihilation operators follow the bosonic commutation rules:

$$\left[\hat{a}_k, \hat{a}_l^\dagger\right] = \delta_{lk} \quad \text{and} \quad \left[\hat{a}_k^\dagger, \hat{a}_l^\dagger\right] = [\hat{a}_k, \hat{a}_l] = 0\,. \tag{1.2}$$

In a quantum system, the operators $\hat{n}$ and $\hat{H}$ share the same set of eigenvectors if their commutation, i.e., $[\hat{n},\hat{\mathcal{H}}] = 0$, is satisfied. This means that both operators can be simultaneously diagonalized on a specific basis. This characteristic allows the state of the system to be precisely described in terms of definite values for both energy and particle number at the same time.

Photon number state

The quantized field can be characterized in terms of the energy eigenstates of its Hamiltonian. In general, the state of any radiation field can be expressed as a superposition of energy eigenstates:

$$|\Psi\rangle = \sum_n c_n |n\rangle\,. \tag{1.3}$$

Here, c_n represents the complex amplitude associated with the photon number state $|n\rangle$. Consequently, $|n\rangle$ denotes an energy eigenstate of a single-mode field with the energy eigenvalue E_n:

$$\hat{\mathcal{H}}|n\rangle = \hbar\omega\left(\hat{a}^\dagger\hat{a} + \frac{1}{2}\right)|n\rangle = \hbar\omega\left(\hat{n} + \frac{1}{2}\right)|n\rangle = E_n|n\rangle\,. \tag{1.4}$$

For the ground state, the energy eigenvalue takes the form:

$$\hat{\mathcal{H}}|0\rangle = \hbar\omega\left(\hat{a}^\dagger\hat{a} + \frac{1}{2}\right)|0\rangle = \frac{1}{2}\hbar\omega|0\rangle\,, \tag{1.5}$$

resulting in the lowest-energy eigenvalue, referred to as the zero-point energy $\hbar\omega/2$. The energy eigenvalues follow the relation $E_{n+1} = E_n + \hbar\omega$, giving:

$$E_n = \hbar\omega\left(n + \frac{1}{2}\right), \qquad n = 0, 1, 2, \ldots\,. \tag{1.6}$$

For the number operator $\hat{n}$, its action on the number state $|n\rangle$ is defined as:

$$\hat{n}\,|n\rangle = n\,|n\rangle\,. \tag{1.7}$$

In the context of multimode photon number states, such a state is simply a product of individual number states for all modes, expressed as:

$$|n_1\rangle\,|n_2\rangle\,|n_3\rangle\,.... \equiv |n_1, n_2, n_3, ...\rangle = |\{n_j\}\rangle\,. \tag{1.8}$$

This state serves as an eigenstate of the Hamiltonian operator $\hat{\mathcal{H}}$:

$$\hat{\mathcal{H}}\,|\{n_j\}\rangle = E\,|\{n_j\}\rangle\,. \tag{1.9}$$

The associated eigenvalue E is determined by the sum of energies across all modes:

$$E = \sum_j \hbar\omega_j \left(n_j + \frac{1}{2}\right). \tag{1.10}$$

These number states are mutually orthogonal, following the orthogonality relation:

$$\langle n_1, n_2, n_3, ...|n_1', n_2', n_3', ...\rangle = \delta_{n_1 n_1'}\delta_{n_2 n_2'}... \,. \tag{1.11}$$

When considering the actions of two distinct non-Hermitian operators, it can be articulated as:

$$\hat{a}_j\,|n_1, n_2, n_3, ...n_j, ...\rangle = \sqrt{n_j}\,|n_1, n_2, n_3, ...n_J - 1, ...\rangle\,, \tag{1.12a}$$

$$\hat{a}_j^\dagger\,|n_1, n_2, n_3, ...n_j, ...\rangle = \sqrt{n_j + 1}\,|n_1, n_2, n_3, ...n_J + 1, ...\rangle\,. \tag{1.12b}$$

These equations delineate the actions of the annihilation operator $\hat{a}_j$ and the creation operator $\hat{a}_j^\dagger$ on multimode number states. The square roots of n_j and $n_j + 1$ in the respective equations capture the quantum behavior of these operations.
The multimode vacuum state is represented as:

$$|\{0\}\rangle = |0_1, 0_2, 0_3, ...0_j, ...\rangle\,, \tag{1.13}$$

for which the action of the annihilation operator $\hat{a}_j$ results in:

$$\hat{a}_j\,|\{0\}\rangle = 0\,, \tag{1.14}$$

for all modes j. All possible number states can be generated from the vacuum state through:

$$|\{n_j\}\rangle = \prod_j \frac{\left(\hat{a}^\dagger\right)^{n_j}}{\sqrt{n_j!}}\,|\{0\}\rangle\,. \tag{1.15}$$

This expression encapsulates the generation of multimode number states from the vacuum state, illustrating the versatility and power of the creation operator.

Quantization of the electric field

We introduce the quantized vector potential at position r and time t through the non-Hermitian operators:

$$\hat{A}(r,t) = \sum_j \left(\frac{\hbar}{2\omega_j\varepsilon_0 V}\right)^{1/2} i\mathbf{e}_j \left[\hat{a}_j e^{i(\mathbf{k}_j r - \omega_j t)} + \hat{a}_j^\dagger e^{-i(\mathbf{k}_j r - \omega_j t)}\right]. \tag{1.16}$$

Here, ε_0 represents the vacuum permittivity, $\mathbf{e}_j$ is the real polarization vector of mode j, V is the volume of the free space modeled as a cavity, and $\mathbf{k}$ is the wave vector.
The electric field operator is expressed as:

$$\hat{E}(r,t) = i\sum_j \left(\frac{\hbar\omega_j}{2\varepsilon_0 V}\right)^{1/2} \mathbf{e}_j \left[\hat{a}_j e^{i(\mathbf{k}_j r - \omega_j t)} + \hat{a}_j^\dagger e^{-i(\mathbf{k}_j r - \omega_j t)}\right]. \tag{1.17}$$

It can be decomposed into positive and negative frequency components:

$$\hat{E}(r,t) = \sum_j \left[\hat{E}_j^{(+)}(r,t) + \hat{E}_j^{(-)}(r,t)\right]. \tag{1.18}$$

The positive and negative frequency components are related by $\hat{E}_i^{(-)}(r,t) = \hat{E}_i^{(+)}(r,t)^\dagger$, with † indicating the Hermitian conjugate. The positive part is defined as:

$$\hat{E}_i^{(+)}(r,t) = i\sum_j \left(\frac{\hbar\omega_j}{2\varepsilon_0 V}\right)^{1/2} \mathbf{e}_j \hat{a}_j e^{i(\mathbf{k}_j r - \omega_j t)}. \tag{1.19}$$

Following the introduction of the $\hat{A}$ and $\hat{E}$ operators, we can use the relations $\hat{E} = -\frac{\partial \hat{A}}{\partial t}$ and $\hat{B} = \nabla \times \hat{A}$ to define the Hamiltonian of the electromagnetic field in terms of the electric and magnetic fields. The Hamiltonian $\mathcal{H}$ therefore has the following form:

$$\hat{\mathcal{H}} = \frac{1}{2}\left(\varepsilon_0 E^2 + \frac{1}{\mu_0} B^2\right). \tag{1.20}$$

Substituting $\hat{E}$ and $\hat{B}$ into this expression yields:

$$\hat{\mathcal{H}} = \frac{1}{2}\left(\varepsilon_0 \left(-\frac{\partial \hat{A}}{\partial t}\right)^2 + \frac{1}{\mu_0}\left(\nabla \times \hat{A}\right)^2\right). \tag{1.21}$$

Substituting the eq. (1.16) into $\mathcal{H}$ enables us to express the Hamiltonian in terms of creation and annihilation operators. The resulting Hamiltonian represents a collection of harmonic oscillators, thereby reflecting the quantized nature of the system.

Continuous-mode operators

In the contest of non-monochromatic fields, the continuous-mode creation and annihilation operators are defined as

$$\left[\hat{a}(\omega), \hat{a}^\dagger(\omega')\right] = \delta(\omega - \omega') \quad \text{and} \quad \left[\hat{a}^\dagger(\omega), \hat{a}^\dagger(\omega')\right] = \left[\hat{a}(\omega), \hat{a}(\omega')\right] = 0. \tag{1.22}$$

The number operator in this case is

$$\hat{n}_j = \int d\omega \hat{a}_j^\dagger \hat{a}_j(\omega), \tag{1.23}$$

and the positive component of the electric field becomes

$$\hat{E}_j^{(+)}(r,t) = \int d\omega \varepsilon_j \mathbf{e}_j \hat{a}_j e^{i(k_j r - \omega_j t)}, \tag{1.24}$$

where $\varepsilon_j = \left(\frac{\hbar\omega_j}{2\varepsilon_0 V}\right)^{1/2.}$.

Pulsed Light Consideration

When producing photon wave packets using pulsed light, the operator is expressed as:

$$\hat{a}_{j,k}^{\dagger} = \int d\omega F_j(\omega)\hat{a}_j^{\dagger}(\omega)\,, \tag{1.25}$$

where $F_j(\omega)$ is the spectral profile of the photon wavepacket in mode j, and the positive frequency component becomes

$$\hat{E}_j^{(+)}(r,t) = \int d\omega \varepsilon_j \mathbf{e}_j F_j(\omega)\hat{a}_j(\omega)e^{i(k_j r-\omega_i t)}\,. \tag{1.26}$$

If the non-zero band of the spectrum is significantly narrow around ω_i, the following approximation is applied:

$$\hat{E}_i^{(+)}(r,t) \simeq \varepsilon_i \mathbf{e}_i e^{i(k_i r-\omega_i t)} \int d\omega F_i(\omega)\hat{a}_i(\omega)\,. \tag{1.27}$$

Quadrature operators of a single-mode field

Quadrature operators play a crucial role as fundamental mathematical tools. Denoted conventionally as $\hat{X}_1$ and $\hat{X}_2$, these operators, respectively, follow the canonical commutation relation:

$$[\hat{X}_1, \hat{X}_2] = \frac{i}{2}\,. \tag{1.28}$$

This equation represents the quantum uncertainties related to making measurements of position and momentum at the same time. It helps to explain the basic principles of quantum optics. The quadrature operators can be expressed using the two field operators, $\hat{a}$ and $\hat{a}^{\dagger}$ as:

$$\hat{X}_1 = \frac{1}{2}\left(\hat{a} + \hat{a}^{\dagger}\right)\,, \tag{1.29a}$$

$$\hat{X}_2 = \frac{1}{2i}\left(\hat{a} - \hat{a}^{\dagger}\right)\,. \tag{1.29b}$$

These expressions provide a detailed representation of the quadrature operators within the framework of the electric field, establishing a basis for the analysis of the quantum field characteristics.

The uncertainty relation holds:

$$\langle(\Delta\hat{X}_1)^2\rangle\,\langle(\Delta\hat{X}_2)^2\rangle \geq \frac{1}{16}\,. \tag{1.30}$$

Here $\Delta\hat{X}_1$ and $\Delta\hat{X}_2$ are the uncertainties associated with $\hat{X}_1$ and $\hat{X}_2$. Additionally, for number states $|n\rangle$, it is observed that:

$$\langle n|\hat{X}_1|n\rangle = \langle n|\hat{X}_2|n\rangle = 0\,. \tag{1.31}$$

Additionally,

$$\langle n|\hat{X}_1^2|n\rangle = \langle n|\hat{X}_2^2|n\rangle = \frac{1}{4}(2n+1)\,. \tag{1.32}$$

This implies that for a number state, the uncertainties in both quadratures are equal. Furthermore, the vacuum state ($n = 0$) minimizes the uncertainty product, as evidenced by:

$$\langle(\Delta\hat{X}_1)^2\rangle = \langle(\Delta\hat{X}_2)^2\rangle = \frac{1}{4}\,. \tag{1.33}$$

1.1.2 Density matrix

The density matrix [35], also known as the density operator, is a mathematical tool used in quantum mechanics to describe the statistical state of a physical system. It facilitates the analysis of quantum system evolution within a statistical framework and the computation of various physical observables.
For a pure state $|\psi\rangle$, if we define the density matrix as:

$$\rho = |\psi\rangle \langle\psi| , \tag{1.34}$$

the expectation value of an observable $\hat{O}$ can be expressed:

$$\langle\hat{O}\rangle = \langle\psi|\hat{O}|\psi\rangle . \tag{1.35}$$

Alternatively, the expectation value can be expressed in terms of the density matrix as

$$\langle\hat{O}\rangle = Tr(\rho\hat{O}) . \tag{1.36}$$

Real-world scenarios frequently involve systems in mixed states, characterized as a statistical combination of pure states. In such instances, the density matrix takes the form as

$$\rho = \sum_i p_i |\psi_i\rangle \langle\psi_i| . \tag{1.37}$$

Here, p_i is the probability of the system being in the pure state $|\psi_i\rangle$ and $\sum_i p_i$ =1. In the case where only one of the coefficients p_i is non-zero, the state is pure and $\hat{\rho} = \hat{\rho}^2$; otherwise, it is a mixed state. The density matrix is Hermitian, enabling its diagonalization through a unitary transformation. Its utility extends to scenarios involving multiple subsystems. For a composite system A and B, the density operator ρ_A is effectively described by the reduced density operator for system A [2]:

$$\hat{\rho}_A \equiv Tr_B\{\hat{\rho}_{AB}\}. \tag{1.38}$$

The partial trace over B (Tr_B) allows the extraction of accurate observable quantities related to subsystems within a composite quantum system. It is defined by

$$Tr_B\{|a_1\rangle \langle a_2| \times |b_1\rangle \langle b_2|\} \equiv |a_1\rangle \langle a_2| \, Tr\{|b_1\rangle \langle b_2|\}. \tag{1.39}$$

The purity of a quantum system can be quantified starting from the density matrix. Purity ($\mathcal{P}$) serves as a metric to understand how closely a state resembles a pure state in quantum mechanics, calculated as the trace of the square of the density matrix (ρ^2) [35]:

$$\mathcal{P} = Tr(\rho^2) . \tag{1.40}$$

In the scenario of a pure state, where the density matrix functions as a projection operator onto that state, the square of the density matrix ($\rho^2 = \rho$) results in a purity of 1. Conversely, for a mixed state—a statistical ensemble of pure states—the density matrix is expressed as a sum of outer products of individual pure states, each weighted by their probabilities. The purity of such a state is less than 1, signifying the presence of mixedness or uncertainty. Generally, the lower purity limit for a mixed state with N dimensions is $\mathcal{P} = 1/N$.
The degree of entanglement in a system is closely linked to the purity of the subsystem states involved in the correlation. For maximally entangled states, the purity serves as an indicator of the degree of entanglement. Conversely, when the system exhibits no correlation ($N = 1$), the subsystem states are pure, and the state of the composite system is separable into the produced states of the subsystems. In cases of maximally

entangled states ($N > 1$), the composite states become completely mixed, signifying the impossibility of assigning a defined pure state to the subsystems.

1.1.3 The Schmidt decomposition

A common mathematical method in quantum mechanics for representing a bipartite quantum state is the Schmidt decomposition [36]. This method is particularly useful when dealing with composite quantum systems and understanding the separability of the two subsystems.

Consider orthonormal bases $\{|a_i\rangle, i = 1,2,3,...\}$ and $\{|b_j\rangle, j = 1,2,3,...\}$ for subsystems $\mathcal{U}$ and $\mathcal{V}$ respectively. For any state $|\Psi\rangle \in \mathcal{H} = \mathcal{H}_\mathcal{U} \otimes \mathcal{H}_\mathcal{V}$, it can be expressed as

$$|\Psi\rangle = \sum_{i,j=1} c_{ij} |a_i\rangle \otimes |b_j\rangle , \tag{1.41}$$

where c_{ij} are non-negative coefficients satisfying $\sum_{ij} |c_{ij}|^2 = 1$. The density matrix for the composite system is given by

$$\hat{\rho} = |\Psi\rangle \langle\Psi| = \sum_{i,j,k,l} c_{ij} c^*_{kl} |a_i\rangle \langle a_k| \otimes |b_j\rangle \langle b_k| , \tag{1.42}$$

with $c_{ij}c^*_{kl} = \rho_{ijkl}$. For a pure state described by a projection operator $\hat{\rho}$, an orthonormal basis $\{|u_i\rangle\} \in \mathcal{H}_\mathcal{U}$ and $\{|v_i\rangle\} \in \mathcal{H}_\mathcal{V}$ exist such that

$$|\Psi\rangle = \sum_i g_i |u_i\rangle \otimes |v_i\rangle , \tag{1.43}$$

where the number of terms in the sum, referred to as the Schmidt rank, provides information about the entanglement between the two subsystems. In terms of the density operator $\hat{\rho}$, this becomes

$$\hat{\rho} = \sum_{i,k} g_i g^*_k |u_i\rangle \langle u_k| \otimes |v_i\rangle \langle v_k| , \tag{1.44}$$

with g_i as the Schmidt coefficients and $\sum_i |g_i|^2 = 1$.

The Schmidt decomposition stands out by requiring only a single summation index, unlike the typical basis change involving two indices. This representation illustrates that for a pure state in subsystem A, there exists only one nonzero Schmidt coefficient, resulting in a factorizable state and simplifying the quantum system's representation.

It's important to note some remarks [36]:

1. The single-index summation in the Schmidt decomposition extends to the smaller of the dimensions of the two Hilbert spaces $\mathcal{H}_\mathcal{U}$ and $\mathcal{H}_\mathcal{V}$;
2. The decomposition is not unique and generally cannot be extended to multipartite systems with more than two subsystems;
3. In the chosen bases for the Schmidt decomposition, both $\rho_\mathcal{U}$ and $\rho_\mathcal{V}$ are diagonal and have the same positive spectrum.

The purity of a state in the context of Schmidt decomposition can be expressed in terms of the Schmidt coefficients. Referring to the density matrix previously calculated in eq. (1.40), the purity $\mathcal{P}$ is defined as:

$$\mathcal{P}_\mathcal{U} = Tr(\hat{\rho}^2_\mathcal{U}) , \tag{1.45a}$$

$$\mathcal{P}_v = Tr(\hat{\rho}_v^2)\,, \tag{1.45b}$$

where the reduced density matrices are

$$\hat{\rho}_u = Tr_v(\hat{\rho}) = \sum_i |g_i|^2 \,|u_i\rangle \,\langle u_i|\,, \tag{1.46a}$$

$$\hat{\rho}_v = Tr_u(\hat{\rho}) = \sum_i |g_i|^2 \,|v_i\rangle \,\langle v_i|\,. \tag{1.46b}$$

The Schmidt number (K) measuring the number of Schmidt modes is defined as [37]:

$$K \equiv \frac{1}{\sum_i |g_i|^4} \equiv \frac{1}{Tr(\hat{\rho}_u^2)} \equiv \frac{1}{Tr(\hat{\rho}_v^2)}\,, \tag{1.47}$$

from which it is easy to deduce the following relationship

$$\mathcal{P} = \sum_i |g_i|^4 = \frac{1}{K}\,. \tag{1.48}$$

When $K = 1$, the state is pure. As K increases, the entanglement between subsystems increases, making the total state less factorizable.

1.1.4 Coherent light and squeezed light

Coherent State

In quantum mechanics, a coherent state [38, 39] is a unique quantum state that exhibits characteristics similar to classical states. Often regarded as the quantum analog of the simple harmonic motion of a classical harmonic oscillator, coherent states are defined as eigenstates of the annihilation operator:

$$\hat{a}\,|\alpha\rangle = \alpha\,|\alpha\rangle\,, \tag{1.49}$$

where the eigenvalue $\alpha = ae^{i\phi}$ with $a = |\alpha|$. By relating the equations (1.49) and (1.15), we can express the state α as [39]:

$$|\alpha\rangle = e^{-|\alpha|^2/2} \sum_{n=0}^{\infty} \frac{\alpha^n}{\sqrt{n!}}\,|n\rangle\,. \tag{1.50}$$

Here, α denotes the displacement properties of the coherent state, while $|n\rangle$ represents the number of states in the harmonic oscillator.

It is possible to define the coherent state using the displacement of the vacuum. The displacement operator $\hat{D}(\alpha)$ is define as [40]:

$$\hat{D}(\alpha) = \exp\left(\alpha\hat{a}^\dagger - \alpha^*\hat{a}\right). \tag{1.51}$$

The coherent states are given as:

$$|\alpha\rangle = \hat{D}(\alpha)\,|0\rangle\,. \tag{1.52}$$

Applying the displacement operator to the vacuum state $|0\rangle$ results in the generation of a coherent state $|\alpha\rangle$.

It is important to introduce several properties of the coherent states. The average number of photons in the coherent state $|\alpha\rangle$ is given by:

$$\bar{n} = \langle \hat{n} \rangle = \langle \alpha | \hat{n} | \alpha \rangle = |\alpha|^2, \tag{1.53}$$

where the variance is

$$\Delta n = \sqrt{\langle \alpha | \hat{n}^2 | \alpha \rangle - \langle \alpha | \hat{n} | \alpha \rangle^2} = \sqrt{\bar{n}} = \alpha \,. \tag{1.54}$$

This characteristic indicates a Poisson process, with the fractional uncertainty in the number of photons given by:

$$\frac{\Delta n}{\bar{n}} = \frac{1}{\sqrt{\bar{n}}} \,, \tag{1.55}$$

which decreases as $\bar{n}$ increases. When measuring the number of photons in the field, the probability of detecting exactly n photons is:

$$P_n = |\, \langle n | \alpha \rangle \,|^2 = e^{-|\alpha|^2} \frac{|\alpha|^{2n}}{n!} = e^{-\bar{n}} \frac{\bar{n}^n}{n!} \,. \tag{1.56}$$

This distribution follows a Poisson distribution with a mean denoted by $\bar{n}$. Let's consider the case where the intensity of a coherent field is significantly reduced to the mean number $\bar{n} \ll 1$ ($\alpha \ll 1$) referred to as the weak coherent state (WCS). We observe a higher probability of the field being in its fundamental state ($n = 0$), with a decreasing probability for states $n = 1$ and $n = 2$, respectively. The probabilities associated with generating states where $\bar{n} \gg 2$ become negligible. Utilizing a first-order approximation, the measured field state can be effectively approximated as [38]:

$$|\alpha\rangle = |0\rangle + \alpha \,|1\rangle + o(\alpha^2) \ldots \,. \tag{1.57}$$

This behavior makes the WCS useful for representing single-photon state.

Another aspect of the coherent state involves its description in terms of its quadrature dimensionless variables, as expressed in eq. (1.33):

$$\langle (\Delta \hat{X}_1)^2 \rangle_\alpha = \langle (\Delta \hat{X}_2)^2 \rangle_\alpha = \frac{1}{4} \,, \tag{1.58}$$

where $\hat{X}_1 = (\omega/\hbar)^{1/2} \hat{q}$ and $\hat{X}_2 = (\omega\hbar)^{-1/2} \hat{p}$ where $\hat{q}$ and $\hat{p}$ are the canonical variables of the harmonic oscillator. We can write

$$\Delta p_0 = \left(\frac{1}{2} \hbar \omega \right)^{1/2} , \tag{1.59a}$$

$$\Delta q_0 = \left(\frac{\hbar}{2\omega} \right)^{1/2} . \tag{1.59b}$$

By proving that these states contain vacuum fluctuations, the coherent states contain equal, vacuum-like uncertainties in each quadrature, minimizing (in fact, equalizing) the uncertainty product with respect to the field quadrature operators. This property provides another way to define coherent states.

Squeezed State

A squeezed state is a quantum state where the equality relation between the two observables' uncertainty, Δp_s and Δq_s, is no longer applicable [14, 41]. This deviation,

known as quantum squeezing, is characterized by one of the following inequalities:

$$\Delta p_s < \left(\frac{1}{2}\hbar\omega\right)^{1/2}, \qquad \Delta q_s > \left(\frac{\hbar}{2\omega}\right)^{1/2}, \tag{1.60a}$$

or

$$\Delta p_s > \left(\frac{1}{2}\hbar\omega\right)^{1/2}, \qquad \Delta q_s < \left(\frac{\hbar}{2\omega}\right)^{1/2}, \tag{1.60b}$$

where s indicates the term squeezing. When one of these conditions is met, the fluctuations in one quadrature are compressed, resulting in reduced noise compared to a coherent or vacuum state. However, to uphold the uncertainty principle, the fluctuations in the complementary quadrature must increase. Hence, while one variance is reduced (squeezed), the other expands. Mathematically, this can be expressed in terms of the ground state uncertainties as:

$$\Delta q_s = e^{-r}\Delta q_0\,, \tag{1.61a}$$

$$\Delta p_s = e^{r}\Delta p_0\,, \tag{1.61b}$$

where r is the squeeze parameter.

A more general generator of squeezed states is given by the unitary squeeze operator $\hat{S}$. It is responsible for transforming the vacuum state into a squeezed state and it can be written as:

$$\hat{S} = \exp(-\xi\hat{a}^{\dagger 2} + \xi^{*}\hat{a}^{2})\,, \tag{1.62}$$

where $\xi = re^{i\theta}$ is the complex squeeze parameter, representing the strength of squeezing with $0 \leq r < \infty$ and $0 \leq \theta \leq 2\pi$.

The canonical variables are compressed and expanded along directions inclined at angles $\theta/2$ to the $\hat{X}_1$ and $\hat{X}_2$ axes, under this transformation.

Preparing the initial state of light as a squeezed state allows for the reduction of uncertainty in one of the optical field quadratures [42].

1.2 Entangled Biphoton state

Let's discuss the quantum representation of biphoton (two-photon) states [38] and how a composite system composed of two photons can be characterized, even if the subsystems undergo significant spatial separation. According to quantum theory, a composite system can be described within a Hilbert space, even if the subsystems are spatially separate. This Hilbert space is constructed as the direct or tensor product of the individual Hilbert spaces associated with the two subsystems, as shown in the equation:

$$H = H_1 \otimes H_2\,. \tag{1.63}$$

If the state $|\Psi_1\rangle \in H_1$ and the state $|\Psi_2\rangle \in H_2$, then their composite state $|\Psi\rangle$ can be expressed as:

$$|\Psi\rangle = |\Psi_1\rangle \otimes |\Psi_2\rangle\,. \tag{1.64}$$

The inner product between two composite states $|\Psi\rangle$ and $|\Psi'\rangle$ is given by:

$$\langle\Psi|\Psi'\rangle = \langle\Psi_1| \otimes \langle\Psi_2|\Psi_1'\rangle \otimes |\Psi_2'\rangle = \langle\Psi_1|\Psi_1'\rangle\,\langle\Psi_2|\Psi_2'\rangle\,. \tag{1.65}$$

Now, considering the two orthogonal Schmidt bases $|m\rangle$ (orthogonal to H_1) and $|n\rangle$ (orthogonal to H_2), the composite system can exhibit two different configurations: independent or correlated/entangled.
In the case of independence, the wavefunction can be written as:

$$|\Psi\rangle = \sum_{m,n} C_{m,n} |m\rangle |n\rangle , \tag{1.66}$$

where the coefficient $C_{m,n}$ is factorizable, i.e., $C_{m,n} = C_m C_n$. Conversely, in a correlated or entangled scenario, although the wavefunction remains similar, the coefficient $C_{m,n}$ is non-factorizable, resulting in a non-factorizable state. The two subsystems are described by a correlated state dependent on the form of $C_{m,n}$.

An example of an entangled state is the two-photon state. The simplest two-photon state is the Fock state:

$$|\Psi\rangle = \hat{a}_1^\dagger(\omega)\hat{a}_2^\dagger(\omega') |0\rangle = |0,..,0,1_1(\omega),0,...,1_2(\omega'),0\rangle . \tag{1.67}$$

In general, the two-photon Fock state can be represented as:

$$\Psi = \iint_{\omega} \iint_{\omega'} f(\omega,\omega')\hat{a}_1^\dagger(\omega)\hat{a}_2^\dagger(\omega') |0\rangle , \tag{1.68}$$

where $\iint$ means that is possible to have a sum or an integral depending on the state. The $f(\omega,\omega')$ represents the amplitude of probability for the quantized state to be in the two-photon Fock state.

Now, focusing on $f(\omega,\omega')$, if it is factorable ($f(\omega,\omega') = f(\omega)f(\omega')$), then the state is factorable into the product state of two independent single photons. Conversely, if the coefficient is not factorable, we are dealing with an entangled two-photon state.

Various mechanisms, such as atomic cascade [43], can generate entangled two-photon states. In photonics, this can be achieved through nonlinear parametric processes like SPDC [44, 45] or sFWM [46–48].

1.2.1 Squeezing parameter

As previously noted, it is feasible to produce two-mode squeezed vacuum states through nonlinear processes like SPDC or sFWM. Before delving into the details of these processes, let us establish some fundamental aspects of these two-mode squeezed vacuum states.

In this section, we introduce the standard description of two types of squeezers: the single-beam squeezer, also known as the degenerate case, and the twin-beam squeezer, known as the non-degenerate case [28].

Degenerate squeezed state

In the degenerate scenario, the Hamiltonian describing the single mode squeezing is given by:

$$\int dt \hat{\mathcal{H}}_{SMS} = i\frac{\hbar}{2}\left(\xi\hat{a}^{\dagger 2} + \xi^*\hat{a}^2\right) , \tag{1.69}$$

where "SMS" denotes single-mode squeezing. The evolution of any quantum mechanical system is determined by its Hamiltonian $\mathcal{H}(t)$ through the Schrödinger equation.

This leads to the unitary operator $\hat{\mathcal{U}}_{SMS}$:

$$\hat{\mathcal{U}}_{SMS} = e^{-\frac{i}{\hbar}\int dt \mathcal{H}_{SMS}} = e^{1/2\left(\xi \hat{a}^{\dagger 2} + \xi^* \hat{a}^2\right)}. \tag{1.70}$$

Following the steps outlined in the reference [12], we derive the following relationship for this degenerate scenario:

$$|\Psi\rangle_{SMS} = \mathcal{U}_{SMS}\,|0\rangle = \frac{1}{\sqrt{\cosh r}} \sum_{n=0}^{\infty} e^{in\phi} \tanh^n r \frac{\sqrt{2n!}}{2^n n!}\,|2n\rangle\,. \tag{1.71}$$

Here, $|n\rangle$ represents the Fock states defined as $|n\rangle = \frac{\hat{a}^{\dagger n}}{\sqrt{n!}}|0\rangle$. In a multimode scenario under low-gain conditions, a simplified description is obtained:

$$\hat{\mathcal{U}}_{MMS} = \exp\left(\frac{1}{2}\sum_{k,l} J_{kl}\hat{a}_l^{\dagger}\hat{a}_k^{\dagger} - \text{h.c.}\right), \tag{1.72}$$

The unitary operator $\mathcal{U}$ can then be described as a tensor product of N beam squeezers:

$$\begin{aligned} |\Psi\rangle_{MMS} &= \exp\left(\frac{1}{2}\sum_{k,l} J_{kl}\hat{a}_l^{\dagger}\hat{a}_k^{\dagger} - \text{h.c..}\right)|0\rangle \\ &= \exp\left(\frac{1}{2}\sum_{\lambda=1} r_\lambda A_\lambda^{\dagger 2} - \text{h.c..}\right)|0\rangle \\ &= \bigotimes_{\lambda=1} \exp\left(\frac{1}{2} r_\lambda A_\lambda^{\dagger 2} - \text{h.c..}\right)|0\rangle \\ &= \bigotimes_{\lambda} \mathcal{S}_\lambda^{a^2}(-r_\lambda)\,|0\rangle\,, \end{aligned} \tag{1.73}$$

with $A_\lambda^{\dagger} = \sum_{k=1} a_k^{\dagger} F_{k\lambda}$ represents the joint amplitude of the squeezed state, defined as $J = F(\bigotimes_{\lambda=1} r_\lambda)F^T$ and $\mathcal{S}_\lambda^{a^2}(-r_\lambda) = \exp(\frac{1}{2} r_\lambda A_\lambda^{\dagger 2})$ [49].
Considering the eq. (1.71) it is possible to define the probability of detecting $2n$ photons in the field as

$$\mathcal{P}_{2n} = |\,\langle 2n|\Psi\rangle\,|^2 = \frac{(2n)!}{2^{2n}(n!)^2}\frac{(\tanh r)^{2n}}{\cosh r}\,, \tag{1.74}$$

while the probability to detect $2n+1$ photons it is

$$\mathcal{P}_{2n+1} = |\,\langle 2n+1|\Psi\rangle\,|^2 = 0\,. \tag{1.75}$$

The photon probability distribution for a squeezed vacuum state oscillates, with the probability vanishing for all odd photon numbers, as illustrated in Fig. 1.1(a). Despite the oscillatory pattern, the distribution resembles that of thermal radiation, although the squeezed vacuum state is pure while the thermal state is mixed.
The statistical distribution of photons in this degenerate case is given by:

$$\langle \hat{n} \rangle = \langle \Psi | \hat{a}^{\dagger}\hat{a} | \Psi \rangle = \frac{1}{(\cosh r)^2} \sum_{n=0}^{\infty} n(\tanh r)^{2n} = \ldots = (\sinh r)^2\,. \tag{1.76}$$

It is useful to write the variance of the squeezed state as:

$$\langle \Delta\hat{n} \rangle = \langle \Psi | (\hat{a}^{\dagger}\hat{a} - \langle \hat{n} \rangle)^2 | \Psi \rangle = (\sinh r)^2(1 + (\sinh r)^2)\,. \tag{1.77}$$

Non-degenerate squeezed state

In this analysis, we focus on a specific scenario involving the partitioning of modes into two categories: idler and signal modes, denoted as a_i and b_i respectively. The canonical commutation relations are satisfied for these modes. The unitary operator $\mathcal{U}$ for this non-degenerate scenario is described as:

$$\mathcal{U}_{TMS} = \exp\left(\sum_{i=1}^{l_a}\sum_{i=1}^{l_b} J_{ij}^{a,b} a_i^\dagger b_j^\dagger - \text{h.c.}\right) . \tag{1.78}$$

The two-mode squeezed (TMS) vacuum states, in terms of number states, are represented as:

$$|\Psi\rangle_{TMS} = \mathcal{U}_{TMS}\,|0\rangle = \frac{1}{\cosh r}\sum_{n=0}^{\infty}(-1)^n e^{in\phi}(\tanh r)^n\,|n,n\rangle\,. \tag{1.79}$$

Similar to the degenerate case, the unitary operator $\mathcal{U}$ can be described as a tensor product of N beam squeezers:

$$\begin{aligned}
|\Psi\rangle_{TMS} &= \exp\left(\frac{1}{2}\sum_{k,l} J_{kl}\hat{a}_l^\dagger \hat{b}_k^\dagger - \text{h.c.}\right)|0\rangle \\
&= \exp\left(\frac{1}{2}\sum_{\lambda=1} r_\lambda A_\lambda^\dagger B_\lambda^\dagger - \text{h.c.}\right)|0\rangle \\
&= \bigotimes_{\lambda=1}\exp\left(\frac{1}{2} r_\lambda A_\lambda^\dagger B_\lambda^\dagger - \text{h.c.}\right)|0\rangle \\
&= \bigotimes_{\lambda} \mathcal{S}_\lambda^{a,b}(-r_\lambda)\,|0\rangle\ ,
\end{aligned} \tag{1.80}$$

with

$$A_\lambda^\dagger = \sum_{k=1}^{l_a} a_k^\dagger F_{k,\lambda}^a\,, \tag{1.81a}$$

$$B_\lambda^\dagger = \sum_{k=1}^{l_b} b_k^\dagger F_{k,\lambda}^b\,. \tag{1.81b}$$

From eq. (1.79) the joint probability $\mathcal{P}n_a, n_b$ of finding n_a photons in mode a and n_b in mode b is given by:

$$\mathcal{P}(n_a, n_b) = |\,\langle n_a, n_b|\Psi\rangle\,|^2 = \frac{(\tanh r)^{2n}}{(\cosh r)^2}\delta_{n_a,n}\delta_{n_b,n}\,. \tag{1.82}$$

Fig. 1.1(b) illustrates the probability $\mathcal{P}(n_a, n_b)$ concerning the variables n_a and n_b. It is evident that the joint probability exhibits a monotonic decrease along the diagonal where n_a equals n_b.
To analyze the properties of individual modes, we introduce the density operator for the state $|\Psi\rangle_{TMS}$:

$$\hat{\rho}_a = \sum_{n=0}^{\infty}\frac{(\tanh r)^{2n}}{(\cosh r)^2}\,|n_a\rangle\,\langle n_a|\ , \tag{1.83a}$$

$$\hat{\rho}_b = \sum_{n=0}^{\infty}\frac{(\tanh r)^{2n}}{(\cosh r)^2}\,|n_b\rangle\,\langle n_b|\ . \tag{1.83b}$$

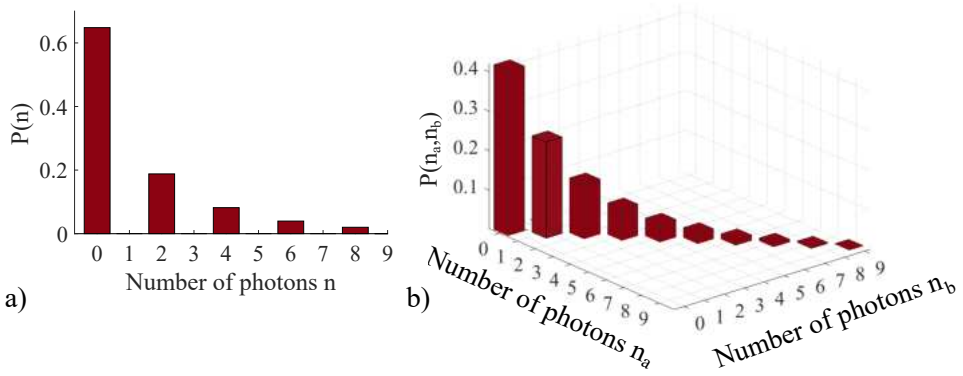

Figure 1.1: a) The probability $\mathcal{P}_n$ for the degenerate squeezed vacuum state for $r = 1$. b) The probability $\mathcal{P}_{n_1,n_2}$ for the non-degenerate squeezed vacuum state for $r = 1$.

The probability of finding n photons in a single mode a or b is given by:

$$\mathbf{P}_n^{(a/b)} = \langle n|\hat{\rho}_{a/b}|n\rangle = \frac{(\tanh r)^{2n}}{(\cosh r)^2}\,. \tag{1.84}$$

Due to correlations and symmetry between the modes, the average photon number and the variance in each mode are the same:

$$\langle \hat{n}_i\rangle = (\sinh r)^2\,, \tag{1.85}$$

$$\langle \Delta\hat{n}_i\rangle = (\sinh r)^2(1+(\sinh r)^2)\,. \tag{1.86}$$

This implies that the radiation field in one mode, when the other is neglected within the context of the two-mode compressed vacuum, resembles radiation from a thermal source. However, $\langle \Delta\hat{n}_i\rangle > \langle \hat{n}_i\rangle$ $(i = a, b)$, indicating super-Poissonian photon statistics for both modes. Indeed, the squeezed source exhibits emission statistics that can range between thermal and Poissonian distributions [50].

1.2.2 Photon statistics and second order coherence function

The investigation of photon statistics is fundamental for understanding the behavior of light, offering insights into the distribution and correlation patterns of photons within a given field. To explore this domain, the concepts of "bunching" and "anti-bunching" are introduced [51].

Bunching and anti-bunching statistics

Temporal correlations between photon detections can be qualitatively understood through observations of bunching and anti-bunching behaviors. While photon anti-bunching is a quantum phenomenon observed in nonclassical light sources, photon bunching is associated with classical light sources. The definitions of bunching and antibunching are shown in Fig. 1.2. Assume that each row's spheres correspond to a collection of photons' locations along a timeline. (They might also stand for the timings of arrival at a detector.)

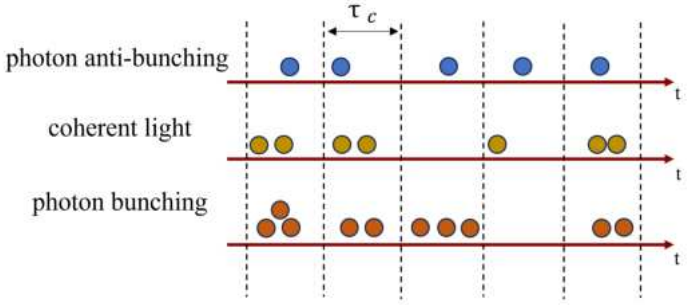

Figure 1.2: Detection of photons as a function of time t. The τ_c is the coherence time. In blue the anti-bunching photons, in gold the Poissonian photons (coherent light) and in orange the bunching photons.

In the central row, coherent photons are represented by gold spheres. This coherent state displays Poissonian photon number statistics, where each sphere's position is independent of others, resembling random arrangements. Such a source, characterized by Poissonian statistics, exhibits neither bunching nor anti-bunching behavior.

The lower row, depicted in orange, illustrates photons exhibiting bunching behavior. These photons tend to cluster together more frequently compared to independent particles.

The upper row, shown in blue, represents particles demonstrating anti-bunching behavior. In this scenario, there is a reduced probability of detecting a second photon when one has been observed at an earlier time.

Second order coherence function

To characterize these statistics, it is useful to introduce the second-order coherence function $g^{(2)}$. It serves as a fundamental concept in quantum optics, providing a means to quantify the degree of bunching or anti-bunching and offering insights into the statistical properties of photon distribution over time. Mathematically, the second-order coherence function between two modes j and k at a fixed position r is defined as [52]:

$$g^{(2)}_{j,k}(\tau) = \frac{\langle \hat{E}^{(-)}_j(r,t)\hat{E}^{(-)}_k(r,t+\tau)\hat{E}^{(+)}_k(r,t+\tau)\hat{E}^{(+)}_j(r,t)\rangle}{\langle \hat{E}^{(-)}_j(r,t)\hat{E}^{(+)}_j(r,t)\rangle \langle \hat{E}^{(-)}_k(r,t+\tau)\hat{E}^{(+)}_k(r,t+\tau)\rangle}, \tag{1.87}$$

which represents the conditional probability of detecting a photon at $t+\tau$ given that one was detected at t, where $\tau = t_2 - t_1$ and t_1 and t_2 are the detection times of the two modes.
In the case where only one mode is measured ($j = k$) and in the presence of a stationary source (e.g., continuous-wave source), the second-order coherence function is defined as the normalized correlation function of the photon field operators:

$$g^{(2)}(\tau) = \frac{\langle \hat{a}^\dagger(t)\hat{a}^\dagger(t+\tau)\hat{a}(t+\tau)\hat{a}(t)\rangle}{\langle \hat{a}^\dagger(t)\hat{a}(t)\rangle \langle \hat{a}^\dagger(t+\tau)\hat{a}(t+\tau)\rangle}, \tag{1.88}$$

with $\tau = 0$, and recalling the relation $\hat{n} = \hat{a}^\dagger \hat{a}$, we derive [53]:

$$\begin{aligned} g^{(2)}(0) &= \frac{\langle \hat{a}^\dagger(t)\hat{a}^\dagger(t)\hat{a}(t)\hat{a}(t)\rangle}{\langle \hat{a}^\dagger(t)\hat{a}(t)\rangle \langle \hat{a}^\dagger(t)\hat{a}(t)\rangle} = \frac{\langle \hat{n}(t)(\hat{n}(t)-1)\rangle}{\langle \hat{n}(t)\rangle^2} \\ &= 1 + \frac{\langle (\Delta\hat{n})^2\rangle - \langle \hat{n}\rangle}{\langle \hat{n}\rangle^2}, \end{aligned} \tag{1.89}$$

Where $(\Delta\hat{n}) = \langle \hat{n}^2\rangle - \langle \hat{n}\rangle^2$ represents the variance. It is important to note that $g^{(2)}$ remains unchanged even if the field under investigation is affected by losses, assuming uniform losses across all modes [53]. For pulsed sources, a similar treatment yields the discrete analog of $g^{(2)}[0]$:

$$g^{(2)}[0] = \frac{\langle \hat{a}^\dagger[l]\hat{a}^\dagger[l]\hat{a}[l]\hat{a}[l]\rangle}{\langle \hat{a}^\dagger[l]\hat{a}[l]\rangle \langle \hat{a}^\dagger[l]\hat{a}[l]\rangle} = \frac{\langle \hat{n}(\hat{n}-1)\rangle}{\langle \hat{n}\rangle^2}, \tag{1.90}$$

where l is the integer indicating the pulse number and the average is taken over l. In the case of pulsed sources, photon statistics are averaged throughout the pulse.

For coherent state $|\alpha\rangle$ described in eq. (1.50), it follows that:

$$g^{(2)}(0) = 1, \tag{1.91}$$

indicating that the probability of a delayed coincidence is independent of time, where $(\Delta\hat{n})^2 = \hat{n}$. In the case of the super-Poissonian field, it can be shown that:

$$1 < g^{(2)}(0) \leq 2, \tag{1.92}$$

typical of bunching behavior where the variance is larger than the mean value, indicating a higher probability of detecting coincident photons.
In the case of the variance is smaller than the mean value, the anti-bunching behavior is observed, and the $g^{(2)}(0)$ is:

$$g^{(2)}(0) \leq 1, \tag{1.93}$$

here we observe the sub-Poissonian light. In addition, $g^{(2)}(0) < 1/2$ is often defined as the condition for a single photon behavior [18].
In Fig. 1.3 is reported the $g^{(2)}(\tau)$ for perfect super-Poissonian ($g^{(2)}(0) = 2$), Poissonian ($g^{(2)}(0) = 1$) and perfect sub-Poissonian ($g^{(2)}(0) = 0$) statistics for CW (a) and Pulsed (b) sources.

1.2.3 Heralding method for removing vacuum states

As detailed in Section 1.2.1, individual photons within a biphoton state exhibit Super-Poissonian statistics. However, this section raises the question: Can sub-Poissonian statistics be derived from a biphoton state? The affirmative response to this query is achieved through the heralding method, which enables the elimination of vacuum statistics, thereby increasing the probability of considering only photon pairs.

When photon 1 is successfully detected, it serves as a heralding (or herald) event, providing instantaneous information on the status of photon 2. The concept behind "heralding" is that the presence of the associated photon is indicated by the successful detection. Fig. 1.4(a) illustrates a schematic of the apparatus and the acquisition process. Fig. 1.4(b) depicts the heralding method and the removal of vacuum states using a Click/no-click detector with a positive operator-valued measure (POVM). This

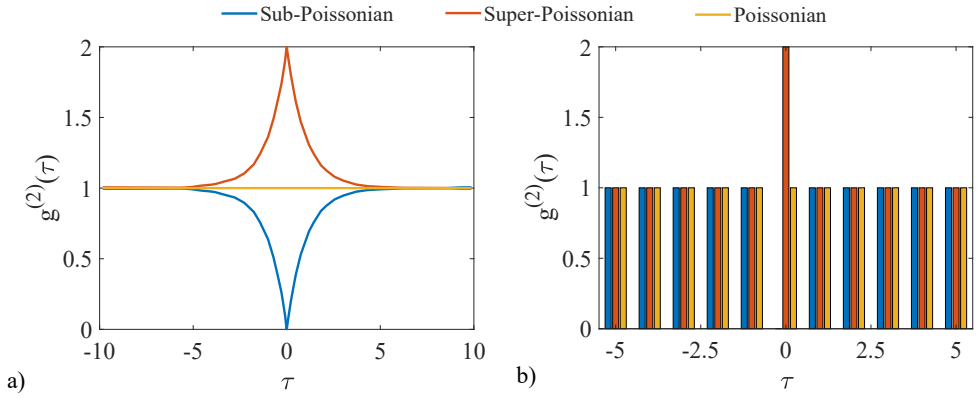

Figure 1.3: Second coherence function $g^{(2)}$ as a function of coincidence time τ for the CW(a) and pulsed(b) source. In blue the anti-bunching photons, in gold the Poissonian photons and in orange the bunching photons.

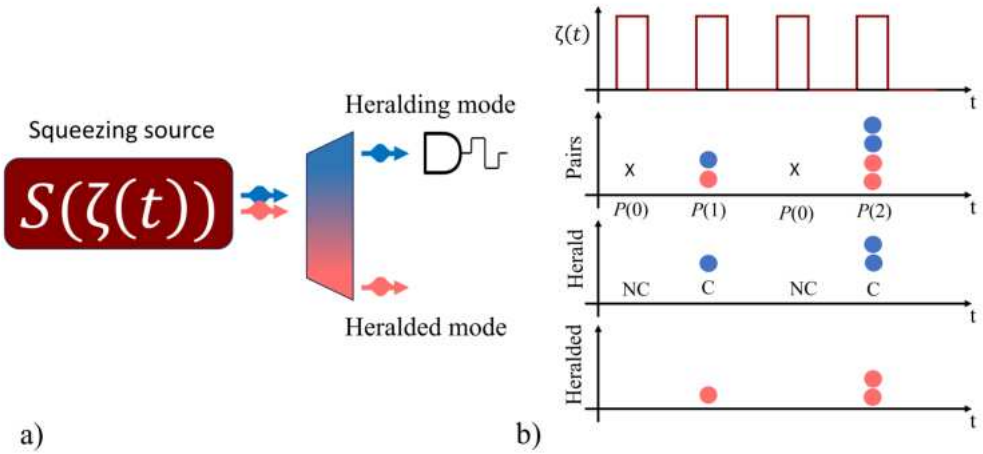

Figure 1.4: a) Schematic description of the heralding process, consisting of squeezing sources that generate the biphoton state and a detector responsible for reading the herald photons. b) Diagram of heralding approach using a click/co-click measurement.

method, dependent on its efficiency η, yields a "Click" (C) event when photons are detected and a "No-Click" (NC) event when no photons are detected. The measurement operators are defined as follows [54]:

$$\hat{\Pi}_{NC} = \sum_{n=0}^{\infty} (1-\eta)^n |n\rangle \langle n| , \tag{1.94a}$$

$$\hat{\Pi}_{C} = \sum_{n=0}^{\infty} [1-(1-\eta)^n] |n\rangle \langle n| . \tag{1.94b}$$

Here, $c_n = (1-(1-\eta)^n)$ represents the probability of detecting at least one out of n

photons. Considering the eqs. (1.79) and (1.94b), the probability of a successful heralding event is then calculated as:

$$\mathcal{P}(r, c_n) = \langle \Psi | \hat{\Pi}_{c_n} | \Psi \rangle = (\sinh r)^2 \sum_{n=0}^{\infty} c_n (\tanh r)^{2n}, \tag{1.95}$$

with the heralded state given by:

$$\begin{aligned} \rho_b^H(r, c_n) = \langle \Psi | \hat{\Pi}_{c_n} | \Psi \rangle &= \frac{\sum_{n=0}^{\infty} c_n (\tanh r)^{2n} \, |n_b\rangle \langle n_b|}{\sum_{n=0}^{\infty} c_n (\tanh r)^{2n}} \\ &= \frac{\sum_{n=1}^{\infty} (\tanh r)^{2n-1}}{(\cosh r)^2} \, |n_b\rangle \langle n_b| \, . \end{aligned} \tag{1.96}$$

Subsequently, the heralding probability of photon b is:

$$\mathcal{P}_b^H = \frac{(\tanh r)^{2n-1}}{(\cosh r)^2} \, . \tag{1.97}$$

The strategic use of heralding allows for the elimination of vacuum state probability while significantly increasing the likelihood of observing a single photon, heralded by the presence of its counterpart within the photon pair. This heralding mechanism serves as a discriminating factor, facilitating the selective detection of photon pairs. Depending on the chosen squeezing parameter (r), the probability distribution can be tailored to favor the generation of exclusively single pairs, thereby reducing the occurrence of multipair events. Fig. 1.5 graphically illustrates the different probabilities asso-

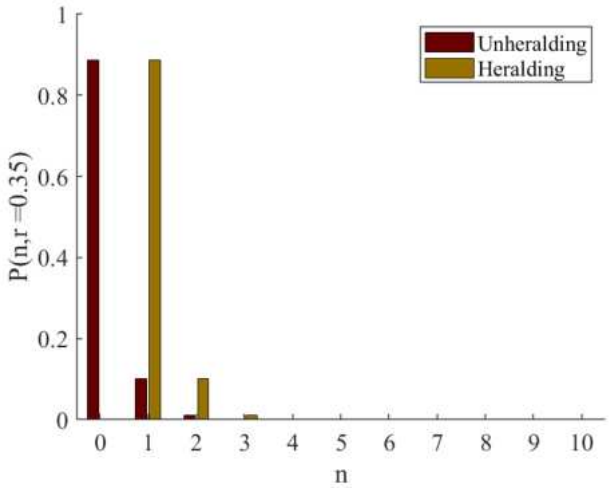

Figure 1.5: a) Normalized photon number distribution of a super-Poissonian signal beam. b) Normalized photon number distribution of a super-Poissonian signal beam under heralding detection. The presence of twin photons gives rise to a conditional probability. n represents the mean photon number per pulse. In the two cases $r = 0.35$.

ciated with detecting a two-photon state, both in the absence and presence of heralding. In this particular scenario, we encounter conditional probability, which emerges when a twin photon is present. As a result, occurrences where no photons are detected are neglected, as the system only acknowledges photon counts when accompanied by their twin counterparts.

1.2.4 Joint Spectral amplitude

The joint spectral amplitude (JSA) describes how photon pairs are spectrally correlated [26, 55]. The generic biphoton state can be expressed as:

$$|\Psi\rangle = \int d\omega_1 d\omega_2 F(\omega_1, \omega_2) \hat{a}^\dagger(\omega_1) \hat{a}^\dagger(\omega_2) |0\rangle , \tag{1.98}$$

with

$$\langle \Psi | \Psi \rangle = \int d\omega_1 d\omega_2 |F(\omega_1, \omega_2)|^2 = 1 , \tag{1.99}$$

where $F(\omega_1, \omega_2)$ denotes the JSA, and the modulus square defines the joint spectral intensity (JSI). The JSI is directly related to the field intensity, a measurable quantity. Utilizing the Schmidt decomposition for the JSA and two complete sets of orthonormal functions $\{u_n^{1/2}\}$ the expression for $F(\omega_1, \omega_2)$ becomes:

$$F(\omega_1, \omega_2) = \sum_\lambda \sqrt{r_\lambda} u_\lambda^{(1)}(\omega_1) u_\lambda^{(2)}(\omega_2) . \tag{1.100}$$

Here $u_\lambda^{(1/2)}$ represents the orthonormal functions, satisfying:

$$\iint d\omega u_{\lambda_1}^{(1/2)}(\omega) u_{\lambda_2}^{*(1/2)}(\omega) = \delta_{\lambda_1, \lambda_2} \quad \text{and} \quad \sum_\lambda r_\lambda = 1 . \tag{1.101}$$

This allows the bi-photon state to be expressed as a sum of product states:

$$|\psi\rangle = \sum_\lambda \sqrt{r_\lambda} \left[\int d\omega_1 u_\lambda^{(1)} \hat{a}^\dagger(\omega_1) \right] \otimes \left[\int d\omega_2 u_\lambda^{(2)} \hat{a}^\dagger(\omega_2) \right] |0\rangle . \tag{1.102}$$

Here, the coefficients $\{r_\lambda\}$ are referred to as the Schmidt coefficients. The Schmidt number K allows quantification of the entanglement degree, where $\frac{1}{K} = \sum_\lambda r_\lambda^2$. Typically, employing a single value decomposition of the square root of the JSI provides a lower bound for the Schmidt number, facilitating the determination of the purity of the heralded single photon, expressed as $P = 1/K$. The JSI maintains a direct correlation with

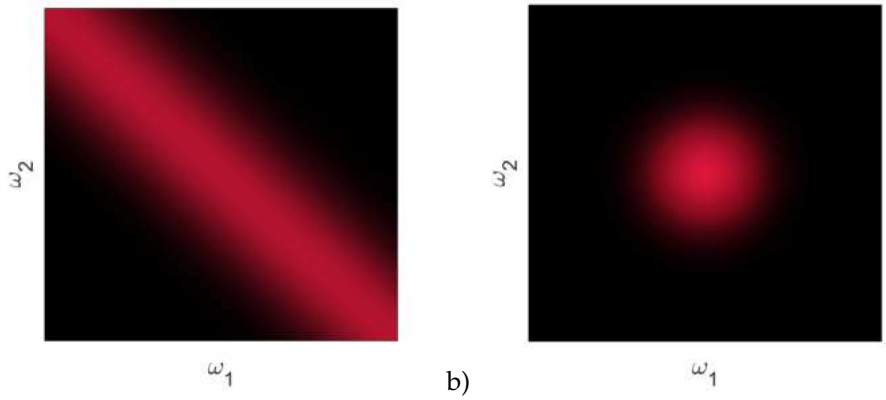

Figure 1.6: JSI for (a) correlated and (b) uncorrelated photon pairs.

the degree of correlation, manifesting as an oblique line for perfect correlation or a circular shape for perfect uncorrelation, as depicted in Fig. 1.6. The circular JSI indicates a separable state, reflecting maximum purity ($P = 1$), where $F(\omega_1, \omega_2) = F_1(\omega_1) F_2(\omega_2)$.

The purity of the bi-photon state is determined by:

$$P = \int d\omega_1 d\omega_2 d\omega_1' d\omega_2' F(\omega_1, \omega_2) F^*(\omega_1, \omega_2') F(\omega_1', \omega_2') F^*(\omega_1', \omega_2) = \sum_\lambda r_\lambda^2 \,. \tag{1.103}$$

This parameter, bounded between 0 and 1, quantitatively delineates the degree of factorizability inherent in the state. The process to obtain the partial trace of the density matrix associated with the state of eq. (1.100) is:

$$\begin{aligned} \hat{\rho}_2 &= Tr_1 \left|\Psi\right\rangle \left\langle\Psi\right| = \int d\omega_2 d\omega_2' \left[d\omega_1 F(\omega_1, \omega_2) F^*(\omega_1, \omega_2')\right] \hat{a}^\dagger(\omega_2) \left|0\right\rangle \left\langle 0\right| \hat{a}(\omega_2') \\ &= \sum_\lambda r_\lambda \left[\int d\omega_2 u_\lambda^{(2)}(\omega_2) \hat{a}^\dagger(\omega_2)\right] \left|0\right\rangle \left\langle 0\right| \left[\int d\omega_2' u_\lambda^{*(2)}(\omega_2') \hat{a}(\omega_2')\right]. \end{aligned} \tag{1.104}$$

The equations presented above reveal that a pure state emerges following the application of a partial trace to the two-photon state when a singular Schmidt coefficient attains unity, and all other coefficients are null. Consequently, in the context of a bi-photon state source, the purity parameter offers a quantitative measure describing the intrinsic value of an individual photon within the ensemble when the pair is in a pure state. This parameter serves as a quality of the state and extends its significance to characterize the source itself.

1.3 Spontaneous Four-Wave Mixing process

1.3.1 Nonlinear optical processes

The generation of a two-photon state in optics is often based on the leverage of nonlinear optical processes that produce entangled pairs of photons.

The theoretical basis of optical nonlinearities is derived from the polarization vector (or polarization density), which describes the reaction of material to an external electromagnetic field. Let us consider a general dielectric structure. At low optical powers, the relationship between the applied electric field ($\mathbf{E}$) and the resulting polarization ($\mathbf{P}$) comprises a linear segment and a nonlinear component. This relationship can be expressed as [28]:

$$\mathbf{P} = \mathbf{P}_L + \mathbf{P}_{NL} \,, \tag{1.105}$$

where $\mathbf{P}_L$ is the linear polarization, and $\mathbf{P}_{NL}$ is the nonlinear part. For sufficiently weak optical fields, the polarization, considering only the first two terms, can be expanded as a Taylor series:

$$\begin{aligned} \mathbf{P}_i(\mathbf{r}, t) &= \mathbf{P}_L(\mathbf{r}, t) + \mathbf{P}_{NL}(\mathbf{r}, t) \\ &= \mathbf{P}_L(\mathbf{r}, t) + \mathbf{P}_i^{(2)}(\mathbf{r}, t) + \mathbf{P}_i^{(3)}(\mathbf{r}, t) + ... \\ &= \varepsilon_0 \left[\sum_{jk} \chi_j^{(1)}(\mathbf{r}) \mathbf{E}_j(\mathbf{r}, t) + \sum_{jk} \chi_{jk}^{(2)}(\mathbf{r}) \mathbf{E}_j(\mathbf{r}, t) \mathbf{E}_k(\mathbf{r}, t) + \sum_{jkl} \chi_{jkl}^{(3)}(\mathbf{r}) \mathbf{E}_j(\mathbf{r}, t) \mathbf{E}_k(\mathbf{r}, t) \mathbf{E}_l(\mathbf{r}, t) + ...\right], \end{aligned} \tag{1.106}$$

with $\mathbf{P}^{(2)}(\mathbf{r}, t)$ and $\mathbf{P}^{(3)}(\mathbf{r}, t)$ are the second and third-order nonlinear polarization vectors respectively, while $\chi^{(2)}(\mathbf{r})$ and $\chi^{(3)}(\mathbf{r})$ are the second and third order susceptibilities, which are tensors of third and fourth order respectively.
The nonlinear susceptibility of order j is, in general, a tensor of rank $(j+1)$: in the case

of isotropic or amorphous materials (like silica-based optical fibers), it can be regarded as a scalar quantity, but in the case of crystalline structures (like silicon), it must be regarded as a tensorial quantity. Higher-order susceptibility terms only work at high field strengths because they get smaller and smaller.
The displacement field $\mathbf{D}(\mathbf{r},t)$ is given by $\mathbf{D}(\mathbf{r},t) = \varepsilon_0\mathbf{E}(\mathbf{r},t) + \mathbf{P}(\mathbf{r},t)$. Expressing $\mathbf{E}(\mathbf{r},t)$ in terms of $\mathbf{D}(\mathbf{r},t)$, we have:

$$\mathbf{E}_i(\mathbf{r},t) = \frac{\mathbf{D}_i(\mathbf{r},t)}{\varepsilon_0\varepsilon_1(\mathbf{r})} - \frac{\chi^{(2)}_{ijk}(\mathbf{r})}{\varepsilon_1(\mathbf{r})}\mathbf{E}_j(\mathbf{r},t)\mathbf{E}_k(\mathbf{r},t) - \frac{\chi^{(3)}_{ijkl}(\mathbf{r})}{\varepsilon_1(\mathbf{r})}\mathbf{E}_j(\mathbf{r},t)\mathbf{E}_k(\mathbf{r},t)\mathbf{E}_l(\mathbf{r},t) + \dots \quad (1.107)$$

where $\varepsilon_1(\mathbf{r}) = 1 + \chi^{(1)}(\mathbf{r})$. At the first order,

$$\mathbf{E}_i(\mathbf{r},t) = \mathbf{D}_i(\mathbf{r},t)/\left[\varepsilon_0\varepsilon_1(\mathbf{r})\right], \quad (1.108)$$

leading to:

$$\mathbf{E}_i(\mathbf{r},t) = \frac{\mathbf{D}_i(\mathbf{r},t)}{\varepsilon_0\varepsilon_1(\mathbf{r})} - \frac{\Gamma^{(2)}_{ijk}(\mathbf{r})}{\varepsilon_0}\mathbf{D}_j(\mathbf{r},t)\mathbf{D}_k(\mathbf{r},t) - \frac{\Gamma^{(3)}_{ijkl}(\mathbf{r})}{\varepsilon_0}\mathbf{D}_j(\mathbf{r},t)\mathbf{D}_k(\mathbf{r},t)\mathbf{D}_l(\mathbf{r},t) + \dots \quad (1.109)$$

where $\Gamma^{(2)}_{ijk}(\mathbf{r})$ and $\Gamma^{(3)}_{ijkl}(\mathbf{r})$ are related to the second and third-order susceptibilities, respectively:

$$\Gamma^{(2)}_{ijk}(\mathbf{r}) = \frac{\chi^{(2)}_{ijk}(\mathbf{r})}{\varepsilon_0\varepsilon_1^3(\mathbf{r})}, \quad (1.110a)$$

$$\Gamma^{(3)}_{ijkl}(\mathbf{r}) = \frac{\chi^{(3)}_{ijkl}(\mathbf{r})}{\varepsilon_0^2\varepsilon_1^4(\mathbf{r})} - 2\frac{\chi^{(2)}_{ijm}(\mathbf{r})\chi^{(2)}_{mkl}(\mathbf{r})}{\varepsilon_0^2\varepsilon_1^5(\mathbf{r})}. \quad (1.110b)$$

Finally, using eq. (1.109), and considering the variation of the electromagnetic field energy h for a variation of $\mathbf{B}$ and $\mathbf{D}$ fields [56]:

$$dh = \mathbf{H}\cdot d\mathbf{B} + \mathbf{E}\cdot d\mathbf{D}, \quad (1.111)$$

we can express the Hamiltonian $\mathcal{H}$ of the electric field as [28]:

$$\begin{aligned}\mathcal{H} = &\int\left[\frac{\mathbf{D}(\mathbf{r},t)\cdot\mathbf{D}(\mathbf{r},t)}{2\varepsilon_0\varepsilon_1(\mathbf{r})} + \frac{\mathbf{B}(\mathbf{r},t)\cdot\mathbf{B}(\mathbf{r},t)}{2\mu_0}\right]d\mathbf{r}\\ &- \frac{1}{3\varepsilon_0}\int\left[\Gamma^{(2)}_{ijk}(\mathbf{r})\mathbf{D}_i(\mathbf{r},t)\mathbf{D}_j(\mathbf{r},t)\mathbf{D}_k(\mathbf{r},t)\right]d\mathbf{r}\\ &- \frac{1}{4\varepsilon_0}\int\left[\Gamma^{(3)}_{ijkl}(\mathbf{r})\mathbf{D}_i(\mathbf{r},t)\mathbf{D}_j(\mathbf{r},t)\mathbf{D}_k(\mathbf{r},t)\mathbf{D}_l(\mathbf{r},t)\right]d\mathbf{r} + \dots,\end{aligned} \quad (1.112)$$

representing the total energy, the last two terms in the expression above correspond to the nonlinear terms.

1.3.2 First-order processes

In nonlinear optics, linear susceptibility, denoted as $\chi^{(1)}$, continues to occupy a central position. This parameter reflects the material's ability to undergo electronic excitations induced by single photons. The relationship between $\chi^{(1)}$ and the refractive index n is [57]:

$$n^2 = 1 + \chi^{(1)}. \quad (1.113)$$

Here, the real parts of $\chi^{(1)}$ and n are intertwined, while the imaginary part signifies the gains or losses within the material [58]. In semiconductor materials, the first-order susceptibility coefficient must account for the influence of free carriers. The presence of free carriers induces alterations in both the real and imaginary components of the refractive index, giving rise to Free Carrier Absorption (FCA) and Free Carrier Dispersion (FCD) effects. Incorporating these effects yields the complex refractive index of silicon as [57]:

$$n(\lambda, N_e, N_h) = n_0(\lambda) + \delta n_{FC}(N_e, N_h) + i\frac{\lambda}{4\pi}[\alpha_0(\lambda) + \delta\alpha_{FC}(N_e, N_h)]\,, \tag{1.114}$$

here, δn_{FC} and $\delta\alpha_{FC}$ represent the alterations in refractive index and additional losses induced by free carriers, respectively. $n_0(\lambda)$ and $\alpha_0(\lambda)$ denote the standard refraction and absorption coefficients dependent on the wavelength λ.

In nonlinear optical processes, free carriers primarily arise from two-photon absorption (TPA), a third-order nonlinear process discussed in Section 1.3.4.

1.3.3 Second-order processes

A nonlinear optical phenomenon known as a second-order process occurs when the photons interact with a material. This process is nonlinear since it depends on the intensity of the incident light. More in detail, a second-order nonlinear process involves interactions between 3 photons. We can write the relation between polarization vector $\mathbf{P}^{(2)}$ and the two waves $\mathbf{E}_1$ and $\mathbf{E}_2$ as a superposition [57]

$$\begin{aligned}
\mathbf{P}^{(2)}(r,t) = \quad & \varepsilon_0\chi^{(2)} : \left[\mathbf{E}_1^2(r,\omega_1)e^{-i2\omega_1 t}\right] \\
& + \varepsilon_0\chi^{(2)} : \left[\mathbf{E}_2^2(r,\omega_2)e^{-i2\omega_2 t}\right] \\
& + \varepsilon_0\chi^{(2)} : \left[2\mathbf{E}_1(r,\omega_1)\mathbf{E}_2(r,\omega_2)e^{-i(\omega_1+\omega_2)t}\right] \\
& + \varepsilon_0\chi^{(2)} : \left[2\mathbf{E}_1(r,\omega_1)\mathbf{E}_2^*(r,\omega_2)e^{-i(\omega_1-\omega_2)t}\right] \\
& + \varepsilon_0\chi^{(2)} : \left[\mathbf{E}_1(r,\omega_1)\mathbf{E}_1^*(r,\omega_1)\right] \\
& + \varepsilon_0\chi^{(2)} : \left[\mathbf{E}_2(r,\omega_2)\mathbf{E}_2^*(r,\omega_2)\right] \\
& + \text{c.c.}\,,
\end{aligned} \tag{1.115}$$

with c.c. the complex conjugate. The first two terms correspond to the second harmonic generation (SHG). In this case, a photon with frequency $2\omega_1$ is generated from the annihilation of two photons at frequency ω_1. A virtual state diagram of this process is shown on the left side of Fig. 1.7. The polarizations related to frequency sum generation (SFG) and difference generation (DFG) are shown in the third and fourth lines of the eq. (1.115). In SFG, shown on the center side of Fig. 1.7, two photons at ω_1 and ω_2 vanish to generate a new photon with frequency $\omega_1 + \omega_2$. In DFG, shown on the right side of Fig. 1.7, the created photon has frequency $\omega_1 - \omega_2$. The last terms give rise to the generation of a DC component of the polarization vector. This process is called optical rectification (OR). In the context of integrated optics, the utilization of second-order nonlinearity is typically precluded due to our reliance on non-centrosymmetric semiconductors. This restriction stems from the intrinsic centrosymmetry of the material, which lacks inversion symmetry, thus preventing the manifestation of even-order

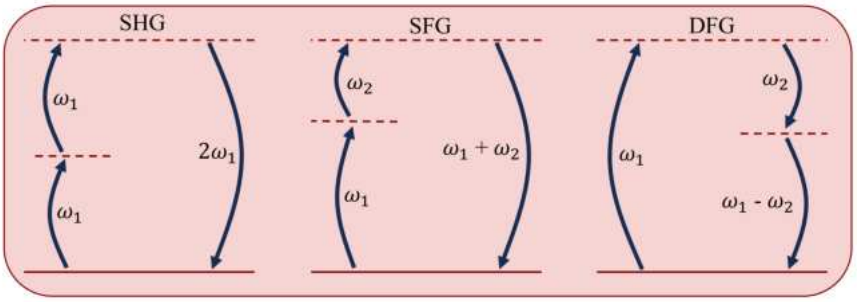

Figure 1.7: Scheme diagram for SHG, SFG, and DFG nonlinear processes.

nonlinearity. This deduction is drawn from an examination of the second-order polarization in the absence of the inversion operator

$$\mathbf{P}_i^{(2)} = \varepsilon_0 \left[\sum_{jk} \chi_{jk}^{(2)} E_j E_k \right]. \tag{1.116}$$

The inversion operator is

$$-\mathbf{P}_i^{(2)} = \varepsilon_0 \left[\sum_{jk} \chi_{jk}^{(2)} (-E_j)(-E_k) \right]. \tag{1.117}$$

with $\chi_{jk}^{(2)} = -\chi_{jk}^{(2)}$ holds according to the inversion symmetry of materials as silicon. Due to this behavior, we can obtain

$$-\mathbf{P}_i^{(2)} = \varepsilon_0 \left[\sum_{jk} \chi_{jk}^{(2)} (-E_j)(-E_k) \right] = \varepsilon_0 \left[\sum_{jk} \chi_{jk}^{(2)} E_j E_k \right] = \mathbf{P}_i^{(2)}, \tag{1.118}$$

which is valid only for $\chi_{jk}^{(2)} = 0$. The property of centrosymmetry, particularly evident in materials such as silicon and silicon nitride, introduces a distinctive pathway for exploring nonlinear effects rooted in third-order polarization phenomena.

1.3.4 Third-order processes

Third-order nonlinearity in optics refers to the nonlinear optical effects that result from the interaction of three photons within a material. The third-order nonlinear polarization vector $\mathbf{P}^{(3)}$ can be expressed by expanding the total electric field as the sum of these three waves, as in the second-order case [57].

$$
\begin{aligned}
\mathbf{P}^{(3)}(r,t) = \quad & \varepsilon_0\chi^{(3)}\vdots\left[\mathbf{E}_1^3(r,\omega_1)e^{-i3\omega_1 t}\right] \\
& + \varepsilon_0\chi^{(3)}\vdots\left[3\mathbf{E}_1^2(r,\omega_1)\mathbf{E}_2(r,\omega_2)e^{-i(2\omega_1+\omega_2)t}\right] \\
& + \varepsilon_0\chi^{(3)}\vdots\left[3\mathbf{E}_1^2(r,\omega_1)\mathbf{E}_2^*(r,\omega_2)e^{-i(2\omega_1-\omega_2)t}\right] \\
& + \varepsilon_0\chi^{(3)}\vdots\left[6\mathbf{E}_1^2(r,\omega_1)\mathbf{E}_2^*(r,\omega_2)\mathbf{E}_3(r,\omega_3)e^{-i(\omega_1+\omega_2+\omega_3)t}\right] \\
& + \varepsilon_0\chi^{(3)}\vdots\left[6\mathbf{E}_1^2(r,\omega_1)\mathbf{E}_2^*(r,\omega_2)\mathbf{E}_3^*(r,\omega_3)e^{-i(\omega_1+\omega_2-\omega_3)t}\right] \\
& + \varepsilon_0\chi^{(3)}\vdots\left[3|\mathbf{E}_1(r,\omega_1)|^2\mathbf{E}_1(r,\omega_1)e^{-i\omega_1 t}\right] \\
& + \varepsilon_0\chi^{(3)}\vdots\left[3|\mathbf{E}_2(r,\omega_2)|^2\mathbf{E}_1(r,\omega_1)e^{-i\omega_1 t}\right] \\
& + \text{c.c.}\,.
\end{aligned}
\tag{1.119}
$$

For reasons of simplicity, all potential combinations of the photon indices, or the waves,

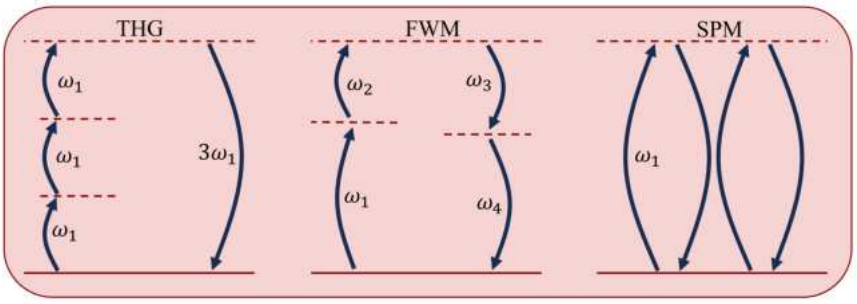

Figure 1.8: Scheme diagram for THG, FWM, and SPM nonlinear processes.

have been left out of this formula. Third harmonic generation (THG) is associated with the first term in this equation. Three photons with the same frequency, ω_1, combine to form a triple-frequency photon, $3\omega_1$, as the diagram illustrates on the left in Fig. 1.8. Four-wave mixing (FWM), which is caused by the annihilation of two incident photons, the pump photons, results in the generation of two additional frequencies, the signal photons and idler photons, which are identified as photons at frequencies ω_3 and ω_4. This process is carried out by the second through fifth elements of the summation. The illustration shows a possible diagram for this method, positioned at the center. Both TPA and self-phase modulation (SPM) are described by the sixth term of the summation. The scheme for THG, FWM, and SPM are reported in Fig. 1.8. SPM is related to the real part of the third-order susceptibility $\chi^{(3)}$, while TPA is related to the imaginary part of $\chi^{(3)}$. Plugging this term into the nonlinear wave equation yields intensity-dependent perturbations of the refractive index and absorption coefficient in the form [57]

$$
n = n_0 + n_2 I + i\frac{\lambda}{4\pi}[\alpha_0 + \beta_{TPA} I]\,,
\tag{1.120}
$$

with I is the field intensity, n_2 is the Kerr coefficient or nonlinear coefficient and β_{TPA} is the TPA coefficient. The coefficients n_2 and β_{TPA} are related to the third-order susceptibility by [57]

$$n_2 = \frac{3}{4\varepsilon_0 c n^2}\mathbb{R}(\chi^{(3)}_{ijkl}), \tag{1.121a}$$

$$\beta_{TPA} = \frac{3\omega}{2\varepsilon_0 c^2 n^2}\mathbb{I}(\chi^{(3)}_{ijkl}), \tag{1.121b}$$

with c the speed of light, $\mathbb{R}$ and $\mathbb{I}$ are the real and the imaginary parts. The absorption of two photons whose combined energies equal the energy needed to excite an electron from the valence band to the conduction band is the physical source of the TPA process. As a result of this process, one electron is excited from the valence band to the conduction band, changing the initial and final quantum-mechanical states. Because of this, the TPA effect can be considered a non-parametric process as opposed to a parametric process, which has the same initial and final quantum-mechanical states and allows the population to shift from the fundamental state to a virtual level only momentarily.
The cross-phase modulation (XPM) is the result of the final term in the equation. Although the signal at frequency ω_2 affects the propagation of the signal at frequency ω_1, XPM is still related to an intensity-dependent refractive index in this scenario. The coefficients in the equation show that the refractive index is altered by XPM by a factor of two with respect to SPM.

In addition to the TPA process mentioned earlier, another noteworthy non-parametric process in nonlinear optics is Stimulated Raman Scattering (SRS) [59]. SRS is a phenomenon that arises from the interaction between propagating photons and the vibrational modes of the material structure. More specifically, within the context of SRS, the energy exchange process involves the annihilation of a photon at frequency ω and the simultaneous generation of a Stokes-shifted photon at ω_{SRS}. This relationship adheres to the conservation of energy, expressed as ω_{SRS} = ω - ω_M, where $\hbar\omega_M$ represents the energy associated with the phonons exchanged within the medium. In addition to SRS, another significant Raman-scattering-related effect is Coherent Anti-Stokes Raman Scattering (CARS). In the CARS process, the interaction of two pump photons at a frequency ω with a signal photon at a frequency ω_S leads to the generation of an output photon at a frequency ω_{CARS} = 2ω - ω_s [60, 61]. This nonlinear optical phenomenon amplifies the vibrational signal in a coherent manner, offering valuable insights into the molecular structure of materials.

1.3.5 Four-Wave Mixing

FWM is a nonlinear optical process that can be used to generate a two-photon state [28, 62–64]. In FWM, when two photons of frequency, say ω_1 and ω_2, are combined, they can produce two photons with frequencies ω_3 and ω_4. The prevalent approach employed for FWM involves a scheme shown in Fig. 1.9(a), in which two input photons, referred to as pump photons with frequencies ω_{p1} and ω_{p2}, undergo a conversion process. This transformation results in generating signal photons with frequency ω_s and idler photons with frequency ω_i respectively. Throughout this thesis, the convention $\omega_i \geq \omega_s$ will be adopted to distinguish the idler photons from the signal photons.

Before describing in detail the aspects of this process, it is important to define different cases. In general the FWM process is categorized into two main regimes based on the frequencies of the generated photons: non-degenerate and degenerate FWM. In instances where the two generated photons possess identical frequencies $\omega_i = \omega_s$, the corresponding process is termed degenerate. The term "degenerate" means the

identical nature of the generated frequencies. Conversely, the process is denoted as non-degenerate when the frequencies differ $\omega_i > \omega_s$. The term "non-degenerate" emphasizes the disparity in the frequencies of the generated photons. In Fig. 1.9(b) these two processes are shown.

Two distinct scenarios in FWM are often delineated based on the nature of the photon generation process: stimulated FWM (SFWM) and spontaneous FWM (sFWM). In the context of SFWM, the introduction of a seed signal at either the signal or idler frequency enhances the FWM process. Conversely, the absence of a seed characterizes sFWM. While SFWM can be adequately described using classical electromagnetic theory, sFWM necessitates a quantum framework. From the quantum perspective, one can consider quantum vacuum fluctuations as the initiating seed for the process, drawing an analogy with stimulated FWM.

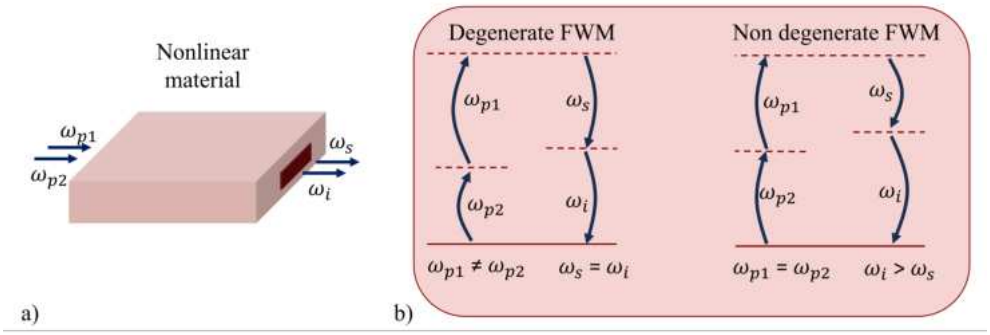

Figure 1.9: a) Illustration of FWM in a waveguide: Pump photons enter through the waveguide facet and undergo FWM, generating signal and idler frequencies, which exit from the end facet of the structure. b) Scheme diagram for degenerate FWM and non-degenerate FWM processes.

The parametric process of FWM is linked to the conservation of two fundamental aspects: the conservation of energy and the conservation of momentum, often referred to as the phase-matching condition [65]. In the case where two input photons are annihilated to produce a signal-idler pair, the energy of the resulting pair must precisely match the energy of the input pump photons [26]. This first conservation principle is expressed mathematically as:

$$\omega_{p1} + \omega_{p2} = \omega_i + \omega_s \,, \tag{1.122}$$

where ω_j is the frequency and $j = p1, p2, i$ and s are the pumps, idler and signal photons, respectively. The second aspect arises from the phase-sensitive nature of FWM. The efficiency of FWM depends upon the phase relationship among the waves involved in the process. This condition is represented by the equation:

$$k_{p1} + k_{p2} = k_i + k_s \,. \tag{1.123}$$

It is important to note that, when dealing with nonlinear processes, the conservation of momentum is not automatically satisfied. The lack of phase matching is quantified by the phase mismatch parameter, denoted as Δk, and is calculated as [48]:

$$\Delta k = k_{p1} + k_{p2} - k_i - k_s \,. \tag{1.124}$$

This parameter provides a quantitative measure of the deviation from phase-matching

conditions in FWM processes. Understanding and controlling these conservation principles are imperative for the precise manipulation and optimization of FWM in various optical applications. In the case where $\Delta k = 0$, the phase matching condition is achieved, and the maximum efficiency of the process is obtained. otherwise, where $\Delta k \neq 0$, the process is not optimized and the generation efficiency is lower than in the previous case.

This thesis will primarily focus on spontaneous photon generation. A feature of sFWM is the simultaneous emission of the idler and signal photons in pairs. The degree of correlation in this emission depends on the bandwidth of the pump and the inherent characteristics of the FWM process.
The quantum description of the sFWM process in waveguide will be extensively analyzed at the end of chapter 2 and in Appendix A after the introduction of the material description.

1.4 Parameters of quantum correlated photon sources

An important aspect is the study of different experimental parameters that are fundamental in revealing the characteristics of the generated photon pairs.

1.4.1 Coincidence to accidental ratio

In the context of quantum optics, the Coincidence-to-Accidental Ratio (CAR) is a parameter used to quantify the goodness degree of generated pairs in an experimental setup [65–67]. It is a sort of signal-to-noise ratio of the coincidence measurement between the correlated pair photons and the uncorrelated noise. This useful parameter is introduced to assess the coincidences between the idler and the signal when pair creation occurs through parametric processes. Thus, CAR is dependent on both the generating process and the experimental setting. The probability that the detection of a signal or idler photon includes the simultaneous detection of its twin partner decreases with increasing losses on the signal or idler detection arm. Losses are an important challenge since they lower the coincidence rate by increasing the probability of coincidences between other detections, such as noise or successive/previous photons, and the idler (signal). The so-called effective net coincidences, which define the temporal correlation of the emitted pairs, are the coincidences that take place between the signal and the idler that belong to the same pair. Accidental coincidences are those that happen between two photons of the noise, between a photon from the pair and the noise, or between signal and idler photons that belong to different pairs. Mathematically it can be defined as [68]

$$CAR = \frac{CC}{AC} = \frac{R_{si}}{R_{acc}}, \tag{1.125}$$

where CC or R_{si} is the idler-signal net coincidence rate, commonly referred to as brightness. The AC or R_{acc} is the accidental coincidence rate. CC is defined as

$$CC = \sigma\eta_\alpha^2\eta^2\eta_s\eta_i\varsigma = \sigma\eta_\alpha^2\eta^2\eta_s\eta_i\xi P_0^2. \tag{1.126}$$

Here σ is the duty cycle parameter, $\sigma = \tau B$, where B is the pulse repetition rate and τ is the pulse width. For continuous wave (CW), $\sigma = 1$. The pair-photon loss in the waveguide is taken into account by the parameter η_α; the waveguide-fiber (or waveguide-objective lens) coupling efficiency is denoted by η; the detection efficiencies for the signal and idler photons are represented by η_s and η_i, respectively. ς describes the pair

generation probability defined as

$$\varsigma = \xi P_0^2 = \Delta\nu(\gamma P_0 L_{eff})^2 \mathrm{sinc}^2[\Delta k L/2 + \gamma P_0 L]\,, \tag{1.127}$$

where ξ is the generation probability coefficient, γ is the nonlinear coefficient based on the nonlinear refractive index, and $\Delta\nu$ is the pair-photon channel's bandwidth; ν is the signal frequency shifted from the pump channel; P_0 is the input power, L_{eff} is the effective waveguide length taking into account the propagation loss α (i.e., $L_{eff} = [1-\exp(-\alpha L)]/\alpha$); L is the waveguide length; and Δk is the phase mismatch parameter. In eq. (1.125) AC is defined as:

$$AC = R_s R_i \Delta t\,, \tag{1.128}$$

where

$$R_{s/i} = \sigma\eta\eta_{s/i}(N_{s/i} + \eta_\alpha r) + dc_{s/i}\,, \tag{1.129}$$

where the noise photon generation rates for idler and signal photons, respectively, are represented by $N_{s/i}$. The dark count rates for signal (s) and idler (i) photons in the detectors are $dc_{s/i}$; $N_{s/i}$ has all the non-correlated photons inside. This aspect is important in the process where also SRS is involved. Δt is, for the CW situation $\Delta t = t$ where t is the time window for the coincidence measurement (i.e., the FWHM of the coincidence peak), and is, for the Pulsed case, $\Delta t = 1/B$.
Note that singles and coincidence rates are determined by multiplying the probabilities by the repetition rate of the pump laser. In the real experiment the measured coincidence $CC^{(m)}$ is the sum of the net coincidences CC and the accidentals AC. Therefore [66, 69]

$$CAR_{exp} = \frac{CC^{(m)} - AC}{AC}\,. \tag{1.130}$$

One method of performing CAR measurements is the "start-and-stop" technique. In this approach, an electronic timing device employs an internal timer that starts counting when a photon is detected by detector D1. The timer stops counting when another photon is registered by detector D2. The time duration between the start and the stop of the timer produces the delay, denoted "t" which represents the time separation between the two detected photons.

Next, a histogram is generated that captures the distribution of all observed delays between the paired photons. At time t=0, the histogram reflects a sum of pure generation coincidences and accidental coincidences. In contrast, at time points other than t=0, the histogram shows accidental coincidences. Fig. 1.10 illustrates on the left the sketch of

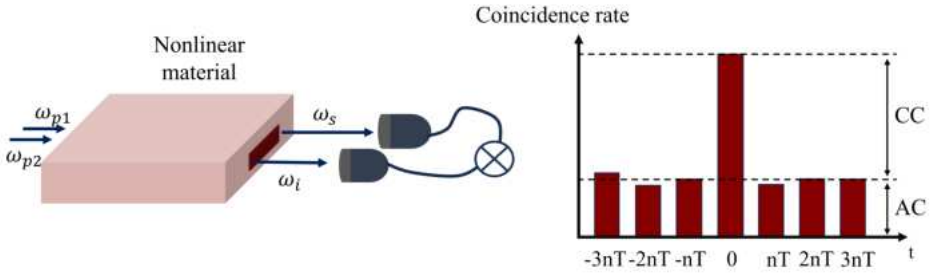

Figure 1.10: Setup for Coincidence-to-Accidental Ratio (CAR) measurement with Pulsed sFWM in Waveguide, featuring a pump repetition rate of 1/T. The timing electronics acquires the coincidences and the single counts.

the CAR measurement and on the right the histogram of coincidence acquisitions.

1.4.2 Second order coherence function: experimental point of view

The second-order coherence function, $g^{(2)}$, is another helpful experimental parameter. As described in Section 1.2.2, based on its value, the photon statistics can be defined. In the case of the biphoton state generated by the FWM process, we expect the value of $g^{(2)}$ for the single photon signal/idler beam to be bounded between 1 and 2. This value generally describes the super-Poissonian statistic. The experimental $g^{(2)}$ is obtained performing the Hanbury Brown-Twiss (HBT) interferometric measurement [16].

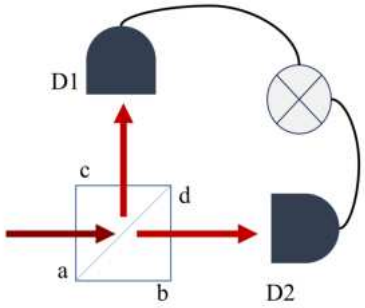

Figure 1.11: Schematic of the Hanbury-Brown and Twiss (HBT) interferometer, illustrating the light field exclusively in input port a, with the vacuum field present in input port b. The output detection signals from the two detectors are analyzed using appropriate electronics to yield the measured $g^{(2)}(t)$.

The schematic representation of the HBT interferometer is depicted in Fig. 1.11. In this setup, a photon beam is directed into the a-port of a beam splitter. Subsequently, the photons are detected by D1, located in the reflected path (c-port), or D2, situated in the transmitted path (d-port). The electrical signals generated upon photon detection are then subjected to processing by either a correlator or a start-and-stop timing system. The fundamental concept underlying the HBT experiment is rooted in the idea that when only one photon at a time interacts with the beam splitter, the probability of both detectors simultaneously registering the photon is essentially zero at $t = 0$. This condition translates to a zero coincidence value, signifying $g^{(2)}(0) = 0$. On the contrary, if more than one photon is present, coincidences occur, leading to a non-zero value of $g^{(2)}(0)$.
Furthermore, the HBT interferometer allows for an exploration of $g^{(2)}(t)$ at time intervals later or earlier than the zero-delay coincidence. This is achieved by introducing a time shift or electronic delay, denoted as Δt, to one of the detectors. Notably, when Δt is non-zero, the expectation is that in sub-Poissonian statistics, $g^{(2)}(0)$ will be less than $g^{(2)}(\Delta t)$.

The parameter measured via the start-and-stop electronics is the R_{cc} coincidence rate between the two HBT detectors. The resulting $g^{(2)}$ is then expressed as a function of the delay Δt between the detections made by the two HBT detectors in this form

$$g^{(2)}(\Delta t) = \frac{R_{cc}(\Delta t)}{R_1 R_2} t_b^{-1} = \frac{p_{cc}(\Delta t)}{p_1 p_2}, \tag{1.131}$$

where t_b is the time coincidences window, $p_{cc}(\Delta t)$ is the probability of a coincidence detection at a fixed delay Δt and $p_1(p_2)$ is the probability of a signal detection on one of the two detectors. Notice that the time delay is not explicit in $p_1(p_2)$, since $p_1(t) = p_1(\Delta t)$ is a constant probability.
In practical terms, while the process coherence time (t_c) is ideally substituted for t_b in eq. (1.131) due to the typical relationship $t_b \ll t_c$, it is crucial to note that t_b represents the actual time interval within which a coincidence can occur. From an experimental standpoint, the calculation of $g^{(2)}(0)$ is facilitated by monitoring the coincidence and single rates at $\Delta t = 0$. The expression for $g^{(2)}(0)$ can be articulated as follows

$$g^{(2)}(0) = \frac{R_{cc}(0)}{R_1 R_2} t_b^{-1} = \frac{p_{cc}(0)}{p_1 p_2}\,. \tag{1.132}$$

From this equation, we can then conclude that $g^{(2)}(0)$ can be measured as the ratio of coincidences at time $\Delta t = 0$ to coincidences at $\Delta t \neq 0$.
Based on this parameter, we can determine the values of Purity and Schmidt number K through the following relation

$$P = \frac{1}{K} = 1 - g^{(2)}(0)\,. \tag{1.133}$$

From this relationship we can experimentally trace the purity of the photons generated by the integrated source.

As previously mentioned, performing measurements on the photon, such as the signal depicted in Fig. 1.12(a), enables the derivation of a super-Poissonian statistic for the photon. The recovery of sub-Poissonian behavior is contingent upon the application of heralding, as described in Section 1.2.2. In this context, we assume the idler photon as the "herald photon" and the signal photon as the "heralded photon".

The introduction of heralding fundamentally alters the $g^{(2)}$ expression. In this configuration, the conditional $g^{(2)}$, denoted as heralded $g^{(2)}$ ($g_H^{(2)}$), emerges. It is defined as the autocorrelation of the signal beam, contingent upon the detection of its idler twin. This conditional approach allows the selection of only those photons in the signal beam that correlate with the photons in the idler beam. The experimental setup is accordingly modified, as illustrated in Fig. 1.12(b), where an additional detector for the idler beam is added to the system. The detection of the herald beam serves as a trigger, initiating the acquisition of signal/signal coincidences. This heralded $g^{(2)}$ can be expressed as follows

$$g_H^{(2)}(\Delta t) = \frac{R_{s_1 s_2 i}}{R_{s_1 i}(t) R_{s_2 i}(\Delta t)} R_i(t) = \frac{p_{s_1 s_2 i} p_i}{p_{s_1 i} p_{s_2 i}}\,, \tag{1.134}$$

where $R_{s_1 s_2 i}$ is the three-fold coincidence rate and $R_{s_1 i}$ and $R_{s_2 i}$ are the rates of coincidences between the idler and the signal1 or idler and signal2. $p_{s_1 s_2 i}$ is the probability of having a threefold coincidence, $p_{s_1 i}$ and $p_{s_1 i}$ are the probability of having a twofold coincidence. This equation works for both CW and pulsed situations.

1.4.3 Heralding efficiency

A critical parameter defining the practical viability of a heralding approach for a biphoton source is the heralding (or herald) efficiency, denoted as η_H. This parameter quantifies the probability that, upon detecting the herald photon, the heralded photon will also be detected. In this straightforward definition, η_H, known as the Klyshko

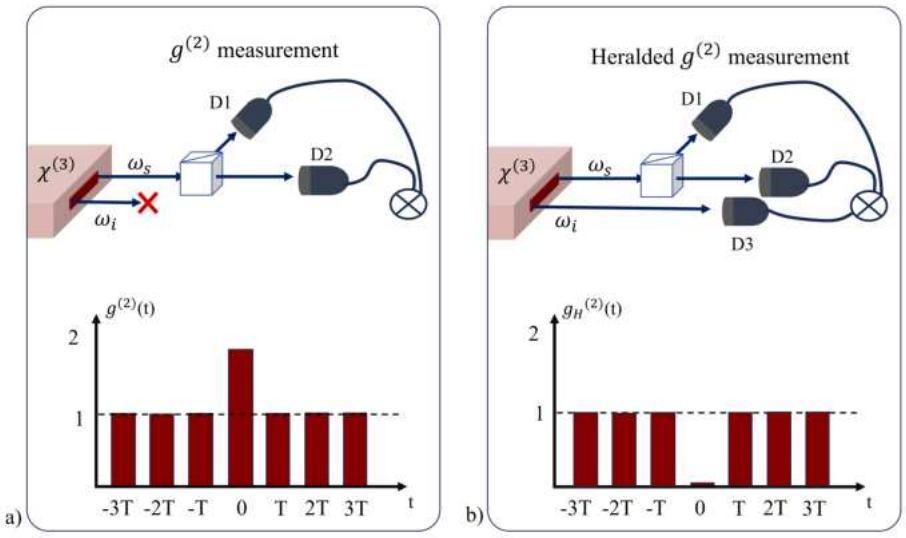

Figure 1.12: a) On the top, the setup for the $g^{(2)}$ measurement for the sFWM process is depicted, along with a typical outcome showing super-Poissonian statistics on the bottom. The pump is pulsed with a repetition rate of 1/T. b) On the top, the setup for the measurement of the heralded second-order correlation function, $g_H^{(2)}$, in the case of sFWM is shown, with a typical anti-bunching dip, indicating non-classical single-photon (sub-Poissonian) statistics, displayed on the bottom. The pump is pulsed with a repetition rate of 1/T.

efficiency η_K, can be measured by [65, 69]

$$\eta_K^{s(i)} = \frac{R_{is}}{R_{i(s)}}, \tag{1.135}$$

where R_{is} is the rate of coincidences between signal and idler photons, while $R_{i(s)}$ is the generation rate of the idler (signal) photons. A more favored definition of heralding efficiency takes into account the detection efficiency of the detector, denoted as η_d. In this scenario, the heralding efficiency is defined as:

$$\eta_H^{s(i)} = \frac{R_{is}}{R_{i(s)}\eta_d^{s(i)}}, \tag{1.136}$$

with $\eta_d^{s(i)}$ the detection efficiency of the signal (idler) detector. The presence of η_d allows us to decouple the quality of the overall source from the available detectors.
Another parameter to consider is the intrinsic heralding efficiency, denoted as η_I. This parameter takes into consideration the efficiency of the heralding process by excluding losses dependent solely on the quality of the instrumentation, encompassing factors such as filter losses, detector efficiencies, coupling losses, and, broadly, all losses from the source to the detectors. This approach allows for the exclusive consideration of intrinsic losses associated with the photon source. The intrinsic efficiency of the photon source is evaluated as:

$$\eta_I^{s(i)} = \frac{\eta_I^{s(i)}}{\eta_T^{s(i)}}, \tag{1.137}$$

where $\eta_T^{s(i)}$ represents the transmission efficiency of the (idler) signal through the photon source.

An important consideration is the use of filters, built-in or otherwise, to improve source purity. This aspect will be comprehensively discussed in the comparison of sources in Chapter 3. In this context, efficiency must also encompass the impact of filtering on state purification. Hence, a correlated efficiency is introduced for comparing different filtered sources, referred to as the heralding filtered efficiency, denoted as η_F. This efficiency quantifies the probability that, given the herald has passed its filter, the heralded photon will also pass the corresponding filter. From the Joint Spectral Intensity (JSI), this parameter can be defined as:

$$\eta_F = \frac{S_{JSI}^F}{S_{JSI}}, \tag{1.138}$$

where the regions of unfiltered and filtered JSI are denoted by S_{JSI} and S_{JSI}^F, respectively. The most promising solutions to guarantee excellent purity and efficiency in a PIC are based on intermodal phase matching or microring resonators, which can achieve the JSI with high purity without the need for external filters thanks to their discrete-by-discrete band emission. These points will be covered in Section 3.

1.4.4 Single photon detectors

Single photon detectors (SPDs) are devices engineered for the detection of single photons, converting optical input signals into electronic signals [53, 70]. In the ideal scenario, this conversion would be instantaneous with a detection efficiency of $\eta_{\mathrm{DE}} = 1$. However, real-world devices are subject to limitations, partly due to the experimental setup. To characterize the detection efficiency of SPDs in different configurations, we define the parameters η_{DE} for free-space detectors and for fiber-coupled detectors as follows [53]:

$$\eta_{\mathrm{DE}}^{\mathrm{x}} = \eta_{\mathrm{coupl}}^{\mathrm{x}} \eta_{\mathrm{abs}}^{i} \eta_{\mathrm{QE}}^{i} \eta_{\mathrm{th}}\,. \tag{1.139}$$

Here, $\eta_{\mathrm{coupl}}^{\mathrm{x}}$ represents the coupling efficiency associated with the collection optics, denoted as $\eta_{\mathrm{coupl}}^{\mathrm{area}}$ for the free-space SPD or $\eta_{\mathrm{coupl}}^{\mathrm{fiber}}$ for the fiber-coupled SPD. η_{abs}^{i} quantifies the probability of photon absorption at the detector's active area. η_{QE}^{i} denotes the internal quantum efficiency of the detector, and η_{th} refers to the efficiency related to the external electronics recording the electrical signal.

In practical scenarios, several other parameters must be considered to effectively manage the detection process. These parameters, illustrated in Fig. 1.13, include:

- Timing latency (t_{lat}): The delay between photon arrival and the output pulse crossing a threshold.
- Rise time (t_{rise}): Duration for the output pulse to transition between 10% and 90% of its maximum value.
- Timing jitter: Variation in timing between successive pulses.
- Dead time (t_{dead}): Interval during which the detector cannot produce an output pulse.
- Reset time (t_{reset}): Time required to restore maximum detection efficiency after dead time.
- Recovery time ($t_{\mathrm{recovery}} = t_{\mathrm{dead}} + t_{\mathrm{reset}}$): Time to return to optimal efficiency after a detection event.

- Dark count rate (dc): Average counts per second in the absence of incident light.
- Afterpulse probability ($P_{\text{afterpulse}}$): Probability of additional output signals after a previous detection event.

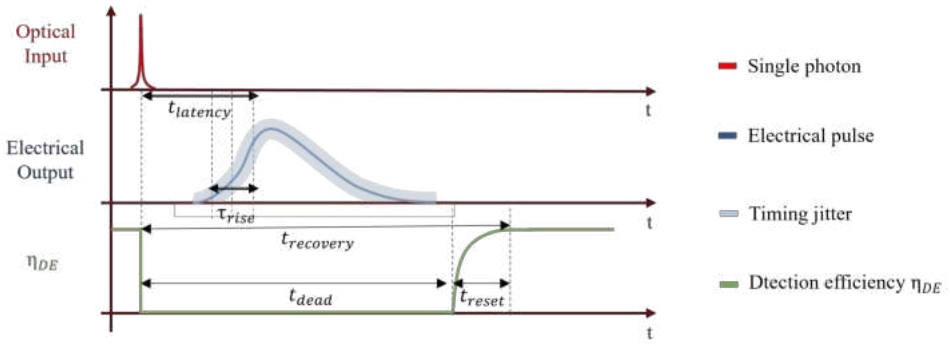

Figure 1.13: Timing relationship among parameters involved in the detection process.

The detection efficiency crucially determines the probability of the detector producing an output signal when photons reach its active area. For ideal threshold detectors like single photon avalanche detectors (SPADs), unable to resolve the number of photons detected, the probability of remaining inactive ($p_{\text{DE}}(0)$) when $P(n)$ represents incident light flux is [71]:

$$p_{\text{DE}}(0) = \sum_{n=0}^{\infty} (1 - \eta_{\text{DE}})^n P(n)\,, \tag{1.140}$$

while the probability of producing an output signal is:

$$p_{\text{DE}}(n) = \sum_{n=1}^{\infty} [1 - (1 - \eta_{\text{DE}})^n] P(n)\,. \tag{1.141}$$

Chapter 2

Silicon quantum photonics

2.1 Basics on integrated Photonics

In recent decades, silicon photonics has emerged as a prominent technology platform for photonic integrated circuits (PICs), representing a significant advancement in the design of complex optical devices and systems that can be integrated onto a single substrate or chip [72, 73]. This technological evolution can be traced back to the 1960s when integrated optics were developed, laying the foundation for such innovations. The success of silicon photonics is based on two important features: high refractive index contrast and compatibility with complementary metal-oxide-semiconductor (CMOS) processes [74, 75].

The index contrast, achieved by utilizing a silicon waveguide core and a silicon oxide cladding, facilitates the development of circuits within a compact system, allowing for the efficient production of multiple chips per wafer. The compatibility with CMOS processes further empowers the production of silicon photonic products at both moderate and high volumes, leveraging existing CMOS factories primarily dedicated to electronic integrated circuits (ICs). This, coupled with high energy efficiency, positions silicon photonics as a distinct advantage over other photonic integration platforms relying solely on photonic ICs to mitigate manufacturing costs [72].

It is noteworthy that integrated photonics has recently ventured into the field of quantum optics [76]. This expansion, occurring approximately 15 years ago, has spurred extensive research into novel platforms, including glass, silica, III-V semiconductors, diamond, lithium niobate, silicon carbide, silicon, and silicon nitride waveguides, for applications related to photon manipulation at the quantum scale [77]. Against this backdrop, this thesis concentrates on devices and circuits based on silicon and silicon nitride. The following chapter will discuss the differences between these two materials.

2.1.1 Silicon vs Silicon Nitride waveguide

Silicon (Si) and Silicon Nitride (SiN) photonic platforms play a key role in today's technology landscape, and the choice of a platform is influenced by various parameters, including the intended application and spectral region. This section aims to outline the common aspect and divergence between these two platforms [78, 79].
Currently, silicon-on-insulator (SOI) wafers [80], composed of a crystalline silicon layer atop a silicon oxide buffer layer, dominate the field of photonic products. This technology, with a silicon layer typically ranging from 200 to 400 nm, facilitates the implementation of various passive optical structures. The integration of electrically controllable thermo-optical micro-heaters or P-N junctions further increases functionality by allowing tunable or switchable operations.
Despite its prevalence, the desire to operate in spectral bands where silicon exhibits

absorption has led to the exploration of materials beyond SOI. SiN waveguide systems, featuring a silicon nitride core while maintaining CMOS compatibility, emerge as significant contenders in this regard. Unlike SOI-based waveguides, SiN waveguides offer transparency across a broader spectrum, extending from 0.35 µm to 7 µm (or up to 3.0 µm if embedded in silica) [79]. This makes them suitable for implementing "silicon photonics" at wavelengths in the visible and mid-infrared (MIR) spectral regions [81]. SiN's versatility extends to applications such as the direct integration of single-photon silicon detectors in the visible [30, 82] and compatibility with various quantum dot semiconductor compounds [83, 84].
An application arises from the trapped ion systems, which operate in the visible range (493 nm, 650 nm, etc.), falling within SiN's transparency window. This paves the way for integrated devices that benefit from trapped ion platforms. Silicon nitride, commonly deposited through LPCVD or PECVD, offers manufacturing flexibility, enabling seamless integration with other photonic structures. The combination of SiN and SOI waveguides on a single platform allows the unique characteristics of both materials to be combined.
Comparatively, SiN waveguides exhibit a lower index contrast than SOI waveguides, striking a balance between functionality and reduced susceptibility to scattering losses. In terms of nonlinearity, SiN presents a weaker n_2 nonlinear coefficient [85] but practically zero two-photon absorption (TPA), a limiting factor in silicon waveguides for nonlinear applications [86].
In essence, SiN emerges as a versatile alternative to SOI, boasting advantages such as transparency in the visible, lower losses, and greater manufacturing flexibility, particularly in integrated quantum photonic applications [34].
The upcoming sections will delineate the fundamental aspects of structures adaptable for integration into both Si and SiN platforms, laying the groundwork for subsequent chapters. The primary distinction in fabricating these structures lies in the cross-section and size, intimately tied to the variance in refractive index between the materials.

2.2 Integrated photonic building blocks

2.2.1 Optical waveguide

Waveguides are essential components within optical circuits and play an essential role in the efficient transport of optical signals. These elements are composed of a core of material with a higher refractive index (n_{core}) than a cladding with a lower refractive index (n_{clad}), where $n_{clad} < n_{core}$ [87]. Similar to the operation of optical fibers, light is confined within the core due to the phenomenon of total internal reflection, which allows efficient transport of optical signals through the waveguide.

In the specific context of channel waveguides [88], as illustrated in the Fig. 2.1(a-b), the core is fully embedded in the cladding, allowing the maximum degree of light confinement and enabling the manipulation of optical signals along the desired path within the optical circuit. Light propagates in the form of discrete modes with electric field profiles described by $\mathbf{e}_m(x, y, \omega)$, where m represents the mode index. These modes are solutions to the Helmholtz equation, expressed as [88]:

$$(\nabla^2_{xy} + \beta^2_m)\mathbf{e}_m(x, y, \omega) = \frac{\omega^2}{c^2} n^2(x, y)\mathbf{e}_m(x, y)\,, \tag{2.1}$$

where ω is the frequency of the optical wave, n the refractive index spatial distribution, c the light velocity. Owing to the constancy of the refractive index distribution, denoted as $n(x; y)$, along the direction of propagation z, we can express the field propagating in

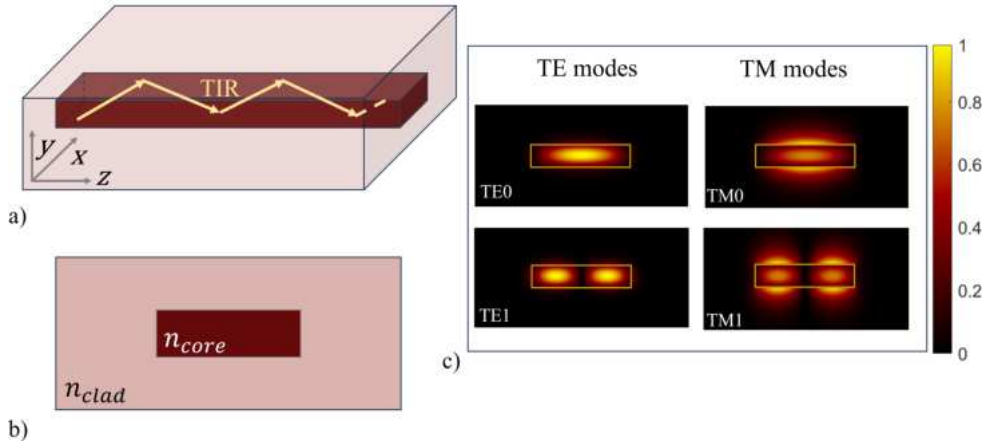

Figure 2.1: a) Schematic representation of a channel waveguide. b) Cross-section of the channel waveguide. The refractive index of the cladding material is denoted as n_{clad}, while the refractive index of the core is denoted as n_{core}. The propagation direction is indicated by z. c) Distribution of the dominant electric field component (Ex for TE modes, Ey for TM modes) for the two lowest-order TE and TM modes of a silicon waveguide with a cross-section of 1.6 µm × 0.25 µm.

the waveguide as a superposition of different modes [88]:

$$\mathbf{E}(x,y,z;\omega) = \sum_{m=0}^{M} \mathbf{e}_m(x,y) e^{-i\beta_m(\omega)z}\,, \tag{2.2}$$

where $\beta_m \approx \frac{\omega}{c} n_{eff,m}$ represents the propagation constant. $n_{eff,m}$ denotes the effective refractive index on the mode m, a complex quantity in which the real component reveals information about the phase acquired during the wave's propagation, while the imaginary component is proportional to the losses sustained within the waveguide. The relations are described as:

$$\mathbf{e}(z) = \mathbf{e}_0 e^{-\alpha_m z} \qquad \alpha_m = \frac{2\omega}{c} \Im(n_{eff,m})\,, \tag{2.3}$$

where $\mathbf{e}(z)$ is the field after the length z, $\mathbf{e}_0$ is the input field, α_m is the attenuation coefficient and $\Im(n_{eff,m})$ is the imaginary part of the effective refractive index $n_{eff,m}$. Different effective refractive indices arise for each mode m due to the interplay of waveguide geometry and light polarization. This dependency is further mirrored in the confinement factor Γ_{conf} of the optical mode:

$$\Gamma_{conf} = \frac{\iint_{core} n^2(x,y)|e_m(x,y)|^2 dxdy}{\iint_{A_\infty} n^2(x,y)|e_m(x,y)|^2 dxdy}\,, \tag{2.4}$$

in which the integral at the numerator is performed only in the core region. As the modal order increases, the modal Γ_{conf} decreases. This phenomenon becomes evident in the decreasing effective index as the modal order increases, indicating that the optical field interacts less with the core's refractive index.
Another property is the mode effective area $\mathcal{A}_{eff,m}$. It is defined as:

$$\mathcal{A}_{eff,m} = \frac{\left(\int |\mathbf{e}_m(x,y)|^2 dxdy\right)^2}{\int |\mathbf{e}_m(x,y)|^4 dxdy}\,, \tag{2.5}$$

which is a measure of the effective extension of the optical mode into the core and cladding regions.
Waveguide modes can be categorized into different types, including transverse electric modes (TE) and transverse magnetic modes (TM). Each mode exhibits distinct characteristics influenced by various factors such as the waveguide geometry, polarization, modal order, chromatic dispersion of the core and cladding, and the wavelength of the optical beam.

As illustrated in Fig. 2.1(c), the classification between TE and TM modes is determined by the dominant electric field component — aligning with the x direction for TE modes and the y direction for TM modes. Additionally, the effective index of each mode is wavelength-dependent; with increasing wavelength, the mode experiences reduced confinement, resulting in a corresponding decrease in its effective index.
In waveguides characterized by micrometer-scale dimensions, geometric dispersion takes precedence over chromatic dispersion, distinguishing it from the behavior observed in optical fibers [89]. The high-order dispersion coefficients $\beta_m^{(i)} = \frac{d^i \beta_m}{d^i \lambda}$ serve as indicators for the dispersion in the effective index. Considering the first order $(i = 1)$:

$$\beta_m^{(1)} = \frac{d\beta_m}{d\lambda} = \frac{1}{c}\left(n_{eff,m} - \lambda \frac{dn_{eff,m}}{d\lambda}\right) = \frac{n_{g,m}}{c} = v_{g,m}^{-1}, \tag{2.6}$$

the dispersion coefficient is related to the inverse of the group velocity $v_{g,m} = c/n_{g,m}$, where $n_{g,m}$ is the group index. In the situation of $i = 2$, the $\beta_m^{(2)}$ is called Group Velocity Dispersion (GVD). The GVD in a waveguide emerges from the differing propagation speeds of various frequencies. This dispersion stems from the wavelength-dependent group velocity characteristics, impacting the pulse's temporal expansion or contraction during its passage through the waveguide.

2.2.2 Couplers

A challenge in the implementation of photonic chips is the efficient coupling of light into waveguides. Various structures can be used including objective lenses or fibers. The most used are the latter. This challenge arises due to the substantial difference in effective mode area between the fibers and waveguides. For instance, a typical single-mode silica fiber operating at a wavelength of 1550 nm has a core size of approximately 10 µm and an effective mode area of about 315 µm^2, while the mode area of a silicon waveguide is typically around 1 µm^2, representing a difference of more than two orders of magnitude. Conical lens fibers have been developed to address this issue, gradually tapering one end to approximately 2.5 µm in diameter. This design effectively focuses light into an area of about 9 µm^2, resulting in coupling losses close to 1.5 dB. However, achieving even lower losses necessitates engineering the input side of the waveguide.

Two primary approaches have been devised for this purpose: tapering and grating couplers. Tapering involves gradually adjusting the size of the waveguide core as it approaches the fiber while grating couplers involve the design of periodic sub-wavelength structures at the waveguide ends. Both approaches are illustrated in Fig. 2.2.

Tapering can be implemented in two main forms: direct tapering (a), where the waveguide end smoothly increases to match the fiber spot size, and inverse tapering (b), where the waveguide end gradually decreases to spread the modal profile outside the core. Both approaches offer comparable performance, although the specific coupling efficiencies and dimensions may vary depending on the material of the PIC and the operating wavelength.

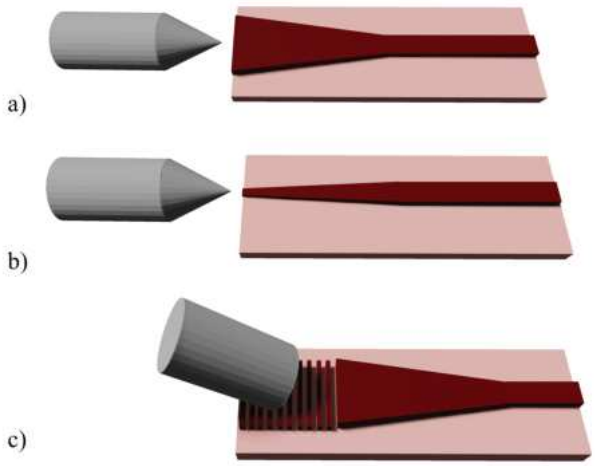

Figure 2.2: a) Waveguide with direct tapering coupled with a lensed fiber. b) Waveguide with inverse tapering coupled with a lensed fiber. c) Grating coupler with fiber tilted by an angle relative to the grating's normal. In all the representations the fiber size is not depicted to scale.

Grating couplers (c) operate on a distinct principle compared to tapering methods. These structures are composed of silicon that is periodically etched with specific periodicity, resulting in alternating regions with varying refractive indices. This periodicity causes the propagation mode to convert into a diffracted wave, which exits the cladding at an angle relative to the propagation direction. This phenomenon occurs when the periodicity, expressed with Λ, satisfies a particular phase-matching relationship given by:

$$\sin\theta = \frac{\Lambda n_{\text{eff}} - \lambda}{\Lambda n}. \tag{2.7}$$

Here, n_{eff} represents the effective index of the mode diffracting light, λ denotes the wavelength, and n represents the refractive index of the medium through which the wave is radiated. A fiber positioned at an appropriate angle θ can then collect the diffracted light, and conversely, this process can be utilized to couple light from the fiber into the waveguide.

2.2.3 Integrated Beam splitter

Beam splitters or beam couplers are components in integrated optics, playing a key role in the functionality of PICs. These devices are designed to split or couple optical signals, enabling a wide range of functionalities in integrated photonics. Their versatility is demonstrated through various applications:

- Power Splitting: Beam splitters divide an input optical signal into two or more output channels, ensuring a balanced distribution of optical power [90];
- Interferometry: These devices are fundamental to the creation of on-chip interferometers, enabling the manipulation of light waves to generate intricate interference patterns [91];

- Wavelength Division Multiplexing (WDM): Integrated beam splitters can be adapted to separate different wavelengths of light, facilitating wavelength-specific filtering, routing, and manipulation [92].

The multifaceted utility of these components extends to the specific type of beam splitter employed. In the context of this thesis, two distinct types will be developed and exploited: the multi-mode interferometer (MMI) [93] and the directional coupler (DC) [94, 95]. This chapter will offer an overview, while a more in-depth exploration of various aspects will be presented in the subsequent chapters.

Directional Coupler

A DC [96], as illustrated in Fig. 2.3, consists of two closely spaced waveguides, where the proximity is defined by the coupling distance (c_g). The coupling length (L) designates the region where the waveguides are in close proximity. Both L and the size of the gap depend on factors such as material properties, wavelength, and intended application.

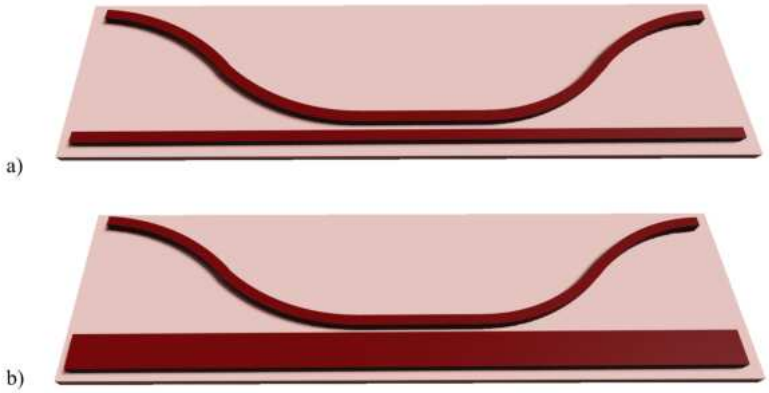

Figure 2.3: a) Sketch of a directional coupler (DC). It is formed by two waveguides with the same dimension. The gap between the two waveguides is called the coupling gap c_g. b) Sketch of an asymmetric-directional coupler (ADC). It is formed by two waveguides with different widths.

During the design, the coupling gap must be carefully determined. It should be small enough to enable the evanescent tail of the optical mode from each waveguide to extend through the cladding and penetrate the core of the adjacent waveguide. This design facilitates modal cross-talk between the two waveguides, ensuring effective interaction.

When the waveguides are of equal size, the configuration is termed a DC as shown in Fig. 2.3(a). In contrast, if the two waveguides have different widths, as illustrated in Fig. 2.3(b), the device is referred to as an asymmetric DC (ADC). The ADC functions as a mode coupler. Specifically, when a single-mode waveguide is positioned adjacent to a multi-mode waveguide, the ADC facilitates the selective excitation of one of the supported higher-order modes. DCs and ADCs exhibit bidirectional functionality in this context. In general, Coupled Mode Theory (CMT) examines the coupled modes of the structure, which are combinations of individual waveguide modes. In this part I follow the notation of [88]. The theoretical framework involves solving a set of coupled mode equations to describe the evolution of amplitudes for these coupled modes as

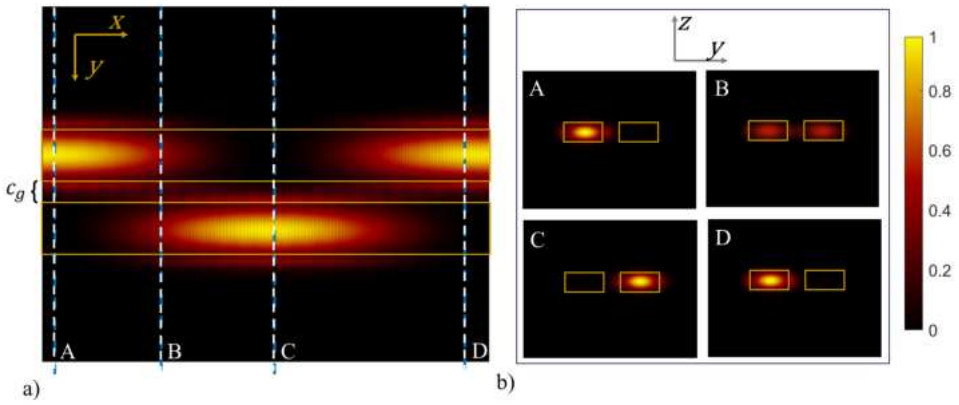

Figure 2.4: a) Simulation of the field profile entering point (A) in the upper single-mode waveguide. The close coupling between the two waveguides enables the field to pass between them. Different coupling lengths result in beam splitting (B), total beam transfer into the adjacent waveguide (C), or total beam return into the principal waveguide. b) Modal cross-sections are depicted in various sections. On the left is the principal waveguide (top in Fig. 2.4(a)), and on the right is the secondary waveguide.

light traverses the coupler's coupling region. In the presence of both waveguides, these changes can be expressed as [88]:

$$\mathbf{e}_1(y,z) = a_1(z)u_1(y)e^{-i\beta_1 z}\,, \tag{2.8a}$$

$$\mathbf{e}_2(y,z) = a_2(z)u_2(y)e^{-i\beta_2 z}\,. \tag{2.8b}$$

The coupling between the two waveguides exclusively alters the amplitudes $a_{1/2}(z)$. During z propagation, these amplitudes undergo changes according to the following relationships:

$$\frac{da_1}{dz} = -ic_{21}e^{i\Delta\beta z}a_2(z)\,, \tag{2.9a}$$

$$\frac{da_2}{dz} = -ic_{12}e^{i\Delta\beta z}a_1(z)\,, \tag{2.9b}$$

where the phase mismatch per unit length is $\Delta\beta = \beta_1 - \beta_2$ and the coupling coefficients are described as

$$c_{21} = \frac{k_0^2}{2\beta_1}(n_2^2 - n^2)\int_a^{a+d} u_1(y)u_2(y)dy\,, \tag{2.10a}$$

$$c_{12} = \frac{k_0^2}{2\beta_1}(n_1^2 - n^2)\int_{-a-d}^{-a} u_2(y)u_1(y)dy\,. \tag{2.10b}$$

When the amplitude $a_1(0)$ is launched into waveguide 1 without exciting waveguide 2, at a specific propagation distance z, the amplitudes in the two waveguides $a_1(z)$ and $a_2(z)$ evolve as follows:

$$a_1(z) = a_1(0)\left(\cos(\gamma z) - i\frac{\Delta\beta}{2\gamma}\sin(\gamma z)\right)e^{i\Delta\beta z/2}\,, \tag{2.11a}$$

$$a_2(z) = a_1(0)\frac{c_{12}}{i\gamma}\sin(\gamma z)e^{-i\Delta\beta z/2}\,, \tag{2.11b}$$

where $\gamma^2 = (\Delta\beta/2)^2 + \mathbf{c}^2$ and $\mathbf{c} = \sqrt{c_{12}c_{21}}$.

Thus the optical power $\mathbf{P}_1(z)$ and $\mathbf{P}_2(z)$ are:

$$\mathbf{P}_1(z) = P_1(0)\left(\cos^2(\gamma z) + \left(\frac{\Delta\beta}{2\gamma}\right)^2 \sin^2(\gamma z)\right), \tag{2.12a}$$

$$\mathbf{P}_2(z) = \mathbf{P}_1(0)\frac{|c_{21}|^2}{\gamma^2}\sin^2(\gamma z)\,. \tag{2.12b}$$

In the situation where the two waveguides are equal ($\beta_1 = \beta_2$, $\Delta\beta = 0$) the relations become [97]:

$$\mathbf{P}_1(z) = \mathbf{P}_1(0)\cos^2(\mathbf{c}z) = \mathbf{P}_1(0)\cos^2\left(\frac{\pi}{2}\frac{z}{L_c}\right) = |r|^2\mathbf{P}_1(0)\,, \tag{2.13a}$$

$$\mathbf{P}_2(z) = \mathbf{P}_1(0)\sin^2(\mathbf{c}z) = \mathbf{P}_1(0)\sin^2\left(\frac{\pi}{2}\frac{z}{L_c}\right) = |k|^2\mathbf{P}_1(0)\,. \tag{2.13b}$$

The term $L_c = \frac{\pi}{2\mathbf{C}}$, known as the transfer length, designates the length of the coupler required for a complete power transfer between the two waveguides. Power splitting between the two outputs occurs up to $z = \frac{L_c}{2}$. In this scenario, the DC can be configured as a beam splitter. Fig. 2.4 illustrates the field profile in a top view (a) and the modal cross-section (b) at different points. It can be seen that by "cutting" the coupling length is possible to achieve various outcomes: (A) the light is totally in the upper waveguide, (B) a beam splitter configuration, (C) complete intensity transfer into the adjacent waveguide, or (D) full field return into the primary waveguide. Therefore, the selection of the length enables different behaviors to be realized.

In general, the coupler is defined by its reflection coefficient (r) and transmission coefficient (k). Without losses, these coefficients follow the relation $|r|^2 + |k|^2 = 1$. The transmission matrix representing the DC, for $\Delta\beta = 0$, is:

$$\mathcal{U}_{CD} = \begin{pmatrix} r & -ik \\ -ik & r \end{pmatrix}. \tag{2.14}$$

In the case of a balanced DC ($r = k = 1/\sqrt{2}$) the matrix becomes:

$$\mathcal{U}_{CD} = \frac{1}{\sqrt{2}}\begin{pmatrix} 1 & -i \\ -i & 1 \end{pmatrix}. \tag{2.15}$$

In the context of an ADC, where varying waveguide widths and spatial modes come into play, it is sufficient to consider the propagation constants β for the corresponding modes and geometries. In the case of a DC, the coupling efficiency is obtained when the waveguides are identical. In the case of ADCs, the optimal efficiency is achieved when the n_{eff} of the single-mode waveguide matches with the n_{eff} of a specific higher-order mode of the multimode waveguide. Although CMT may exhibit lower precision for ADCs compared to DCs, it still provides a reliable approximation of the true coupling and is widely employed in device design. Fig. 2.5 depicts the field profile in a top view (a) and the modal cross-section (b) at different points for the asymmetrical structure. Similar to the DC case, different behaviors can be achieved by adjusting the coupling length at different points. At point (B), a beam splitter behavior is evident, where half of the intensity is converted into the upper mode while the other half remains in the fundamental mode, split across two distinct waveguides. At point (C), the fundamental mode undergoes conversion into the first excited mode within the multi-mode waveguide. Finally, at point (D), the entire field is recovered in the primary waveguide.

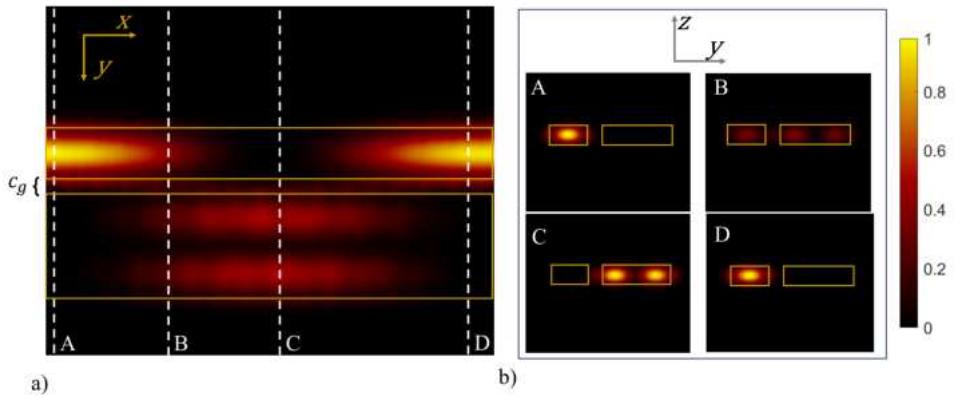

Figure 2.5: a) Simulation of the field profile entering point (A) of the upper single-mode waveguide of an ADC. The tight coupling between the two waveguides allows the field to pass between them. Different coupling lengths result in various behaviors: beam splitting (B) into two different modes on the two waveguides, total transfer of the beam into the adjacent multi-mode waveguide and its conversion into an excited mode (C), or total return of the beam into the single-mode waveguide. b) Modal cross-sections are shown in several sections. On the left is the single-mode waveguide (top of Fig. 2.5(a)), and on the right is the multi-mode waveguide.

There are cases where it is preferred to incorporate more robust structures in the manufacturing process, a strategic choice aimed at improving their reliability and stability.

Multimode Interferometer

The multimode interferometer (MMI) [90, 93] is an integrated optical device that leverages interference effects within a multimode waveguide to perform various functions in integrated photonic circuits. The MMI offers a compact and efficient method for either splitting or recombining photon beams. These configurations consist of a spec-

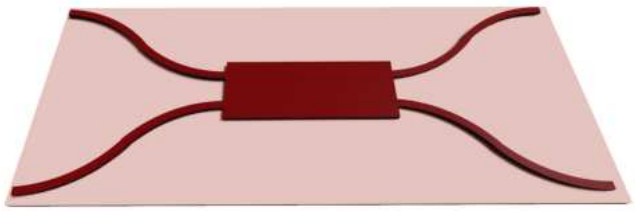

Figure 2.6: Layouts of a MMI 2x2. It is formed by two single-mode input waveguides and by two single-mode output waveguides connected by a wide multimode waveguide.

ified number of single-mode input and output waveguides connected by a wide multimode waveguide. The operational principle hinges on the self-imaging phenomenon [98, 99]. At the heart of an MMI device is a waveguide designed to support different modes. These devices are commonly referred to as MMI $(N \times M)$ couplers [100], where N represents the number of input waveguides, and M represents the number of output waveguides. In this contest, only MMIs 2×2 are described. Fig. 2.6 shows the representation of the MMI 2×2.

A thorough examination of full-modal propagation is likely the most comprehensive theoretical approach to describe self-imaging phenomena in multimodal waveguides [98]. The field profile, expressed in eq. (2.2), in the multimodal waveguide is described as [90]:

$$\mathbf{E}(\bar{x}, y, z) = e^{-i\beta_0 z} \sum_{m=0}^{M} \mathbf{e}(\bar{x}, y) e^{i(-\beta_m + \beta_0)z}, \tag{2.16}$$

where the input light injected into the multimode waveguide originates from the waveguide centered at $(\bar{x}, y)$. It can be demonstrated that [90]:

$$\beta_0 - \beta_m = \frac{m(m+2)\pi}{3L_\pi}, \tag{2.17}$$

where

$$L_\pi = \frac{\pi}{(\beta_0 - \beta_1)} \simeq \frac{4n_{mw}W}{3\lambda}, \tag{2.18}$$

is the beating length of the mode with n_{mw}, the refractive index of the multimode waveguide, W, the width of the multimode waveguide, and λ, the working wavelength. The eq. (2.16) becomes:

$$\mathbf{E}(\bar{x}, y, z) = e^{-i\beta_0 z} \sum_{m=0}^{M} \mathbf{e}(\bar{x}, y) e^{\left[i\frac{m(m+2)\pi}{3L_\pi} z\right]}, \tag{2.19}$$

where β_m is the propagation constant of the mode m. Taking note of the phase term, under specific conditions, the field $\mathbf{E}(\bar{x}, y, z)$ will manifest a duplicate (self-image) of the input field $\mathbf{E}(\bar{x}, y, 0)$. Indeed, the output varies based on the value of z, leading to scenarios ranging from the reconstruction of single images to the generation of multiple images. Let's examine the relationship

$$z = \frac{n}{2}(3L_\pi) \qquad (n = 0, 1, 2, 3, ..). \tag{2.20}$$

A single image is obtained in cases where n is even. Conversely, when n is odd, two images are obtained. By utilizing eq. (2.19), we can observe that by adjusting the length of the multi-mode waveguide while keeping its width fixed, different outputs can be achieved. These include splitting the beam into two different waveguides (B), completely transferring it into a waveguide at the bottom (C), or retaining it within the waveguide at the top (D). This behavior mirrors that of the DC but leverages the self-imaging mechanism. Fig 2.7 illustrates this behavior. It is easy to observe that at point (B), the implementation of 2 x 2 couplers achieving 3-dB coupling is achieved. The Scattering Matrix U_{MMI} that describes the MMI 2X2 50/50 is:

$$U_{MMI} = \frac{1}{\sqrt{2}} \begin{pmatrix} 1 & i \\ i & 1 \end{pmatrix}. \tag{2.21}$$

Typically, the MMI bandwidth is higher than the DC bandwidth.

2.2.4 Waveguide Crossing

A waveguide crossing, often abbreviated as CR, is used when one or more waveguides intersect. These crossings are typically constructed using MMIs as the core component, as depicted in Fig. 2.8(a). The primary objective of a CR is to facilitate the intersection of two waveguides without causing coupling between the light propagating in each waveguide. The desired outcome is to achieve a transmission coefficient close to unity and minimal crosstalk between the different lateral waveguides. This is possible

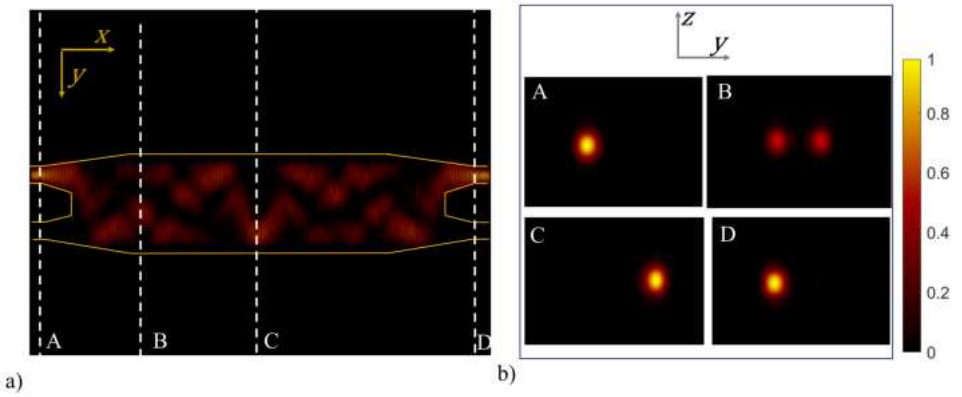

Figure 2.7: a) Simulation of the field profile entering point (A) in the multi-mode waveguide of the MMI 2X2. The field is propagating along x axes. For different lengths of the multi-mode waveguide, it is possible to obtain the splitting of the beam into two beams of equal intensity (B), the total transfer of the beam into the adjacent waveguide (C), or the total return of the beam into the main waveguide. b) The modal cross-sections are shown in several sections. On the left is the main output waveguide (top in Fig. 2.7(a)) and on the right is the bottom output waveguide.

through the self-imaging mechanism of MMI. In the simulation depicted in Fig. 2.8(b),

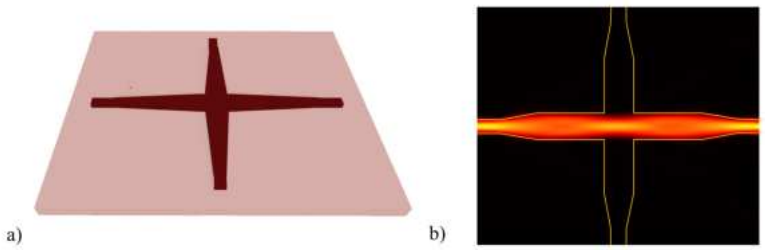

Figure 2.8: a) Sketch of Waveguide crossing. b) Simulation of the field profile in one input of the CR.

it can be observed that the electromagnetic field propagates exclusively in the main waveguide, with no observable crosstalk occurring in the lateral waveguide.

2.2.5 Integrated MZI

The Mach-Zehnder interferometer (MZI) is a device used for different applications, including signal modulation and quantum information processing. The MZI, illustrated in Fig. 2.9, comprises two integrated beam splitters, which can be constructed using either MMIs or DCs, connected by two waveguides. The process of splitting and recombining an incoming optical signal generates an interference pattern based on the phase difference between the light propagating in the two arms. In detail, light is guided through the waveguides, and phase modulation is achieved by introducing a phase change in one or both two arms. The output interference pattern depends on the relative phase between the arms, allowing precise control and manipulation of the optical signal. The constructive interference condition of the MZI at the output is expressed as:

$$\Delta\phi = \phi_1 - \phi_2 = \frac{2\pi\Delta n_{eff}}{\lambda} L\,, \tag{2.22}$$

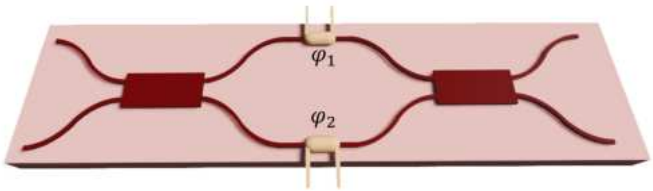

Figure 2.9: Sketch of an integrated MZI. The dark red sections represent the waveguides comprising the integrated structure, while the bottom cladding material is depicted in pink. The removal of the top cladding material highlights the internal arrangement of the MZI. Additionally, gold marks indicate the phase shifters (PSs) required to induce the phase shifts ϕ_1 and ϕ_2 due to the thermo-optic effect in the so-called push and pull configuration.

where $\Delta\phi$ represents the phase difference between the phases, ϕ_1 and ϕ_2, of the two arms and Δn_{eff} is a variation of the refractive index induced by a variation of its temperature, and it is described as:

$$\Delta n_{eff} = \frac{dn}{dT}\Delta T\,, \tag{2.23}$$

where $\frac{dn}{dT}$ is the thermo-optic coefficient [101]. To achieve Phase Shifting (PS), a metal wire is strategically positioned above the waveguide, ensuring minimal impact on propagation losses. By passing a current through the wire and leveraging the Joule effect, the wire's temperature rises, consequently heating the waveguide and changing the n_{eff} locally. In integrated photonics, PS is also achieved by carrier injection into a *p-i-n* waveguide. This method achieves higher speed but with high insertion losses.

Considering the MMI matrix representation in eq. (2.21) and the matrix representation of the phase operator

$$U_{Ph}(\phi_1,\phi_2) = \begin{pmatrix} e^{2i\phi_1} & 0 \\ 0 & e^{2i\phi_2} \end{pmatrix}\,, \tag{2.24}$$

the matrix representation of the MZI is:

$$U_{MZI}(\phi_1,\phi_2) = ie^{i(\phi_1+\phi_2)} \begin{pmatrix} \sin(\Delta\phi) & \cos(\Delta\phi) \\ \cos(\Delta\phi) & -\sin(\Delta\phi) \end{pmatrix}\,. \tag{2.25}$$

When $\phi_1 = \phi_2 = 0$, the MZI effectively implements the SWAP operation, albeit with a global phase $\frac{\pi}{2}$:

$$\begin{pmatrix} 0 \\ i \end{pmatrix} = i \begin{pmatrix} 0 & 1 \\ 1 & 0 \end{pmatrix} \begin{pmatrix} 1 \\ 0 \end{pmatrix}\,, \tag{2.26a}$$

$$\begin{pmatrix} i \\ 0 \end{pmatrix} = i \begin{pmatrix} 0 & 1 \\ 1 & 0 \end{pmatrix} \begin{pmatrix} 0 \\ 1 \end{pmatrix}\,. \tag{2.26b}$$

In the case where $\Delta\phi = \pi/2$, it is possible to obtain the identity or through configuration:

$$\begin{pmatrix} i \\ 0 \end{pmatrix} = i \begin{pmatrix} 1 & 0 \\ 0 & 1 \end{pmatrix} \begin{pmatrix} 1 \\ 0 \end{pmatrix}\,, \tag{2.27a}$$

$$\begin{pmatrix} 0 \\ i \end{pmatrix} = i \begin{pmatrix} 1 & 0 \\ 0 & 1 \end{pmatrix} \begin{pmatrix} 0 \\ 1 \end{pmatrix}\,. \tag{2.27b}$$

In the scenario with minimal energy consumption (where no current is applied), the system adopts the SWAP configuration as described in eq. (2.26). However, when trying to achieve a specific configuration, energy consumption becomes necessary.

In practical settings, it's common to have spurious phases caused by fabrication imperfections. To achieve the desired configuration, an electrical current must be supplied. To reduce power dissipation and energy consumption, the best approach is to use a push-pull configuration, which involves installing heaters in both arms of the MZI. Additionally, trenching techniques can be employed to minimize the required current and reduce thermal crosstalk in adjacent structures. This will help to optimize efficiency and save costs.

Asymetric MZI

An alteration of the traditional MZI, known as an asymmetric MZI (aMZI), intentionally features mismatched arm lengths. This difference induces a phase mismatch between the arms, leading to a modification in the output interference pattern. Fig. 2.10 shows the schematic design of this device. The aMZI is suitable for diverse applications, ranging from wavelength selection to the creation of integrated filters, offering precise control over interference conditions. The optical path length difference ΔL between the two MZI arms can be written as:

$$\Delta L = \frac{m\lambda_{res}}{n_{eff}}, \tag{2.28}$$

with m the order, λ_{res} the center resonance wavelength of the targeted spectrum. The aMZI produces an output transmission pattern characterized by an FSR described as

$$FSR = \frac{\lambda^2}{n_g \cdot \Delta L}, \tag{2.29}$$

and resonance wavelength, $\lambda_{\text{res}} = \frac{n_{\text{eff}} \cdot \Delta L}{m}$, where n_g is the group index of the propagating mode in the waveguide [102, 103]. In the 2×2 aMZI, when light propagates from

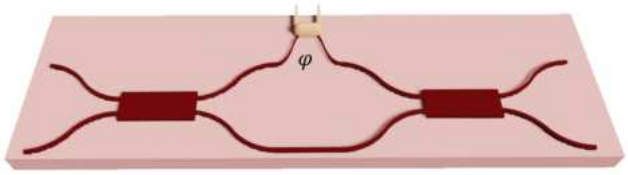

Figure 2.10: A schematic design of the aMZI is shown. The two MMI structures are connected by two waveguides with different lengths. In the longer waveguide, the heater is located.

left to right, it functions as a demultiplexer, splitting distinct wavelengths into the two output paths. However, reciprocity dictates that if these wavelengths enter through the same port on the right side, they will be combined at the same output on the left side, effectively operating as a multiplexer. The repetition of aMZIs in series can accentuate this behavior, selectively filtering certain wavelengths and enabling the realization of an integrated filter. This aspect will be explored in detail in Chapter 5.

2.2.6 Microring resonator

Microring resonators [104–106] play a crucial role in integrated quantum photonics, serving as compact structures that facilitate essential functionalities like the nonlinear generation of biphoton states, filtering, and modulation. In the context of this thesis, their primary application revolves around the generation of biphoton states [27, 107]. In the field of silicon photonics, microresonators are typically composed by wrapping a

Figure 2.11: Sketch of microring resonator in All pass configuration for the point coupler (a), pulley (b), and racetrack (c) configurations.

waveguide around itself to form a ring, strategically positioned near a straight waveguide, resulting in the "All Pass" (AP) configuration [108]. AP configuration possesses an input and an output port. Various geometries, including point coupler (a), pulley (b), and racetrack (c) configurations, as depicted in Fig. 2.11, present distinct advantages and disadvantages. The careful selection of the most suitable resonator type for an experiment becomes imperative. Regardless of the chosen geometry, the shared aspect of each resonator involves the coupling of light from the straight waveguide with the closed ring path, selectively supporting specific wavelengths λ_m. For traveling-wave resonators like microrings or racetracks, these wavelengths adhere to the resonance condition [104]:

$$m\lambda_m = n_{eff}L\,, \tag{2.30}$$

where m is an integer number, L is the microring perimeter, and n_{eff} is the effective refractive index.
The electric field's amplitude at the output port E_{out} is linked to the amplitude at the input port E_{in} by the transfer function $H(\omega)$, a complex function dependent on the light frequency ω. Obtaining the transfer function $H(\omega)$ involves employing the transfer matrix method (TMM), and its mathematical representation is [109]:

$$H(\omega) = \frac{E_{out}}{E_{in}} = \frac{r - \tau e^{-i\phi(\omega)}}{1 - r\tau e^{-i\phi(\omega)}}\,, \tag{2.31}$$

Here, $\tau = e^{-\alpha L}$ (where α is the scattering loss coefficient) represents the roundtrip losses, r is the reflection coefficient of the coupler, and $\phi(\omega) = \frac{\omega}{c} n_{\text{eff}}(\omega) L$ denotes the roundtrip phase. The magnitude of $|H(\omega)|^2$ is depicted in Fig. 2.12 as a function of ϕ. The resonance criterion is met anytime $\phi = 2m\pi$, which causes a transmission dip to develop in the spectral response. Energy accumulates inside the resonator during this event, with some of it being lost due to scattering caused by the roughness of the side walls, among other factors. Consequently, the transmission power decreases. When the resonance criterion is not met, such as by changing the input wavelength, no light is coupled into the resonator, and the device functions as a straight waveguide.

Below, we outline essential properties that characterize a resonator: the quality factor (Q), the free spectral range (FSR), and the field enhancement factor (FE). The quality factor Q for the mth resonant order is defined as the ratio of the resonant wavelength

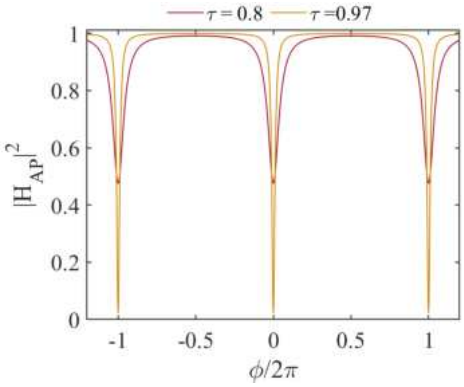

Figure 2.12: $|H_{AP}|^2$ as a function of the roundtrip phase ϕ. For all the curves, the reflectance of the coupler is set to $r = 0.95$.

λ_m to the Full Width at Half Maximum (FWHM) $\Delta\lambda_m$ of the peak [88, 110]:

$$Q = \frac{\lambda_m}{2\Delta\lambda_m} = \frac{\pi n_g(\lambda_m) L\sqrt{r\tau}}{(1-r\tau)\lambda_m}\,. \tag{2.32}$$

The peak follows a Lorentzian function. The FSR, representing the separation between two consecutive resonance wavelengths, is denoted as:

$$FSR = \frac{\lambda_m^2}{n_g(\lambda_m)L}\,. \tag{2.33}$$

Finally, the FE factor is the ratio between the internal field of the resonator and that of the input waveguide. The expressions for this parameter are provided as follows:

$$FE = \frac{ik}{1-r\tau e^{-i\phi(\omega)}}\,. \tag{2.34}$$

where k is the cross-coupling of the microring resonator.

2.3 Quantum description of sFWM in photonic waveguides

In this section, I will explain the quantum description of the parametric nonlinear sFWM process in waveguide. The comprehensive analytical procedures are detailed in the appendix A; here, I present only the key steps[1]. We can describe the Hamiltonian of the nonlinear process of sFWM in the material as [26, 28]:

$$\mathcal{H}_{sFWM} = \frac{3}{\epsilon_0}\int \Gamma^{(3)}_{ijkl}(\mathbf{r})\mathbf{D}_s^-(\mathbf{r},t)\mathbf{D}_i^-(\mathbf{r},t)\mathbf{D}_p^+(\mathbf{r},t)\mathbf{D}_p^+(\mathbf{r},t)d\mathbf{r} + \text{h.c.}\,, \tag{2.35}$$

where

$$\mathbf{D}^+ = \sum_j \mathbf{D}_j^+ = \sum_j \int \sqrt{\frac{\hbar\omega_{jk}}{4\pi}}a_j(k,t)d_{Jk}(y,z)e^{ikx}dk + \text{h.c.}\,, \tag{2.36}$$

[1]For readers seeking further insight, I recommend the following two papers: [26] and [28].

with $j = p, i$ or s. From eq. (1.110b):

$$\Gamma^{(3)}_{ijkl}(\mathbf{r}) = \frac{\chi^{(3)}_{ijkl}(r)}{\epsilon_0^2 \epsilon_1^4(r)} \,. \tag{2.37}$$

The Hamiltonian in frequency domain becomes

$$\begin{aligned}\mathcal{H}_{sFWM} = \frac{\gamma_{SiP_1P_2}\hbar^2\omega_{ISP_1P_2}}{4\pi^2} \int d\omega_P d\omega_P d\omega_i d\omega_s a_i^\dagger(\omega_i) a_s^\dagger(\omega_s) a_P(\omega_P) a_P(\omega_P) \\ \times e^{i\Delta k x} e^{i(\omega_p+\omega_p-\omega_i-\omega_s)t} + \text{h.c.}\end{aligned} \tag{2.38}$$

where $\Delta k = k_p + k_p - k_i - k_s$ with k the wavevector of the four photons, and the coupling coefficient $\gamma_{SiP_1P_2}$ is the parameter that characterizes the strength of the FWM process [28], is

$$\gamma_{SiP_1P_2} = \frac{n_2 \omega_{SIP_1P_2}}{c \mathcal{A}^{eff}_{SIP_1P_2}} \,, \tag{2.39}$$

with n_2 the non linear coefficient, $\mathcal{A}^{eff}_{SIP_1P_2}$ the effective area, c the speed of light and $\omega_{SIP_1P_2} = \sqrt[4]{\omega_i \omega_s \omega_{P_1} \omega_{P_2}}$.

We are ready to examine how a quantum state evolves under the influence of this Hamiltonian. If the initial state is in the vacuum state, the state's evolution is characterized by:

$$|\Psi\rangle = \hat{\mathcal{U}} \, |0,0\rangle_{i,s} = \exp\left[\frac{-i}{\hbar} \int_{-\infty}^{\infty} dt \hat{\mathcal{H}}_{sFWM}(t)\right] |0,0\rangle_{i,s} \,, \tag{2.40}$$

where $|0,0\rangle_{i,s} = |vac\rangle$.

Let us consider the case of coherent laser pumps α_p. Since we are interested in weak interactions, we can expand the unitary evolution operator from eq. (2.40) using a first-order Taylor series. We discard the residual pump:

$$\begin{aligned}|\Psi\rangle &= \hat{\mathcal{U}} \, |0,0\rangle_{i,s} \simeq \\ &= \mathcal{I} \, |0,0\rangle_{i,s} + \Big(\frac{\gamma_{SiP_1P_2}\hbar\omega_{ISP_1P_2} L}{2\pi} \int d\omega_P d\omega_i d\omega_s a_i^\dagger(\omega_i) a_s^\dagger(\omega_s) \\ &\times \alpha_P(\omega_{P1}) \alpha_P(\omega_i + \omega_s - \omega_{P1}) \phi(\omega_s, \omega_i, \omega) + \text{h.c.} \Big) \, |0,0\rangle_{i,s} \\ &= |0,0\rangle_{i,s} + \beta \, |II\rangle_{i,s} \,,\end{aligned} \tag{2.41}$$

where $\phi(\omega_s, \omega_i, \omega)$ is the phase matching function. The biphoton wavefunction, denoted as $|II\rangle_{i,s}$, can be expressed in a general form using a two-dimensional complex function $F(\omega_s, \omega_i)$, referred to as the joint spectral amplitude (JSA). The JSA can be written as

$$F(\omega_s, \omega_i) = \int \mathrm{d}\omega \, \alpha_P(\omega) \alpha_P(\omega_s + \omega_i - \omega) \phi(\omega_s, \omega_i, \omega) \,, \tag{2.42}$$

where $\alpha(\omega)$, which is typically thought of as having a Gaussian profile, is the complex amplitudes of the pump beams. The $|II\rangle_{i,s}$ can be write:

$$|II\rangle_{i,s} = \iint d\omega_i \, d\omega_s \, F(\omega_i, \omega_s) \hat{a}_i^\dagger(\omega_i) \hat{a}_s^\dagger(\omega_s) \, |0,0\rangle_{i,s} \,. \tag{2.43}$$

We used the method described in [26] to determine the power of each photon in a pair

generated by continuous wave sFWM in a channel waveguide when pumped at ω_P. This was done within a limited spectral range of bandwidth $2\pi B$. The mean power calculation is given by [26]:

$$P_{i(s)} = B\hbar\omega_p(\gamma_{SIP1P2}P_P L)^2 \mathrm{sinc}^2\left[(2k(\omega_P) - k(\omega_P + \Omega) - k(\omega_P - \Omega))L/2\right] . \quad (2.44)$$

where $P_{i(s)}$ is the power of the idler (signal) photons. In the context of the microring resonator, we specifically examine the filtered case where the filter's bandwidth is narrower than the resonator's band. Under these conditions, the relationship is given by [26]:

$$P_{i(s)} = \hbar B(\gamma P_P)^2 \frac{64\nu_{\mu_P}^4}{\pi^2\omega_{\mu_P}^3}\frac{Q_{\mu_P}^4}{R^2} , \quad (2.45)$$

where Q_{μ_P} is the quality factor of the ring, R is the radius, and ν_{μ_P} is the group velocity. For the unfiltered case (without filter), we obtained:

$$P_{i(s)} = \hbar(\gamma P_P)^2 \frac{8\nu_{\mu_P}^4}{\pi^2\omega_{\mu_P}^2}\frac{Q_{\mu_P}^3}{R^2} . \quad (2.46)$$

There is a difference also in the description of $F(\omega_s, \omega_i)$ in the microring resonator case. Here, the enhancement effect due to the microring can be taken into account.

$$F(\omega_s, \omega_i) = l_s(\omega_s)l_i(\omega_i)\int \mathrm{d}\omega\, \alpha_P(\omega)l_p(\omega)\alpha_P(\omega_s + \omega_i - \omega)l_p(\omega_s + \omega_i - \omega)\phi(\omega_s, \omega_i, \omega) , \quad (2.47)$$

where $l_j(\omega)$ (with j = i,s) is the Lorentzian function, which corresponds to the microring resonance linewidth of the jth resonance involved in the process.

Chapter 3

Comparison of sFWM integrated Sources

This chapter conducts an analysis of different approaches to initiate the sFWM process while examining the characteristics of the biphoton state generated.

3.1 Which type of source performs best among integrated probabilistic sources?

Determining the optimal integrated probabilistic source for quantum computing is a multifaceted effort. The complexities involved stem from several factors, amplified by the limitations of current quantum technology. In this context, the search for the most suitable photon source is closely intertwined with the specific requirements of the chosen algorithm. Considerations such as photon generation rate, indistinguishability between photons, spectral purity, robustness of fabrication, and scalability are important in choosing the appropriate source.

In the context of quantum computing applications, this chapter aims to provide an evaluation of different integrated silicon sFWM sources in the C-band, highlighting their respective strengths and weaknesses in the given configuration.

3.2 Comparison between waveguide and microring resonator sources for sFWM

This chapter is the result of a collaboration with the ETRI center. Dr. Jong-Moo Lee and coworkers designed the photonic integrated circuit (PIC) and performed the experimental measurements at the ETRI center. Dr. Alessio Baldazzi and I conducted the analytical treatment and simulations at the University of Trento. We perform a direct comparison of two distinct sources for the generation of degenerate photon pairs ($\omega_s = \omega_i$) within the same silicon PIC [111]. These sources are based on microring resonators and waveguides, as illustrated in Fig. 3.1.

Before delving into the results, I introduce a quantum measure that furnishes experimental insights into the characteristics of the generated photons: the Hong-Ou-Mandel (HOM) interference measure [112–114]. The HOM interference measurement offers experimental insights into the nature and quantum properties of generated photons [115]. As a fundamental tool in quantum optics and quantum computing, it holds significant importance for characterizing photon behavior and verifying the indistinguishability of quantum particles.

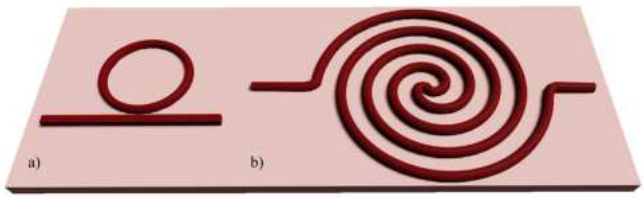

Figure 3.1: Graphical representation of integrated sources for the sFWM process. The microring resonator is depicted on the left (a), while the spiral waveguide is shown on the right (b). The waveguides are in dark red, while the cladding is represented in pink.

3.2.1 Hong-Ou-mandel effect

Quantum interference plays a central role in various quantum protocols, such as boson sampling and quantum linear optical computation [116–118], and has been the subject of intense study. A notable example of quantum interference is the HOM effect. This effect occurs when two indistinguishable photons simultaneously encounter the two inputs of a beam splitter [119]. Due to their indistinguishability, they give rise to a distinct interference pattern in the coincidence detection probabilities, as shown in Fig. 3.2. The beam splitter is characterized by two input ports with associated photon annihila-

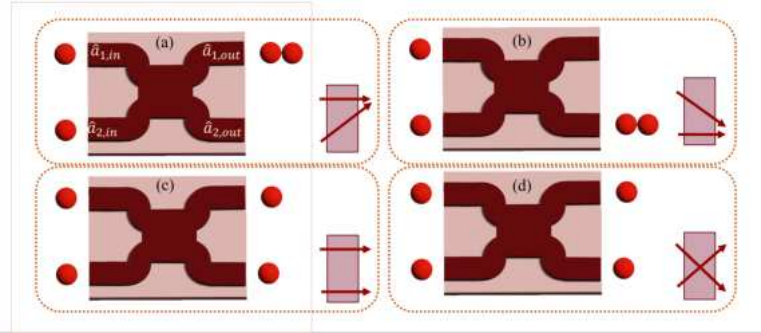

Figure 3.2: Configuration of the HOM experiment and possible output configurations. The dark red corresponds to the integrated beam splitter (MMI), and the pink is the cladding. In each configuration, the directions of the photons entering the two entrances of the BS, which may either be reflected or transmitted, are depicted at the bottom right. If the experiment is performed with indistinguishable photons, configurations (c) and (d) are identical and have different signs; therefore, they cancel out, and no coincidence detection is observed at the output.

tion operators $\hat{a}_{1,in}$ and $\hat{a}_{2,in}$, and two output ports with associated photon annihilation operators $\hat{a}_{1,out}$ and $\hat{a}_{2,out}$. The connection between the input and output operators is represented by the matrix relation [119]:

$$\begin{bmatrix} \hat{a}_{1,out} \\ \hat{a}_{2,out} \end{bmatrix} = \mathcal{U}_{BS} \begin{bmatrix} \hat{a}_{1,in} \\ \hat{a}_{2,in} \end{bmatrix} = \frac{1}{\sqrt{2}} \begin{bmatrix} 1 & i \\ i & 1 \end{bmatrix} \begin{bmatrix} \hat{a}_{1,in} \\ \hat{a}_{2,in} \end{bmatrix}, \tag{3.1}$$

where $\mathcal{U}_{BS}$ corresponds to the unitary matrix of an ideal integrated 50:50 beam splitter expressed in eq. (2.21) constituted by the MMI.
Consider a scenario in which the two inputs include two indistinguishable single photons, i.e., $|\text{in}\rangle = |1\rangle_1|1\rangle_2 = \hat{a}^\dagger_{1,in}\hat{a}^\dagger_{2,in}|0\rangle_1|0\rangle_2$. The state at the output of the beam splitter can be determined by considering the transformation on the mode operators $\hat{a}^\dagger_{\text{out}} = U^\dagger_{BS}\hat{a}^\dagger_{\text{in}}$. Through the inverse evolution of the mode operators, we can explicitly

express the output state as:

$$\begin{aligned}\hat{a}^\dagger_{1,\text{in}}\hat{a}^\dagger_{2,\text{in}}|0\rangle_1|0\rangle_2 &= \frac{1}{2}\left(\hat{a}^\dagger_{1,\text{out}}+i\hat{a}^\dagger_{2,\text{out}}\right)\left(\hat{a}^\dagger_{2,\text{out}}+i\hat{a}^\dagger_{1,\text{out}}\right)|0\rangle_1|0\rangle_2 \\ &= \frac{1}{2}\left[i\left(\hat{a}^\dagger_{1,\text{out}}\right)^2+\left(\hat{a}^\dagger_{2,\text{out}}\right)^2+\hat{a}^\dagger_{1,\text{out}}\hat{a}^\dagger_{2,\text{out}}-\hat{a}^\dagger_{1,\text{out}}\hat{a}^\dagger_{2,\text{out}}\right]|0\rangle_1|0\rangle_2 \\ &= \frac{i}{\sqrt{2}}(|2\rangle_1|0\rangle_2+|0\rangle_1|2\rangle_2)\,.\end{aligned} \tag{3.2}$$

To obtain the final expression, I utilized the relation $|n\rangle = (\hat{a}^\dagger_y)^n/\sqrt{n!}|0\rangle$. Eq. (3.2) captures the effect of quantum interference with indistinguishable photons. The probability amplitudes for both transmitted photons ((c) component in Fig. 3.2) and both reflected photons ((d) component) emerge with opposite signs, resulting in a cancellation effect. Hence, the output state forms an equal superposition of both photons in output mode 1 and both photons in output mode 2. Consequently, only cases where the two photons are grouped in the same output mode persist, i.e., $P_{\text{coinc}} = 0$. No coincidences are observed.

In the case of coherent states $|\alpha\rangle$ and $|\beta\rangle$ into modes $a_{1,\text{in}}$ and $a_{2,\text{in}}$, respectively, the situation changes. Considering the BS as described in eq. (2.21) and the displacement operator described in eq. (1.51), we can express the output state as:

$$\begin{aligned}|\Psi_{\text{out}}\rangle &= e^{\alpha\hat{a}^\dagger_{1,\text{in}}+\beta\hat{a}^\dagger_{2,\text{in}}}|0\rangle \\ &= e^{\alpha\left(\frac{\hat{a}^\dagger_{1,\text{out}}+i\hat{a}^\dagger_{2,\text{out}}}{\sqrt{2}}\right)+\beta\left(\frac{i\hat{a}^\dagger_{1,\text{out}}+\hat{a}^\dagger_{2,\text{out}}}{\sqrt{2}}\right)}|0\rangle \\ &= e^{\hat{a}^\dagger_{1,\text{out}}\left(\frac{\alpha+i\beta}{\sqrt{2}}\right)+\hat{a}^\dagger_{2,\text{out}}\left(\frac{i\alpha+\beta}{\sqrt{2}}\right)}|0\rangle\,.\end{aligned} \tag{3.3}$$

The average number of photons, denoted as $\langle\hat{n}_{a_1}\rangle$ and $\langle\hat{n}_{a_2}\rangle$, in the two output ports can be computed as follows:

$$\langle\hat{n}_{a_1}\rangle = \left|\frac{\alpha+i\beta}{\sqrt{2}}\right|^2 = \frac{\alpha^2+\beta^2}{2}\,, \tag{3.4}$$

$$\langle\hat{n}_{a_2}\rangle = \left|\frac{i\alpha+\beta}{\sqrt{2}}\right|^2 = \frac{\alpha^2+\beta^2}{2}. \tag{3.5}$$

Here, α and β are complex numbers representing the field amplitudes in the two output ports. The expressions show that the average photon numbers in both output ports are equal and given by $\frac{\alpha^2+\beta^2}{2}$.

General case of HOM

The aforementioned analysis illustrates the quantum interference principle. However, to incorporate the individual distinguishability and mixing of the two interfering photons, a more comprehensive framework is required [119]. For this purpose, let us consider the scenario in which the two photons in spatial input modes 1 and 2 possess spectral amplitude functions φ_1 and φ_2. The two-photon input state is then defined by:

$$\begin{aligned}|\psi\rangle_{in} &= |1;\varphi_1\rangle_{a_1}|1;\varphi_2\rangle_{a_2} \\ &= \int d\omega_1\varphi_1(\omega_1)\hat{a}^\dagger_{1,in}(\omega_1)\int d\omega_2\varphi_2(\omega_2)\hat{a}^\dagger_{2,in}(\omega_2)\,|0\rangle_1|0\rangle_2\,.\end{aligned} \tag{3.6}$$

Our purpose is to investigate variations in the coincidence probability related to the overlap between photons. To explore this aspect, we introduce a time delay τ, typically implemented in mode a_2. The creation operator becomes:

$$\hat{a}^{\dagger}_{2,in}(\omega) \rightarrow \hat{a}^{\dagger}_{2,in}(\omega)e^{-i\omega\tau}. \tag{3.7}$$

Considering the $\hat{\mathcal{U}}_{BS}$ the state of the two photons becomes:

$$\begin{aligned}
|\psi\rangle_{in} =& \frac{1}{2}\int d\omega_1 \varphi_1(\omega_1)\left(\hat{a}^{\dagger}_{1,\text{out}}(\omega_1) + i\hat{a}^{\dagger}_{2,\text{out}}(\omega_1)\right) \\
&\times \int d\omega_2 \varphi_2(\omega_2)\left(\hat{a}^{\dagger}_{2,\text{out}}(\omega_2) + i\hat{a}^{\dagger}_{1,\text{out}}(\omega_2)\right) e^{-i\omega_2\tau}\,|0\rangle_1\,|0\rangle_2 \\
=& \frac{1}{2}\int d\omega_1 \varphi_1(\omega_1)\int d\omega_2 \varphi_2(\omega_2)e^{-i\omega_2\tau} \\
&\times \Big(\hat{a}^{\dagger}_{1,\text{out}}(\omega_1)\hat{a}^{\dagger}_{2,\text{out}}(\omega_2) + i\hat{a}^{\dagger}_{1,\text{out}}(\omega_1)\hat{a}^{\dagger}_{1,\text{out}}(\omega_2) + \\
&+ i\hat{a}^{\dagger}_{2,\text{out}}(\omega_1)\hat{a}^{\dagger}_{2,\text{out}}(\omega_2) - \hat{a}^{\dagger}_{2,\text{out}}(\omega_1)\hat{a}^{\dagger}_{1,\text{out}}(\omega_2)\Big)\,|0\rangle_1\,|0\rangle_2\,.
\end{aligned} \tag{3.8}$$

Determining the coincidence probability requires explicit calculation. We will represent each detector with a flat frequency response. The projectors describing the detection in mode a_1 and a_2 are then given by

$$\hat{P}_{a_1} = \int d\omega \hat{a}^{\dagger}_1(\omega)\,|0\rangle_1\,\langle 0|_1\,\hat{a}_1(\omega)\,, \tag{3.9a}$$

$$\hat{P}_{a_2} = \int d\omega \hat{a}^{\dagger}_2(\omega)\,|0\rangle_2\,\langle 0|_2\,\hat{a}_2(\omega)\,. \tag{3.9b}$$

The coincidence probability of detecting one photon in each mode is

$$p = Tr[|\psi\rangle_{out}\,\langle\psi|_{out}\,\hat{P}_{a_1}\otimes\hat{P}_{a_2}] = \langle\psi_{out}|\hat{P}_{a_1}\otimes\hat{P}_{a_2}|\psi_{out}\rangle\,. \tag{3.10}$$

Considering the equations, the coincidence probability is:

$$p = \frac{1}{2} - \frac{1}{2}\int d\omega_1 \varphi^*_1(\omega_1)\varphi_2(\omega_1)e^{-i\omega_1\tau}\int d\omega_2 \varphi^*_2(\omega_2)\varphi_1(\omega_2)e^{-i\omega_2\tau}. \tag{3.11}$$

In the case where both photons have identical Gaussian spectral amplitude function ($\varphi_1 = \varphi_2$), the coincidence probability becomes [119]:

$$p = \frac{1}{2} - \frac{1}{2}e^{-\frac{\sigma^2\tau^2}{2}}, \tag{3.12}$$

where σ is the spectral width and τ is the time delay. Eq. (3.12) indicates that having a delay increases the distinguishability between the two photons.

Based on the eq. (3.11) it is common to define a quantum-interference visibility as:

$$\mathcal{V}_{HOM} = \frac{p_{\max} - p_{\min}}{p_{\max}} = \frac{P_{a_1a_2}(\infty) - P_{a_1a_2}(0)}{P_{a_1a_2}(\infty)}\,, \tag{3.13}$$

which is a measure of the depth of the HOM dip, and it depends on the overlap of the photon spectra. This definition of Visibility has been chosen in the analysis of the experimental data, but there are other choices [120], which lead to different values of visibility. Additional details will be included in section 3.2.2.

Reversed Hong-Ou-Mandel effect

The standard HOM effect involves photons initially occupying separate modes, represented by the state $|11\rangle$. They then evolve into a uniform superposition $(|20\rangle + |02\rangle)/\sqrt{2}$, signifying the possibility of both photons being in the top mode or both in the bottom one. Another quantum interference phenomenon is the time reversal of the HOM effect, known as the reversed HOM effect (rev-HOM).
In this configuration, we start from the superposition $(|20\rangle + |02\rangle)/\sqrt{2}$, introduce a phase shift to the lower mode, combine the two modes using a beam-splitter, and detect coincidences in the two output modes. The impact of a phase shifter on a mode operator is expressed as $\hat{a}_k^\dagger \rightarrow e^{i\phi}\hat{a}_k^\dagger$, where ϕ is the phase shift. Accordingly, the state injected into the beam-splitter can be represented as:

$$|\psi\rangle_{in} = \frac{1}{\sqrt{2}}\left[(\hat{a}_1^\dagger)^2 + e^{i2\phi}(\hat{a}_2^\dagger)^2\right]|0\rangle\,. \tag{3.14}$$

Please note that the phase in the superposition state undergoes a factor of 2, attributed to the fact that two photons pass through the phase shifter. After applying the BS transformation as previously described, we obtain the output state, up to a global phase

$$|\psi\rangle_{out} = \cos(\phi)\,|11\rangle - \sin(\phi)(|20\rangle - |02\rangle)/\sqrt{2}\,. \tag{3.15}$$

The probability of detecting a coincidence denoted as p_{coinc}, is dependent on the applied phase and is expressed as

$$p_{\text{coinc}} = \cos^2(\phi)\,. \tag{3.16}$$

As shown in Fig. 3.3, quantum interference fringes in the rev-HOM effect arise through phase variation ϕ. Compared to classical light interference, where the power in one of the output ports fluctuates as $\propto \cos^2(\phi/2)$, quantum interference fringes have a frequency that is two times higher.

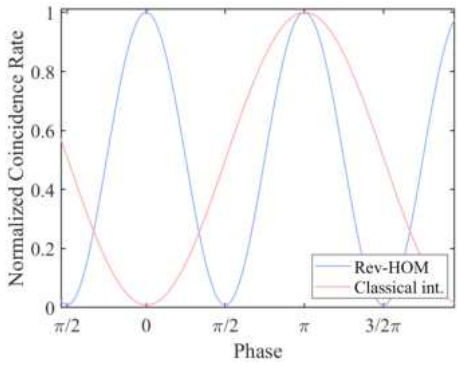

Figure 3.3: Classical light interference (red line) compared with the Reversed HOM interference (blue line).

As in the HOM situation, let us now treat the case of distinct photons. Specifically, we can examine a broad scenario where the frequency of the two photons differs. The input state in this generic case is provided by

$$|\psi\rangle_{in} = \frac{1}{\sqrt{2}}(|\psi\rangle_1 + |\psi\rangle_2)\,, \tag{3.17}$$

where

$$|\psi\rangle_1 = \int d\omega_1 \phi(\omega_1)\hat{a}^\dagger(\omega_1)\,, \tag{3.18a}$$

$$|\psi\rangle_2 = \int d\omega_2 \varphi(\omega_2)\hat{a}^\dagger(\omega_2)\,. \tag{3.18b}$$

Considering these equations, the coincidence probability will be

$$\begin{aligned} p &= \frac{1}{2} - \frac{1}{2}\mathbf{Re}\left[e^{2i\phi}\int d\omega_1 d\omega_2 \varphi^*(\omega_2)\phi(\omega_1)\right] \\ &= \frac{1}{2} - \frac{1}{2}\cos\left(2\phi+\theta_0\right)\left|e^{2i\phi}\int d\omega_1 d\omega_2 \varphi^*(\omega_2)\phi(\omega_1)\right|\,, \end{aligned} \tag{3.19}$$

where $\theta_0 = \frac{1}{2}\arg\int d\omega_1 d\omega_2 \phi(\omega_1)\varphi(\omega_2)^*$. The visibility of the fringes precisely is related to the overlap between the two joint spectral amplitudes. Defining visibility in terms of coincidence probabilities as:

$$\mathcal{V}^{exp}_{rev-HOM} = \frac{p_{max} - p_{min}}{p_{max}}\,, \tag{3.20}$$

and considering:

$$N = \left|e^{2i\phi}\int d\omega_1 d\omega_2 \varphi^*(\omega_2)\phi(\omega_1)\right|\,, \tag{3.21}$$

the visibility becomes:

$$\mathcal{V}^{exp}_{rev-HOM} = \frac{2N}{1+N}\,. \tag{3.22}$$

3.2.2 Rev-HOM effect from waveguide spiral sources

We expand on the rev-HOM effect to photons generated by two identical degenerate sFWM sources constructed with spiral waveguides, as shown in Fig. 3.4. These results come from our work [111].

Quantum silicon PIC and experimental setup

The generation of photon pairs in the silicon PIC is achieved through degenerate sFWM processes ($\omega_i = \omega_s$) in a low squeezing regime [28, 121–123]. The state of the output photons is a single-mode squeezed state [39, 124], and it is described in eq. (1.71). The PIC is packaged on a metal-based printed-circuit board (MPCB) with 24-port electrical wiring and is connected to a 24-channel fiber array. The MPCB is in contact with a thermo-electric cooler (TEC) to control the chip temperature. The PIC is based on silicon waveguides with a nominal 450 x 220 nm^2 cross-section (typically 480 x 210 nm^2 after fabrication) and was fabricated through IMEC foundry using their passive+ Silicon-on-Insulator (SOI) platform.
The measured waveguide propagation loss is 2 dB/cm. Fig. 3.4 shows schematically the experimental setup. Two CW tunable laser diodes (CoBrite from IDPhotonics) at λ_{P1}=1544.08 nm and λ_{P2}=1556.18 nm are combined by a 3-dB fiber-optic (FO) coupler and provide the pump photons. The combined beam is passed through an optical notch filter (NF) [114] to eliminate photon noise within 1.6 nm bandwidth around $\lambda_i = \lambda_s = 1550.12$ nm, which is the wavelength of the on-chip generated photon pairs. Then, the pump photons are inserted into the selected input fiber of the fiber array which is coupled to the chip by grating couplers, whose coupling loss is measured to be 4.2 dB.
In the PIC, the circuit is based on 2 MZIs with two nominally identical photon-pair

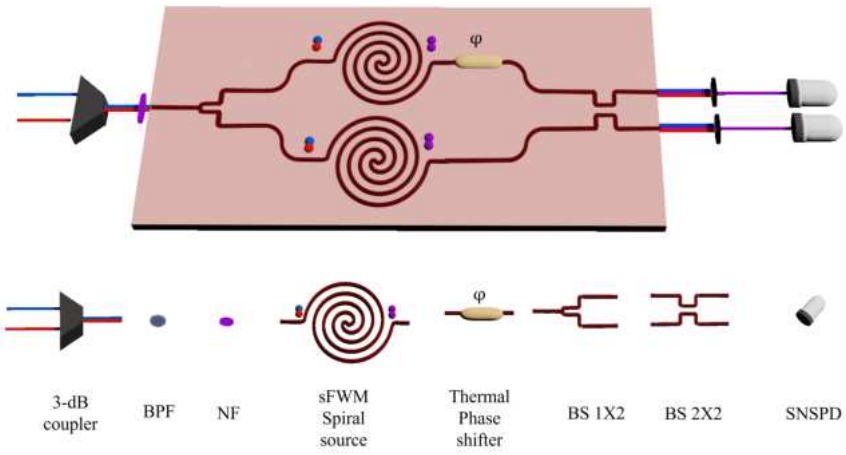

Figure 3.4: On the top the experimental setup for measuring photon pair generation and integrated multi-source quantum interference. From left to right: two lasers of different wavelengths coupled into the chip via a 3-dB coupler and grating coupler after appropriate filtering with a notch filter (NF). Blue and red spheres denote the two pump photons with distinct frequencies. The circuit illustrates the photon pair sources based on spiral waveguides forming the arms of a MZI. The two outputs of the MZI feature BPF to isolate the generated degenerate photons (depicted by purple spheres), two superconducting nanowire single-photon detectors (SNSPDs), and a time-correlated single-photon counting module interfaced with a computer. On the bottom, all components are shown.

sources located in their arms. The photon-pair sources are based on 15 mm-long waveguide spirals. Micro-heaters are also integrated into one arm of the MZI to act as phase shifters (ϕ) in order to compensate for unwanted phase differences between the two arms. The efficiency of the micro-heater of the MZI is measured to be about 25 mW/π with an overall resistance of about 50 Ω. At the output of the PIC, the photons are extracted via a grating coupler by the fiber arrays, filtered off the pump photons with bandpass filters (BPFs, with a 0.8 nm bandwidth centered at 1550.12 nm), and detected by using super-conducting-nanowire single-photon detectors (SNSPDs, EOS from Single Quantum) [114, 125]. Then the SNSPD single-photon events are counted by a time-correlated single-photon counter (TCSPC, Logic16 from UQdevices) and analyzed by logical post-selection.

Figure of merit of the integrated sources

The examination of the overall quality of the integrated sources involved simulation of the JSI of the generated pairs and measurements of the CAR [125], the heralding rate [114, 125], and the zero-delay heralded second-order coherence function $g_H^{(2)}(0)$ [115]. To determine $g_H^{(2)}(0)$, a 3-dB fiber splitter was introduced between the PIC outputs and the SNSPDs, creating a HBT interferometer [115]. The theoretical description of these parameters is provided in Chapter 1.

Fig. 3.5 illustrates the JSI for 15 mm long spiral waveguides. Notably, even in a degenerate sFWM process, the wavelengths of the generated photon pairs are dispersed around $\lambda_s \simeq \lambda_i$ due to the spectral width of the pump laser and the generation band of the FWM process. Additionally, the broad shapes of the JSIs for the waveguides suggest a significant correlation in the photons generated by these waveguides. The

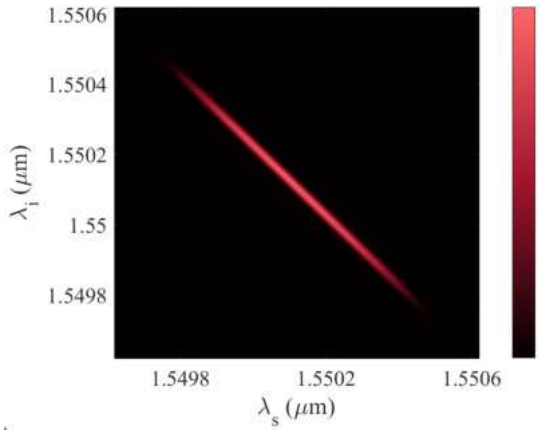

Figure 3.5: Simulated JSI for a 15-mm-long waveguide spiral plotted against signal (λ_s) and idler (λ_i) wavelengths after applying a BPF centered at 1550.12 nm with a bandwidth of 100 GHz (0.8 nm) using CW pump lasers.

filtering process reduces this correlation and the brightness of the photon pair source. The purity was calculated using eq. (1.103), yielding a value of 81%. Fig. 3.6(a) displays

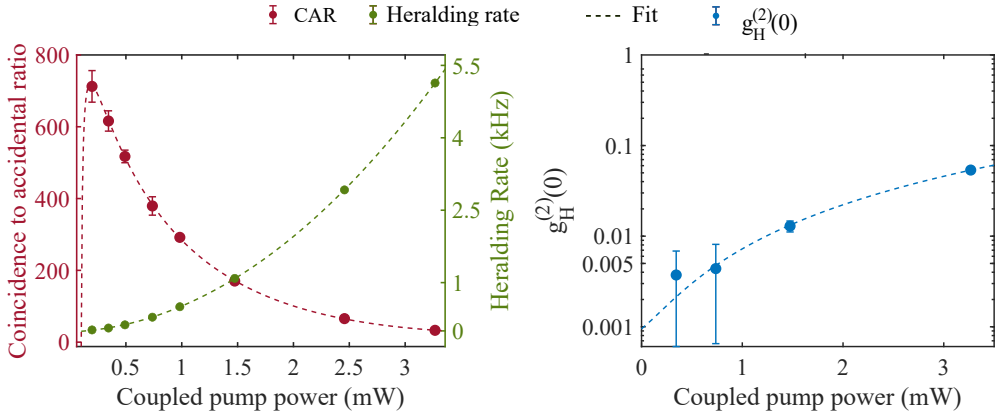

Figure 3.6: a) The CAR is plotted (red dots) against the pump power coupled to the chip. Additionally, the heralding rate (green dots) is shown as a function of the coupled pump power. b) The heralded second-order correlation function $g_H^{(2)}(0)$ is depicted as a function of the coupled pump power (blue dots).

the measured CAR and heralding rate. The CAR is calculated as eq. (1.130). The maximum value obtained is 715 at 0.2 mW on-chip pump power. The heralding rate for a spiral waveguide is 1 kHz with a pump power of 1.5 mW (equivalent to a conversion efficiency of -126 dB for heralding). The chosen coincidence time window of the time-correlated single-photon counter (TCSPC) is set to 0.2 ns.

In Fig. 3.6(b), the $g_H^{(2)}(0)$ of the photons generated by the spiral waveguide sources is depicted. At low input pump power, high-quality heralded single photons are present. With an increase in pump power, $g_H^{(2)}(0)$ increases due to multiphoton contributions. Remarkably, antibunching behavior is observed across all pump power levels.

Our experiments were conducted with low pump powers to achieve optimal values

of CAR and $g_H^{(2)}(0)$, where the quadratic behavior of the generation rate is observable. This places us in a regime where TPA does not limit performance. Indeed, at low pump powers, the conversion efficiency of photon-pair generation is low, but nonlinear losses due to TPA and FCA can be neglected compared to linear losses from scattering [126]. Consequently, we can assert that sFWM in PIC should be exclusively performed at low optical pump powers to avoid a sudden decline in performance at higher powers [127].

Evolution state description of the rev-HOM interference

Before proceeding with the measurement, we reconstruct the output state from the interferometer. To facilitate this, we segment the Fig. 3.4 into four parts, identified by the Roman numerals I-V in Fig. 3.7. In Section **I**, the pump photons are divided into

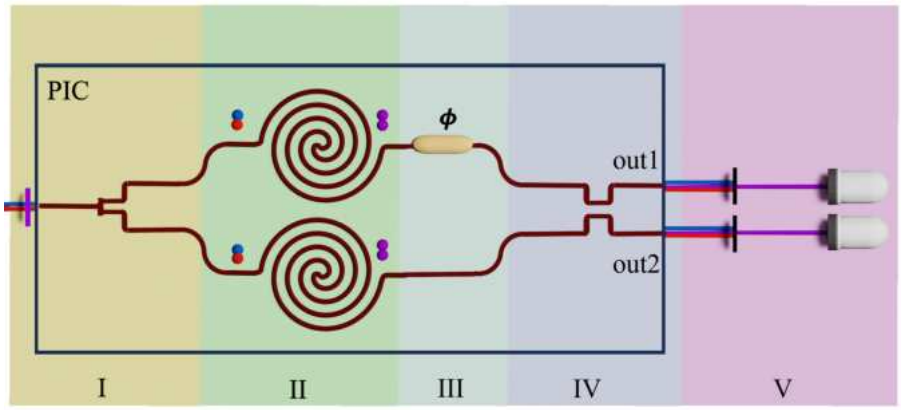

Figure 3.7: The scheme depicted in Fig. 3.4 is displayed, and divided into five parts to facilitate its analytical description. the rectangular block corresponds to the PIC.

two paths, denoted as path 1 (upper) and path 2 (lower), utilizing the first 1X2 MMI. Section **II** includes the degenerate sFWM process, generating a pair of photons along the two designated routes. Section **III** introduces a phase shifter ϕ in path 1, thereby incorporating a relative phase compared to path 2. Subsequently, Section **IV** employs a 2X2 MMI to induce interference between the photons propagating in the two arms. In Section **V**, the filtering and detection of the two pathways are carried out.
The initial state, consisting of two pump beams at the frequencies ω_{P1} and ω_{P2}, can be expressed as:

$$|\Psi\rangle_0 = \exp\left[\int d\omega \, (\alpha(\omega) + \beta(\omega)) \, \hat{A}^\dagger(\omega)\right] |\text{vac}\rangle \tag{3.23}$$

Here, $\hat{A}^\dagger(\omega)$ represents the creation operator, while α and β are the amplitude functions of the pump beams centered at ω_{P1} and ω_{P2}, respectively. It is important to note that we are dealing with unnormalized states; consequently, any meaningful quantity must arise from a proper ratio.

Due to the filter at the entrance of the chip, we can make the assumption that

$$\int d\omega \, \alpha(\omega)\bar{\beta}(\omega) = 0\,. \tag{3.24}$$

In **Section I**, the pump photons undergo interference with a 1X2 MMI. Applying this evolution to the initial state, we obtain:

$$|\Psi\rangle_{\mathrm{I}} = \exp\left[\int \mathrm{d}\omega \frac{(\alpha(\omega)+\beta(\omega))}{\sqrt{2}}\left(\hat{a}_1^\dagger(\omega)+\hat{a}_2^\dagger(\omega)\right)\right]|\mathrm{vac}\rangle, \tag{3.25}$$

where $\hat{a}_1^\dagger$ corresponds to the upper waveguide and $\hat{a}_2^\dagger$ to the lower one.

In **Section II**, the degenerate sFWM mechanism generates correlated photons that annihilate two pump photons (see chapter 2 for details). As we explained in the eq. (2.43), the state is

$$|\Psi\rangle_{\mathrm{II}} = \exp\left\{\frac{\xi}{2}\int \mathrm{d}\omega_i \mathrm{d}\omega_s \left[F_1(\omega_i,\omega_s)\ \hat{a}_1^\dagger(\omega_i)\hat{a}_1^\dagger(\omega_s) + F_2(\omega_i,\omega_s)\ \hat{a}_2^\dagger(\omega_i)\hat{a}_2^\dagger(\omega_s)\right]\right\}|\mathrm{vac}\rangle. \tag{3.26}$$

Here, $F_{1/2}$ represents the JSA of the source in the upper/lower waveguides. We omit the residual contribution from the pumps and the non-degenerate generation process since our detection will focus solely on the contributions around the degenerate generation process.

In **Section III**, a phase shifter is introduced into path 1. This allows the photons from that path to undergo an additional phase shift. The resulting state will be:

$$|\Psi\rangle_{\mathrm{III}} = \exp\left\{\frac{\xi}{2}\int \mathrm{d}\omega_i \mathrm{d}\omega_s \left[F_1(\omega_i,\omega_s)\mathrm{e}^{2\mathrm{i}\phi}\ \hat{a}_1^\dagger(\omega_i)\hat{a}_1^\dagger(\omega_s) + F_2(\omega_i,\omega_s)\ \hat{a}_2^\dagger(\omega_i)\hat{a}_2^\dagger(\omega_s)\right]\right\}|\mathrm{vac}\rangle\,. \tag{3.27}$$

In Section IV, we consider the interference between two paths, 1 and 2, through a 2X2 MMI. In eq. (2.21) its unitary matrix is provided. Applying this unitary matrix, the state evolves.

$$\begin{aligned}|\Psi\rangle_{\mathrm{IV}} = \exp\Big\{\frac{\xi}{4}\int \mathrm{d}\omega_i \mathrm{d}\omega_s \Big[&F_1(\omega_i,\omega_s)\,\mathrm{e}^{2\mathrm{i}\phi}\left(\hat{a}_1^\dagger(\omega_i)+\mathrm{i}\,\hat{a}_2^\dagger(\omega_i)\right)\left(\hat{a}_1^\dagger(\omega_s)+\mathrm{i}\,\hat{a}_2^\dagger(\omega_s)\right) \\ &+ F_2(\omega_i,\omega_s)\left(\hat{a}_2^\dagger(\omega_i)+\mathrm{i}\,\hat{a}_1^\dagger(\omega_i)\right)\left(\hat{a}_2^\dagger(\omega_s)+\mathrm{i}\,\hat{a}_1^\dagger(\omega_s)\right)\Big]\Big\}|\mathrm{vac}\rangle \\ = \exp\Big\{\frac{\xi}{4}\int \mathrm{d}\omega_i \mathrm{d}\omega_s \Big[&\left(F_1(\omega_i,\omega_s)\,\mathrm{e}^{2\mathrm{i}\phi} - F_2(\omega_i,\omega_s)\right)\left(\hat{a}_1^\dagger(\omega_i)\,\hat{a}_1^\dagger(\omega_s) - \hat{a}_2^\dagger(\omega_i)\,\hat{a}_2^\dagger(\omega_s)\right) \\ &+ 2\mathrm{i}\left(F_1(\omega_i,\omega_s)\,\mathrm{e}^{2\mathrm{i}\phi} + F_2(\omega_i,\omega_s)\right)\hat{a}_1^\dagger(\omega_i)\,\hat{a}_2^\dagger(\omega_s)\Big]\Big\}|\mathrm{vac}\rangle\,.\end{aligned} \tag{3.28}$$

Considering the filtering in the eq. (3.9) of operator describing the detection, we obtain:

$$\hat{P}_i := \int \mathrm{d}\omega f(\omega) \sum_{n\neq 0}\frac{1}{n!}\left(\hat{a}_i(\omega)^\dagger\right)^n |\mathrm{vac}\rangle\langle\mathrm{vac}|\left(\hat{a}_i(\omega)\right)^n, \tag{3.29}$$

where the function f represents the spectral amplitude of the filter. Note that we have implemented operators that take into account threshold detectors. The probability of detecting coincidences in channels 1 and 2 is given by the eq. (3.10). We obtain:

$$\begin{aligned}p_{12} &\approx \frac{1}{4}\int \mathrm{d}\omega_i \mathrm{d}\omega_s f(\omega_i) f(\omega_s)\left[|F_1(\omega_i,\omega_s)|^2 + |F_2(\omega_i,\omega_s)|^2 + 2\mathrm{Re}\left[F_1(\omega_i,\omega_s)\bar{F}_2(\omega_i,\omega_s)\mathrm{e}^{2\mathrm{i}\phi}\right]\right] \\ &= \frac{1}{2}\left\{1+\mathrm{Re}\left[\mathrm{e}^{2\mathrm{i}\phi}\int \mathrm{d}\omega_i \mathrm{d}\omega_s f(\omega_i) f(\omega_s) F_1(\omega_i,\omega_s)\bar{F}_2(\omega_i,\omega_s)\right]\right\}.\end{aligned} \tag{3.30}$$

The approximation consisting of keeping only the leading term is based on the fact that we can choose to work in the low gain regime once the sources have been characterized. In terms of JSAs overlap, p_{12} takes the form

$$p_{12}(\phi, \delta, N) = \frac{1}{2}\left\{1 + N\cos\left(2\phi + \delta\right)\right\}, \tag{3.31}$$

$$\text{where} \quad N\,\mathrm{e}^{\mathrm{i}\delta} := \int \mathrm{d}\omega_i \mathrm{d}\omega_s f(\omega_i) f(\omega_s) F_1(\omega_i, \omega_s) \bar{F}_2(\omega_i, \omega_s)\,. \tag{3.32}$$

It is easy to see that $F_1 = F_2$ implies $N = 1$ and $\delta = 0$ and, therefore, $p_{12} = \cos(\phi)^2$ and $p_{12}^{\max} = p_{12}(\phi = 0)$ and $p_{12}^{\min} = p_{12}(\phi = \pi/2)$.
In the generic case, the maxima of p_{12} are located at $2\phi + \delta = 2N\pi$ and the minima at $2\phi + \delta = N\pi$ with $N \in \mathbf{Z}$ and the visibility reads

$$V = \frac{2N}{1+N}, \tag{3.33}$$

$$\text{where} \quad N := \left| \int \mathrm{d}\omega_i \mathrm{d}\omega_s f(\omega_i) f(\omega_s) F_1(\omega_i, \omega_s) \bar{F}_2(\omega_i, \omega_s) \right|. \tag{3.34}$$

Hence, from the experimental value of V, we can determine the JSA overlaps N for our two sources. The normalized coincidence probability is given by:

$$p_{12}^{\mathrm{norm}}(\phi, \delta, N) = \frac{1}{1+N}\left\{1 + N\cos\left(2\phi + \delta\right)\right\}. \tag{3.35}$$

From the formula for the normalized coincidence probability, we observe that a relative phase difference between the JSAs of the two sources can shift the interference pattern of the rev-HOM experiment. However, it's essential to acknowledge that such a relative phase can be easily obscured from our observation due to non-idealities arising from the fabrication process. In our case, even a small difference in the length of the two arms of the MZI involved in the HOM dynamics could significantly contribute to these non-idealities.

Rev-HOM effect measurement

We conduct a quantum rev-HOM interference measurement between photons generated by the two degenerate sources. As previously outlined in the chapter's introduction, this measurement serves to assess the indistinguishability of the photons produced by these sources. Fig. 3.8 shows the counts detected on the two output channels of the MZI, representing the classical transmission of light (a), and the coincidence rates (b) between the two channels. These coincidence rates reveal the quantum interference among photons generated as a result of the phase ϕ introduced by the thermal phase shifter in one of the arms of the MZI. Notably, these measurements were conducted at a fixed on-chip power of 1.5 mW. The outcome of the coincidence measurement is attributed to the rev-HOM interference of degenerate photon pairs at the second MMI of the MZI. The high visibility of 98.8% was obtained by applying the formula (3.20). This result confirms the indistinguishability of photon pairs generated by the two spirals [113, 115]. As explained in eq. (3.33), we can determine the overlap coefficient of the JSAs from the visibility. The calculated value of the JSAs overlap is 97.6%. This parameter provides information on the difference between the two JSAs and, therefore, the distinguishability of the generated photons and sources.

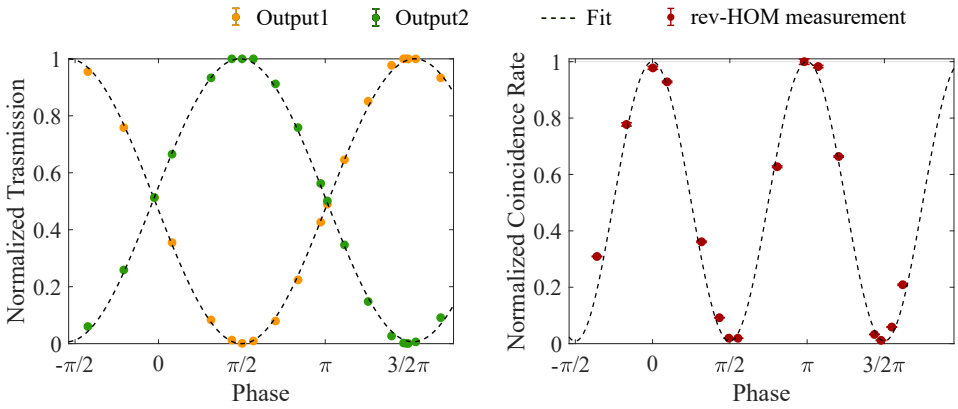

Figure 3.8: a) Classical transmissions measured from the two outputs (yellow dots for output 1, green dots for output 2) of the MZI in Fig. 3.7 plotted as a function of the phase ϕ. The theoretical predictions are the dashed lines. (b) Measured (dark red dots) and theoretical (dashed line) coincidence rates between the two outputs of the MZI as a function of the phase ϕ.

3.2.3 Comparative analysis of microring resonator and spiral waveguide photon pair sources

Quantum silicon PIC and experimental setup RHR-HOM

A schematic illustration of the experimental setup, designed to compare spiral and microring waveguide sources directly, is illustrated in Fig. 3.9. This configuration expands upon the previously mentioned concept, as shown in Fig. 3.7, by integrating an experimental HOM configuration with the rev-HOM effect.

In this new PIC, two nominally identical microring resonators are coupled to two nominally identical spiral waveguides forming the arms of an MZI. Similar to the previous case, the PIC is pumped by two lasers at different wavelengths, at 1543.78 nm and 1556.53 nm, to generate pairs of degenerate photons at 1550.12 nm through spontaneous four-wave mixing. Specifically, microring resonators can be thermally tuned to enter or exit resonance with the pump wavelengths, allowing the selection of microring resonators or waveguides as sources of photon pairs, respectively. Fine-tuned microrings exclude the spiral waveguides placed next to them due to their efficient rejection of the pump wavelengths.

The microrings have 28.5-µm radius, a Q factor of 3×10^4, and an FSR of 3.2 nm. The spiral waveguides have the same length as in the previous experiment (15 mm). The grating couplers exhibit a measured coupling efficiency of 3.3 dB.

The photon pump filters formed by aMZIs are placed after the first MZI to eliminate residual pumps and reduce accidental coincidence counts. The asymmetric length of the aMZI is designed to be 47.2-µm, resulting in an FSR of 12.8 nm (1600 GHz) and a pump rejection ratio exceeding 30 dB.

The circuit then incorporates an additional MZI to measure the quantum interference of the generated photon pairs (HOM-revHOM interference). This is achieved through a thermal phase shifter ϕ_2 after achieving perfect source matching with ϕ_1.

At the output of the PIC, the photons are coupled through gratings from the fiber array. Outputs 1 and 2 are filtered by pump photons using BPF with a bandwidth of 0.8 nm centered at 1550.12 nm and detected by SNSPDs. A small portion (1% of the power) is extracted before the two filters and directed to two photodiodes PD_1 and PD_2. Outputs

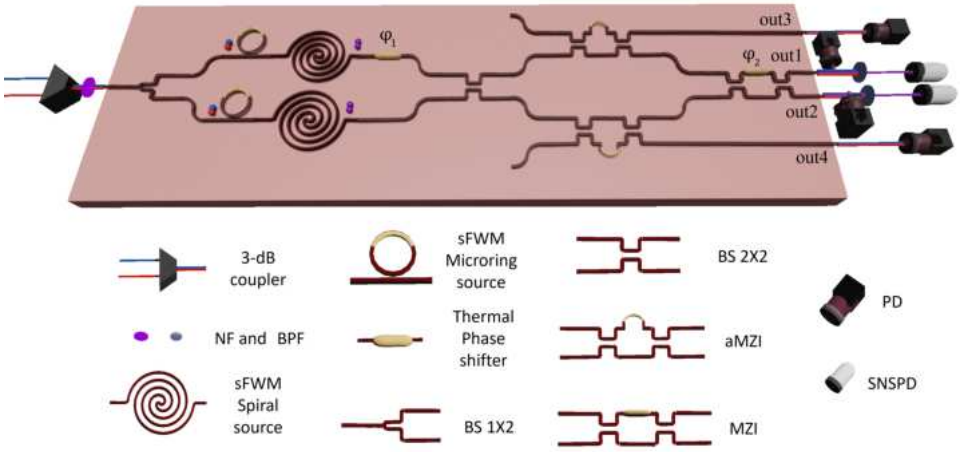

Figure 3.9: The PIC formed by composite photon-pair sources utilizing both waveguides and microrings. These sources are then subjected to a second MZI to measure the quantum interference of the generated photons. On the right, the detection channels (out1-out4) are depicted. These channels consist of a series of optical fibers, BPFs, superconducting nanowire SNSPDs, and a time-correlated single photon counting module linked to a computer for subsequent data processing.

3 and 4 are coupled to two additional photodiodes PD_3 and PD_4.

Fig. 3.10 displays the normalized transmission spectra measured with the photodiodes (PD_1-PD_4) visible in Fig. 3.9. Thermal tuning of filters allows them to match the wavelength of the generated photons and appropriately remove the pump wavelengths. PD_1 and PD_2 indicate the transmission of the generated photons and pump removal, while PD_3 and PD_4 allow tracking of the residual power and proper filter operation.

Figure of merit of the integrated sources

Similar to the rev-HOM case, we analyze various performance metrics for the two types of sources under consideration. Fig. 3.11 illustrates the simulated JSI as a function of signal (λ_s) and idler (λ_i) wavelengths after applying a BPF centered at 1550.12 nm using CW pump lasers for (a) waveguide spiral and (b) microring resonator. The simulation carried out for the JSI of the spiral source is consistent with Fig. 3.5. Notably, even in a degenerate sFWM process, the wavelengths of the generated photon pairs are distributed around $\lambda_s \simeq \lambda_i$ due to the spectral width of the pump laser lines and the generation bandwidth of the FWM process. The JSI shapes of the waveguides are broader than those of the microring resonators, indicating a higher correlation in the photons generated by the waveguides compared to the microring resonators. These broad JSIs are attributed to the BPF filtering of the broad waveguide generation band (between the two wavelengths of pump photons). The filtering also diminishes the brightness of the photon pair source. In the case of microring resonators, the effect of the BPF is negligible due to the narrow width of the microring resonance spectrum. Additionally, high Q-factor values result in narrow JSIs and increased probability of photon pair generation, which follows a cubic law with respect to the Q-factor value, as given in eq. (2.46). However, high Q-factor values make the microring resonator more susceptible to thermal crosstalk, and TPA.
In the simulations for JSI and purity, the two microring waveguides/resonators are

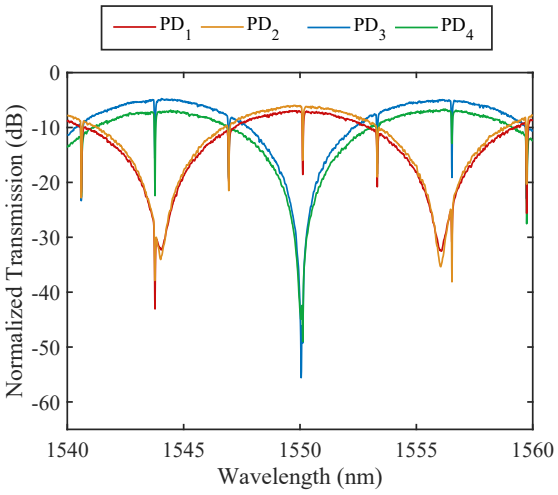

Figure 3.10: Normalized transmission spectra measured by different photodiodes are depicted, with the red line representing PD_1, the orange line representing PD_2, the blue line representing PD_3, and the green line representing PD_4. These measurements were obtained while scanning the wavelength of one of the tunable laser diodes.

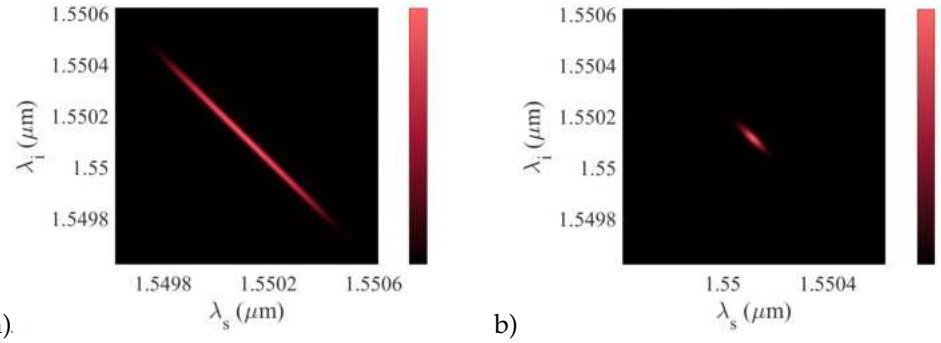

Figure 3.11: Simulated JSI plotted as a function of signal (λ_s) and idler (λ_i) wavelengths after applying a BPF centered at 1550.12 nm with a bandwidth of 100 GHz (0.8 nm) using CW pump lasers for two configurations: (a) a 15-mm-long waveguide spiral, and (b) a microring resonator with a FSR approximately 3.2 nm and a quality factor of 3×10^4 (resulting in a FWHM of 0.05 nm).

assumed to be identical to their nominal design values. This implies that the simulated values are not affected by small variations in the nominal parameters present in the fabricated structures. The purity was calculated using eq. (1.103). The simulated purity corresponds to 81% for the spiral waveguide source and 90% for the microring resonator. An interesting aspect to note is that the purity in the case of the waveguide source without an inserted filter decreases dramatically, reaching a simulated value of 20%. The simplicity of fabricating a waveguide source faces a bottleneck in the need to use a high-quality BPF to produce photons with high spectral purity.

Fig. 3.12 presents the CAR (a) and heralding rate (b) measurements for the two sources. Throughout the measurements, the phase ϕ_2 of the second MZI is fixed at zero. Two ways are possible in this configuration: microring in resonance, where the generation contribution of the microring resonator is considered (blue dots), and microring out of

resonance, where only the generation contribution of the spiral waveguide is considered (red dots). The maximum CAR value surpasses 1000 for spirals and 600 for microring resonators. These values emphasize the effectiveness of pump photon removal achieved by incorporating on-chip aMZI-based pump filters in addition to external filters placed before detection.

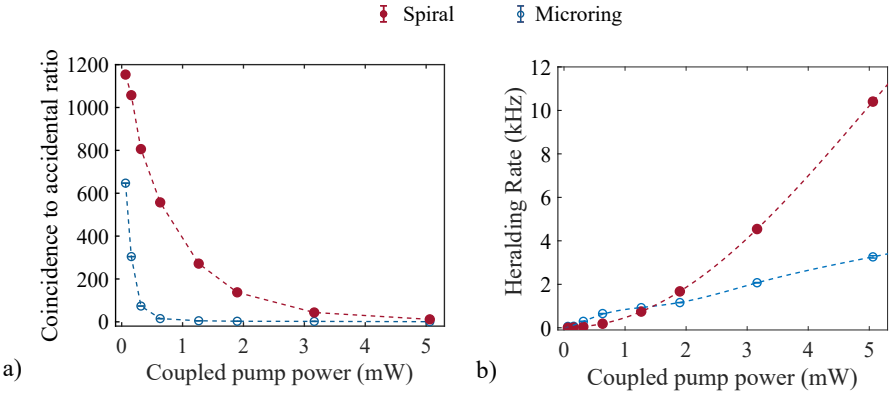

Figure 3.12: Measurements of the characteristics of the photon-pair sources are presented. a) The coincidence to accidental ratio as a function of the pump power coupled to the chip, where dark red dots correspond to the spiral waveguide (indicating that the microrings are off-resonant with the pump photons wavelengths), and empty blue dots represent the microring source (denoting that the microrings are resonant with the pump photons wavelengths). b) The heralding rate as a function of the coupled pump power is shown for the spiral waveguide (dark red dots) and microring resonator (empty blue dots).

In Fig. 3.12(b), the heralding rate is depicted, with a rate of 10 kHz for the spiral waveguide and 3 kHz for the microring resonator at 5 mW pump power. Both the CAR and the heralding rate for the rings are influenced by propagation losses due to the 15 mm long spirals following the microring on the arms of the first MZI, as well as substantial TPA losses in the microring due to the high Q factor.
To minimize the impact of TPA, our comparative experiments were conducted using low pump powers to achieve optimal CAR values, where the quadratic behavior of the generation rate is observable. Using low pump powers results in low conversion efficiency of photon pair generation, but nonlinear losses due to TPA and FCA can be neglected in comparison to linear losses due to scattering [126].

Evolution state description of the RHR-HOM interference

Let's examine the theoretical aspect of the reverse HOM-HOM-reverse HOM experiment, as seen in the integrated system shown in Fig. 3.9. For convenience, I define this experiment as RHR-HOM.
We divided the integrated system into different sections, as shown in Figure 3.13. Notably, by replacing ϕ with ϕ_1, the circuit remains unchanged up to Sec. IV, mirroring the setup displayed in Figure 3.7. In **Sec. V**, the two paths undergo further division into two new paths using two aMZIs. At this stage, path 1 is split into two additional paths, denoted as path 1 (corresponding to detection channel 1) and path 3 (corresponding to detection channel 3). Similarly, path 2 is split into path 4 (corresponding to detection channel 4) and path 2 (corresponding to detection channel 2). In **Sec. VI**, an integrated MZI composed of two 2X2 MMIs and a phase shifter ϕ_2 induces interactions between

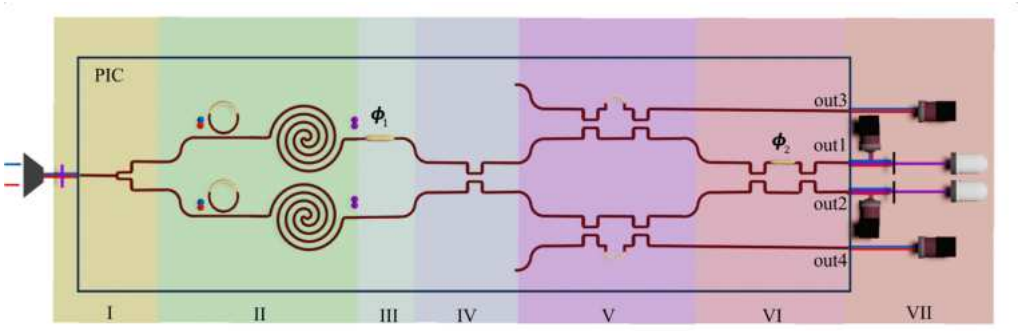

Figure 3.13: The chip design of Fig. 3.9 is partitioned into 7 distinct sections for ease of discussion.

photons from paths 1 and 2. The final steps involve filtering and detection of the two internal pathways in **Sec. VII**. Let's start from the state in **Sec. IV**:

$$|\Psi\rangle_{\mathrm{IV}} = \exp\left\{\frac{\xi}{4}\int \mathrm{d}\omega_i \mathrm{d}\omega_s \Big[F_1(\omega_i,\omega_s)\,\mathrm{e}^{2\mathrm{i}\phi_1}\,\left(\hat{a}_1^\dagger(\omega_i)+\mathrm{i}\,\hat{a}_2^\dagger(\omega_i)\right)\left(\hat{a}_1^\dagger(\omega_s)+\mathrm{i}\,\hat{a}_2^\dagger(\omega_s)\right) + F_2(\omega_i,\omega_s)\,\left(\hat{a}_2^\dagger(\omega_i)+\mathrm{i}\,\hat{a}_1^\dagger(\omega_i)\right)\left(\hat{a}_2^\dagger(\omega_s)+\mathrm{i}\,\hat{a}_1^\dagger(\omega_s)\right)\Big]\right\}|\mathrm{vac}\rangle\,. \tag{3.36}$$

In **Section V**, we treat the effect of aMZIs as if they were acting as filters. For simplicity, we assume that the two aMZIs are identical, meaning that their frequency responses are the same, denoted as $f_{aMZI1} = f_{aMZI2} = f_{aMZI}$. In principle, aMZIs do not affect the generated photons but are designed solely to eliminate the residual pump. However, to account for their dependence on the frequency, I denote them with the notation $f_{aMZI}(\omega)$. The state is

$$|\Psi\rangle_{\mathrm{IV}} = \exp\left\{\frac{\xi}{4}\int \mathrm{d}\omega_i \mathrm{d}\omega_s f_{aMZI}(\omega)\Big[F_1(\omega_i,\omega_s)\,\mathrm{e}^{2\mathrm{i}\phi_1}\,\hat{b}_1^\dagger(\omega_i)\hat{b}_1^\dagger(\omega_s) - F_2(\omega_i,\omega_s)\,\hat{b}_2^\dagger(\omega_i)\hat{b}_2^\dagger(\omega_s)\Big]\right\}|\mathrm{vac}\rangle\,. \tag{3.37}$$

with

$$\hat{b}_1^\dagger = \hat{a}_1^\dagger(\omega_i) + \mathrm{i}\,\hat{a}_2^\dagger(\omega_i)\,, \tag{3.38a}$$

$$\hat{b}_2^\dagger = \hat{a}_1^\dagger(\omega_i) - \mathrm{i}\,\hat{a}_2^\dagger(\omega_i)\,. \tag{3.38b}$$

In **Section VI**, the second MZI exclusively influences photons propagating along central pathways $\hat{a}_1$ and $\hat{a}_2$. Therefore, the resulting state in **Section VI** reads

$$|\Psi\rangle_{\mathrm{VI}} = \exp\left\{\frac{\xi}{4}\int \mathrm{d}\omega_i \mathrm{d}\omega_s f_{aMZI}(\omega)\Big[F_1(\omega_i,\omega_s)\,\mathrm{e}^{2\mathrm{i}\phi_1}\,\hat{b}_3^\dagger(\omega_i)\,\hat{b}_3^\dagger(\omega_s) - F_2(\omega_i,\omega_s)\,\hat{b}_4^\dagger(\omega_i)\,\hat{b}_4^\dagger(\omega_s)\Big]\right\}|\mathrm{vac}\rangle\,, \tag{3.39}$$

where $\hat{b}_3^\dagger(\omega) \equiv -\hat{a}_1^\dagger(\omega) + \mathrm{i}\,\hat{a}_2^\dagger(\omega)\,,$

and $\hat{b}_4^\dagger(\omega) \equiv \mathrm{e}^{\mathrm{i}\phi_2}\left(\hat{a}_1^\dagger(\omega) + \mathrm{i}\,\hat{a}_2^\dagger(\omega)\right)\,.$

In the final **Section VII**, the filtering and detection are represented by the operators defined in eq. (3.29). Consider the probability after **Sec. VII** we find:

$$p_{12} = \frac{1}{4}\left\{1 + \mathrm{Re}\left[e^{2i(\phi_1-\phi_2)} \int d\omega_i d\omega_s f(\omega_i) f(\omega_s) F_1(\omega_i,\omega_s)\bar{F}_2(\omega_i,\omega_s)\right]\right\}. \tag{3.40}$$

Visibility is defined as

$$V = \frac{p_{12}^{\max} - p_{12}^{\min}}{p_{12}^{\max}}. \tag{3.41}$$

By performing the same manipulations as detailed in the rev-HOM case, we arrive at identical formulas. This consistency stems from the fact that all the designs leverage the same features, especially when normalizing the coincidence data. The visibility in the context of the overlap of JSAs can be expressed as follows:

$$V = \frac{2\int d\omega_i d\omega_s F_1(\omega_i,\omega_s)\bar{F}_2(\omega_i,\omega_s)}{1 + \int d\omega_i d\omega_s F_1(\omega_i,\omega_s)\bar{F}_2(\omega_i,\omega_s)}. \tag{3.42}$$

RHR-HOM effect measurement

The measured RHR-HOM interference for this new configuration is shown in Fig. 3.14(a). These measurements were conducted by varying the ϕ_2 phase of the second MZI. For the configuration with the resonant microring (blue dots), a HOM interference visibility of 94% is measured at a pump power of 0.3 mW. For the configuration with the spiral

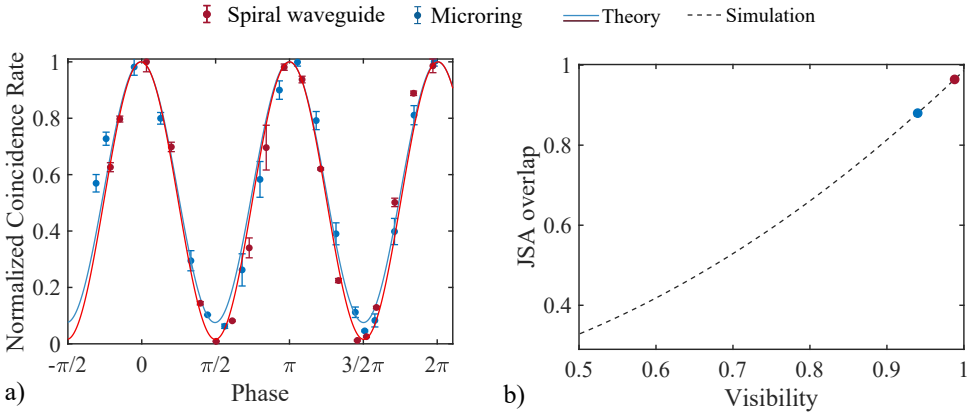

Figure 3.14: a) Coincidence rates between the output channels of the second MZI are plotted against the phase ϕ_2 of the second MZI. The blue line represents the HOM interference for the microring resonator configuration with an input pump power of 0.3 mW, while the red line illustrates the quantum interference for the spiral waveguide sources with two different pump powers, 0.6 mW. Experimental data are depicted as dots, while the lines correspond to theoretical fits obtained from eq. (3.40). b) The relationship between visibility and the overlap of JSAs is shown.

waveguide (red dots), a remarkable 99% visibility HOM interference is achieved at a pump power of 0.6 mW. In both cases, the theoretical behaviors expressed in eq. (3.40), as represented by the red and blue lines, align with the experimental results. The visibility is related, via eq. (3.42), to the overlap of JSAs of the considered sources. These

results suggest that in the case of spirals, the indistinguishability of the generated photons is greater than in the case of microring resonators. This implies that microring resonators are more susceptible to manufacturing defects than spiral waveguides. Specifically, in the case of spirals, an overlap of JSAs of 97.6% is obtained, while in the case of microring resonators, an overlap of JSAs of 88.7% is achieved.
The relationship between visibility and the overlap of JSAs is illustrated in Fig. 3.14(b), displaying data for the two types of sources.

Spiral Waveguide vs. Microring Resonator: Unveiling the optimal Source for Integrated Spontaneous Four-Wave Mixing

I present a comprehensive comparison between the two types of sources, combining simulation results and experimental analyses. Table 3.1 outlines the key characteristics of microring resonators and spiral waveguides analyzed in the different configurations.

	Observed Visibility	Simulated Purity	Computed JSAs overlap
Spirals (rev-HOM)	98.8%	81%	97.6%
Spirals (RHR-HOM)	99%	81%	98%
Microrings (RHR-HOM)	94%	90%	88.7%

Table 3.1: Summary of the relevant properties of the analyzed photon-pair source.

In the simulations for JSI and purity, both microrings-waveguides are assumed to be identical to their nominal design values. This ensures that the simulated values remain unaffected by small variations in the nominal parameters present in the fabricated structures. Purity calculations were executed using eq. (1.103), and the JSAs overlaps were determined based on experimental visibility results.

From a purity perspective, it is evident that the microring resonator exhibits higher purity without the need for an additional BPF. On the other hand, while demonstrating more robustness in fabrication, the spiral waveguide requires appropriate filtering to generate photons with high spectral purity. Plots showing the behavior of the JSA overlap when perturbations in one of the two sources' parameters occur are shown in Fig. 3.15. In particular, we investigate fluctuations in L_{eff} ($\delta L_{\text{eff}} = \Delta L_{\text{eff}}^{\text{error}} / L_{\text{eff}}^{\text{nominal}}[\%]$) for spiral waveguides and the Q-factor ($\delta Q = \Delta Q$) for microring resonators. This result emphasizes the greater sensitivity of ring resonators to fabrication errors, leading to distinguishing generated photons.
The comparison of the indistinguishability of generated photons reveals that the visibility in the case of the spiral waveguide is higher than that of the microring resonator, despite the opposite trend observed in purity. An important aspect in our case is the interdependence of the sources, which distinguishes our experiment from many published experiments where sources are independent [119, 128, 129]. In the context of independent sources, non-degenerate sFWM is commonly employed to generate two pairs of idler photons and signals, resulting in a separable overall wave function of the state. In our case, the state is not separable, and the generated state involves a superposition of pairs of photons from the two sources. The state generated by the source pair, expressed in eq. (3.26), is

$$|\Psi\rangle_{\text{II}} \sim \int \mathrm{d}\omega_i \mathrm{d}\omega_s \left[F_1(\omega_i, \omega_s)\ \hat{a}_1^\dagger(\omega_i)\hat{a}_1^\dagger(\omega_s) + F_2(\omega_i, \omega_s)\ \hat{a}_2^\dagger(\omega_i)\hat{a}_2^\dagger(\omega_s) \right] |\text{vac}\rangle \,.$$

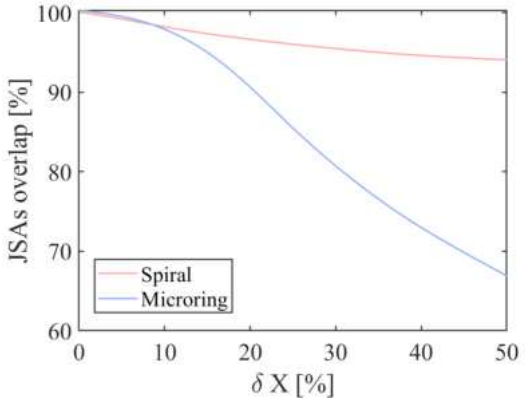

Figure 3.15: Simulated JSAs overlap as a function of variations in L_{eff} for spiral waveguides (red line), and JSAs overlap as a function of variations in Q-factor for microring resonators (light blue line). δX represents δL_{eff} for the waveguide case and δQ for the microring case.

In this equation, F_1 and F_2 are the JSAs of the two sources. It is important to note that $|\Psi\rangle_{\text{II}}$ represents a superposition of photon pairs generated in the two sources[1].

When choosing between source types of generated photons, it is important to consider the trade-offs between their purity and indistinguishability and choose a source based on the specific needs of the application.

3.3 Intra-modal and Inter-modal approaches

The sFWM needs to conserve energy and momentum:

$$\omega_{p1} + \omega_{p2} = \omega_i + \omega_s$$

$$k_{p1} + k_{p2} = k_i + k_s\,.$$

Considering that the wave vector is expressed as $k = \omega\, n_{eff}/c$, with c the speed of light, ω the frequency, and n_{eff} the effective refractive index, we can write the conservation of momentum in the waveguide as:

$$\Delta k = \frac{\omega_p}{c} n^j_{eff}(\omega_p) + \frac{\omega_p}{c} n^q_{eff}(\omega_p) - \frac{\omega_s}{c} n^l_{eff}(\omega_s) - \frac{\omega_i}{c} n^m_{eff}(\omega_i)\,, \tag{3.43}$$

where j, q, l, m represent the modes of the fields.

We define the sFWM process as intramodal when all 4 photons involved belong to the same mode ($j = q = l = m$). In contrast, we define the process intermodal when the different propagation constants of different order modes can be exploited to obtain an additional degree of freedom in the design of phase matching (PM). In this case, higher-order waveguide modes with different effective index profiles are employed. The intermodal PM condition offers more flexibility than the intramodal case due to the degree of freedom introduced by the waveguide modes.

An aspect of intermodal PM is the possibility, depending on the excited optical modes and geometry, to obtain discrete phase-matched bands with controllable wavelengths.

[1] In our case, a photon pair is generated in a superposition of two paths. In the case of non-degenerate FWM, two pairs are generated, and after the heralding, a state with one heralded photon in each path is obtained.

This feature allows for broadly tunable spectral conversions, with detunings that vary widely. In this contest, I will assume a specific scenario where $p1 = s$ denotes the first excited mode TE1, and $p2 = i$ represents the fundamental mode TE0. To ensure clarity I term this particular process as "intermodal 1221-TE sFWM", where the numerical values denote whether the photon propagates in the fundamental mode (1) or the first excited mode (2). The sequence of numbers denotes the involvement of the pumps $p1$, $p2$, and the corresponding idler (i) and signal (s) photons in the process.

3.3.1 Intermodal 1221-TE sFWM vs. intramodal 1111-TE sFWM

In the context of intermodal phase matching, it is imperative to adopt a comprehensive design approach that takes into account all effective index profiles involved in the PM relationship, particularly when dealing with substantial spectral shifts. Comparing intermodal and intramodal PM, it is observed that intermodal PM shows discrete behavior, offering the flexibility to be fine-tuned away from the pump wavelength. In contrast, intramodal PM is characterized by a narrow PM condition restricted in proximity to the pump wavelength, forming a continuous band.
In Fig. 3.16(a), by comparing the intramodal case (red line) with the intermodal case (blue line), we can observe the spectral dependence of the generation efficiency. Fig. 3.16(b)

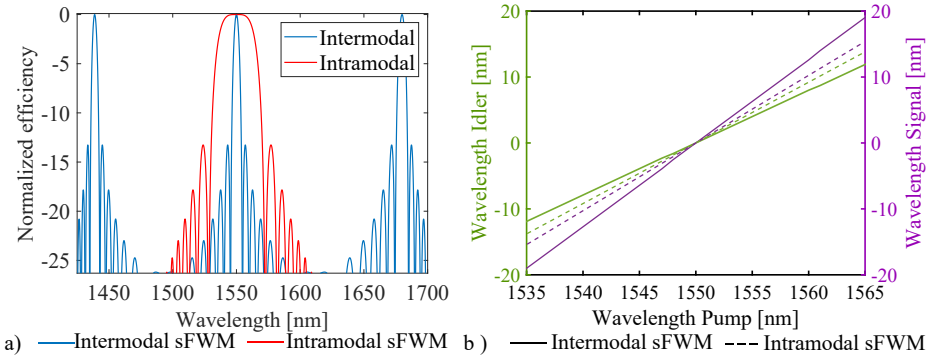

Figure 3.16: a) The PM relationship for the intramodal process is depicted by the red line, showing a continuous band, whereas for the intermodal process, it is represented by the blue line, displaying a discrete band. The cross-section of the waveguide is (2.45 $\times$ 0.22) µm. b) The PM relation of the generated photons varies as the wavelength of the pump photons changes. For the intramodal case, illustrated by dashed lines, and the intermodal case, portrayed by solid lines, this variation is shown.

illustrates the PM relationship for idler and signal photons as the pump wavelength varies for both the parametric cases. A comparison is made in a 3.45-µm-wide waveguide with a height of 220 nm. It is important that in the intramodal case, a small change in pump wavelength results in a substantial change in the signal photon wavelength. In contrast, the intermodal case exhibits a more modest change in the signal photon wavelength with variations in the pump wavelength as visible in Fig. 3.16(b). This characteristic, coupled with the influence of waveguide size variations, enables the selection of the generation region even at a considerable distance from that of the pump. A detailed analysis of this aspect will be presented in Chapter 4.

Mode field overlap efficency

Another aspect between the intramodal and intermodal processes is the efficiency (η) of the FWM in a waveguide of length L, scaled with the phase mismatch Δk. This

efficiency parameter is closely connected to the mode field overlap (f_{jklm}), where j, k, l, and m denote the mode orders for the two pump photons, the signal, and the idler photons. The mode field overlap (f_{jklm}) can be described as:

$$f_{jklm} = \frac{\int_{A_0} e_j(r,\omega_j) e_k(r,\omega_k) e_l^*(r,\omega_l) e_m^*(r,\omega_m)\, dA}{\prod_{i=jqlm} \left[\int_{A_\infty} n_{wg}(r,\omega_i)^2 |e_i(r,\omega_i)|^2 dA\right]^{\frac{1}{2}}}. \tag{3.44}$$

This parameter is significantly influenced by the chosen waveguide width and the modes considered. For instance, if we configure the cross-section to favor the existence of excited modes, we observe $f = 1$ for the intramodal process and $f = 0.639$ for the intermodal process. This results in lower efficiency in the process that exploits different modes compared to the process that exploits equal modes. Consequently, this aspect allows us to make a well-informed choice between the two types of processes based on the specific application requirements and desired characteristics.

JSI and purity

The comparison between intramodal and intermodal sources also involves a crucial aspect of the purity of the generated photons. The intramodal process, especially in the context of the ring resonator, attains purity values of up to 0.93 without requiring additional filtering. In contrast, the intramodal waveguide source necessitates appropriate filtering to enhance purity. Fig. 3.17 illustrates the JSI for both intramodal (a)

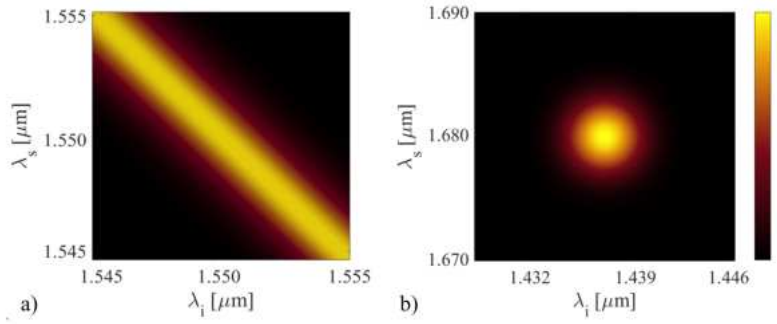

Figure 3.17: JSI in the intramodal case (a) and in the intermodal case (b) for a waveguide long 2 cm.

and intermodal (b) cases in a spiral waveguide with a length of 2 cm. Remarkably, in the intramodal scenario, a strong correlation is observed between the generated photons, resulting in a purity of 0.2 without filters. On the other hand, in the intermodal case, a remarkable purity of 0.99 is achieved even without the use of additional filters. This highlights the advantages of using the intermodal process to enhance efficiency and purity in the specific configuration under consideration. Clearly, the use of filters can increase the purity for the intramodal case, although reducing the brightness of the source.

3.4 Conclusions

In this chapter, we conducted a comparison of different integrated sources of correlated photons. By presenting these comparative analyses, readers can make informed choices

based on their specific application requirements and the type of instrumentation for their experiments. It is worth noting that the results obtained refer to a specific spectral region with silicon sources. Appropriate studies for different regions, materials, and configurations are necessary according to application requirements. Subsequent chapters will delve into practical applications that involve both intramodal and intermodal processes, further illustrating their respective strengths in diverse scenarios.

Chapter 4

2 µm sensing

4.1 Mid-infrared sensing

This chapter explores the use of the intermodal sFWM source to produce entangled photon pairs at long wavelengths that reach the mid-infrared. The source is used as a proof of concept for measuring Ghost spectroscopy. The data shown here are taken from papers [130–132].

4.1.1 Mid-infrared gas sensing through biphoton state source

Mid-infrared (MIR) light (2–15 µm) has diverse technological applications, including free space telecommunication [133], LIDAR [134], environmental monitoring [135], medicine [136], and biology [137]. MIR's strong absorption bands in molecules are particularly useful for gas sensing [138], which greatly increases absorption spectroscopy sensitivity [139]. Despite the growing interest in MIR applications, progress is hampered by immature optical MIR devices [140]. These limitations can be addressed by quantum optics, where sub-Poissonian light and entangled photons allow for novel applications like ghost imaging [141], ghost spectroscopy [132], undetected photon measurements [142, 143], surpassing shot-noise limit.

A source of single or entangled photons beyond 2 µm is crucial to obtain quantum-enhanced MIR metrology. Traditional techniques rely on bulky and expensive instrumentation based on free-space nonlinear crystals [144, 145]. However, miniaturization and cost-effectiveness are imperative to develop feasible, robust, and affordable quantum technologies. Silicon photonics integrated circuits, offer a solution with mature CMOS fabrication technology, providing robust, stable, low power consumption, and efficient light manipulation at the chip scale [75]. On-chip MIR quantum measurements can pave the way for efficient and cost-effective sensors, advancing MIR and quantum technologies.

In my study, I investigated the generation of a biphoton state using an intermodal sFWM source within silicon waveguides. This innovative approach resulted in the creation of a state where one photon is situated in the near-infrared (NIR) range while the other resides in the MIR range, facilitated by a standard C-band laser pump [130]. By leveraging this approach, both pump- and sensing-specific MIR technologies are eliminated. Thus, this novel source was used to demonstrate Ghost spectroscopy measurement of CO_2 in the MIR spectrum.
The chapter is divided into two sections. Section 4.2 describes the characterization of the intermodal source for photon generation in the mid-infrared (MIR). Section 4.4 explores its application in Ghost spectroscopy measurements.

4.2 Intermodal sFWM and generation of single photons at 2 µm

This section builds upon my work [130]. The results presented were obtained through collaboration with Dr. Stefano Signorini.

4.2.1 Chip design and experimental set-up

We use TE modes, namely the fundamental (TE0) and first excited (TE1) modes, in the intermodal process of the 1221-TE combination as described in Chapter 3.3. These modes are generated within a rib SOI waveguide. For this initial experiment, the samples were fabricated by the Centre for Sensors and Devices of the Bruno Kessler Foundation (FBK) in Trento, Italy. The multi-mode waveguide used for generation has a width of 1.95 µm and a height of 0.190 µm on a 0.3 µm thick slab, with a total length of 1.5 cm. The waveguide and slab materials are silicon, while the top and bottom coatings are silica. Simulated intensity profiles of the TE0 and TE1 modes are presented

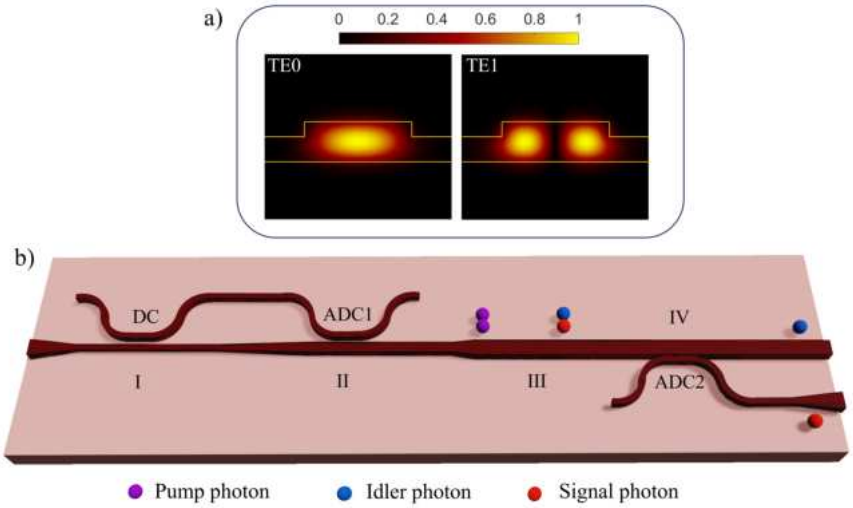

Figure 4.1: a) Simulated intensity profiles of the TE0 and TE1 spatial modes in the multimode waveguide. b) Schematic diagram of the PIC comprising DC to split the pump photons into two paths, ADC for converting between TE0 and TE1 modes, and a multimode waveguide to generate correlated photons. The violet balls indicate the input photons, the red balls are the signal photons, and the blue balls are the idler photons.

in Fig. 4.1(a). Fig. 4.1(b) shows the design, illustrating how the PIC is segmented into sections, each of which includes all the integrated structures employed in the setup[1]. In step I, the input pump is split into two waveguides using a 50-50 DC. In step II, the lower waveguide was gradually expanded to accommodate the presence of the first excited mode, TE1. An asymmetric directional coupler (ADC1) couples, with an efficiency of 92%, the higher-order mode TE1 into this waveguide where half of the pump is already propagating on the fundamental order mode TE0. Subsequently, the multimode waveguide (MMWG) is tapered to the width w_{FWM} required for the PM of the intermodal 1221-TE sFWM (III).

[1] Dr. Stefano Signorini realized the design of the PIC.

By using this configuration, it is possible to generate a signal photon wavelength of approximately 2 µm and an idler photon wavelength of approximately 1.3 µm, using input photons of 1.55 µm. An advantageous feature of intermodal sFWM is the ability to generate the signal and idler photons on separate modes of the waveguide. Since the signal is generated on a higher-order mode, it is extracted using another ADC2 (IV) and converted to the TE0 mode on another waveguide. This device enables the entangled photons to be split over two different waveguide paths in the fundamental TE0 mode.

The design of the DC and ADC mirrors what was illustrated in Section 2.2.3. The lengths were selected so that the DC device functions as a beam splitter, while the ADC device acts as a modal converter. Each ADC is designed to optimize the coupling for the intended wavelength. However, ADCs are broadband devices, allowing them to tolerate deviations from the expected wavelength.
The input and output ports are tapered to a width of 3.7 µm to optimize coupling with the tapered lens fibers used for injection and light extraction. The three fibers used are each mounted on a piezo-controlled translator stage. The experimental setup is

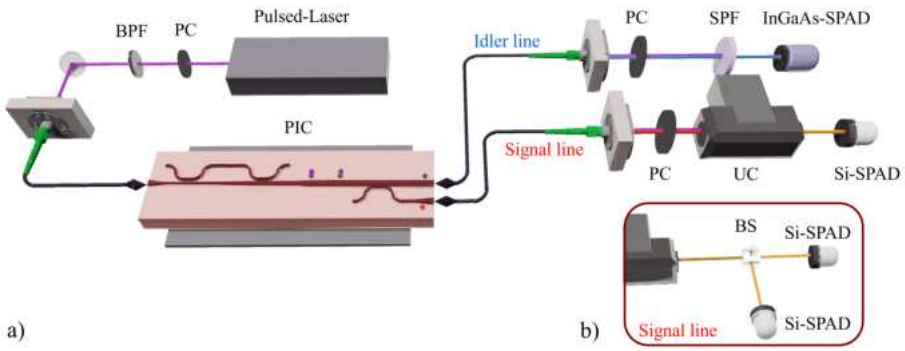

Figure 4.2: a) The experimental setup depicts the detection components, showcasing the idler photon path at the top and the signal photon path at the bottom. From left to right, a pulsed laser operating at a fixed wavelength of 1550 nm undergoes polarization manipulation via PCs and is coupled to the PIC using a tapered fiber. At the output of the PIC, two tapered fibers collect idler and signal photons and guide them along separate paths. In the signal branch, waveplates are employed for polarization selection, followed by the UC unit converting the signal from MIR to VIS wavelengths, and finally, the Si-SPAD for detection. In the idler branch, there is an SPF and an InGaAs-SPAD. b) Schematic representation of the HBT interferometer utilized for measuring the statistics of photons generated in the signal line subsequent to the UC system.

depicted in Fig. 4.2(a). For the pump, we utilized a pulsed laser at 1550.3 nm with a 40 ps pulse width and an 80 MHz repetition rate. After passing through a BPF and a polarization controller (PC), the pump is coupled to the chip via a tapered lensed fiber. The coupling losses from the fiber to the chip are (6.0 $\pm$ 0.5) dB/facet, and the propagation losses are 3 dB/cm in the single-mode waveguide (with a width of 600 nm) at 1.55 µm resulting in a PIC total losses of 15 dB.

The chip allows easy separation of the idler and signal, both of which are subsequently coupled out of the chip using two conical lens fibers. To eliminate pump residue and Raman noise from the idler beam, a short-pass filter (SPF) with a cut-off wavelength of 1335 nm is employed. The idler, shown in Fig. 4.2(a), is then detected by an InGaAs Single-Photon Avalanche Diode (SPAD-ID Quantique IDQ210), triggered

by the pump with a gate width of 1.90 ns. Fig. 4.3 shows a picture (a) and the characterization (b) of the SPF used. The expected extinction ratio surpasses 100 dB, which is not discernible in the measurement results due to the background noise of the detector. From the point of view of losses, the cumulative losses along the idler line, extending

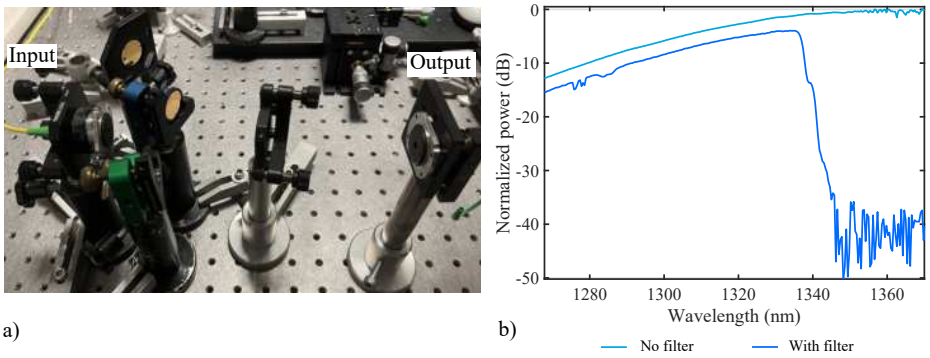

Figure 4.3: a) Photo of the SPF comprising four filters and undergoing seven passes through these filters. b) The experimental characterization of the short-pass filter placed on the idler channel is shown, with the reference signal represented in light blue and the filter transmission in blue. The transmission spectrum shows a cutoff wavelength at 1335 nm. Notably, the measurement visibility, which falls below -40 dB, is limited by the detector noise, which indicates the sensitivity and accuracy of the measurement configuration.

from the collimator to the InGaAs SPAD, amount to 7 dB. This figure includes the contribution of the detector's detection efficiency, which is 28% (-5.5 dB). Consequently, the detected idler counts exhibit an approximately 18.5 dB deviation from the photon pairs generated on-chip.

On the signal side (the Signal line in Fig. 4.2(a)), after leaving the chip, the signal undergoes polarization rotation through a free-space half-wave plate ($\lambda/2$) and is further converted into the visible spectrum through an up-conversion (UC) system [146]. This UC system includes a long-pass filter with a cut-on wavelength of 1900 nm, effectively rejecting the C-band pump. However, it is important to note that the UC system introduces collinear noise photons to the upconverted signal, centered on the same wavelength. To address this, a BPF selectively filters out some of this noise while preserving the upconverted signal.

In instances where the HBT measurement is not required, such as in the measurement of the CAR, the up-converted light is directly detected by a Silicon SPAD (Excelitas SPCM-AQRH-12) with a 100 Hz dark count rate (Fig. 4.2(a)). Conversely, when an HBT measurement is needed, the light is split through a free-space beam splitter (BS) and directed to two visible Si-SPADs, monitoring the BS reflection and transmission ports (Fig. 4.2(b)). The Si-SPADs operate in free-running mode, and a time tagging unit (Swabian Time Tagger 20) is used to monitor individual singles and coincidences among the three detectors.

The total signal losses are 26.6 dB between the on-chip photons and the detected counts. The higher losses in the signal optical line stem from the low efficiency of the UC module and the use of optical elements not optimized for wavelengths beyond 2 µm.

Up-conversion module

To enable signal counting, a detection system capable of measuring photons with wavelengths longer than 2 µm and exhibiting sensitivity down to the single-photon level was employed. SNSPDs, known for their efficiency in the NIR [147], exhibit reduced performance in the MIR with an efficiency of about 30-50% at a 2 µm wavelength [148, 149]. A significant drawback of these detectors is their need for cryogenic temperatures, which adds complexity to the experimental setup. An alternative approach using sum-frequency generation (SFG) allows for single-photon detection at room temperature and tunability across the entire MIR spectrum, although it suffers from low efficiencies [150].

The fundamental principle involves utilizing the SFG[2] process in a periodically poled lithium niobate (PPLN) crystal to up-convert the 2 µm signal photon into a visible photon. The latter is then detectable by high-efficiency Si-SPADs. The PPLN is quasi-phase-matched with respect to the target wavelength. The SFG process follows the energy and momentum conservation relations:

$$\frac{1}{\lambda_s} + \frac{1}{\lambda_{SFG_p}} = \frac{1}{\lambda_{up}}, \tag{4.1a}$$

$$2\pi \frac{n(\lambda_{SFG_p}, T)}{\lambda_{SFG_p}} = 2\pi \left[\frac{n(\lambda_s, T)}{\lambda_s} + \frac{n(\lambda_{up}, T)}{\lambda_{up}} + \frac{1}{\Lambda} \right], \tag{4.1b}$$

where λ_s, λ_{SFG_p}, and λ_{up} represent the signal wavelength at 2 µm, the pump for the SFG process, and the converted wavelength, respectively. T denotes the temperature of the non-linear medium, and Λ represents the poling period. To enhance system efficiency, the used system involves incorporating a PPLN inside a free-space Fabry-Perot cavity, taking advantage of the high circulating power induced by the cavity. For interested readers, I refer to [146]. Here, I report the key points relevant to my application.

The employed up-converter integrates PPLN crystals fabricated for 2 µm with $\Lambda = 15.8$ mm. Coupled with the UC cavity is the pump source, featuring a broad-area diode laser (BAL) pumping an Nd:YVO4 crystal at 880 nm, generating light circulating in the cavity at $\lambda = 1.064$ µm. The cavity construction involves a germanium long-pass filter to confine the pump wavelength within while allowing MIR and up-converted photons to enter and exit.

The PPLN, 2 cm in length, incorporates waveguides of 1 µm in height with varied widths depending on the wavelength for PM. For the experiment, a polarized waveguide of 1 µm width was chosen at a temperature of 102.2°C to phase-match the signal photon at 2.013 µm. A PPLN from HC Photonics, 25 mm in length, was used and tuned in temperature to convert the MIR signal at 2015 nm into visible light at 696 nm. The UC transfer function, displayed in Fig. 4.4(a), exhibits an FWHM of 1.15 ± 0.12 nm. The simulated PM curve as a function of temperature is depicted in Fig. 4.4(b). An essential consideration pertains to the UC functioning as a filtering system for the pump in addition to signal conversion. The overall detection efficiency of the up-converter coupled to the SPAD is approximately 1%.

[2]The SFG is introduced in Chapter 2.

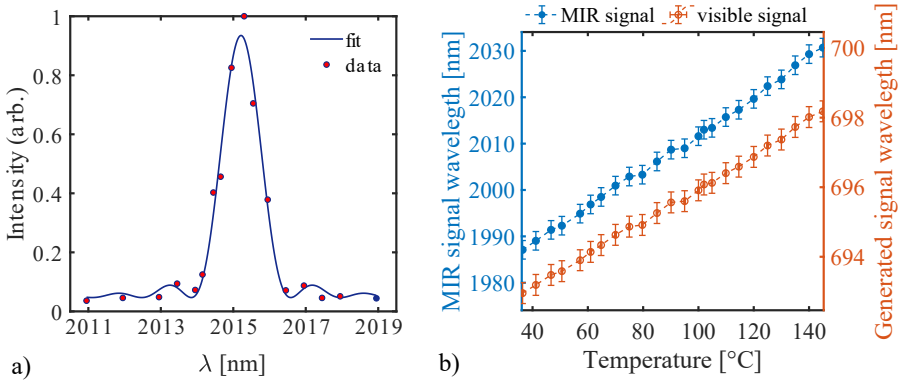

Figure 4.4: a) Spectral response of the upconverter module. The response has been fitted by a squared sinc function, as expected for a sum-frequency generation process. The FWHM is measured to be (1.15 ± 0.12) nm. b) MIR (blue dots) and visible (orange dots) signal peak as a function of the temperature of the UC system.

4.3 2µm heralded single photons generation

4.3.1 Data analysis

To characterize our integrated source, it is useful to start with the formulas presented in eqs. (1.129) and (1.126) and adapt them to our specific context. As detailed in Chapter 2, beyond the sFWM, various linear and nonlinear phenomena manifest in the silicon waveguide. To accurately capture the genuine generation and transmission efficiency of correlated photon pairs, it is important to model TPA, two-photon cross absorption (XTPA), and FCA.

TPA primarily affects pump photons, while XTPA introduces losses for both idler and signal photons, occurring between a pump photon and a signal/idler photon. Notably, XTPA has a more pronounced impact on the idler photon than the signal photon, attributed to the lower energy of the signal photon, resulting in a diminished probability of the process. The collective influence of TPA, XTPA, and FCA contributes to increased losses in the silicon waveguide for both pump and generated photons. Consequently, the probability of detection no longer exhibits a quadratic dependence on the input pump power. Additionally, there is a non-linearity in the response of the idler detector η_{ND} that needs consideration, and these aspects have been modeled in Appendix B. According to this modeling, we can rewrite the detection probabilities per pulse as:

$$p_{si} \simeq \xi \bar{P}_p^2 \bar{\eta}_i \bar{\eta}_s \eta_{ND}\,, \tag{4.2a}$$

$$p_i \simeq (\xi \bar{P}_p^2 \bar{\eta}_i + d_i)\eta_{ND}\,, \tag{4.2b}$$

$$p_s \simeq \xi \bar{P}_p^2 \bar{\eta}_s + d_s\,, \tag{4.2c}$$

with

$$\bar{P}_p = \sqrt{\frac{1}{L}\int_0^L P_p^2(z)dz}\,, \tag{4.3a}$$

$$\bar{\eta}_j = \bar{\eta}_j^{on}\eta_j^{off}\,, \tag{4.3b}$$

$$\bar{n}_j^{on} = \frac{1}{L}\int_0^L \eta_j^{on}(z)dz\,. \tag{4.3c}$$

Here ξ[3] is the pair generation probability without the power coefficient, $j = i, s$, L represents the waveguide length, $P_p(z)$ represents the on-chip pump power along the waveguide, η_j^{on}(z) stands for the transmission efficiency for a photon generated at z along the waveguide, including only linear and non-linear losses on the chip. Correspondingly, η_j^{off} denotes the transmission efficiency, considering exclusively the losses occurring off-chip (fiber-chip coupling and filtering). Given the employed filtering, which has been described, we omit the consideration of noise photons stemming from pump residual and Raman scattering in eqs. (4.2). These noise components, typically linearly correlated with pump power, are negligible in our experimental setup.

4.3.2 Parameters description and measurements

Generation spectra measurements

A crucial aspect of the characterization involves validating the intermodal generation of idler and signal photons. The idler spectrum is analyzed using a custom-designed monochromator with 2.5 nm resolution, illustrated in Fig. 4.5(a). Integrated with an InGaAs SPAD, this monochromator allows a wide dynamic range of 10^5, covering intensities from 1 fW to 0.1 nW. The measured intensity spectrum of the idler beam re-

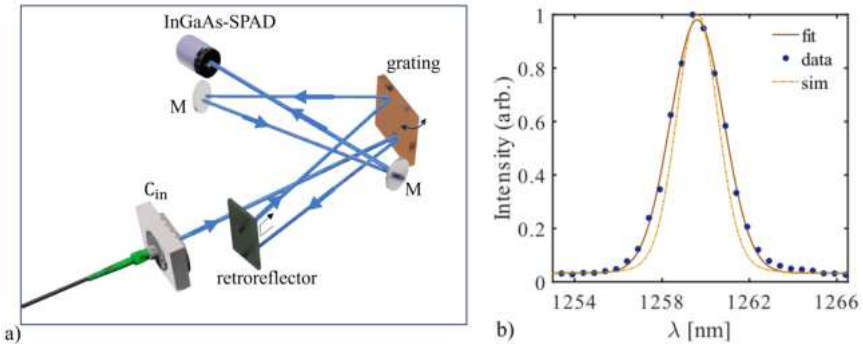

Figure 4.5: a) Schematic of the monochromator utilized in our experiment. The light is introduced into the system via a collimator (C_{in}). It first hits a grating situated on a motorized rotating stage. Subsequently, a retroreflector is employed to send the beam back with a vertical offset, allowing for another pass over the grating. Finally, after being reflected by two mirrors (M), the light is extracted using another collimator and detected via the InGaAs-SPAD. The entire system is managed by software that synchronizes the photon counter and grating rotation, enabling automated spectrum measurements. b) Measured intensity spectrum of the idler beam. A Gaussian function was employed for fitting, revealing a FWHM of 2.87 ± 0.07 nm. This measurement is influenced by the transfer function of the monochromator utilized for the assessment, leading to an apparent enlargement of the generated bandwidth. We simulated the idler spectrum, accounting for the widening induced by the monochromator (illustrated by the orange dashed line). To determine the actual bandwidth of the idler (2.0 ± 0.3 nm), we performed deconvolution using the response function of the monochromator.

veals a distinct band centered at 1259.7 ± 0.5 nm. Fitting this spectrum with a Gaussian function yields an FWHM of 2.87 ± 0.07 nm. It's crucial to acknowledge that this measurement is influenced by the transfer function of the monochromator, contributing

[3] ξ is described in Chapter 1.

to the effective broadening of the generated signal's bandwidth. The simulated idler spectrum, incorporating the broadening effects of the monochromator, is depicted by the yellow dashed line. Deconvolution with the monochromator's response function yields an idler bandwidth of (2.0 ± 0.3) nm. Notably, the measured FWHM of the idler aligns with the simulated value of 1.81 nm, as shown in Fig. 4.5(b).

Due to the conservation principles outlined in eqs. (1.122) and (1.123), the signal is generated at 2015.2 ± 1.5 nm. We estimate a FWHM of 5.1 ± 0.8 nm for the signal. Hence, the UC effectively filters signal photons according to the efficiency spectrum depicted in Fig. 4.4(a). The response is fitted with a squared sinc function, consistent with expectations for a sum-of-frequencies generation process, and the FWHM of the spectral response is determined to be 1.15 ± 0.12 nm.

Joint spectral Intensity Simulation

In our study, the shape of the JSI characterizing the generated biphoton state is influenced by various factors, including the PM function, the spectral response of the upconverter, and the pump spectrum. Notably, the pump spectrum dictates the JSI's shape along the diagonal axis. Leveraging the measured pump spectrum (illustrated in Fig. 4.6(a)) alongside simulated PM functions and the upconverter's measured spectral response (as depicted in Fig. 4.4(a)), we conducted JSI simulations following the methodology outlined by Signorini et al. [115], as presented in Fig. 4.6(b). The asym-

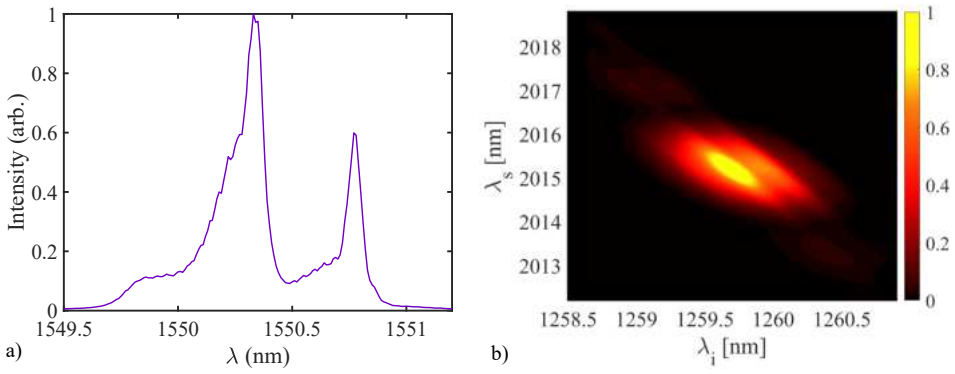

Figure 4.6: a) Measured pump spectrum. b) Simulated JSI computed using the measured pump spectrum, the measured upconverter spectral response, and the simulated PM function. Asymmetry in the JSI is attributed to the pump spectrum.

metrical nature of the JSI, particularly evident along the diagonal axis, primarily stems from the asymmetry in the pump spectrum. The most effective strategy to rectify this and achieve a symmetrical JSI involves shaping the pump to attain a symmetrical spectral profile. For instance, applying a narrow-band filter to the pump can effectively restore a symmetrical JSI. Alternatively, symmetrical JSI can also be attained by applying filters to the signal and idler; however, this comes at the expense of reduced efficiency and lower rates.

Generation probability and heralding efficiency

To quantify the coincidences between signal and idler photons, we implemented a start-and-stop detection system as detailed in Section 1.4, utilizing the idler photon as the initiating trigger and the signal photon as the stopping detection. The assessment of coincidences takes place within a specified coincidence window Δt_c. The detection

rates in the idler channel, encompassing both signal and dark counts, are dictated by the detection gate width of the idler detector (1.90 ns). Conversely, the rates in the signal channel depend on the coincidence window chosen during post-processing. With Rdc_i = 620 cps and Rdc_s = 2150 cps, the dark count rates at the idler and signal detectors are

$$di = \frac{R_{dc,i}}{R_p} = 7.75 \times 10^{-6} \tag{4.4a}$$

$$ds = 1 - e^{-R_{dc,s}\Delta t_c} \tag{4.4b}$$

considering a Poisson distribution for the signal noise (Si-SPAD dark counts and UC noise).

Let us delve into the determination of the generation probability ξ and heralding efficiency η_I. To refine the measured rates and establish the generation probability ξ, we can adapt eqs. (4.2) as follows:

$$y_i = \frac{\bar{p}_i - \eta_{\mathrm{ND}} d_i}{\bar{\eta}_i^{\mathrm{on}} \eta_{\mathrm{ND}}} = \xi \bar{P}_p^2 \eta_i^{\mathrm{off}} = a_i \bar{P}_p^2 , \tag{4.5a}$$

$$y_s = \frac{\bar{p}_s - d_s}{\bar{\eta}_s^{\mathrm{on}}} = \xi \bar{P}_p^2 \eta_s^{\mathrm{off}} = a_s \bar{P}_p^2 , \tag{4.5b}$$

$$y_{si} = \frac{\bar{p}_{si}}{\bar{\eta}_i^{\mathrm{on}} \eta_{\mathrm{ND}} \bar{\eta}_s^{\mathrm{on}}} = \xi \bar{P}_p^2 \eta_i^{\mathrm{off}} \eta_s^{\mathrm{off}} = a_{si} \bar{P}_p^2 , \tag{4.5c}$$

where $a_i = \xi \eta_i^{\mathrm{off}}$, $a_s = \xi \eta_s^{\mathrm{off}}$, and $a_{si} = \xi \eta_i^{\mathrm{off}} \eta_s^{\mathrm{off}}$. The quantities y_i, y_s, and y_{si} can be computed from the measured singles, coincidence, and noise rates, as well as from the simulation of $\bar{\eta}_j^{\mathrm{on}}$ and the measurement of η_{ND}. We estimate the parameters by fitting

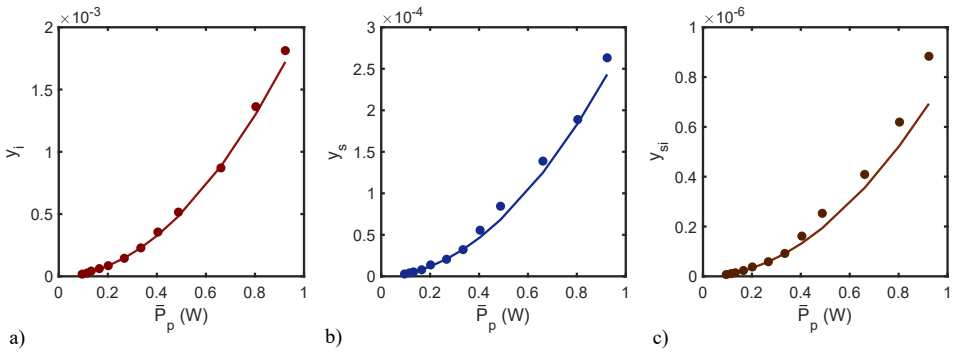

Figure 4.7: Fitting functions (solid lines) applied to the experimental data (dots) for (a) y_i, (b) y_s, and (c) y_{si}.

y_i, y_s, and y_{si} for an input power < 0.5 W ($\bar{P}_p < 0.4$ W), where nonlinear losses are not dominant. We utilize $f(x) = ax^2 + b$ as a fitting function, recovering a_i, a_s, and a_{si}. Fig. 4.7 reports the fits performed on the data, while table 4.1 reports the different parameters extracted by the fits. This enables us to evaluate ξ (in units of W^{-2} of peak power) and off-chip transmissions, resulting in:

$$\xi = \frac{a_i a_s}{a_{si}} = (0.70 \pm 0.10) W^{-2}, \tag{4.6a}$$

$$\eta_{\mathrm{off},i} = \frac{a_{si}}{a_s} = (2.71 \pm 0.17) \times 10^{-3}, \tag{4.6b}$$

Parameter	Value	68% Confidence Bounds
a_i	$1.91 \times 10^{-3}\,\mathrm{W}^{-2}$	$(1.86 \times 10^{-3}, 1.95 \times 10^{-3})\,\mathrm{W}^{-2}$
a_s	$2.81 \times 10^{-4}\,\mathrm{W}^{-2}$	$(2.72 \times 10^{-4}, 2.91 \times 10^{-4})\,\mathrm{W}^{-2}$
a_{si}	$7.63 \times 10^{-7}\,\mathrm{W}^{-2}$	$(7.41 \times 10^{-7}, 7.85 \times 10^{-7})\,\mathrm{W}^{-2}$
b_i	3.92×10^{-6}	$(1.49 \times 10^{-6}, 6.34 \times 10^{-6})$
b_s	5.55×10^{-7}	$(0.47 \times 10^{-7}, 10.64 \times 10^{-7})$
b_{si}	1.44×10^{-9}	$(0.23 \times 10^{-9}, 2.65 \times 10^{-9})$

Table 4.1: Fitting Parameters of y_i,y_s and y_{si}. We use $f(x) = ax^2 + b$.

$$\eta_{\mathrm{off},s} = \frac{a_{si}}{a_i} = (4.00 \pm 0.21) \times 10^{-4}, \tag{4.6c}$$

with $\Delta t_c = 1.1$ ns (3σ bin width). The uncertainties are estimated at 1 standard deviation of the fitting coefficients.

Table 4.2 shows the information regarding the nonlinear parameters and propagation losses utilized in the model. Other calculations correlated to these parameters are reported in appendix B.

Parameter	Value	Reference
$\alpha_{p,TE0}$	$0.104\,\mathrm{cm}^{-1}$ ($0.45\,\mathrm{dB\,cm}^{-1}$)	Experimental
$\alpha_{p,TE1}$	$0.414\,\mathrm{cm}^{-1}$ ($1.80\,\mathrm{dB\,cm}^{-1}$)	Simulated
α_i	$0.067\,\mathrm{cm}^{-1}$ ($0.29\,\mathrm{dB\,cm}^{-1}$)	Simulated
α_s	$0.758\,\mathrm{cm}^{-1}$ ($3.29\,\mathrm{dB\,cm}^{-1}$)	Simulated
σ_p	$1.45 \times 10^{-21}\,\mathrm{m}^2$	[151]
σ_i	$0.96 \times 10^{-21}\,\mathrm{m}^2$	[151]
σ_s	$2.45 \times 10^{-21}\,\mathrm{m}^2$	[151]
$\beta_{TPA}(\omega_p)$	$7.5 \times 10^{-12}\,\mathrm{m\,W}^{-1}$	[57]
$\beta_{TPA}(\overline{\omega}_{i,p})$	$17.5 \times 10^{-12}\,\mathrm{m\,W}^{-1}$	[57]
$\beta_{TPA}(\overline{\omega}_{s,p})$	$7 \times 10^{-12}\,\mathrm{m\,W}^{-1}$	[57]
τ_c	50 ps	from fit
$n_{g,TE0}$	3.7369	Simulated
$n_{g,TE1}$	3.7911	Simulated
$n_{g,i}$	3.8177	Simulated
$n_{g,s}$	3.7714	Simulated
$n_{Si}(\omega_p)$	3.4757	[152]
$n_{Si}(\overline{\omega}_{i,p})$	3.4907	[152]
$n_{Si}(\overline{\omega}_{s,p})$	3.4624	[152]
$\mathcal{A}_0$	$1.95 \times 0.49\,\mathrm{mm}^2$	Experimental
$\gamma_{TPA,TE0}$	$7.00\,\mathrm{m}^{-1}\,\mathrm{W}^{-1}$	Calculated from eq. (B.2a)
$\gamma_{TPA,TE1}$	$6.81\,\mathrm{m}^{-1}\,\mathrm{W}^{-1}$	Calculated from eq. (B.2a)
$\gamma^i_{X,TPA,TE0}$	$5.38\,\mathrm{m}^{-1}\,\mathrm{W}^{-1}$	Calculated from eq. (B.2b)
$\gamma^i_{X,TPA,TE1}$	$3.44\,\mathrm{m}^{-1}\,\mathrm{W}^{-1}$	Calculated from eq. (B.2b)
$\gamma^s_{X,TPA,TE0}$	$0.97\,\mathrm{m}^{-1}\,\mathrm{W}^{-1}$	Calculated from eq. (B.2b)
$\gamma^s_{X,TPA,TE1}$	$1.50\,\mathrm{m}^{-1}\,\mathrm{W}^{-1}$	Calculated from eq. (B.2b)

Table 4.2: Parameters used for TPA, XTPA, and FCA simulation.

With these outcomes, we compute the intrinsic heralding efficiency η_I:

$$\eta_I = \frac{R_{\text{net,si}}}{(R_i - R_{\text{dc,i}})\eta_{\text{off,s}}} = 59 \pm 5\% \,, \tag{4.7}$$

where $R_{\text{net,si}}$ represents the measured net coincidence rate, R_i is the measured idler rate, and $R_{\text{dc,i}}$ is the measured dark count rate. By normalizing for the signal channel losses, η_I enables comparison between different sources based solely on their intrinsic properties, eliminating the influence of specific detectors and off-chip transmission losses of the heralded photon, such as coupling losses. The high value is attributed to low on-chip signal losses and the absence of filtering losses for selecting the signal wavelength. η_I is primarily constrained by signal propagation losses, approximately 3 dB/cm.

To consider the role of the detection system and off-chip losses, we calculate the Klyshko efficiency η_K:

$$\eta_K = \frac{R_{\text{net,si}}}{(R_i - R_{\text{dc,i}})} = \eta_I \eta_{\text{off,s}} = (0.024 \pm 0.002)\% \,. \tag{4.8}$$

This low η_K is mainly attributed to the upconversion system with a low detection efficiency (approximately -20 dB) and a narrow upconversion bandwidth compared to the signal one (approximately -6.5 dB). Additionally, the fiber-chip coupling losses significantly contribute, with (-6.0 $\pm$ 0.5) dB per facet.

Coincidence to accidental ratio

CAR is used to evaluate coincidence detection efficiency. Further details on this metric are provided in Section 1.4.1.

CAR measurements are conducted using start-stop coincidence detection, wherein coincidences between the InGaAsSPAD and Si-SPAD signals are examined. The experimental setup depicted in Fig. 4.2(a) is employed, featuring a single Si-SPAD at the UC output. As depicted in Fig. 4.8(a), coincidences occur with a time delay ($\delta t = 0$ ns), while other peaks, spaced according to the laser repetition period, denote accidental coincidences. The zero-delay peak also contains also accidental coincidences. Accidental counts are determined as the average of all accidental peaks. CAR is computed using the formula (1.130). The choice of Δt_c affects the coincidence-to-accidental ratio within individual bins, consequently influencing CAR. In Fig. 4.8(b), we present measured CAR values alongside corresponding net coincidences, plotted against the peak power of the chip's pump. Notably, the peak power indicated in the graph refers to the power at the multimode waveguide input, adjusted for fiber-chip coupling losses. Results are provided for coincidence windows of 1.1 ns. CAR peaks at 40.4 $\pm$ 0.9 at 115 mW, with a net coincidence rate of (0.316 $\pm$ 0.003) cps at this power. Simulated net coincidences and CAR values, based on parameters derived from previous sections, are shown as the blue and red lines in Fig. 4.8(b) and computed as expressed in eqs (1.125) and (1.126) considering this specific case:

$$CAR = \frac{\bar{p}_{si}}{\bar{p}_i \bar{p}_s} = \frac{\xi \bar{P}_p^2 \bar{\eta}_s \bar{\eta}_i}{(\xi \bar{P}_p^2 \bar{\eta}_s + d_s)(\xi \bar{P}_p^2 \bar{\eta}_i + d_i)} \,, \tag{4.9a}$$

$$N_{si}^{\text{net}} = \xi \bar{P}_p^2 \bar{\eta}_s \bar{\eta}_i \eta_{ND} R_p \,. \tag{4.9b}$$

Simulated and experimental CAR values consistently align across the entire range of pump power used, confirming accurate modeling of the generation process. At lower

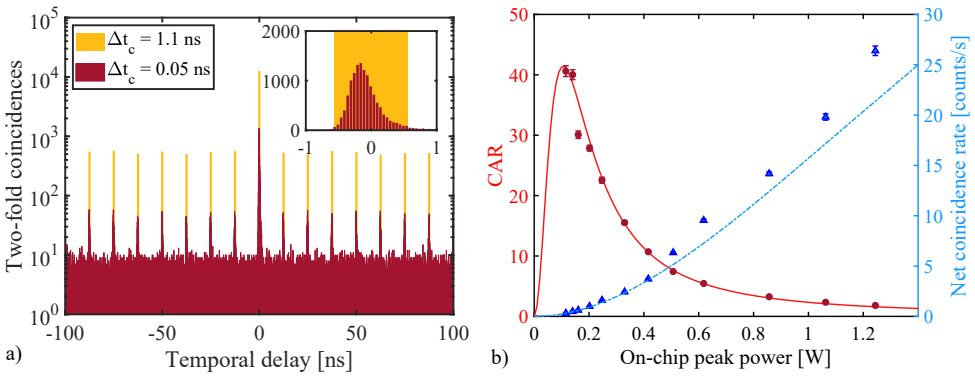

Figure 4.8: a) Twofold coincidences as a function of the delay δt between idler (start) and signal (stop) detections. Coincidence events within a 0.05 ns coincidence window are denoted in dark red, while those processed with a larger window of 1.1 ns are shown in orange to account for a broader range of coincidence events. The primary coincidence peak occurs at δt = 0 ns, with clear indications of the laser repetition period from the accidental peaks. Inset: A magnified view of the zero-delay bin compares the coincidence peak shape with the post-processing coincidence window. b) The measured CAR (dark red dots) and net coincidence rates (blue triangles) for Δt_c = 1.1 ns against the on-chip peak pump power. Experimental data is compared with simulated values for both CAR (solid red line) and net coincidence rates (dashed light blue line).

power levels, net coincidence rates show agreement, albeit a tendency to overestimate nonlinear losses is observed at higher powers. Achieving perfect agreement necessitates a precise understanding of all nonlinear parameters associated with the material. The larger CAR measured in this study, compared to other works [149], indicates the competitiveness of the overall system.

Heralded and Unheralded $g^{(2)}$

To confirm the antibunching behavior and, therefore, the single-photon nature of the emitted photons, we conducted measurements of the heralded second-order coherence function, denoted as $g_H^{(2)}$. This parameter is described in detail in sections 1.2.2 and 1.4.2. Using the setup depicted in Fig. 4.2(b), we adjusted delays to ensure that the signal detection by a Si-SPAD coincided with the detection of the idler by the InGaAs-SPAD. The coincidence between these detectors, within a window of $\Delta t_c = 2$ ns, served as the initial trigger, while the detection from the remaining Si-SPAD, referred to as the "delayed signal", acted as the stop trigger. We then monitored the three coincidences as a function of the delay δt between the start and stop events. Simultaneously, we measured the double coincidences between the idler and delayed signals, employing a 2 ns window to monitor the triple coincidences. The function $g_H^{(2)}$, expressed in eq. (1.134), takes the following form:

$$g_H^{(2)}(\delta t) = \frac{N_{12i}(\delta t)}{N_{1i}(0)N_{2i}(\delta t)} N_i \,, \tag{4.10}$$

where 1, 2, i denote the detector of the first signal, the detector of the second signal (the delayed signal), and the detector of the idler, respectively. N_{12i} corresponds to the triple coincidence counts, N_{1i} and N_{2i} are the double coincidence counts between the idler and signal detectors, and N_i corresponds to the idler counts.

If the emission truly occurs at the single-photon level, $g_H^{(2)}(0)$ should be less than 0.5 [115]. In our measurements, for an input on-chip peak power of 0.33 W, we obtained $g_H^{(2)}(0) = 0.23 \pm 0.08$, demonstrating the single-photon regime of the source and thus the sub-Poissonian statistics of the emitted photons. The corresponding $g_H^{(2)}(\delta t)$, calculated as in eq. (1.134), is presented in the inset of Fig. 4.9. Bins close to the zero delay bin, influenced by spurious coincidences from triggered silicon SPADs, were discarded. To simulate the trend of $g_H^{(2)}(0)$, we employed the formula expressed in eq. (1.134):

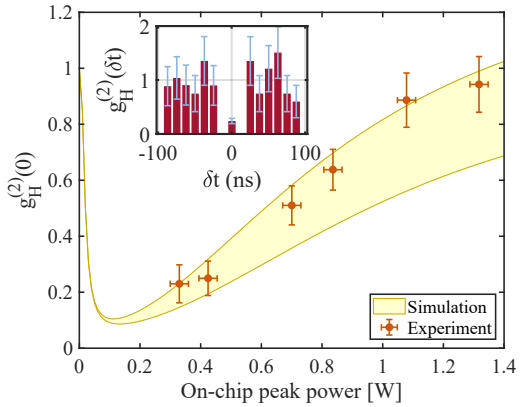

Figure 4.9: The plot displays a comparison between the measured data (orange points) and simulated results (light yellow area) as a function of the on-chip peak power. An inset provides a specific measurement at an on-chip peak power of 0.33 W. Bins adjacent to the zero-delayed one have been omitted due to SPAD-emitted photons.

$$g_H^{(2)}(0) = \frac{\bar{p}_{12i}\bar{p}_i}{\bar{p}_{1i}\bar{p}_{2i}}, \tag{4.11}$$

where $\bar{p}_{12i}$ is the probability per impulse of having a triple coincidence. To model the experimental results, we considered all possible coincidence events involving signal and/or noise detections. For this purpose, we utilized the previously calculated values of ξ, $\bar{P}_p$, $\bar{\eta}_i$, and $\bar{\eta}_s$ developed in the preceding section. We simulated a range for the expected value of $g_H^{(2)}(0)$, bounded at the top by the thermal case and at the bottom by the Poissonian case. Further details of this analysis are provided in Appendix C. The simulation results are presented in Fig. 4.9 as the yellow band. Remarkably, the measured value of $g_H^{(2)}$ is consistent with the simulated values.

Here, we did not perform an adaptation of the measured $g_H^{(2)}$, and the experiment and simulation are entirely independent. The experimental data points in Fig. 4.9 are closer to the upper bound than to the lower one, suggesting emission statistics are more similar to thermal emission. This observation aligns with the unheralded $g^{(2)}$ of the signal beams, as illustrated in Fig. 4.10(b). The unheralded $g^{(2)}$ is measured at 1.67 ± 0.02 at a power of 1.08 W, which is in line with the simulated value of 1.66 (dashed line) calculated from the JSI. These results indicate that the source exhibits emission characteristics closer to thermal emission, thus justifying the experimental value of $g_H^{(2)}$.

Furthermore, in Fig. 4.10(b), we illustrate the simulated values for a source whose statistics lie between the thermal (upper bound) and Poissonian (lower bound) cases.

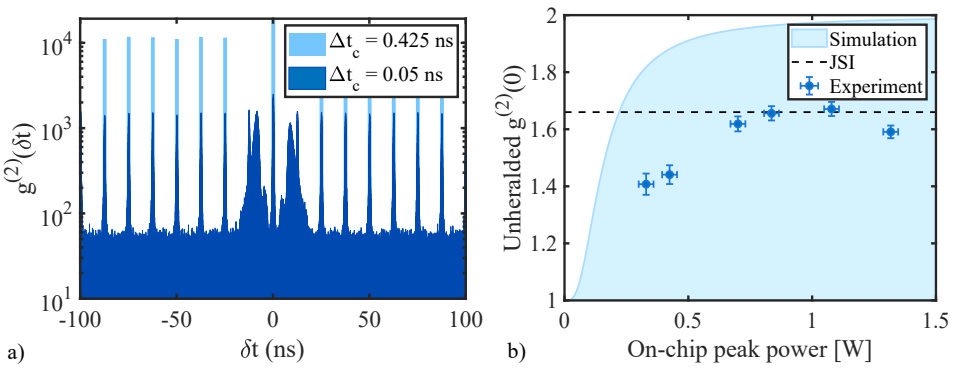

Figure 4.10: a) The experimental $g^{(2)}(\delta t)$ for an on-chip peak pump power of 1.08 W is illustrated, yielding $g^{(2)}(0) = 1.67(2)$. The histogram bins represent the counts at various delay intervals (δt) between start and stop clicks. The blue bars indicate the raw measurements with a coincidence window of 0.05 ns, while the light blue bars depict the measurements integrated with a larger coincidence window (0.425 ns). Broadband peaks surrounding the zero-delay peak are attributed to spurious counts originating from SPADs photon emissions. Hence, coincidence peaks neighboring the zero-delay peak, impacted by SPADs emissions, are disregarded. b) The plot depicts the measured unheralded $g^{(2)}(0)$ (blue dots) as a function of the on-chip peak power. The expected $g^{(2)}$ (dashed black line) is derived from the simulation, showing compatibility with the experiment. Measured points fall within the simulated values (light blue area), upper bounded by a source with thermal emission statistics and lower bounded by a source with Poissonian emission statistics ($g^{(2)} = 1$).

At low powers, dark counts dominate, resulting in a $g^{(2)}$ approaching 1 in both scenarios. However, at higher powers, the $g^{(2)}$ increases asymptotically to its actual value, thus explaining the power-dependent behavior observed in the experimental data. Further details concerning the simulation of $g^{(2)}$ are provided in Appendix C. In Fig. 4.10(a), we present the measured histogram obtained for an on-chip peak pump power of 1.08 W, revealing a $g^{(2)}$ value of 1.67 ± 0.02. In this measurement, we employed a Δt_c value of 0.425 ns to enhance the SNR. This adjustment was necessary due to the influence of spurious coincidences originating from emissions of the Si-SPADs. In Fig. 4.10(a), these coincidences stemming from photons emitted from Si-SPADs are clearly observable [153]. When a photon triggers a detection event on one of the silicon SPADs, the subsequent breakdown process within the detector results in the emission of additional photons. These emitted photons follow the reverse path of the original signal photon. Consequently, the emission from the SPAD is reflected by the UC window and then split by the beam splitter, ultimately causing a correlated detection event on the other detector. It's important to note that these spurious emissions do not elicit a detection event on the emitting SPAD if they arrive within the detector's dead time window.

4.3.3 Conclusions

In this section, I have presented a single heralded photon source operating beyond 2 µm, employing sFWM on a silicon chip. This study introduces a novel approach to MIR quantum photonics, providing a high-quality quantum light source beyond 2 µm without relying on MIR-specific technologies.

This source exhibits two notable features: discrete-band generation and significant detuning between signal and idler photons. Discrete-band generation eliminates

the need for stringent filtering to select signal and idler wavelengths, while the generated photons experience higher transmission compared to standard continuous-band sources, as demonstrated by the high experimental intrinsic efficiency ($\eta_I = 59 \pm 5\%$). Substantial detuning offers two advantages: simplification of the pump treatment and rejection of non-linear noise, and the capability to generate the herald photon in the NIR, taking advantage of efficient detection technology.

Moreover, this intermodal sFWM-based heralded single-photon source utilizes a common C-band pump laser, facilitating integration and operation on a silicon chip.

In the section 4.4, I demonstrate for the first time an application of the integrated source in performing "Ghost" spectroscopy of a specific gas in this spectral region [132]. To achieve this, improvements were made to the source concerning coupling and propagation losses by optimizing the match between signal and upconverter bandwidths.

4.4 2µm Ghost spectroscopy with sFWM source

In this section, we show the practical application of an entangled photon source produced through intermodal sFWM for gas spectroscopy purposes. This section reports my works [131, 132]. The design was implemented by Dr. Stefano Signorini, while the measurements were carried out with the assistance of Mr. Davide Rizzotti and Dr. Stefano Signorini.

4.4.1 Quantum Ghost spectroscopy

Ghost spectroscopy (GS), also known as correlated photon spectroscopy, is a technique that combines the strengths of NIR and MIR spectral domains. In GS, pairs of correlated photons are employed, with one photon probing the sample while the other is spectrally analyzed. This approach provides several advantages over traditional absorption spectroscopy. Firstly, by temporally filtering out non-coincident events, GS significantly reduces the overall noise floor [154], a crucial asset in noisy environments where fluctuating noise levels obscure accurate measurements [155]. Secondly, the energy correlation between the correlated photons enables spectral analysis at wavelengths where optical technologies are more cost-effective and efficient. Notably, any manipulation applied to one photon, such as spectral filtering, is mirrored to the other. Additionally, if the source operates at the single-photon level, measurements can be conducted below the shot noise limit (SNL), a feature particularly beneficial for mitigating illumination effects in light-sensitive samples [156].

The concept of exploiting correlations for quantum-enhanced transmission measurements traces back to 1986 [157], culminating in the pioneering experimental demonstration of ghost imaging (GI) in 1995 [141]. Despite the quantum origin of its initial demonstration, it was discovered a decade later that many features of ghost imaging system could be replicated using classical correlations. By employing two pseudo-thermal light sources, ghost image can be produced [158]. However, in this classical approach, the correlations are partial and influenced by the overlap between the beam pattern and the object, resulting in a nearly uniform background in the final image [159]. In contrast, parametric down-conversion generates entangled photon pairs with perfect correlations, yielding a background-free image. In the single-photon pair detection regime, the entangled case exhibits higher visibility than classically correlated thermal beams [158]. Since then, quantum sensing and pair-based imaging experiments, including GS and GI, have garnered considerable attention. While most efforts in photon pair generation have centered on SPDC in bulk or polarized crystals [160], recent advancements have explored sFWM in birefringent fibers, particularly in the

context of GS between VIS and IR [154]. Fiber-based solutions offer robustness and cost efficiency, with sFWM-based systems offering tunability and simplified spectral measurements through pump wavelength adjustment.

Silicon photonics presents an intriguing prospect, offering potentially greater robustness and lower costs compared to fiber-based solutions. In this section, we leverage the intermodal process to generate photon pairs in both the MIR-NIR regions. Utilizing this photon source, ghost spectroscopy based on a PIC is demonstrated. Here, the analysis and reconstruction of the carbon dioxide (CO_2) spectrum is performed.

4.4.2 Chip design and experimental set-up

The source is based on intermodal sFWM within a multimodal SOI waveguide, similar to the experiment detailed in Section 4.2. Here, we outline the differences from the previous scenario. The sample was fabricated through IMEC foundry, and we observe higher performances with respect to the previous sample. The multimodal waveguide, measuring 1.5 cm in length with a channel waveguide with a cross-sectional area of (2 $\times$ 0.220) μm^2, facilitates PM for signal and idler wavelengths around 2000 nm and 1290 nm, respectively, with a CW pump situated in the L-band. The simulated profiles of the TE0 and TE1 modes are reported in Fig. 4.11(b). Reduced propagation losses, notably at 1.8 dB/cm at 1550 nm, enable tunable CW pumping of sFWM. Another notable change involves substituting the DC with a more robust MMI, known for its resilience against manufacturing defects, to split the input pumps.

Further modifications include the utilization of bends to compactly arrange the PIC while preserving a substantial generation length. The MMWG comprises five extended waveguides, each measuring 0.3 cm in length, interconnected by four Bezier curves, each 42 μm long. Special attention is directed towards the Bezier curves [161], as they induce a distinctive phase variation in the modes compared to the straight waveguides, thereby influencing the PM condition and, consequently, the spectra of the generated twin photons.

Fig. 4.11(a) illustrates a schematic of the setup, wherein no alterations are evident in the detection part with respect to the setup in Fig. 4.2, particularly in the initial characterization stage. The only variation is the use of a tunable CW laser amplified using an erbium-doped fiber amplifier (EDFA). In the detection part, a gas-filled cell (red dotted square) is introduced into the signal path preceding the UC module during the spectroscopy measurement.

4.4.3 Experimental characterization

To characterize the source, various parameters were measured, including the generated spectra, spectral correlation between the generated photons and the pump, coincidence rate, CAR, and $g_H^{(2)}$.

Generated photons

The analysis of the spectra of the generated photons is illustrated in Fig. 4.12 (a), where a comparison between the measured and simulated spectra of idler photons is presented. These measurements were conducted with the chip pumped at $\lambda = 1569$ nm, utilizing the same power levels as employed in the GS experiment (on-chip power of 45 mW). A custom monochromator with 2.5 nm resolution, detailed in Section 4.3.2, facilitated the measurements. The simulated spectrum (orange line), derived from the JSI of the sFWM process, requires special consideration due to the distinct structure of the multi-mode waveguide. The presence of Bezier curves alters the effective modal index,

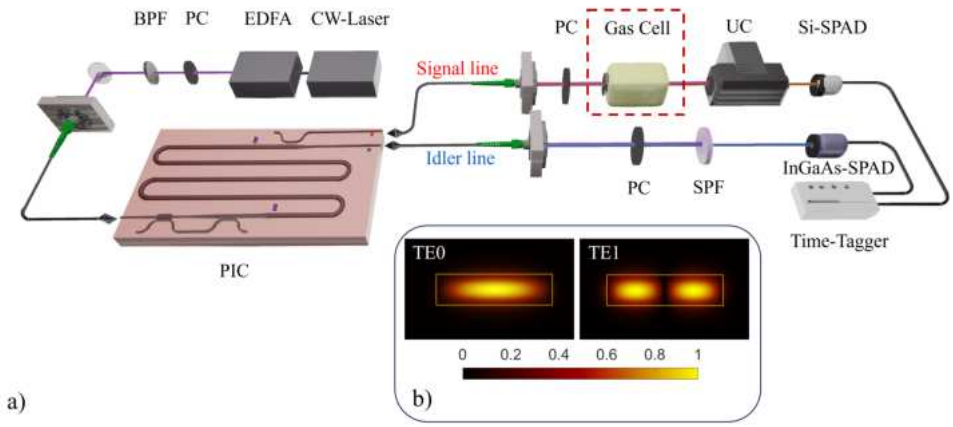

Figure 4.11: a) The scheme of the experimental setup. Initially, a pump beam is produced by a tunable CW laser and amplified using an erbium-doped fiber amplifier (EDFA). A BPF is then employed to eliminate the amplified spontaneous emission (ASE) generated by the EDFA. Polarization adjustments are made using wave-plates, and the light is coupled to the chip through edge-coupling using a lensed tapered fiber. Idler and signal are collected by tapered fibers. The idler is polarization filtered via wave-plates, while Raman and pump photons are rejected using a short-pass filter (SPF) with a cut-off wavelength at 1335 nm. Idler photons are detected using an InGaAs single photon avalanche diode (SPAD model IDQ-id210). Signal photons, once polarization filtered, travel through a CO_2 gas cell before being up-converted to the visible spectrum by the UC. Detection of the up-converted signal occurs through a Silicon SPAD (Excelitas SPCM-AQRH-12). Coincidence counts between the two SPADs are recorded via a time-tagger (time-tagger 20 Swabian Instruments). b) The simulated TE0 and TE1 modes for the channel waveguide with a cross-section of (2×0.220) µm^2.

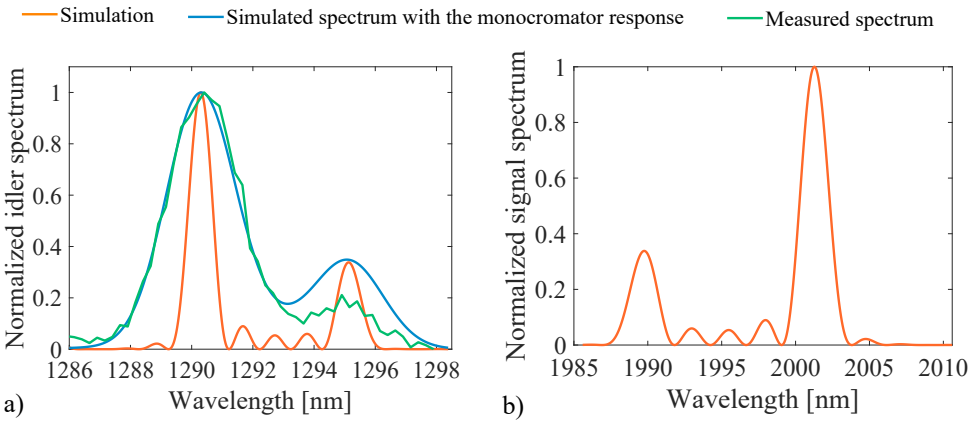

Figure 4.12: a) A qualitative comparison between the idler spectrum obtained from direct measurements (green line) and the simulated spectrum considering the monochromator (light blue line) and without it (orange line). The pump wavelength used is $\lambda = 1569$ nm. It's worth noting that the relative error associated with each data point represented by the blue line is less than 5%. b) The simulation depicted in this panel illustrates the spectrum of signal photons without any influence from the resolution of an instrument.

thus influencing the PM condition. To simulate the impact of these curves, each Bezier curve was divided into segments of approximately constant radius. The effective index for each segment was calculated, and the total phase was determined as the integral of the phases acquired in each segment. The total phase mismatch then comprises the sum of these contributions and those of the straight waveguides. Consequently, rather than a single peak in the PM condition, the generated photons exhibit spectra with multiple peaks due to the coherent sum of the different contributions stemming from the large PM region (orange line). The simulation (light blue line) closely matches the experimental data (green line).

Figure 4.12 (b) illustrates the simulation of the photon spectrum of the signal without the influence of the resolution of any instrument. This represents the intrinsic spectrum of the probe used for measurement. As previously explained, two main unbalanced peaks are observed, surrounded by several smaller peaks resulting from the multiple curves on the chip.

Further validation of the simulation is provided through a quantitative measurement of the FWHM of the generated photons. For the signal line, we measured the spectrum after the up-conversion module using both a MIR laser and GS.

Considering the associated errors, a FWHM of 0.8 ± 0.1 nm for the idler photons and 1.8 ± 0.3 nm for the signal photons were obtained, both of which are consistent with the simulated values.

Frequency correlation of the biphoton state

An essential aspect of GS is the wavelength dependence of the generated photons on the pump wavelength, as illustrated in Figure 4.13. These measurements are conducted by utilizing the monochromator for the idler line. On the signal side, as well as the relationship depicted in Fig. 4.4(b), we use the UC module which correlates the temperature of the system to the wavelength of the up-converted signal. Notably, due to the conservation of energy, it is feasible to determine the dependence of the signal (in the MIR) by measuring only that of the idler (in the NIR). The results reveal

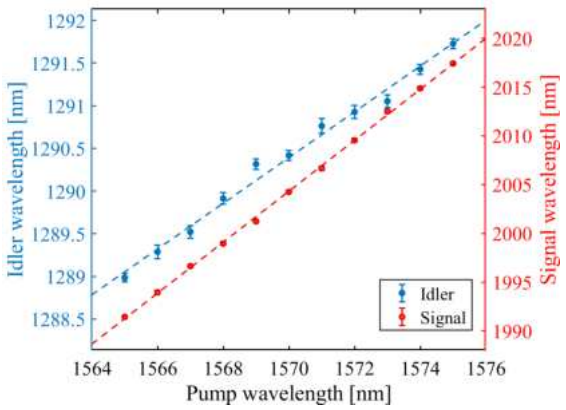

Figure 4.13: Frequency conversion of the sFWM process. The simulations of pump-idler conversion in dotted line blue and of the pump-signal conversion in dotted line red are shown. The blue points represent the measured values of the idler photons, while the red points are calculated through energy conservation from the experimental idler values.

that minor variations in the pump wavelength (within approximately a 12 nm interval) correspond to significant variations in the MIR region (within approximately a 30 nm interval), surpassing what is achievable with commonly used intramodal FWM processes. The waveguide geometry and modes were selected to produce the signal around the absorption peak near 2 µm when pumping takes place in the L-band. This specific absorption peak was chosen due to the absence of H_2O absorption lines [162], and also because the current source is incapable of reaching wavelengths longer than 2020 nm with the available pumping wavelengths (< 1575 nm).

CAR

A parameter to characterize a photon pair source is the CAR, shown in Fig. 4.14. As evident from the figure, the CAR is constrained at lower powers by dark counts and ambient noise, while at higher powers, it is limited by multiple-pair generation. In

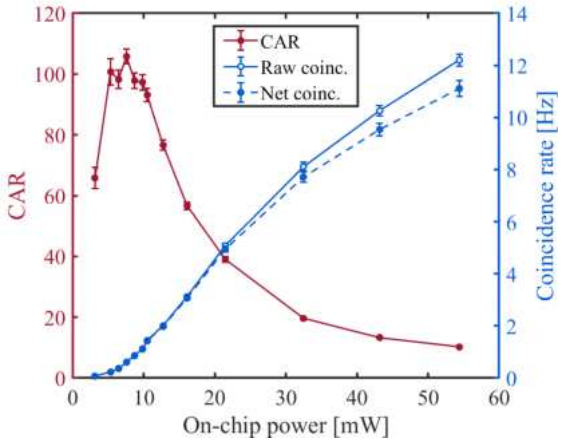

Figure 4.14: In the dark red plot, the CAR is displayed as a function of the on-chip pump power. In blue, both the raw (unfilled dots) and net (filled dots) coincidence rates are shown as a function of the on-chip pump power. Both the CAR and the coincidence rates were measured with a coincidence bin width of 0.35 ns. The lines serve as a visual guide.

this regard, we observed a fourfold enhancement in CAR compared to state-of-the-art silicon sources, achieving a net coincidence rate of approximately 1 Hz [130, 149]. The maximum CAR achieved (105.8 ± 2.5) represents a state-of-the-art for integrated photonics [130] and is close to other approach values reported for $\chi^{(2)}$ crystals [145].

Heralded $g^{(2)}$

To verify the single-photon behavior of the source, the $g_H^{(2)}(0)$ was measured using the signal as the heralded photon and the idler as the herald photon as explained in section 1.4.2. This measurement was conducted using a HBT interferometer in the signal line. The variation of $g_H^{(2)}(0)$ with pump power is depicted in Figure 4.15. A minimum value of $g_H^{(2)}(0) = 0.06 \pm 0.02$ was observed at 10.5 mW, confirming the anti-bunching regime of the generated photons in the MIR and thus establishing the single-photon regime of our source. The inset in Figure 4.15 shows the measurement for $g_H^{(2)}(\Delta t)$ at an on-chip power of 10.5 mW, with the adjacent bins to the zero-delayed one removed due to SPAD-emitted photons.

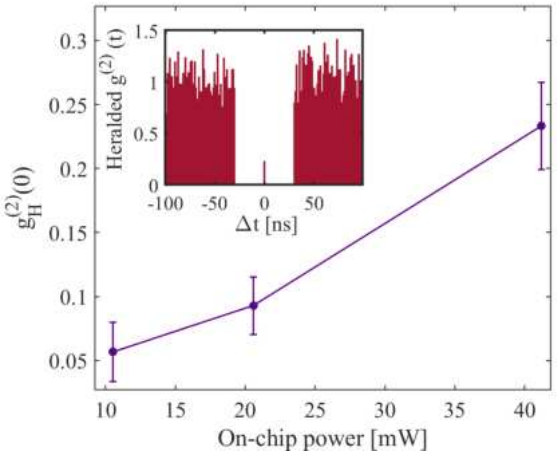

Figure 4.15: The plot shows the $g_H^{(2)}(0)$ as a function of pump power. The measurement for $g_H^{(2)}(\Delta t)$ at an on-chip power of 10.5 mW is presented in the inset. Adjacent bins to the zero-delayed one have been eliminated due to the photons emitted by the Si-SPAD.

4.4.4 Ghost spectroscopy versus Classical Spectroscopy

The time-energy correlation of the photons in the pair offers four concurrent advantages when applied to GS:

- Increased Measurement Visibility: Even under low SNR conditions, the temporal filtering provided by coincidence measurement enhances measurement visibility. This is achieved by rejecting noise counts falling outside the coincidence window.
- Preservation of Sample Integrity: GS can operate at the single-photon level without degrading the sample. Moreover, it maintains higher measurement visibility compared to classical spectroscopy methods [156].
- Real-Time Background Removal: Simultaneous monitoring of coincidences and accidentals enables real-time background removal. This capability allows variable background noise to be managed.
- Spectral Information Conversion: GS facilitates the conversion of spectral information from the MIR to the NIR, thereby simplifying MIR spectral analysis.

Thus, in scenarios characterized by high and fluctuating noise levels, GS surpasses standard absorption spectroscopy methods. It is useful to compare the two cases in terms of SNR to demonstrate the advantage of GS. To achieve this, we compute two parameters: the SNR, also called CAR in the context of coincidence measurements, and the relative error on the transmission measurement.

Assumption and basic parameters

To perform the comparison we assume that the beam generated by the chip follows a Poisson distribution with a rate of ρ, while the constant thermal background noise also follows a Poisson distribution with a rate of ν. Here, η denotes the system efficiency, which contains the detector efficiency and the transmission losses of the system, including gas absorption.

The noise is assumed to be generated before the chip and co-propagating with the generated beam. This assumption holds because the noise, being classical light, retains

its statistics despite experiencing losses. Eventually, we will discard this assumption and reframe the results with ν^M, denoting the measured noise at the detectors.

To facilitate calculations, we rely on fundamental results from the theory of Poisson distributions. For a rate ρ and a time window τ, both the mean value and the variance of the distribution are equal to $\rho\tau$. Furthermore, the probability of encountering zero photons in the time window is given by:

$$P(0) = e^{-\rho\tau}. \tag{4.12}$$

Another crucial parameter for the calculations is the probability of detecting n photons using a bucket detector with efficiency η as reported in eq. (1.141):

$$P_D(n) = 1 - (1-\eta)^n \xrightarrow[\eta \ll 1]{} n\eta. \tag{4.13}$$

Transmission spectroscopy

In classical spectroscopy, the noise cannot be concurrently measured with the signal. An independent measurement is required to enable its subtraction from the transmission measurement. However, this is feasible only if the noise remains constant during measurements. We differentiate between the noise measured without the signal, denoted as $\tilde{\nu}$, and the actual noise present during the signal measurement, denoted as ν. The two noise measurements are uncorrelated and generally distinct. Nonetheless, for our calculations, we assume $\tilde{\nu}$ and ν to have the same statistics, facilitating the removal of the noise contribution from the transmission measurement.

During spectroscopy with intense light, photodiodes (PDs) are commonly employed. These devices are responsive to the number of photons incident on the detector, thus exhibiting behavior distinct from that of bucket detectors. For PDs, the measurement averages the output signal over a time T. Table 4.3 presents the measurements and the calculated last result, along with their respective errors. The final row is computed as the difference between the first and second rows while propagating the errors.

Measurement	Mean	Error (std)
Transmission signal	$\rho\eta + \nu\eta$	$\sqrt{\frac{\rho\eta}{T} + \frac{\nu\eta}{T}}$
Noise	$\tilde{\nu}\eta = \nu\eta$	$\sqrt{\frac{\tilde{\nu}\eta}{T}}$
Transmission signal - Noise	$\rho\eta$	$\sqrt{\frac{\rho\eta}{T} + 2\frac{\nu\eta}{T}}$

Table 4.3: Conventional spectroscopy measurements with a photodiode. η includes the transmission coefficient of the system, that of the gas, and the detector efficiency. The final row assumes that $\tilde{\nu}$ and ν have the same statistics.

From the values in Table 4.3, we can compute the SNR and relative error on the final result:

$$SNR = \frac{\rho}{\nu}, \tag{4.14}$$

$$\sigma_{rel,cl} = \sqrt{\frac{1}{T}}\sqrt{\frac{1}{\rho\eta}\left(1 + 2\frac{\nu}{\rho}\right)} \xrightarrow[T\to\infty]{} 0. \tag{4.15}$$

The limit is for long integration times and represents the best-case scenario for this type of measurement. Notably, neither the SNR nor the relative error depends on the integration time in this limit.

Now, let's consider the scenario where detection is conducted with a bucket detector, as in our experiment. The detector is insensitive to the number of photons, and the counting mechanism yields a binomial distribution to the measurement: either the detector clicks or not. While this alters the statistics of the measurements, it ultimately leads to the same result as described in eq. (4.14) and eq. (4.15), under certain assumptions. The subsequent paragraph elucidates all the approximations used to derive this result.

Quantum ghost spectroscopy

The coincidence time window τ is introduced. A coincidence is registered if both the signal and idler detectors are triggered within this interval; otherwise, the event is disregarded (utilizing the start-and-stop technique). Accordingly, we define the average number of photons within the time window τ originating from the generated beam as r, and from the noise as n. This determines the rates as:

$$r = \rho\tau\,, \tag{4.16a}$$

$$n = \nu\tau\,. \tag{4.16b}$$

Using these parameters, we express the probability that a single bucket detector, with efficiency η, registers a click in the time window τ when both processes are active [71]:

$$P_{\text{click}} = 1 - e^{-(r+n)\eta} \xrightarrow[r\eta, n\eta \ll 1]{} (r+n)\eta + \frac{(r\eta + n\eta)^2}{2}\,. \tag{4.17}$$

The limit in eq. (4.17) characterizes the single-photon regime and corresponds to the second-order Taylor expansion.

The subsequent analysis involves calculating two probabilities: the probability of accidental counting, denoted as P_{acc}, and the probability of coincidence counting, denoted as P_{cc}. The former represents the likelihood of the signal detector triggering after a time $|\Delta t| > \tau/2$ relative to the idler detector, while the latter signifies the probability of both detectors triggering within a time $\tau/2$. Considering coincidences between time-correlated pairs of photons, accidental coincidences are seen as noise. Signal and idler detectors are identified by subscripts s and i, respectively.

The probability of accidental coincidences arises from the product of three probabilities: (1) the probability that the idler detector triggers within a time τ, (2) the probability that the signal detector does not trigger for a time $|\Delta t| > \tau/2$, and (3) the probability that the signal detector triggers within a time τ. The first and third terms are given by eq. (4.17). For the second term, we introduce $\tilde{r} = \rho\Delta t$ and $\tilde{n} = \nu_s\Delta t$, leading to [71]:

$$P_{NOclick}(\Delta t) = e^{-(\tilde{r}+\tilde{n})\eta} \xrightarrow[\tilde{r}\eta, \tilde{n}\eta \ll 1]{} 1 - (\tilde{r}+\tilde{n})\eta + \frac{(\tilde{r}\eta + \tilde{n}\eta)^2}{2}\,. \tag{4.18}$$

Given the typically low probability of photon pair generation, the non-zero order terms in eq. (4.18) are negligible, implying $r\eta, n_i\eta_i, n_s\eta_s \ll 1$ since $\Delta t > \tau/2$. Hence, the probability of an accidental count is:

$$P_{\text{acc}} = (1 - e^{-(r+n_i)\eta_i})(e^{-(\tilde{r}+\tilde{n_s})\eta_s})(1 - e^{-(r+n_s)\eta_s}) \xrightarrow[r\eta, n_i\eta, n_s\eta \ll 1]{} (r+n_i)\eta_i(r+n_s)\eta_s\,. \tag{4.19}$$

To compute the probability of coincidences at time $\Delta t = 0$, occurring within the same time window τ, we consider four distinct events that lead to a coincidence. The optimal approach is to derive this probability as one minus the probability of not having a click. Consequently, we calculate the probability of not having a coincidence for each of the four events and then multiply these probabilities together. These events are: (1) coincidence between the generated idler and signal photons (P_1), (2) coincidence of a generated idler and a noise signal (P_2), (3) coincidence of noise idler and a generated signal (P_3), and (4) coincidence between two noise photons (P_4)[4]. The probabilities of not having these events are given by:

$$P_1 = e^{-r\eta_s} + e^{-r\eta_i} - e^{r\eta_s\eta_i - r\eta_s - r\eta_i}\,, \tag{4.20a}$$

$$P_2 = e^{-r\eta_i} + e^{-n_s\eta_s} - e^{-r\eta_i - n_s\eta_s}\,, \tag{4.20b}$$

$$P_3 = e^{-r\eta_s} + e^{-n_i\eta_i} - e^{-r\eta_s - n_i\eta_i}\,, \tag{4.20c}$$

$$P_4 = e^{-n_i\eta_i} + e^{-n_s\eta_s} - e^{-n_i\eta_i - n_s\eta_s}\,. \tag{4.20d}$$

Therefore, by applying the assumption of a low-intensity regime, the final result is:

$$P_{\text{cc}} = 1 - P_1P_2P_3P_4 \xrightarrow[r\eta, n_i\eta, n_s\eta \ll 1]{} r\eta_s\eta_i + r^2\eta_s\eta_i\left[\frac{1}{2}\eta_s\eta_i - (\eta_s + \eta_i)\right] + P_{\text{acc}}\,. \tag{4.21}$$

This result comprises three terms: the first term is proportional to η_s, representing gas-induced losses and providing a means of recovering the gas spectrum; the third term is identical to P_{acc}, allowing for an independent, simultaneous measurement; and the second term, showing a non-linear dependence on gas-induced losses, presents challenges in recovering spectral information.

We introduce the assumption $\eta_s, \eta_i \ll 1$, valid in our system, which makes the second term negligible with respect to the first. Consequently, P_{cc} can be approximated as:

$$P_{\text{cc}} \simeq r\eta_i + P_{\text{acc}}\,. \tag{4.22}$$

Connecting this theoretical framework to our measurements, we note that the calculated probabilities refer to a time window τ. Defining $M = T/\tau$ to relate the measurement time T to the time window τ, and assuming independence between each time window, we establish the relationship between the counts N (and hence the rate R) and the probabilities:

$$N_{acc} = P_{acc} \cdot M \Longrightarrow R_{acc} = \frac{P_{acc}}{\tau}\,, \tag{4.23a}$$

$$N_{cc} = P_{cc} \cdot M \Longrightarrow R_{cc} = \frac{P_{cc}}{\tau}\,. \tag{4.23b}$$

From these equations, the SNR, or the CAR, is expressed as:

$$CAR = \frac{R_{cc} - R_{acc}}{R_{acc}} = \frac{1}{\tau}\frac{\rho}{(\rho + \nu_s)(\rho + \nu_i)}\,. \tag{4.24}$$

An important feature of this equation relies on its dependence on the time window τ: a smaller τ produces a higher CAR, which represents a "time filtering" of the noisy counts. This occurs because the signal/idler counts leading to informative coincidences occur simultaneously, while the accidental counts are evenly distributed over all possible delay Δt. Although the infinite reduction of the time window is not feasible due to the limitations of the instrument, the principle is valid, with the time window having a

[4]Each P_1, P_2, P_3, and P_4 is calculated as one minus the probability of having the respective event.

lower limit dictated by the temporal resolution of the instrument or the coherence time of the photon.

Finally, considering the relative error on the final measurement, we treat the counts as binomial events, allowing for simple error propagation. The variance of a binomial distribution is given by:

$$\text{var} = MP(1-P) \xrightarrow[P\ll 1]{} MP\,, \tag{4.25}$$

where P denotes P_{acc} or P_{cc}, and the approximation is valid due to the previous assumptions. The relative error on the final measurement, subtracting R_{acc} from R_{cc}, is then given by:

$$\sigma_{\text{rel, qu}} = \frac{1}{\sqrt{T}}\sqrt{\frac{1}{\rho\eta_i\eta_s} + 2\frac{\tau}{\eta_i\eta_s}\left(1 + \frac{\nu_i+\nu_s}{\rho} + \frac{\nu_i\nu_s}{\rho^2}\right)}\,. \tag{4.26}$$

Note that, as in the classical case, a longer measurement duration results in a smaller relative error.

Limit for High Signal Noise

Let's explore the experimental context. We employed a halogen lamp to augment the noise in the signal detector. Consequently, this noise remains localized and can be recalculated by substituting $\nu_{s,i} = \nu_{s,i}^M/\eta_{s,i}$, where the superscript denotes "measured". Furthermore, under the approximation of very high noise, where $\nu_s^M \gg \rho\eta_s$, the SNR and CAR are given by:

$$SNR = \frac{\rho\eta_s}{\nu_s^M}\,, \tag{4.27a}$$

$$CAR = \frac{\eta_i}{\tau(\rho\eta_i + \nu_i^M)} \cdot \frac{\rho\eta_s}{\nu_s^M}\,. \tag{4.27b}$$

The difference between SNR and CAR is represented in the first part of the CAR equation. This parameter shows how CAR can be improved compared to SNR by reducing losses in the idler channel, using shorter time windows, and lowering idler rates. In particular, the former depends on losses and idler noise, showing the dependence of coincidences on both signal and idler rates. In conclusion, eq. (4.27) is true in the low-intensity regime (i.e., when the average number of photons is much less than 1 within a time window τ) and when the noise significantly surpasses the signal itself. Eq. (4.27) demonstrates that, maintaining the same ratio $\rho\eta_s/\nu_s^M$, and considering typical values such as $(\rho\eta_i + \nu_i^M) \simeq 150$ kHz, $\eta_i = 10^{-3}$, and $\tau \simeq 0.35$ ns, the CAR improves by a factor of approximately 38 compared to the SNR.

The relative error can be derived from eqs. (4.15) and (4.26) as follows:

$$\sigma_{rel,cl} = \frac{1}{\sqrt{T}}\frac{\sqrt{2\nu_s^M}}{\rho\eta_s} \qquad \sigma_{rel,qu} = \frac{1}{\sqrt{T}}\frac{1}{\sqrt{\rho\eta_s\eta_i}}\sqrt{1 + \frac{2\tau\nu_s^M}{\eta_s}}\,. \tag{4.28}$$

Eq. (4.28) illustrates that classical error is predominantly influenced by noise, while quantum error comprises Poisson process error with a noise correction. Quantum error, however, suffers from the drawback of being impacted by a significantly lower count rate due to idler losses. Yet, the time filter effectively mitigates much of the noise's contribution to the error. Although this correction is not negligible in our setup, it can be further improved by reducing the time window and losses.

Overall, owing to elevated losses and limitations on the time window τ, our system exhibits higher relative errors during ghost spectroscopy compared to classical spectroscopy. By substituting typical measurement values, we find:

$$\frac{\sigma_{rel,qu}}{\sigma_{rel,cl}} \simeq 6\,. \tag{4.29}$$

Despite not gaining an advantage under our conditions, eq. (4.28) provides insight into critical parameters for improving the relative error in the quantum case.

4.4.5 Ghost spectroscopy measurements

In Fig. 4.11, we illustrate the experimental setup utilized for the GS measurement. By tuning the CW pump wavelength within the range of 1565−1572 nm, we ensure that the signal generation spans the spectral region relevant for probing the CO_2 absorption peak near 2 µm, as depicted in Fig. 4.13. Two distinct measurements were performed, as delineated in Fig. 4.16.

In the initial measurement (a), we acquired the CO_2 spectrum via GS and compared it with the spectrum obtained through direct photon transmission measurement of the signal. In the subsequent measurement (b), we maintained a fixed signal wavelength while varying the CO_2 pressure within the cell to measure the transmission vis-a-vis gas concentration. The process of adjusting the CO2 pressure (concentration) within the cell involved first evacuating the cell to 0.001 mbar using a rotary pump, followed by introducing CO2 until reaching the desired pressure. Pressure monitoring was facilitated by a strain gauge.

To evidence the advantage of GS in noisy environments, we increased the noise floor in the signal channel by employing a halogen lamp positioned between the upconverter and the Si-SPAD, thereby reducing the SNR from 5.8 to 0.04.

Fig. 4.16 (a) depicts the transmission spectrum of CO_2. The blue dots denote measurements conducted via GS using net coincidences, while the red dots represent the ratio between counts of transmitted signal photons in the presence and absence of gas. Notably, noise subtraction was omitted in this scenario to emulate real-time measurement conditions without a separate noise assessment. Normalization of the graphs was achieved using a reference measurement conducted without gas in the cell. Each data point is derived from 45 acquisitions, each lasting 20 seconds. The error bars include both the standard deviation and the error associated with the reference measurement. Furthermore, in Fig. 4.16 (a), a simulation of the transmission under noise (dashed line) and noise-free (solid line) conditions is presented. These simulations were calculated by convolving the Hitran database [163] spectrum with the signal spectrum in the absence of noise. Remarkably, despite the presence of ambient noise, the GS data points (blue dots) align with the expected transmission curve without noise. This implies that, under our conditions (with SNR 0.04), the GS is not affected by ambient noise within the measurement error margin. In contrast, the signal transmission measurements (red dots), representing standard absorption spectroscopy, correspond to the simulated spectrum only when background noise (dashed line) is considered.

In Fig. 4.16 (b), the transmission of the gas at a fixed wavelength ($\lambda = 2003.3$ nm) as a function of gas pressure is depicted. This wavelength selection maximizes gas absorption. While the GS measurements (blue dots) align with the theoretical values expected in the absence of noise (solid line), the signal transmission measurements (red dots) correspond to the model incorporating noise (dashed line). Consequently, in practical scenarios, GS can accurately determine the gas concentration even at low SNR levels,

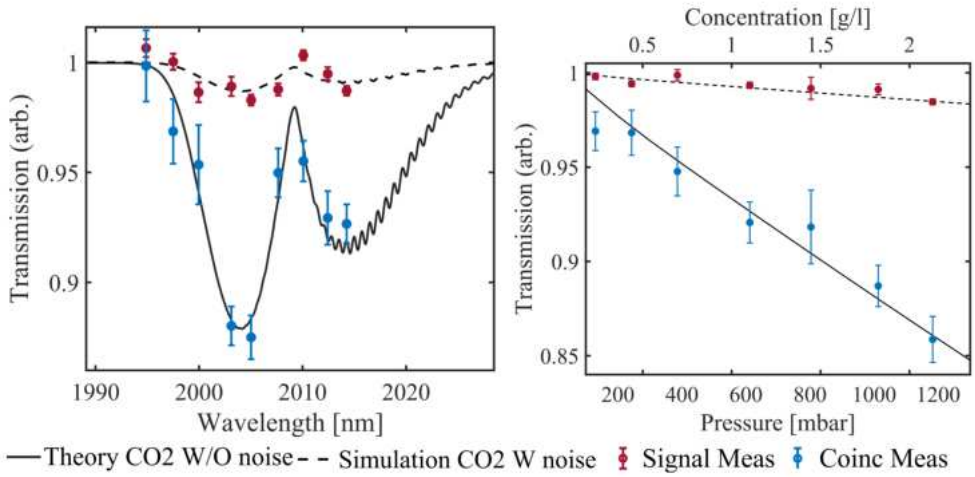

Figure 4.16: a) The transmission spectra of CO_2 in a cell filled with 1 atm CO_2 are depicted, with measurements conducted using both classical absorption spectroscopy with signal photon counts (red dots) and the GS method (blue dots). The black lines represent simulated spectra with (dashed line) and without (solid line) noise, accounting for the spectral resolution of the system. b) Transmission through the gas at a fixed wavelength, $\lambda = 2003.3$ nm, is shown as a function of the CO_2 pressure in the gas cell. Both classical measurements with signal photons (red dots) and GS measurements (blue dots) are presented. The black lines represent simulated values for a system with (dashed line) and without (solid line) noise, using a time window of $\tau = 1.1$ ns around the center.

whereas classical spectroscopy encounters difficulties. To quantitatively compare GS and classical detection, we calculated the sensitivity (S) and limit of detection (LOD) for both methods. These parameters are defined as [164]:

$$S = -\frac{\partial T}{\partial C}, \quad \text{LOD} = \frac{3\sigma}{|S|}. \tag{4.30}$$

Here, T represents the measured transmission for both classical and GS measurements, C denotes the gas concentration in g l^{-1}, and σ denotes the standard deviation of the data. The values obtained through the linear fits of the curves in Fig. 4.16 (b) are summarised in Table 4.4. The sensitivity of the GS measurement exceeds that of the clas-

	Ghost spectroscopy	Classical spectroscopy
S [l g^{-1}]	$(5.7 \pm 0.1) \times 10^{-2}$	$(5.9 \pm 0.1) \times 10^{-3}$
LOD [g l^{-1}]	$(6.7 \pm 1.8) \times 10^{-1}$	(1.3 ± 0.84)

Table 4.4: Sensitivity, S, and limit of detection, LOD, values for conventional and ghost spectroscopy measurements generated from Figure 4.16 (b).

sical measurement by almost an order of magnitude. However, due to the GS's lower coincidence rate than the classical experiment's detection rate, the GS method demonstrates lower measurement statistics, which leads to a higher uncertainty than its classical counterpart. Consequently, although the GS achieves a slightly higher LOD than the classical method, this improvement is modest.

Under equivalent background noise conditions, coincidence-based GS detection allows for smaller concentration changes to be detected than the classical approach. This advantage can be further improved by optimizing the losses in the idler channel, thus increasing the coincidence while maintaining a constant signal rate (i.e., the corresponding classical rate). It is worth noting that, with the classical approach, it is possible to obtain S and LOD values identical to those of the GS, albeit at the expense of a higher illumination intensity. This intensity adjustment becomes necessary to mitigate the impact of background noise.

Ghost spectroscopy: improvements

One way to improve the LOD is to reduce the σ, which is closely related to the relative error in measurements. A model that clarifies this parameter is provided in the previous section (see eq. (4.26)), where we outline its dependence on critical parameters of the system, including losses and the τ time window.

A further way to improve the sensor and its parameters, i.e., the S and the LOD, can be to probe absorption peaks with higher cross sections, such as those occurring around 4.3 µm for CO_2 always using a laser belonging to the C-L band. To achieve this, it is necessary to develop a new source capable of PM at this wavelength. This can be achieved by engineering the mode dispersions, e.g. by modifying the waveguide cross-sections or the spatial modes involved in the process.
To maintain the cost-effectiveness and feasibility of integration, opting for a pump wavelength in the C or L band results in the idler being generated in the NIR region, around 950 nm. Consequently, silicon cannot be used as a waveguide material due to its lack of transparency at this wavelength. Materials such as SiN [165, 166] and Silicon Oxynitide (SiON) [167] with large operating regions can be considered. For our simulations, Si_3N_4 is chosen due to its higher nonlinearity and refractive index than SiON. In this scenario, the PM condition is expressed as:

$$\begin{cases} \Delta k = k_{p1}^{M_{p1}} + k_{p2}^{M_{p2}} - k_s^{M_s} - k_i^{M_i} \\ k_x^{M_x} = \frac{2\pi}{\lambda_x} n_{eff,x}^{M_x}(\lambda_x) \end{cases} \tag{4.31}$$

where $x = p1, p2, i, s$ denote the pumps, idlers and signal respectively, M represents the spatial mode, λ is the wavelength, Δk denotes the phase mismatch and k_i^M denotes the wave vector of the x beam in the M mode. According to our simulations, PM can

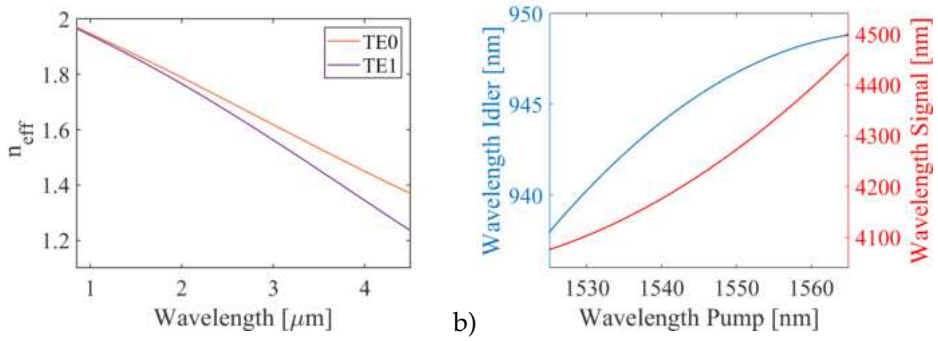

Figure 4.17: a) The simulated dispersion of the TE0 and TE1 modes in the examined region is presented. The MMWG is a channel waveguide composed of SiN, surrounded by air, with dimensions of 6 μm width and 800 nm height. b) The PM condition is illustrated for the intermodal combination 1122-TE.

be achieved around 4.3 µm when the pump photons are in the TE0 mode and the idler and signal are in the TE1 mode.
We adopt a suspended-channel waveguide to circumvent the problem of absorption by the silica coating [168], with a waveguide height of 800 nm, a typical value for MIR photonics. The waveguide width optimized for generation at the wavelength of interest is 6 µm. Fig. 4.17 (a) shows the dispersions of the TE0 mode and the TE1 mode with the chosen waveguide cross-section. Fig. 4.17 (b) shows the generated signal and idler wavelengths as a function of pump wavelength.
This simulation result underlines the versatility of the intermodal sFWM source, demonstrating the feasibility of developing an integrated photonic device suitable for MIR quantum photonics and sensing.

In addition to the increase in visibility, it is possible to exploit other advantages of the energy-time correlation. The first aspect I would like to focus on is the ability to improve the resolution of the measurement without the need for MIR equipment. This improvement can be achieved by narrowing the bandwidth of the idler through filtering. In particular, due to the energy correlation of the photon pair, the impact on the coincidence counts mirrors that of filtering the signal [131]. Fig. 4.18 shows

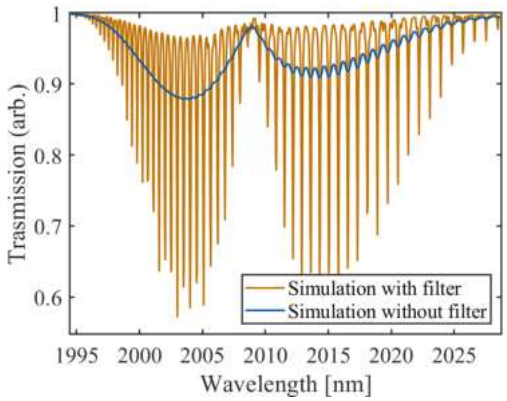

Figure 4.18: Simulation of the CO_2 considering a cell filled with 1 atm without filter in idler side (blue line) and with a 0.2 nm band-pass filter applied to the idler channel (gold line).

the simulated spectrum of CO_2 by inserting a bandpass filter in the idler branch and without its insertion. With its insertion, the spectral resolution of the gas is improved in order to resolve the vibrational modes of CO_2. Therefore, these simulation results show both the time filtering allowed by the correlated twin photon measurements and the resolution improvement due to the spectral correlations between the idler and signal photons. An alternative to inserting the BPF into the idler branch is to employ a longer multi-mode waveguide source. The longer waveguide length produces a narrower generation spectrum, resulting in higher spectral resolution [48]. This simultaneously provides for a device with low propagation losses.

4.4.6 Conclusions and future perspectives

In this chapter, we used an integrated source of silicon photon pairs to experiment with Ghost spectroscopy beyond the 2 µm threshold. Our investigation delves into probing absorption spectra and concentrations under low SNR conditions, showcasing the advantages of Ghost spectroscopy over conventional measurement techniques. Notably, our approach works even when background noise remains unpredictable.

Based on intermodal Spontaneous Four-Wave Mixing, the integrated source outperforms existing silicon sources above 2 µm. Moreover, intermodal sFWM allows spectral tuning for spectroscopic applications. Although our study is a proof-of-concept for the feasibility of gas spectroscopy, the techniques and sources employed are promising in various areas that require high visibility and compact device profiles.

Chapter 5

Toward Quantum Simulator in a monolithic platform

5.1 Quantum Simulator in a Photonic monolithic platform

5.1.1 Quantum Simulation

By the 1980s, it became evident that classical simulation of quantum problems poses a significant challenge [169, 170]. This challenge arises from the fact that simulating the system and its temporal evolution necessitates a computational effort that grows exponentially with its size. This exponential increase is inevitable unless approximation methods, such as Monte Carlo methods [171], tensor networks [172], coupled-cluster [173], density functional theory [174], mean-field dynamical theory [175], density matrix renormalization group theory [176], and others, are employed. These methods have been successfully used to address a variety of problems. However, there remain entire classes of many-body problems that remain beyond the reach of these techniques. The first category includes problems with fermions or spin frustration in two or more spatial dimensions, where conventional Monte Carlo methods face limitations due to the sign problem. A second category of problems involves dynamics, which includes most models that cannot be solved exactly for long periods of time. Despite ongoing research aimed at advancing technology to address current computational barriers [177], simulating quantum systems remains challenging even for supercomputers.

In this context, quantum simulation [178, 179] is emerging as a solution, enabling the modeling and study of complex physical systems using quantum mechanical principles. Quantum simulators (QSs) are physical devices that mimic the behavior of specific complex quantum systems, allowing for the analysis and study of the properties and phenomena of a given quantum problem in a controlled and manipulable environment. Recent demonstrations have highlighted the potential of quantum computers over classical computing. These demonstrations have been based on problems that are artificially tailored to suit specific configurations [180, 181]. QSs are essential for advancing research in various areas, such as simulating materials [182], chemical reactions [183, 184], and quantum computation [185–187]. Several platforms stand out, including ultracold quantum gas systems [188], polar molecules [189], trapped ions [190], photonic systems [181], quantum dots [191], and superconducting circuits [180]. Each of these platforms possesses distinct characteristics and advantages, and the selection among them is contingent upon the particular requirements of the application at hand.

In the past decade, integrated photonics has attracted significant interest due to its ability to manipulate photons with high precision and integrate multiple quantum

components onto a single chip. This approach enables the creation of complex, controllable systems for building high-performance QSs [29]. The potential of integrated photonics platforms is diverse and includes generating quantum states, manipulating and precisely controlling photons, integrating multiple optical components on a single micrometer-sized chip, and offering greater resilience to external factors compared to non-integrated counterparts.
Several papers have discussed QSs using integrated photonics [29, 118, 192, 193]. However, photonics has several challenges, notably losses during photon propagation within waveguides and the incomplete integration of all fundamental building blocks, such as single photon detectors. This partial integration results in photon losses to the system and a hybrid, non-fully integrated configuration.

In response to these challenges, the European project EPIQUS (Electronic-Photonic Integrated Platform for Quantum Simulator) [194] works to construct a quantum photonic simulator where the three primary components—quantum state generation, manipulation, and detection—are integrated within a single monolithic platform. This integrated approach promises a substantial reduction in coupling losses and enhanced simulation efficiency within a unified platform. Within this project, my research has centered on quantum state generation and manipulation. This chapter aims to elucidate the various advancements made, with a particular emphasis on the different photonic components.

5.1.2 EPIQUS platform

The EPIQUS initiative is aimed at demonstrating a cost-effective, user-friendly, and high-performance QS by fully integrating silicon nitride photonics with Si-SPADs [30, 82]. As illustrated in Fig. 5.1, the core concept of EPIQUS revolves around the develop-

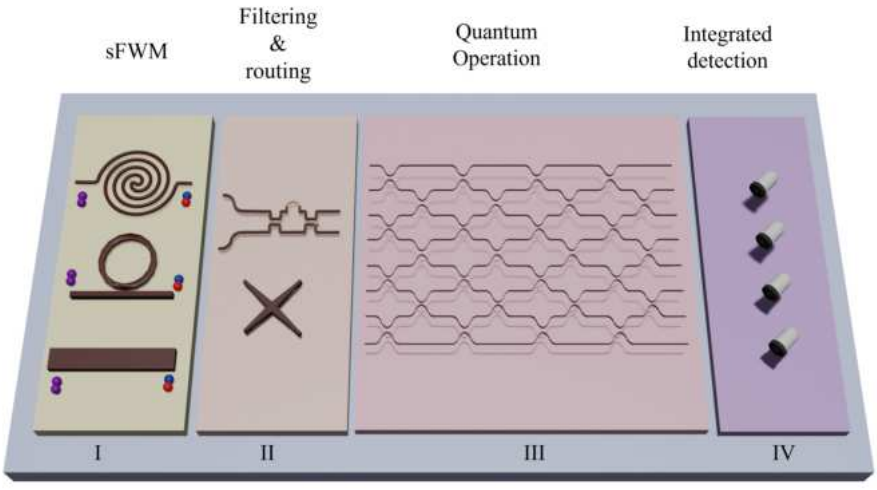

Figure 5.1: Schematic of the Integrated Photon Simulator within the EPIQUS project, segmented into four blocks denoted by Roman numerals. In Block I, entangled photon generation occurs via the Spontaneous Four-Wave Mixing process. Block II contains residual pump filtering and routing of generated photons along the established path. Block III is dedicated to quantum operation, comprising a circuit composed of a collection of MZIs. Finally, Block IV represents integrated detection.

ment of an integrated QS, comprising a quantum photon interference circuit housing

(I) entangled photon sources, (II) the state preparation stage, and (III) the QS component. The integration entails the utilization of Si-SPADs operating within the spectral range of 500 to 850 nm and at room temperature (IV). The quantum algorithm embedded in the hardware will support the simulation, with a customized analog electronic chip orchestrating the QS module. This chip will manage the pump laser, the phase shifters required for QS reconfiguration, and the SPADs to collect the single counts. Subsequently, the output data will be processed by a digital chip to facilitate software algorithm execution. The primary emphasis of the project lies not in the demonstration of its scalability but rather in achieving complete integration of all components constituting the QS.

5.1.3 Quantum Simulator photonic Platform

This thesis exclusively explores the photonic platform, particularly focusing on steps I to III in Fig. 5.1. Specifically, this chapter centers on the study of suitable materials to construct the platform, along with their linear and nonlinear characterization, and on the development of an integrated interferometric system for executing quantum operations. Two distinct materials, silicon oxynitride (SiON) and SiN are examined for the QS. This chapter is based on two of our published papers [166, 167].

5.2 Silicon Oxynitride Material

Stoichiometric silicon nitride (Si_3N_4) emerges as a compelling alternative to silicon; however, to prevent film cracking due to significant tensile stress, film thicknesses must be maintained below 200 nm. Techniques such as Damascene [195] photonic processes and multilayer TriPleX [196] offer solutions to overcome this limitation.

Another strategy to mitigate film stress involves incorporating oxygen into the SiN material through direct deposition of a SiON film. The refractive index of SiON can be finely tuned between 1.45 (similar to SiO_2) and 2.00 (similar to SiN) by controlling the relative content of oxygen and nitrogen in the film. Additionally, SiON exhibits lower material loss compared to SiN in the visible and ultraviolet regions, while maintaining low stress levels for film thicknesses up to a few micrometers. However, this approach may result in an increased device footprint and a reduction of the thermo-optical and nonlinear characteristics due to the reduced refractive index of the material.

In this section, we introduce a photonic platform based on SiON channel waveguides capable of accommodating a wide range of wavelengths in the VIS-NIR region [167]. The base material is SiON with a relatively high refractive index of 1.66 at a wavelength of 850 nm. This material possesses an optical bandgap of 4.0 eV and exhibits a relatively strong optical nonlinearity between SiO_2 and SiN. Its fabrication was performed by the Centre for Sensors and Devices of the FBK in Trento, Italy. Dr. Massimo Borghi and I developed the design of the different structures. Experimental measurements were conducted in collaboration with Mr. Gioele Piccoli from FBK.

5.2.1 SiON Photonic platform

The PIC is structured with a high-index SiON core material and SiO_2 coatings, resulting in an index contrast of approximately 15 percent between the core and coatings. Moreover, the channel waveguide is enclosed between two nm-thick SiN thin films, serving as etch-stop barriers during wet chemical etching. Additionally, the application of a conformal SiN thin film alleviates the sidewall roughness of the SiON waveguides. The cross-section configuration is shown in Fig. 5.2(a). Starting with a 6-inch silicon wafer,

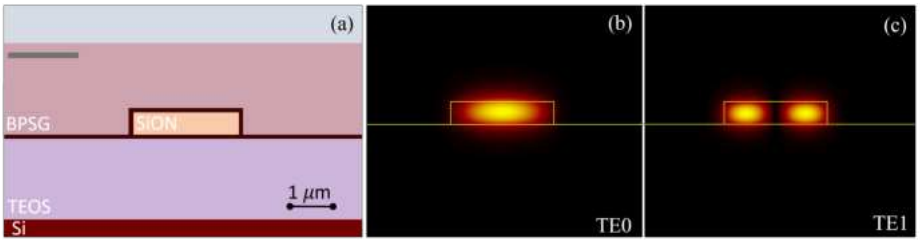

Figure 5.2: a) Cross-sectional view of the SiON core waveguide (0.3 × 2.5) µm. The cladding consists of borophosphosilicate glass (BPSG) above the waveguide and tetraethoxysilane (TEOS)-based silicon oxide as the substrate. b) and c) Simulated electric-field intensity profiles at 750 nm for the fundamental TE0 (b) and TE1 (c) modes.

a 1.7-µm silicon oxide layer is grown (TEOS oxide) at 710°C by a low-pressure chemical vapor deposition tube (LPCVD). Subsequently, a 20-nm-thick stoichiometric SiN film is deposited at 770°C, followed by a 320-nm-thick SiON film in a plasma-enhanced chemical vapor deposition (PECVD) chamber utilizing a mixture of SiH_4, N_2O, and NH_3 gas precursors. The SiON film acts as the waveguide layer for all photonic circuits within this process. Photonic devices are defined through photoresist using i-line stepper lithography (365nm), followed by the transfer of the pattern to the SiON/SiN layers via reactive ion etching (RIE). Thermal treatment of the SiON waveguides at 975°C for 1 hour in an N_2 atmosphere facilitates the release of residual hydrogen and enhances the optical properties of the SiON film, resulting in a film thickness of 300 nm and refractive index dispersion suitable for simulations and PIC design. Subsequently, a second 20-nm deposition of SiN is conducted, followed by the deposition of LPCVD BPSG and SiO_2 PECVD films at 640°C and 300°C, respectively, to form the top coating with a total thickness of 1.6 µm.

A multi-stack composed of 150 nm TiN and 1200 nm Al is sputtered, patterned, and etched with RIE to fabricate metal lines, contact pads, and micro-heaters (phase shifters) for thermo-optical tuning of photonic components. The top Al film is selectively removed atop the micro-heaters by wet chemical etching to create efficient TiN micro-resistors with a sheet resistance of 5 Ω/sq. Subsequently, the wafer is coated with a 500-nm SiO_2 PECVD protective film (overglass), selectively removed from the pad locations to facilitate wiring. The fabrication process ends with the definition of chip boundaries, waveguide facets, and thermal insulation trenches by RIE. An additional 140-µm deep etching in the Si substrate via a Bosch high-aspect-ratio etching process is finally performed at the edges to facilitate butt coupling between the optical fibers and waveguides. Subsequently, the wafers are diced, and the chips are subjected to further optical characterization. Figs. 5.2(b) and (c) illustrate the optical profiles of the TE0 and TE1 modes, respectively.

Propagation and Coupling Losses

Linear characterization measurements were performed utilizing the experimental setup illustrated in Fig. 5.3. This setup shows a supercontinuum laser (FYLA SCT500) as the light source, facilitating the measurement of a broad spectral response spanning wavelengths from 650 to 850 nm. The input polarization was controlled using achromatic half-wave and quarter-wave plates. Output spectra were collected by an Optical Spectrum Analyzer (OSA, Yokogawa-AQ6373B), enabling high-resolution (100 pm) characterization of the optical signals emitted by the supercontinuum laser.

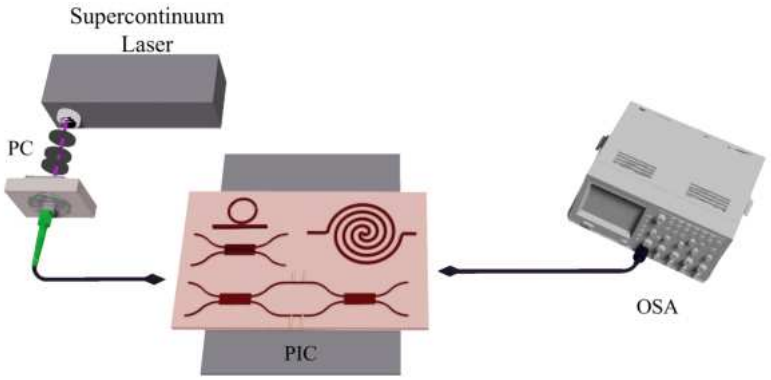

Figure 5.3: A schematic of the experimental setup employed for the characterization of the SiN integrated components. A supercontinuum laser serves as the light source and is coupled with the PIC via a single-mode tapered fiber with a Mode Field Diameter (MFD) of 2.5 µm. The desired polarization state is adjusted using free-space wave-plates $\lambda/4$ and $\lambda/2$. At the output of the PIC, the signal is collected by another single-mode tapered fiber and analyzed using an OSA, enabling high-resolution spectral analysis of the optical signals.

The performance metric used to characterize the fabricated waveguides is insertion losses (ILs), which include propagation losses (PLs) and coupling losses (CLs). To determine PLs and CLs, the cut-back method [197] was employed in waveguides with a cross-section of (1×0.3) µm^2. Based on Lumerical simulations, we have chosen to implement a tapering with a waveguide width of 1.25 µm as the optimal compromise. This choice is made with the goal of achieving coupling losses of approximately 2.2 dB, assuming an MFD of 2.5 µm. Fig. 5.4 illustrates PLs (a) and CLs (b) in the spectral range from 650 to 850 nm, evaluated in TE polarization. The band highlighted in light blue represents the measurement uncertainty, calculated by the standard deviation of measurements on identical structures within different but nominally identical PICs. This approach accounts for potential variations among the fabricated PICs. At around 750 nm, PLs of (2.9 ± 0.3) dB/cm and CLs of (4.2 ± 0.6) dB/facet were observed. Regarding

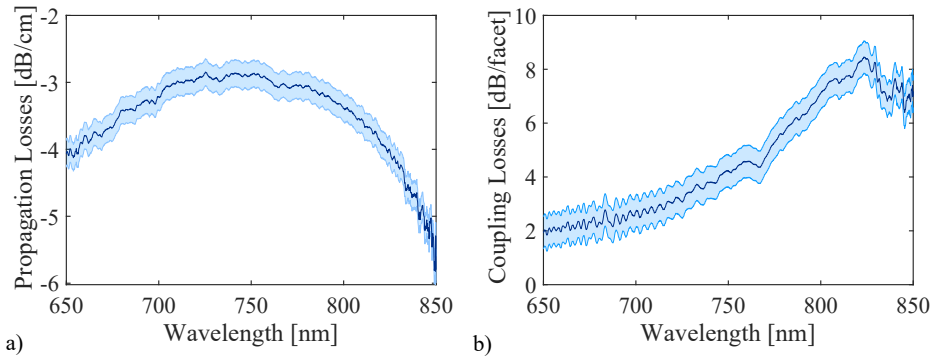

Figure 5.4: Insertion losses across the spectral range from 650 nm to 850 nm. a) Propagation losses for TE polarization in a cross-section of (1×0.3) µm. b) Butt coupling losses using a waveguide edge cross-section of (1.25×0.3) µm, employing a tapered fiber with a spot size of 2.5 µm for TE-polarized light.

PLs, the measured values are significantly higher than the specifications provided by

the FBK center. Initially, this discrepancy was attributed to the metal layer overlaying the optical circuits, which are utilized to control the thermo-optical phase shifters of other structures on the chip. It is hypothesized that the optical modes may undergo substantial interaction with the highly absorbing metal lines, resulting in large losses. This conclusion is drawn from the pronounced scattering observed when the waveguide traverses the metal lines, which indicates a significant interaction between the PIC and the top metal layer. Fig. 5.5 shows an optical image of the chip where scattering can be observed.

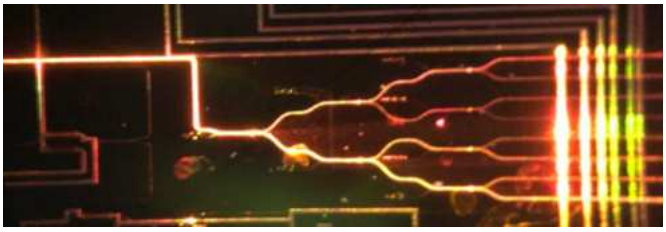

Figure 5.5: An optical image of the fabricated chip shows pronounced light scattering where the waveguide intersects the metal lines.

A "reverse-engineering" approach was performed to validate this hypothesis on one of the measured chips, selectively eliminating the metal film from the chip's top surface, thereby preserving only the photonic layer. Subsequently, the spiral waveguides were re-evaluated to characterize the loss. Meanwhile, various configurations were fabricated to mitigate PLs and prevent issues that could potentially affect the performance of the integrated devices.

The results of these different configurations are reported in the table 5.1. These findings validate this hypothesis. Therefore, other PICs were fabricated with a higher layer separation between the waveguides and the metal layer. However, the obtained

Wafer label	Features	PLs [dB/cm]	CLs [dB/facet]
W1	with 20 nm SiN layer	2.9 ± 0.3	4.2 ± 0.6
W1 Rev-eng.	with 20 nm SiN layer	2.2 ± 0.1	3.9 ± 0.6
W2	No SiN – SiON thickness 300 nm	2.3 ± 0.1	3.2 ± 0.4
W3	No SiN – SiON thickness 300 nm	1.8 ± 0.1	10.4 ± 0.5

Table 5.1: PLs and CLs vary with changes in the manufacturing configuration.

propagation results still exhibit elevated values despite these efforts. This suggests that additional factors beyond the separation distance may be contributing to the observed PLs.

An observation is that in the most recent fabrication cycle (W3) while achieving the lowest PLs to date, there is a notable increase in CLs. This highlights the need for a more detailed examination of the fabrication process and its influence on both PLs and CLs.

5.2.2 Integrated components

This section is dedicated to the analysis of fundamental integrated optical components. The devices were simulated using Lumerical software, with material dispersions from the FBK center. Figs 5.6(a)-(b) depict the designs of various integrated structures opti-

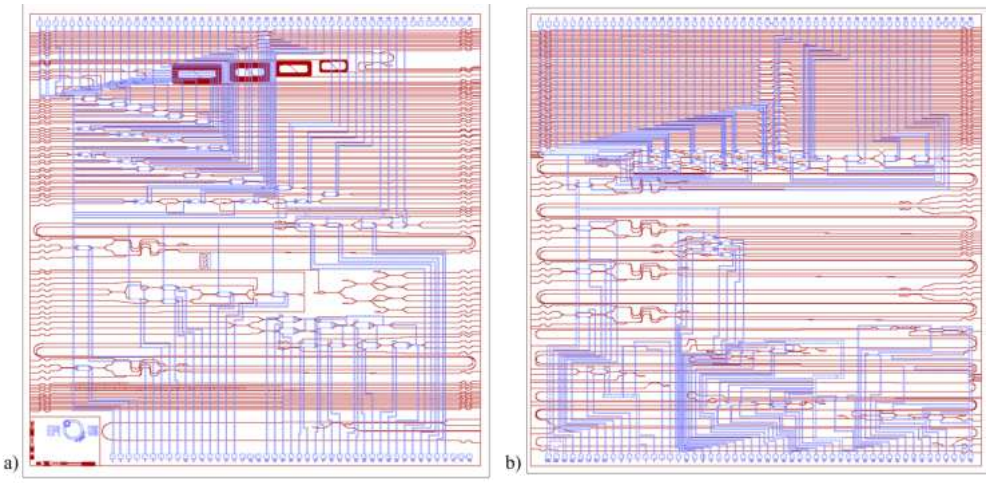

Figure 5.6: Mask layout showing two designs (a-b), where dark red lines represent waveguides and purple denotes metal wires. Overglass and trench layers are removed from the image.

mized for operation around 750 nm, each in a (1×1) cm^2 area. Waveguides are highlighted in dark red, while metal wires are represented in purple. All measurements were carried out with the setup of Fig. 5.3.

Waveguide crossings

The CRs, introduced in Chapter 2, were based on an optimized multimode crossing. This design integrates a symmetrical four-port MMI with a cross-shaped geometry (Fig. 5.7(a)), where geometric parameters are adjusted to concentrate the field profile at the center of the cross. By employing this optimization strategy, crosstalk between adjacent ports is minimized, while propagation to opposite ports is maximized through the self-imaging phenomenon. A scanning electron microscope (SEM) image of a single crossing is presented in Fig. 5.7(a). Fig. 5.7(b) shows the ILs of one CR for TE polariza-

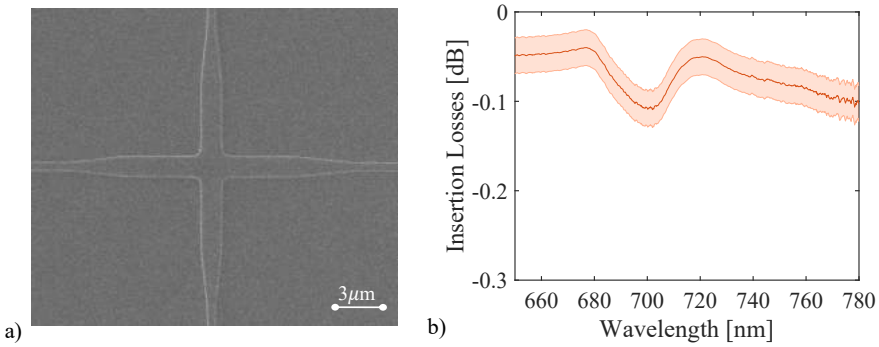

Figure 5.7: (a) SEM image depicting the CR. The multimodal waveguide measures 1.5 µm in width and extends over a total length of 10 µm. (b) ILs of a CR measured in the wavelength range from 650 nm to 780 nm for TE polarization.

tion. To provide an accurate estimation of ILs, the transmission of a sequence of 150 cascaded crossings was used. The uncertainty in these measurements, depicted by the highlighted band, arises from multiple measurements of nominally identical crossings.

Across the spectral range of 650-780 nm, our CRs demonstrate ILs of less than 0.13 dB in the TE polarization.

In contrast, crosstalk could not be directly measured due to its extremely low levels falling below the sensitivity threshold of the setup (-60 dB), consistent with simulations.

MMI Beam Splitters

As described in Section 2, beam splitters can be implemented using MMI devices. We use two configurations: General Interference MMI (G-MMI) and Pairwise Interference MMI (P-MMI). In G-MMIs, the interference mechanism involves all modes, while in P-MMIs, only a few modes of the multi-mode waveguide are excited, resulting in a different interference pattern. Specifically, in this design, termed P-MMI, the second-order, fifth-order, eighth-order, etc. modes are left unexcited, ensuring that for every pair of excited modes, there is one unexcited mode [90]. In general, G-MMIs are longer

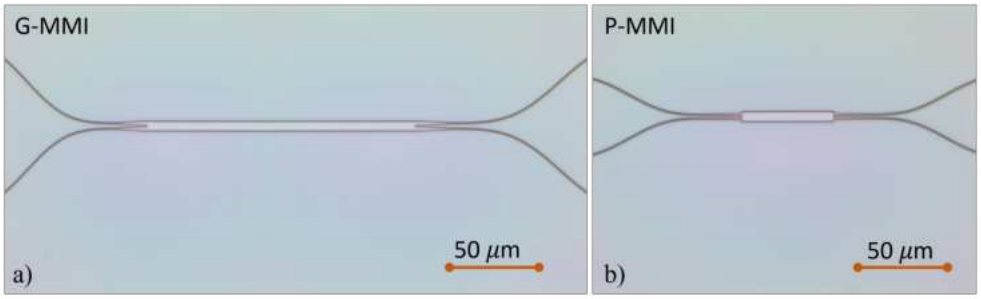

Figure 5.8: a) Optical microscope image illustrating the configuration of G-MMI. The multimodal waveguide has a width of 5.8 µm and a length of 163.11 µm. b) Optical microscope image illustrating the configuration of P-MMI. The multimode waveguide has a width of 6.7 µm and a length of 55.9 µm.

than P-MMIs and are more tolerant to fabrication errors due to their position tolerance of the input waveguide. Fig. 5.8 depicts the optical microscope images of a 2x2 beam splitter based on G-MMI (a) or P-MMI (b), with parameter values obtained from FDTD 3D simulations at 740 nm for a TE0 input. It's worth noting that the length is almost three times shorter for the P-MMI, and the input and output ports of the G-MMI are located at the edge of the multimode waveguide.

Wafer label	Features
C1	with 20 nm SiN layer*
C2	with 20 nm SiN layer*
C3	No SiN – SiON thickness 300 nm
C4	No SiN – Drie etching angled sidewalls
C5	No SiN – No SiN – Oxford SiON
C6	No SiN –No SiN – Oxford SiO_2**
C7	With SiN thin layer – Oxford SiO_2
C8	No SiN –No SiN – Oxford SiO_2**

Table 5.2: The different configurations. These marked with an asterisk (* or **) denote identical settings across different experimental runs.

In the initial fabrication run, a significant unbalance was observed in the integrated

devices, with the disparity between the two outputs exceeding 2 dB. Various configurations were attempted to address the issue, as listed in Table 5.2. However, the unbalance between the outputs persisted.

An observation is the contrasting unbalances in signs observed between the PMMIs and the GMMIs. This discrepancy suggests a manufacturing process-dependent issue, enhanced by the interference mechanisms utilized in these two types of MMIs. An illustrative example of these measurements is presented in Fig. 5.10, which shows

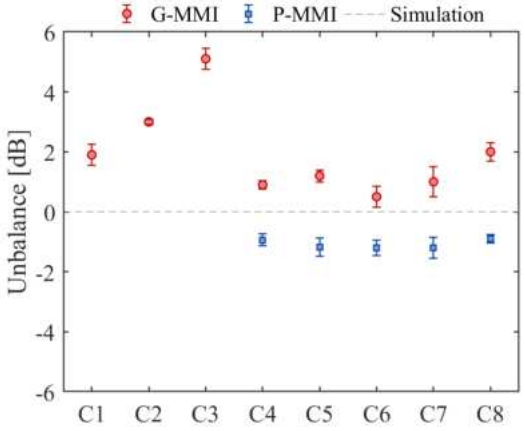

Figure 5.9: Variation in the unbalance (out2/out1) of G-MMIs (red markers) and P-MMIs (blue marker) with different runs. A consistent but specular unbalance is evident in both cases. Positive unbalanced values indicate higher intensity in the output opposite to the input, while negative values suggest greater intensity in the output corresponding to the selected input.

the ILs (blue lines) and output unbalance (black dashed lines) of a 2x2 beam splitter based on G-MMI (a) or P-MMI (b) across a wavelength range of $650 - 850$ nm for the C7 configuration. An unbalance of approximately 1 dB is noticeable at the nominal wavelength of 740 nm. It is evident that the insertion band is shifted towards shorter wavelengths, with a displacement of 20 nm for G-MMIs and 40 nm for P-MMIs, compared to the expected minimum loss at the 740 nm wavelength. For the successful

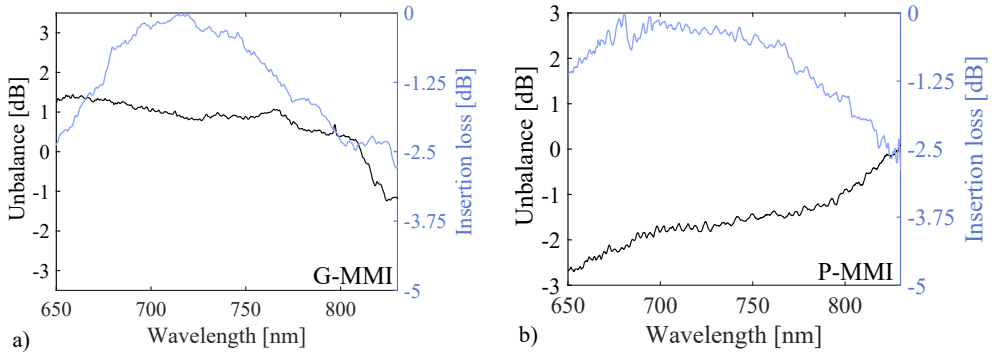

Figure 5.10: Characterization of G-MMI and P-MMI splitters designed for operation at 740 nm for the C7 configuration. The black curve represents the output port unbalance (out2/out1), while the blue curve indicates the ILs of the integrated structure.

implementation of QPICs, the proper functioning of the MMI is paramount, as any unbalance could potentially impact the performance of the entire simulator.

Asymetric Directional Couplers

A crucial component for the successful implementation of the intermodal sFWM process is the ADC, as extensively discussed in Chapter 2. ADCs play a dual role: they are essential for preparing the pump beam in a coherent superposition of TE0 and TE1 modes, and for separating the generated photon pairs propagating in the same multimodal waveguide. Fig. 5.11(a) displays the SEM measurement taken orthogonally to

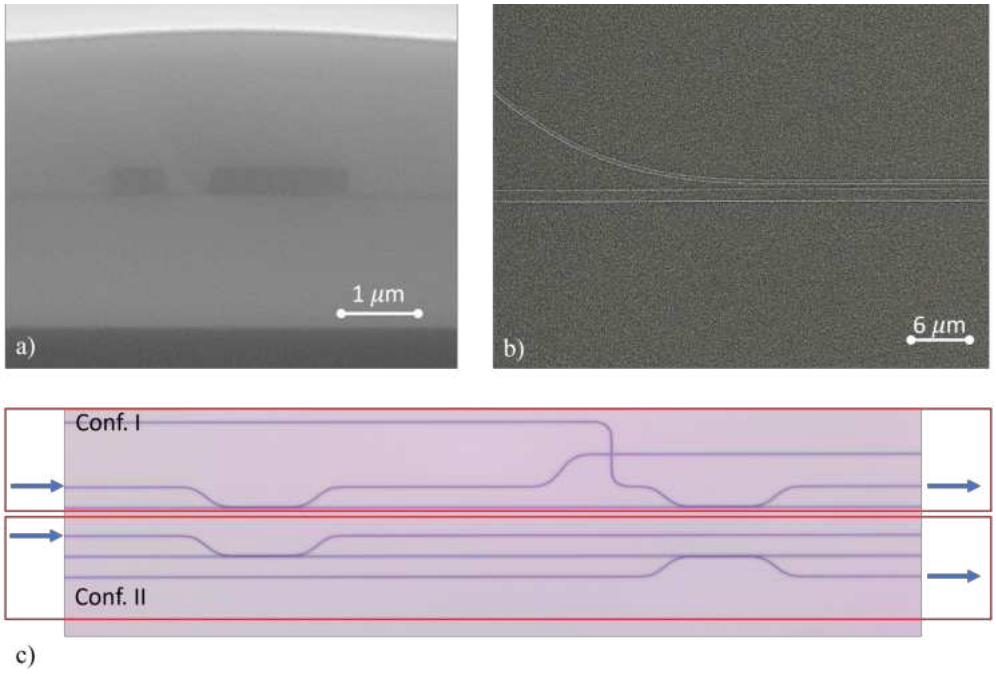

Figure 5.11: (a) SEM image showing the cross-section of the ADC, with the two SiON waveguides surrounded by the cladding clearly visible. (b) Top-view SEM image displaying the single-mode waveguide and the multimode waveguide, which approach each other up to a distance of 600 nm to form the ADC structure. The width of the single-mode waveguide is 0.7 µm, the width of the multimode waveguide is 1.79 µm, and the coupling length is 171.41 µm. c) Optical microscope image depicting two configurations for measuring ADCs: one where the two structures are in the same orientation (configuration 1), and another where they are specular (configuration 2).

the cross-section of the ADC, revealing the single-mode waveguide core and the multimode waveguide core. In Fig. 5.11(b), the SEM photo from the top of the chip zooms in on the coupling area of the two waveguides. To characterize this integrated structure, two ADCs were cascaded. The concept involves total conversion of the field in TE0 mode entering the first single-mode waveguide on the left to the TE1 mode in the multi-mode waveguide through the first ADC, followed by reconversion to the TE0 mode in the second single-mode waveguide through the second ADC. An analysis is performed by studying the output of the second single-mode waveguide (Drop) and the remainder in the first single-mode waveguide (Through). To investigate potential fabrication issues, two different configurations of ADCs shown in Fig. 5.11(c) were

examined. In configuration I, the two ADCs face the same orientation (single-mode waveguide above the multimode waveguide), while in configuration II, the ADCs are mirrored to each other.

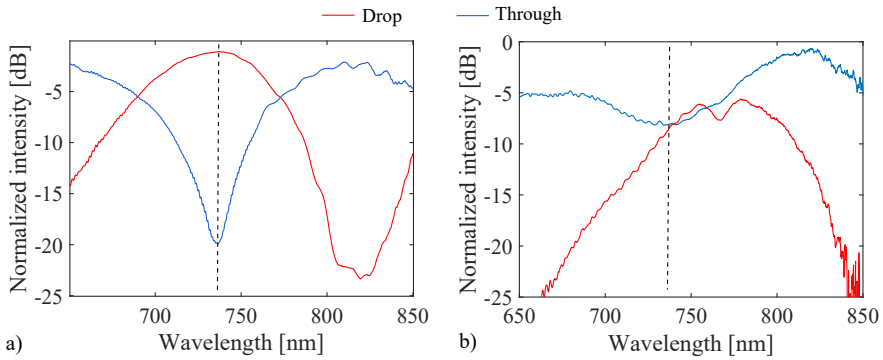

Figure 5.12: Characterization of the ADC in configurations 1 (a) and 2 (b). The red curve represents the transmission of the drop port, indicating the coupling of light carried by the single-mode waveguide into the multimode waveguide. The blue curve represents the transmission in the through port, representing the remaining signal in the single-mode waveguide.

The transmission spectra of these mode converters are presented in Fig. 5.12 for both configurations, normalized with respect to the transmission of a reference single-mode waveguide. Fig. 5.12(a) illustrates the normalized intensity in the drop (red) and pass-through (blue) output channels of the ADC mode converter. In the configuration I, the drop efficiency reaches 98%, indicating very high mode conversion efficiency for the pump beam and negligible loss. This ensures that the pump beam achieves a nearly ideal coherent overlap of TE0 and TE1 modes, as required for the intermodal sFWM process. It is important to note that the normalized intensities shown in Fig. 5.12 have a maximum uncertainty of ±1 dB, arising from variations in ILs between the two different waveguides (single-mode waveguide and analyzed structure) and variations in fiber-chip alignment.

An anomaly is observed in these devices when fabricated in configuration II. In these cases, the expected behavior is not achieved, as illustrated in Fig. 5.12(b). This anomaly is attributed to fabrication problems in the lithographic system. Specifically, the two ADCs do not achieve conversion matching at the same wavelength, greatly reducing the efficiency of the measurement. As a consequence, there is a shift in the coupling length of the device depending on its orientation.

Mach-Zehner Interferometers

A fundamental component for the manipulation and implementation of photonic hardware is the integrated MZI.

In the MZI the phase shifters consist of metal heaters fabricated by depositing a thin layer of titanium nitride via sputtering, positioned approximately 1 µm from the top of the waveguide (with a width of 2 µm) and extending to a length of about 200 µm. Characterization of these phase shifters is performed by transmission measurements while varying the electrical power dissipated through the heater placed on one arm of the MZI. The design of the MZIs was conducted both with and without trenches, positioned 2 µm away from the metal wires which serve as heat diffusion barriers.

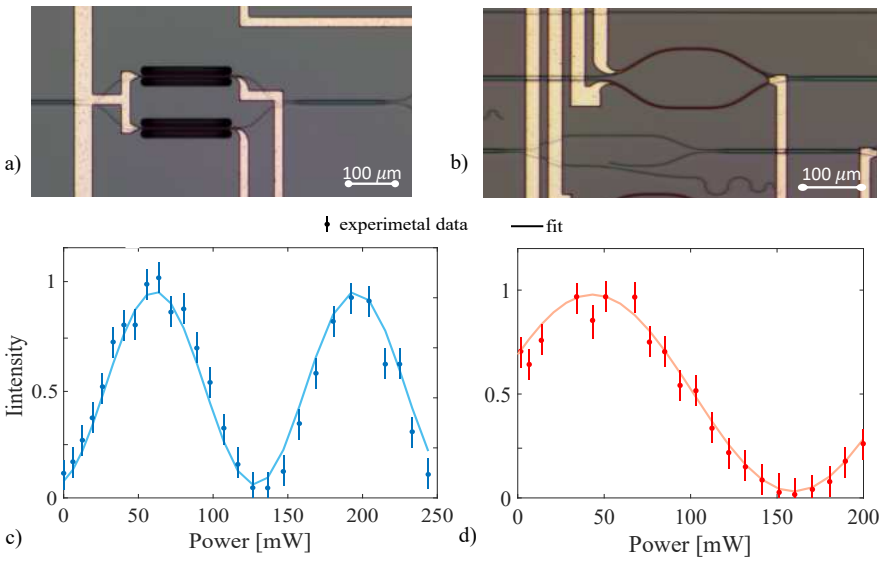

Figure 5.13: Optical microscope images of the two layouts of the MZI with (a) and without (b) trenches. The normalized intensity in one of the two outputs of the MZI as a function of the electrical power for the MZI with the trenches (c) and without the trenches (d). A phase-π is observed with the trenches at 79 mW, while without trenches at 105 mW.

Fig. 5.13 shows an optical microscope image displaying the heater with trenches (a) and without trenches (b).

Fig. 5.13 shows the intensity variation at one MZI output as the heater's electrical power changes. It requires 79 mW (Fig. 5.13(c)) to induce a π phase change in the MZI transfer function when trenches (a) are present, while 105 mW (Fig. 5.13(d)) is required when trenches are absent. This is relevant when numerous phase shifters will be employed, potentially addressing issues associated with high energy dissipation by the chip. Fig. 5.14 displays the percentage change in resistance of the metal wires as a

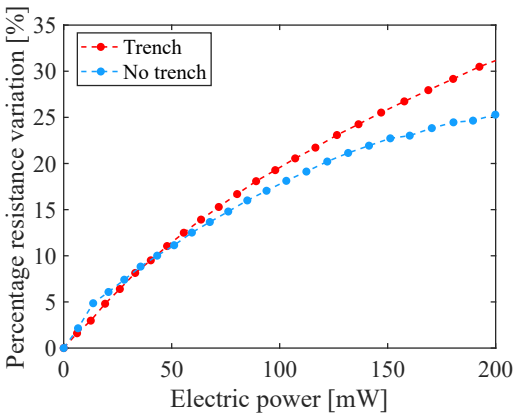

Figure 5.14: Percentage variation of the nominal resistance value as the electrical power varies in the presence (red line) and absence (blue line) of trenches.

function of electrical power. The presence of trenches (red line) results in a higher local temperature, leading to a more pronounced increase in resistance compared to the case

without trenches (blue line). This observation further corroborates that less heat is dissipated with trenches, resulting in effectively higher measured electrical resistance. A push-pull MZI configuration can be used to further reduce the power.

Rejection Filter

A critical component in our integrated QS is an integrated wavelength-selective optical interference notch filter with high rejection capability. Such a filter serves various purposes, including the removal of high-power pump photons from the idler and the signal photons generated in a sFWM process. This functionality can be achieved by employing a cascaded array of aMZIs, effectively summing the rejection provided by individual elements [198]. The design of the filter involves fixing the FSR and the resonance wavelength (λ_{res}) to a specific wavelength. To comprehensively characterize

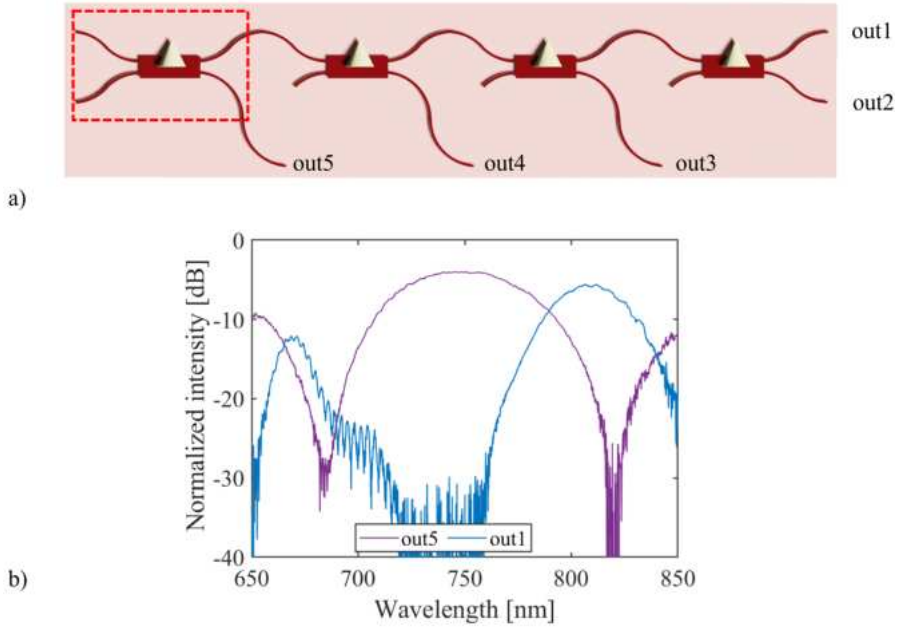

Figure 5.15: a) Schematic representation of the filtering stages for the pump, consisting of a 4 aMZI stage to remove the 740 nm wavelength and to pass 810 nm. In the dashed rectangle an aMZI. The ΔL is 2.32 µm. b) Optical responses of the pump filter designed for the signal wavelength at 810 nm. The output port labeled "out5" (purple line) displays the residual pump port, while "out1" (blue line) illustrates the rejection of this pump after 4 aMZI stages.

the configuration of four cascaded aMZIs, one output port from each aMZI stage is directed to the output of the photonic chip, as depicted in Fig. 5.15(a). The results of the characterization of a typical device tailored to filter only the 805 nm signal photons from the 750 nm pump photons are illustrated in Fig. 5.15(b). This figure shows the normalized transmissions for output channels 1 to 5, where output 1 corresponds to the channel for signal photons with the pump removed at 750 nm. Output 5 represents the residual pump.

Output 1 exhibits a transmission of approximately -5 dB at 812 nm, deviating from the ideal transmission close to 0 dB. This discrepancy is attributed to the use of 50:50 beam splitters, specifically the G-MMI type, which introduces an unbalance of about 2 dB. However, despite this deviation, Fig. 5.15(b) demonstrates that the cascade of four

aMZIs provides a notably high rejection ratio at 750 nm. The low signal-to-noise ratio observed around 750 nm, less than -37 dB, indicates that the measurement intensity has reached the minimum detectable level (-80 dBm) of the OSA.

5.2.3 Non linear measurements

Understanding the nonlinear coefficient (n_2) of the material is essential for generating biphoton states on the platform. One approach is through Self-Phase-Modulation (SPM) measurements [199, 200][1]. In SPM, the interaction of an intense laser pulse with a nonlinear medium induces a localized variation in the refractive index due to intense light-matter interactions. This variation causes a phase shift among the spectral components of the pulse, resulting in a modulation of the pulse spectrum. By measuring the spectral broadening of an ultrashort pulse with known power, we can extract the nonlinear refractive index n_2 of the material.

To estimate n_2, we employed the split-step Fourier method [89, 167], which involves simulating the expected SPM effect for a specific set of parameters, including the material's n_2 coefficient, waveguide geometry, and initial pulse characteristics. We obtained an estimate of the material's nonlinear index by comparing the simulated results with the measured SPM spectra. SPM measurements were carried out using a mode-locked Ti:Sapphire laser, tunable in the wavelength range from 720 nm to 840 nm, with a 3-dB pulse width of 0.2 nm and operating at a repetition rate of 82 MHz. The laser beam was injected into the SiON waveguide with a cross-section of (1.1 $\times$ 0.5) µm using an SM lensed glass optical fiber, and the transmitted pulse was collected with a second identical fiber at the waveguide output. Subsequently, the pulse was analyzed using an optical spectrum analyzer (OSA-Anritsu) with a spectral resolution of 0.04 nm and a sensitivity of -60 dBm.

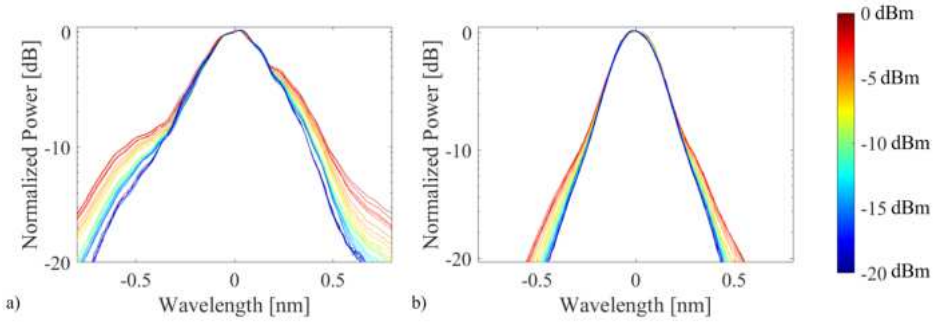

Figure 5.16: Intensity-dependent spectral broadening of ultra-short laser pulses due to SPM in a SiON waveguide. Panels (a) and (b) depict the spectral evolution for pulse wavelengths centered at 780 nm and 840 nm, respectively. The spectra are normalized to their peak powers. The differences observed in the input pulse shapes (represented by the darkest blue lines) at the two central wavelengths are attributed to variations in the experimental setting.

To examine the intensity dependence of SPM, we conducted pulse-broadening experiments for various input powers ranging from 0 dBm to -20 dBm, measured at the waveguide output. Considering the possibility of nonlinear effects occurring in the injection optics, it was imperative to attenuate the power injected into the waveguides after the external optics without altering the power present in the input fiber. This was

[1] Please note that additional information on Self-phase modulation is provided in Chapter 1.3.4. For interested readers, the methodology used is explained in [89].

achieved by adjusting the position of the input fiber relative to the waveguide facet, thereby reducing the coupling efficiency.

Fig. 5.16 presents the experimental data, showing results obtained for two distinct pulses with central wavelengths at 780 nm (a) and 840 nm (b). To determine the unknown Kerr nonlinearity n_2 of the SiON material, we conducted numerical simulations to transform an input pulse spectrum into a broadened spectrum [89]. This process relies on knowledge of the waveguide's length, propagation loss, effective mode area, and effective refractive index. The last two parameters are derived from numerical simulations conducted using Lumerical software.

The estimation of n_2 follows this procedure. Firstly, the lowest power signal (-20 dBm) is taken as the reference input pulse shape for each set of measurements. Subsequently, a series of output signals are simulated using the split-step method, with various values of n_2. Fig. 5.17(a) illustrates the input spectrum (dashed line), the experimental output spectrum at a given power (solid black line), and the differently colored lines corresponding to the numerical simulations conducted at the power of the experimental measurement but with varying values of n_2. The determination of n_2 is then obtained by identifying the value that minimizes the spectral difference between the experimental data and the simulated results, as shown in Fig. 5.17(b). The numerical simulations were performed using MATLAB software. The main source of error in the

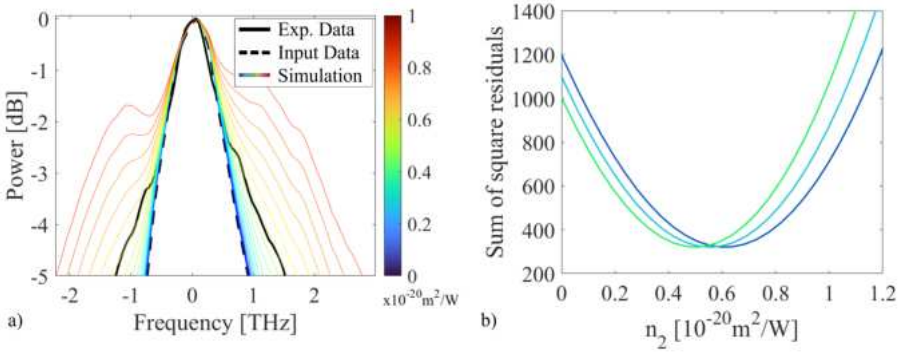

Figure 5.17: Procedure outlining the numerical process to determine the value of n_2 at a wavelength of 840 nm. a) Various output pulse shapes were simulated (ranging from blue to red, with the color-bar indicating units of $10^{-20}\,\mathrm{m}^2/\mathrm{W}$) based on increasing values of n_2 to match the experimental pulse shape (solid black line), starting from the input pulse lineshape (dashed line). (b) The sum of the square residuals between the theoretical and measured pulse shapes. The optimal value of n_2, yielding the best fit to the experimental data, corresponds to the minimum position. n_2 estimates are obtained for three different values of waveguide loss (PLs and CLs): α_{tot}, $\alpha_{\mathrm{tot}} + \sigma_{\alpha_{\mathrm{tot}}}$, and $\alpha_{\mathrm{tot}} - \sigma_{\alpha_{\mathrm{tot}}}$ (shown in light blue, green, and blue, respectively), propagating the error in measured loss onto the estimated n_2 error.

estimation of n_2 by this method stemmed from the uncertainty $\sigma_{\alpha_{\mathrm{tot}}}$ associated with the total waveguide loss, calculated as the sum of PLs and CLs $\alpha_{\mathrm{tot}} = \alpha_{\mathrm{p}} \cdot L + \alpha_{\mathrm{cpl}}$. To quantify the uncertainty of the estimate of n_2, the spectra were simulated with three values of total waveguide loss: α_{tot}, $\alpha_{\mathrm{tot}} + \sigma_{\alpha_{\mathrm{tot}}}$ and $\alpha_{\mathrm{tot}} - \sigma_{\alpha_{\mathrm{tot}}}$. The estimated error of n_2 was then calculated as $\delta n_2 = (n^2_{\mathrm{max}} - n^2_{\mathrm{min}})/2$. To validate the robustness of the employed methodology, we used a set of four waveguides at two distinct wavelengths: 780 nm and 840 nm. Specifically, we investigated a pair of waveguides with nominal widths of 1100 nm and 1300 nm. Table 5.3 presents the n_2 values extrapolated for the different configurations. The validation test illustrates that the estimates of n_2 remain consistent

Device	Waveguide Cross-section	Length	n_2 (780 nm)	n_2 (840 nm)
sample A	(1.1 × 0.5) µm	27 mm	13.1 ± 0.5	5.7 ± 0.4
sample B	(1.1 × 0.5) µm	37 mm	13.5 ± 0.5	5.0 ± 0.4
sample C	(1.3 × 0.5) µm	27 mm	12.3 ± 0.7	5.8 ± 0.5
sample D	(1.3 × 0.5) µm	37 mm	13.5 ± 0.7	5.6 ± 0.5

Table 5.3: Geometrical dimensions and estimated n_2 coefficients (in units of $10^{-20}\,\mathrm{m}^2/\mathrm{W}$), at two different pump wavelengths, for the different investigated devices.

across varying waveguide geometries, within the designated margin of error. Furthermore, our results are in agreement with prior research [201–203], indicating that the n_2 values of our SiON material fall within the expected range between pure SiO_2 and pure SiN. The estimated nonlinear index corresponds to a nonlinear coefficient, γ, of

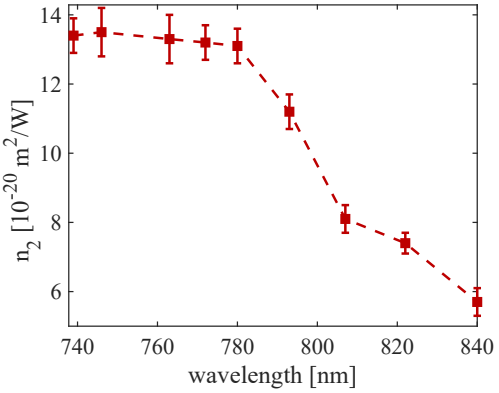

Figure 5.18: The spectral dispersion of the measured nonlinear refractive index n_2 reveals a clear increasing trend towards shorter wavelengths. Error bars represent the half-interval $\delta n_2 = (n^2_{\mathrm{max}} - n^2_{\mathrm{min}})/2$ between the minimum and maximum estimated n_2 values for each waveguide, factoring in various assumed waveguide losses.

1.5 $\mathrm{m}^{-1}\mathrm{W}^{-1}$ at a wavelength of 780 nm and 0.7 $\mathrm{m}^{-1}\mathrm{W}^{-1}$ at 840 nm for waveguides 1.1 µm wide.

Then, we selected one of the 1100 nm wide waveguides (sample A) and conducted a spectral analysis to examine the variation of n_2 with wavelength. Fig. 5.18 illustrates that the Kerr coefficient substantially increases as the pump wavelength decreases from the near-infrared to the red-visible region. This observed behavior aligns with the theoretical model, which predicts a maximum of the nonlinear index near the TPA edge at $E_g/2$ [201], corresponding to a wavelength of approximately $\lambda_{TPA} \approx 310$ nm for our SiON platform.

5.2.4 Spontaneous Four-Wave mixing in SiON

Exploiting the intermodal sFWM process, Fig. 5.19(a) shows the simulated discrete band of the idler and signal generation with a 740 nm pump wavelength and photon pairs at 690 nm (idler photons) and 796 nm (signal photons). Fig. 5.19(b) shows the simulated idler and signal photon wavelengths relative to the pump photon wavelength.

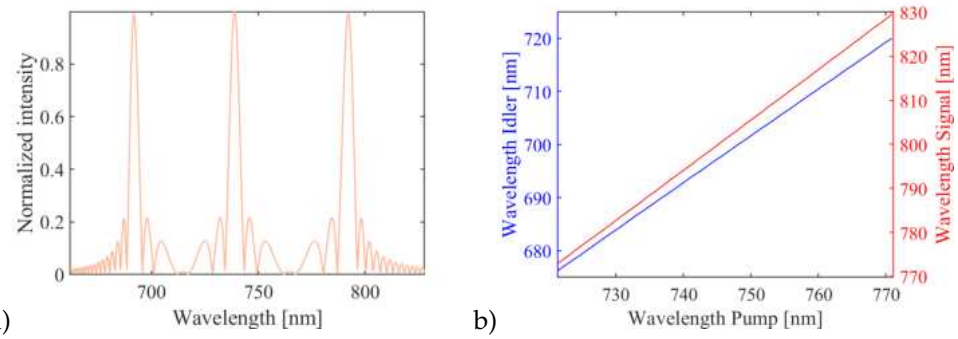

Figure 5.19: a) Simulated generation band of the intermodal sFWM process in SiON waveguide. b) Generated photon wavelength relation at the pump wavelength variation. In red is the signal wavelength, and in blue is the idler wavelength.

Fig. 5.20(a) shows the experimental setup to measure photons generated via the intermodal process. Here, a Ti:Sa laser operating at 740 nm serves as the light source. A Band-pass filter (BPF) is used to filter the pump wavelength. To mitigate input waveguide effects, an optical lens facilitates butt coupling of the free-space optical beam onto the chip. At the output, two fibers are employed to capture signal and idler photons, preceded by a Notch filter (NF) to eliminate the pump wavelength. Subsequently, a motorized grating is employed to select the wavelength by adjusting the angle, enabling reconstruction of the photon spectrum post-NF. Several measurements were conducted under varying run configurations, focusing on spectral analysis in both the signal and idler regions. Despite extensive efforts, the measurements proved to be challenging due to considerable background noise. This pervasive noise likely originates from Raman scattering and intense photoluminescence. Fig. 5.20(b)-(c) illustrates intensity measurements of waveguide photons within the expected idler range of 670 nm to 730 nm (b) and signal range of 755 nm to 845 nm (c). Notably, despite varying on-chip power levels, no signal or idler peaks are observed around the two generation wavelengths.

Many problems are present in these measurements:

1. The sensitivity of the intermodal approach to fabrication variations can lead to substantial shifts in photon generation.
2. The directional sensitivity of the ADCs which results in low modal conversion efficiencies at the wavelengths of the generated photons.
3. The non-ideal MMI with an unbalance of approximately 1.5 dB and an IL of 1.4 dB.

The simulation of the signal and idler spectrum generation rate yields generation rates below 900 Hz in the detection. This conclusion takes into account various factors, including PLs (2.6 dB/cm), ILs of integrated devices (6 dB), CLs (4 dB), and losses in the detection branch (4 dB).

As a result, a decision was made to use the intramodal process based on SiN. This shift was driven by the potential for improved device performance achievable with a material commonly utilized by manufacturers and the higher tabulated n_2 value of SiN [85] compared to SiON. Moreover, opting for the intramodal process allowed for the elimination of ADCs. Additionally, microring resonators can be used, and the higher refractive index of SiN allows for more compact structures leading to size reductions and greater integration capabilities. It is crucial to compare the nonlinear parameter

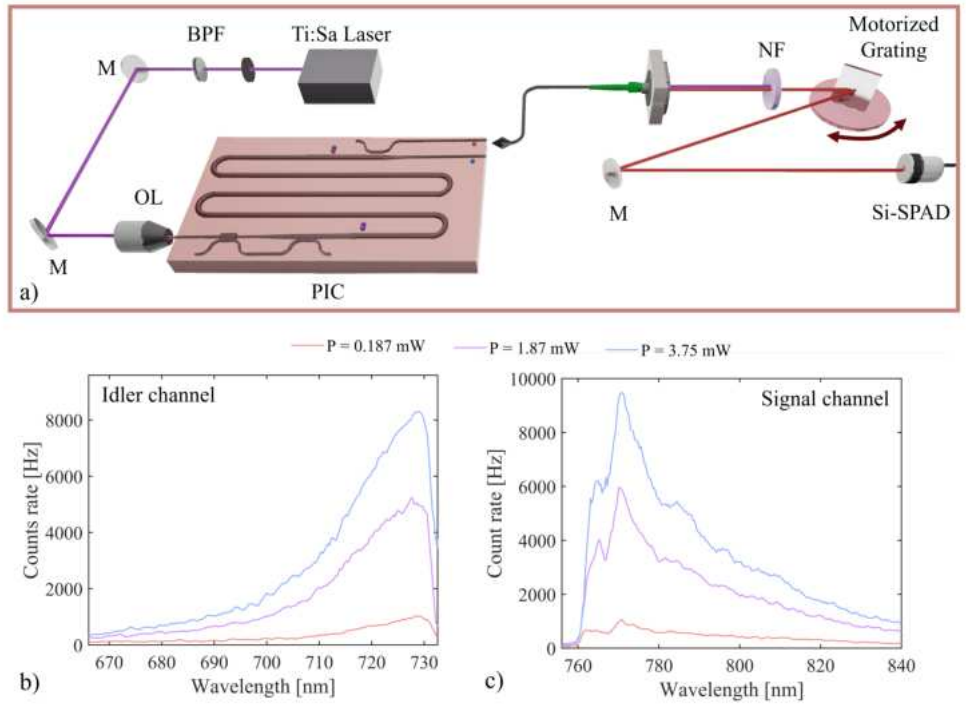

Figure 5.20: a) Setup for the characterization of photon pair sources in the SiON PIC. Starting from the left, we have the PBF and the waveplates ($\lambda/2$ and $\lambda/4$) to select the TE polarization at the input of the PIC. The light is coupled to the chip via an objective lens. After the PIC, two fibers are used to address the signal and idler in the detection part. For simplicity, only the signal branch is depicted here, although the idler branch is identical. Following the pump, which is filtered through a notch filter, the beam of one of the two generated photons is sent through free space to a motorized grating that selects the desired wavelength and directs it to the Si-SPAD. By adjusting the angle of the grating, the spectrum of the idler and signal can be reconstructed. b-c) Spectra of the light coupled out of the PIC in the detection for the idler line (b) and the signal line (c) for different input on-chip powers. The peak pump is at 740 nm, and the generated photons are at 690 nm (idler) and 796 nm (signal).

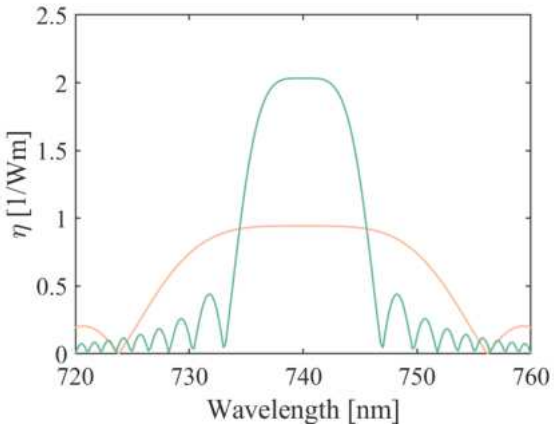

Figure 5.21: Simulation of the continuous band generation for the SiON waveguide (pink line) with a cross-section of (1 × 0.3) µm and the SiN waveguide (green waveguide) with a cross-section of (0.14 × 0.65) µm.

γ governing the generation of correlated photon pairs between SiON and SiN waveguides. For SiON, the nonlinear parameter is 0.94 [1/Wm], while for SiN (with a cross-section of 140 nm x 650 nm), it is approximately 2.05 [1/Wm]. Fig. 5.20 depicts simulations of the nonlinear parameter γ multiplied by the phase matching function ϕ as a function of the idler and signal photons, considering a 1.5 cm-long waveguide and a pump wavelength of 740 nm. Despite the wider generation band of SiON compared to SiN, the actual generation value is less than half of the SiN case. For the SiN simulation, a value of $n_2 = 23 \times 10^{-20}$ [m^2/W] was employed [85].

5.3 Silicon Nitride Material

In this section, I focus on the linear and nonlinear characterization of the SiN, based on our work [166].

5.3.1 SiN Photonic platform

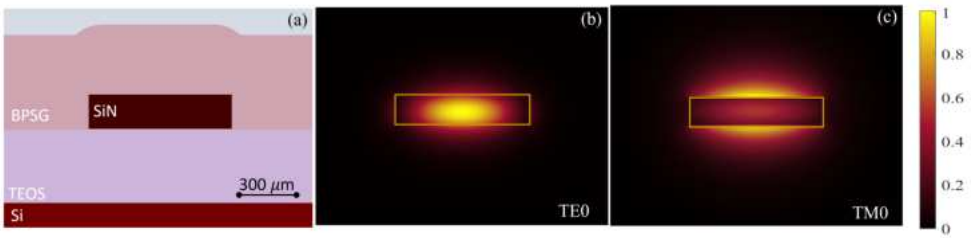

Figure 5.22: a) Cross-sectional view of the SiN core waveguide ($n_{SiN} = 1.991$ at 750 nm). The cladding comprises two distinct materials: BPSG above the waveguide ($n_{BPSG} = 1.459$ at 750 nm) and TEOS-based silicon oxide as the substrate ($n_{TEOS} = 1.441$ at 750 nm). b)-c) Simulated electric-field intensity profiles at 750 nm for the fundamental TE (b) and TM (c) modes.

The PICs were fabricated using stoichiometric SiN via LPCVD at the FBK cleanroom facilities. The fabrication process began with the growth of a bottom SiO_2 cladding,

1.7 µm in thickness, utilizing TEOS gas precursor at a chamber temperature of 710°C. This was followed by the deposition of a 140 nm-thick SiN film at 770°C. The photonic circuits were then patterned on standard photoresist using i-line stepper lithography and transferred onto the SiN layer through inductively coupled plasma reactive ion etching. Finally, a top cladding, 1.6 µm thick, composed of BPSG was applied at 640°C, after which the wafer was diced into individual chips.

The SiN channel waveguides have a refractive index of $n_{SiN} = 1.991$ at 750 nm, featuring a cross-section of 140 nm $\times$ 650 nm (Fig. 5.22(a)). These dimensions were selected to ensure single-mode operation at 750 nm for both TE and TM polarizations, as demonstrated by the mode field distribution depicted in Fig. 5.22(b)-(c) [204].

Propagation and Coupling Losses

Linear characterization measurements were carried out using the experimental setup outlined in Fig. 5.3. The cut-back method [197] was employed for this purpose. Fig. 5.23(a)

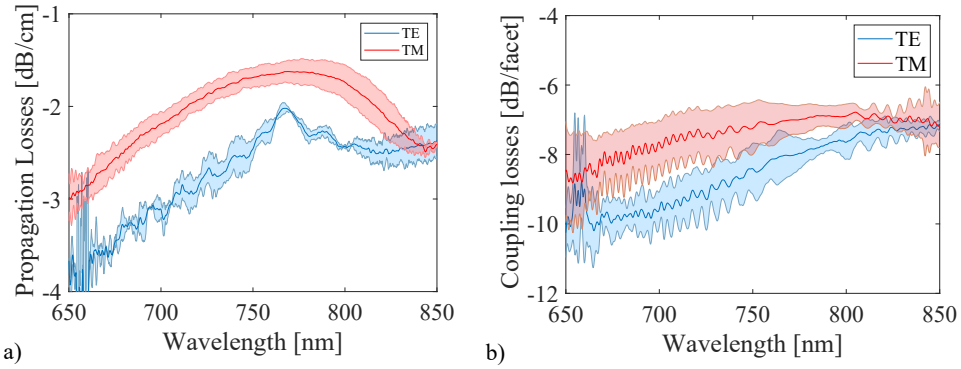

Figure 5.23: Measured ILs across the spectral range from 650 nm to 850 nm. (a) Propagation losses for TE polarization (blue) and TM polarization (red). (b) Butt coupling losses utilizing a waveguide edge cross-section of 0.14 μm $\times$ 3.25 μm, employing a tapered fiber with a spot size of 2.5 μm for TE (blue) and TM (red) polarized light.

illustrates the PLs across a wavelength range from 650 to 850 nm, evaluated separately for TE (blue line) and TM (orange line) polarizations. The highlighted band represents the standard deviation, calculated from measurements conducted on identical structures within different, albeit nominally identical, PICs.

Within the operational range centered around 750 nm, PLs of (2.4 $\pm$ 0.2) dB/cm were observed in the TE polarization, while in the TM polarization, PLs were (1.6 $\pm$ 0.2) dB/cm. This asymmetry in the PLs arises from higher scattering losses in the TE polarization due to more significant mode overlap with the waveguide's side walls, where roughness contributes to the loss [205, 206].

PLs performance falls short of the current state-of-the-art [207, 208], encouraging further investigation into fabrication methods aimed at reducing roughness induced by film deposition, lithography, and waveguide etching.

Butt coupling was employed for light injection and collection, utilizing lensed fibers with an MFD of 2.5 μm to interface with the chip. The access waveguides of the PIC feature an adiabatic tapering section spanning 150 μm in length. Here, the waveguide width gradually narrows from 3.25 μm at the facets to 0.65 μm. These dimensions were optimized via FDTD simulations, ensuring optimal overlap between the lensed fiber's mode and the waveguide's fundamental modes across different widths.

Following the adiabatic tapering, three Euler S-bends with an effective radius of 40 μm were incorporated to scatter spurious light associated with higher-order modes. This design choice ensures that only the fundamental modes of the two polarizations are guided within the PIC, while also offsetting the input and output ports of the PIC to minimize stray light collection.

Coupling Losses (CLs) are depicted in Fig. 5.23(b), revealing values of (8.4 ± 0.8) dB per facet in the TE polarization and (7.2 ± 0.8) dB per facet in the TM polarization at 750 nm. These values, although satisfactory, are not up to the existing state of the art [208]. The polarization dependence of CLs can be attributed to the varying overlap between the fiber mode and the waveguide mode, which is more pronounced for the TM polarization.

5.3.2 Integrated components

The integrated structures for this material were simulated using Lumerical software, followed by fabrication and characterization. These structures operate near 750 nm. Fig. 5.24 illustrates the chip design, showing various structures including spirals of different lengths, ring resonators, MMIs, and aMZIs.

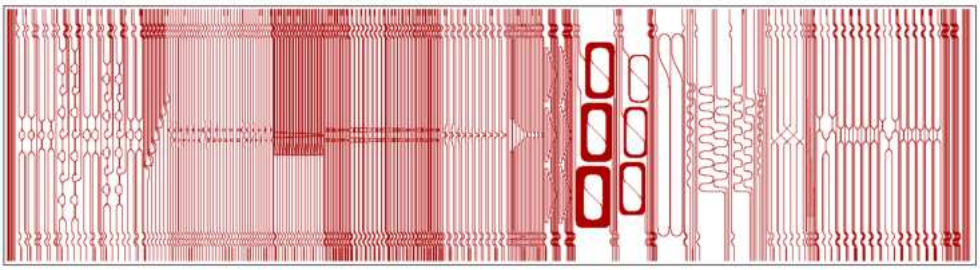

Figure 5.24: Schematic design of various structures integrated into the SiN material. This design was fabricated without the presence of metal heaters to simplify the fabrication procedure at this stage.

Waveguide crossings

In Fig. 5.25(a) the SEM image of the single CR is shown. In Fig. 5.25(b), the ILs for both TE (blue line) and TM (red line) polarizations of a single CR are depicted. To ensure an accurate estimation of ILs, the transmission of a total of 40 cascaded crossings was measured. The uncertainty in these measurements, depicted by the highlighted band, arises from multiple measurements of nominally identical crossings. Across the spectral range of 650-850 nm, our crossings demonstrate ILs below 0.13 dB in the TE polarization and below 0.25 dB in the TM polarization.

MMI Beam Splitters

Two MMI configurations were also fabricated for this material: G-MMI and P-MMI. Fig. 5.26 shows optical microscope images of a fabricated G-MMI (a) and a P-MMI (b). Consistent with SiON, it is observed that the P-MMI is smaller in size than the G-MMI.

Fig. 5.27 illustrates the ILs (green lines), and output unbalances (blue lines) of 2x2 beam splitters based on G-MMI or P-MMI within a wavelength range of $650 - 850$ nm and for different polarizations. The uncertainties in the measurements, represented by the highlighted bands, arise from multiple measurements of nominally identical MMIs.

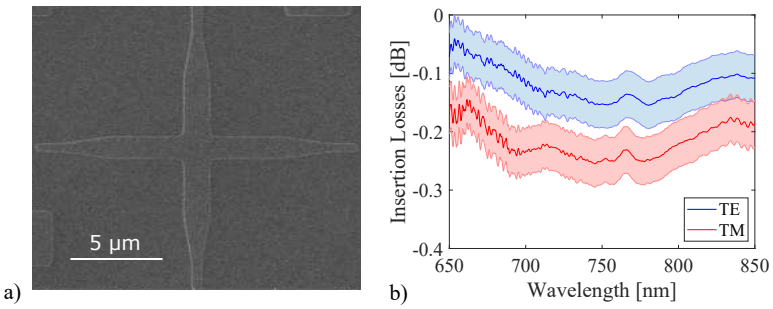

Figure 5.25: a) SEM image of a SiN CR. b) ILs in TE (blue line) and TM polarization (red line) across the spectral range of 650 − 850 nm.

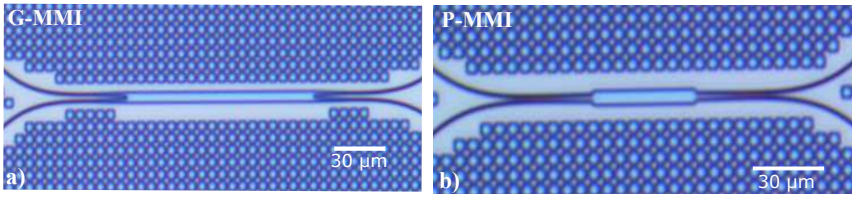

Figure 5.26: Optical microscope images of a fabricated (a) G-MMI and (b) P-MMI.

The dashed curves depict the simulated spectra from 3D FDTD calculations. The ILs reach a minimum at the design wavelength of 730 nm, with ILs < 0.5 dB for G-MMI, while this occurs at 720 nm for P-MMIs.

For the G-MMI, the output unbalance (defined as the ratio between the transmission intensities at the two outputs) remains flat over a 650-800 nm wide bandwidth with a maximum value of (0.2± 0.2) dB for TE and (0.3± 0.2) dB for TM polarization. In P-MMIs, an unbalance of approximately (0.7± 0.6) dB is observed at the design wavelength for TE polarization. However, the behavior is suboptimal for TM polarization, displaying unbalanced values exceeding (1.2± 0.2) dB.

Thus, G-MMIs exhibit polarization insensitivity and demonstrate excellent output balance. In contrast, P-MMIs are adversely affected by polarization, leading to noticeable performance degradation in TM compared to TE. This discrepancy arises from the fact that P-MMIs were optimized for a TE0 input mode, resulting in a wavelength and polarization-sensitive device. Despite being less robust in terms of unbalance, P-MMIs exhibit a wider bandwidth of minimal ILs compared to G-MMIs.

Table 5.4 provides a comparison of the 2x2 G-MMI beam splitter to the state-of-the-art for SiN in the VIS-NIR region. It is important to note that the different components refer to different spectral regions.

MMI ref.	Op. wavelength	Unbalance	Polarization	ILs [dB]
MMI 1X2 [209]	484.8 nm	1.1 dB	TE	(0.19-0.47)
MMI 1X2 [210]	633 nm	0.2 dB	TE	/
This work G-MMI 2X2	730 nm	0.2-0.3 dB	TE-TM	<0.5

Table 5.4: Comparison of SiN MMIs in the VIS-NIR spectral region.

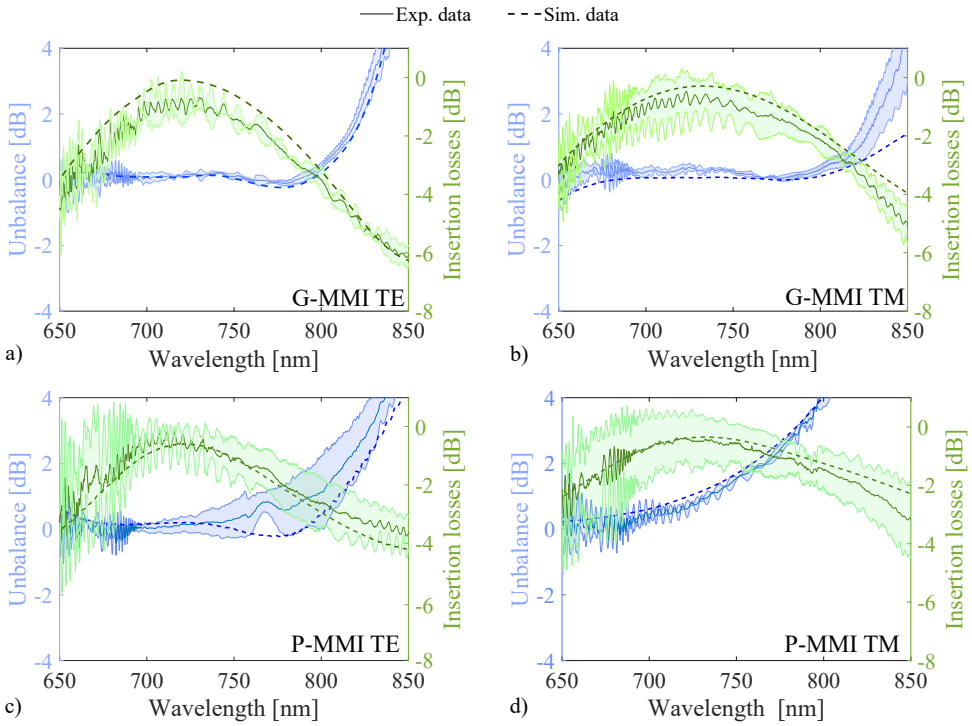

Figure 5.27: ILs (green lines) and output unbalance (blue lines) of 2x2 beam splitters based on G-MMI or P-MMI within the 650 − 850 nm wavelength range and for different polarizations.

Mach-Zehner Interferometers

The study of the aMZI in the SiN material has shown that it has a wide range of uses and functions. Given the close proximity of the generated photons to the pump (approximately 5 nm), we implemented an aMZI with $\delta L = 30.6$ μm, yielding a FSR = 8.9 nm, considering $n_g = 1.961$ at $\lambda = 730$ nm. Each arm of the aMZI has a width of 1 μm and consists of four identical 45° Euler curves with an effective radius of 80 μm. These arms are interconnected by straight waveguides, ensuring a total length difference equal to δL. This configuration was designed to mitigate potential loss. While the ILs of the aMZIs are primarily influenced by the MMIs, the visibility of the interference pattern is dependent on the unbalance of the MMIs. Consequently, the spectral bandwidth of the MZIs is linked to the bandwidth of the MMIs. Resonance matching requires active phase shifters along the inner arms despite operating in a fully passive configuration.

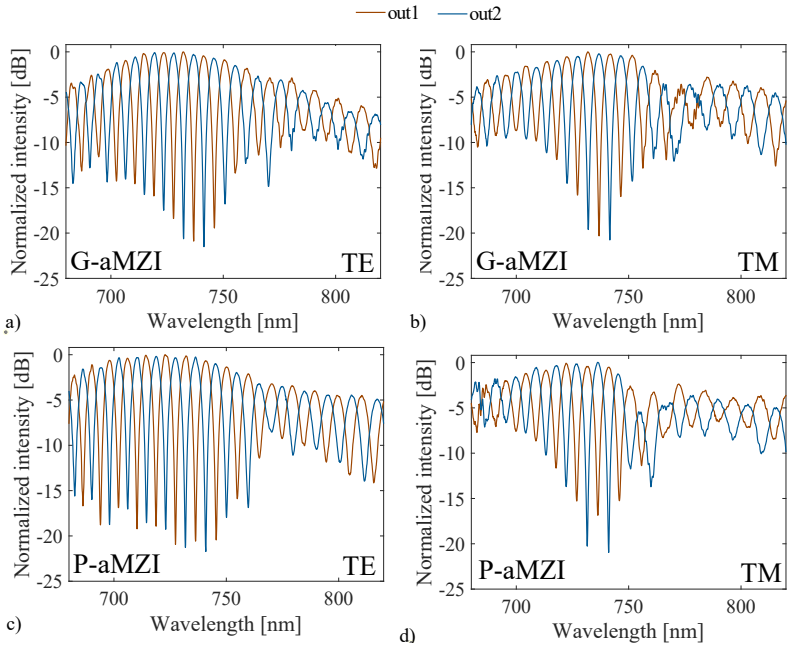

Figure 5.28: The spectral transmission characteristics of aMZIs based on G-MMIs and P-MMIs for both TE and TM polarizations. Panels (a) and (b) depict the spectral transmission of an aMZI with G-MMIs for TE and TM polarizations, respectively, while panels (c) and (d) show the same for an aMZI with P-MMIs.

In Fig. 5.28, the spectral responses of aMZIs based on G-MMIs (G-aMZI, panels a-b) or P-MMIs (P-aMZI, panels c-d) are presented for TE and TM polarizations, respectively. The optical signal is input at port 1 (in1), and the transmission out of output ports 1 ($out1$, blue lines) and 2 ($out2$, red lines) is measured.

For the G-aMZI, ILs are (-0.8 $\pm$ 0.6) dB at 730 nm with a maximum rejection ratio of (-21.1 $\pm$ 0.4) dB for TE polarization (Fig. 5.28(a)). The experimental FSR is extrapolated by analyzing the peaks in the 50 nm region, confirming a value of (9.00 $\pm$ 0.12) nm, consistent with the design.

In the case of TM polarization (Fig. 5.28(b)), ILs within the 730 nm band are (-0.7 $\pm$ 0.8) dB, with a rejection ratio of (-20.6 $\pm$ 0.6) dB. Conversely, for the P-aMZI

(Fig. 5.28(c)), ILs centered at 720 nm show a minimum of (-0.8 ± 0.8) dB and a rejection ratio of (-20.9 ± 0.4) dB for TE polarization. The measured FSR is (9.0 ± 0.3) nm. Fig. 5.28(d) demonstrates that for TM polarization, ILs are (-0.8 ± 0.8) dB within a band consistently centered at 720 nm, with a rejection ratio of (-18.7 ± 1.2) dB.

The different performances are attributed to the inferior behavior of P-MMIs in TM polarization, characterized by larger ILs and a consequent low rejection ratio. Additionally, visibility decreases outside the design wavelength region, leading to increased ILs and reduced rejection, primarily due to MMI bandwidth limitations. These findings lead to the choice of the G-aMZIs for both signal polarizations, while P-aMZIs are suitable for TE polarization exclusively.

Rejection Filter

We characterized a sequence of four aMZIs, to filter out pump photons while preserving the generated photons. In Fig. 5.29, we illustrate the results for G-aMZIs and P-

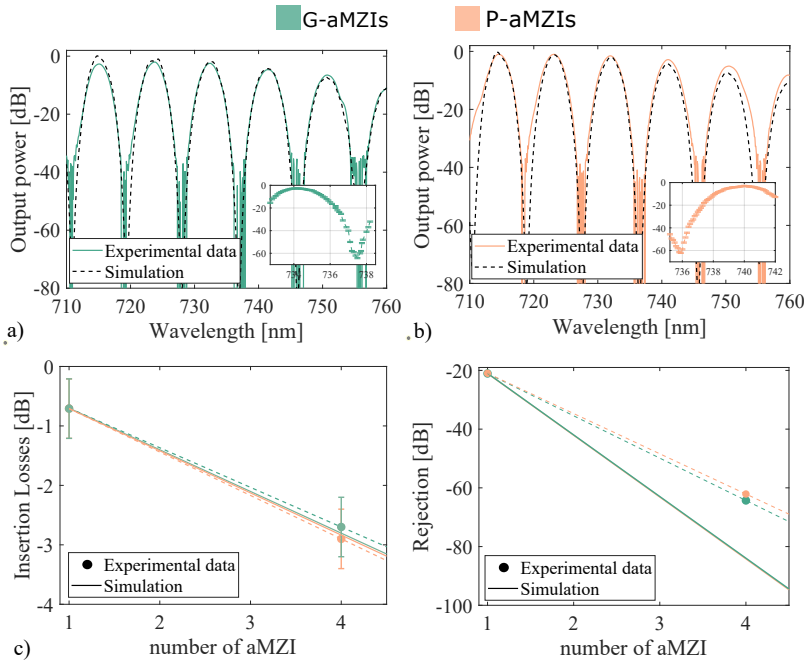

Figure 5.29: Spectral response of a high-rejection filter based on a sequence of 4 aMZIs. The filter is constructed with 4 G-aMZIs (a) and 4 P-aMZIs (b). The dashed lines represent the simulated response, while the insets display high-resolution measurements. Panel (c) depicts the measured (dots) and simulated (line) ILs at the transmission peak (near 734 nm) versus the number of aMZIs in the sequence (green G-aMZI, pink P-aMZI). Panel (d) illustrates the measured (dots) and simulated (line) rejection ratio at the transmission minimum (near 736 nm) as a function of the number of aMZIs in the sequence (green G-aMZI, pink P-aMZI).

aMZIs, in TE polarization. These components were evaluated without any adjustment of the MZI phases. We observed ILs of (-2.7 ± 0.3) dB for the G-aMZIs and (-2.9 ± 0.4) dB for the P-aMZIs. The rejection ratio was determined using a tunable wavelength

titanium-sapphire (Ti:Sa) laser and an optical power meter (Thorlabs-PM100USB), resulting in values of (64 ± 2) dB and (61 ± 2) dB for G-aMZIs and P-aMZIs, respectively (as shown in the insets of Fig. 5.29(a-b)). Fig. 5.29(c) displays the ILs at approximately 735 nm for a single aMZI and for the sequence of four aMZIs (represented by data points), with simulated results depicted as a continuous line, consistent with experimental findings. However, when considering the rejection ratio (as shown in Fig. 5.29(d)), a discrepancy is noted between the simulated and measured values. This discrepancy could be attributed to the absence of active tuning in the four cascaded aMZIs, which could enhance rejection through phase synchronization with the use of thermal phase shifters. Despite this, the observed rejection ratio remains high, reflecting the robustness of the MMI manufacturing process and its suitability for this specific application. Our results cannot be directly compared with existing literature due to the absence of similar studies in this spectral region. However, alternative filter structures, such as cascaded grating-assisted contra-directional couplers (GACDC) and DC interwoven with Bragg gratings (BG), have been investigated in previous studies [211–213]. For instance, a sequence of 16 GACDC structures achieved a rejection of 68.5 dB with ILs of -5.6 dB. Our aMZI-based structures, while achieving a comparable rejection level, exhibited significantly reduced ILs. Additionally, simulations of the second alternative filter structure showed a rejection of 60 dB. Table 5.5 provides a summary of this comparison.

Filters	Op. wavelength	ILs	Rejection	Ref.
GACDC	770-786 nm	-5.6 dB	68.5 dB	[212]
DC with BG	785 nm	Not reported	60 dB (sim.)	[213]
Sequence of aMZIs	700-800 nm	-2.7 dB	(64 ± 2) dB	This work

Table 5.5: Comparison of SiN integrated filters in the VIS-NIR spectral region.

Micro-ring resonantors

Micro-ring resonators (MRs) play a crucial role in PICs due to their resonant characteristics and compact footprint [2] [104, 105, 214]. In quantum PICs, the resonant field enhancement offered by MRs can be utilized to enhance nonlinear optical processes, such as the generation of single photon pairs through four-wave mixing [27, 86, 107]. Fig. 5.30 illustrates an SEM image of a racetrack MR in the all-pass configuration, com-

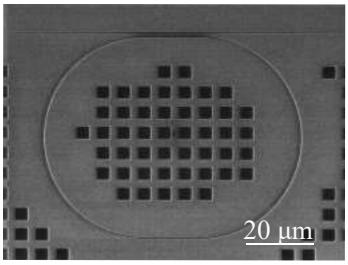

Figure 5.30: SEM image of the racetrack microring with radius 30 µm.

prising two semicircles of radius $R = 30\ \mu$m connected by two straight waveguides of length L_C, resulting in a total cavity length of $\mathcal{L} = 2\pi R + 2L_C$. The bus waveguide runs parallel to one of the straight arms at a distance of 600 nm, determining the

[2] Further details regarding the micro-ring resonator can be found in Chapter 2.

evanescent coupling strength. Using Lumerical's 2.5D FDTD Propagation Method, we conducted simulations of this design with various coupling lengths L_C within the spectral range of $650 - 850$ nm. In order to identify the critical-coupling working point of

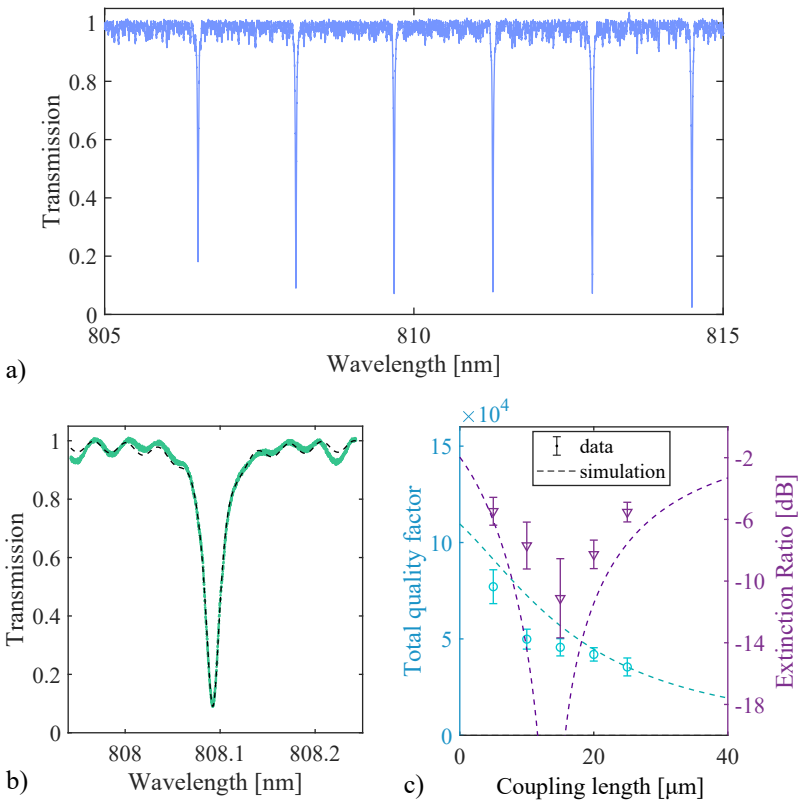

Figure 5.31: Spectral characterization of racetrack microresonators with a radius of 30 µm. (a) Transmission spectrum. (b) Fit of a single resonance, with background ripples attributed to Fabry-Perot interference in the chip. (c) Total Q-factor (light blue) and Extinction ratio (purple) as functions of the coupling length L_C. Experimental data points are represented by solid lines, while dashed lines indicate simulation results obtained by fixing the intrinsic quality factor to the estimated value $Q_i = 1.2 \times 10^5$ and varying the value of Q_{LC} within the measured region.

our MR, we fabricated a series of racetrack MRs with varying L_C, ranging from 5 μm to 25 μm. Importantly, adjusting L_C alters the expected Free-Spectral-Range of the MR, $\mathrm{FSR}(\lambda) = \frac{\lambda^2}{n_g \cdot \mathcal{L}}$, while leaving its intrinsic quality factor unchanged. The intrinsic quality factor depends solely on the PLs, defined as $Q_i = \frac{\pi \cdot n_g}{\lambda \cdot \mathrm{PLs}}$ [110]. By examining MRs with different customized L_C, we can pinpoint the critical-coupling regime, identified as the point where the extinction ratio (ER) reaches a minimum and the total quality factor $Q_{\mathrm{tot}}^{-1} = Q_i^{-1} + Q_{L_C}^{-1}$ decreases to half of its intrinsic value [110, 214, 215].

Due to the spectral resolution limitations of the setup in Fig. 5.3, which is not ideal for measuring high-Q factor, an alternative measurement configuration was adopted. This involved employing a tunable Extended-Cavity Diode Laser (ECDL) source (Sacher Lion) in conjunction with an optical wavelength meter (HighFinesse WS6) offering 1 pm accuracy. A series of MRs was examined in TE polarization within the $805 - 815$ nm range, resulting in normalized transmission spectra as shown in Fig. 5.31(a). To

characterize the resonant dips' lineshape, as illustrated in Fig. 5.31(b), a fitting procedure was employed utilizing a single Lorentzian function adjusted for the background contribution induced by Fabry-Perot interference, stemming from the reflectance at the chip facet. Fig. 5.31(c) displays the dependence of the Q-factor (light blue points) and the Extinction Ratio (ER) (purple points) on the coupling length, compared with simulation results (dashed lines). A near-critical coupling regime is evident for $L_C^{crit} = 15.0\ \mu$m, with a measured $Q_{tot}^{crit} = (4.5 \pm 0.2) \times 10^4$ and an ER of (-11 $\pm$ 3) dB. These values align closely with the estimated intrinsic $Q_i = (1.20 \pm 0.05) \times 10^5$, indicating a PL inside the MR (PLs_{ring}) of 2.6 ± 0.1 dB/cm, consistent with the directly measured PLs at 810 nm in straight waveguides.

5.3.3 Spontaneous Four-Wave mixing in SiN

The experimental setup utilized for biphoton state generation demonstration in spirals and microrings is depicted in Fig. 5.32. Beginning from the left, two lasers are employed: the Ti:Sa laser capable of achieving on-chip powers exceeding 20 mW but with a spectral width of 0.2 nm, and the tunable CW laser from LEOS-solutions (Leos laser), offering maximum on-chip powers of 9 mW with a spectral width of less than 100 kHz.

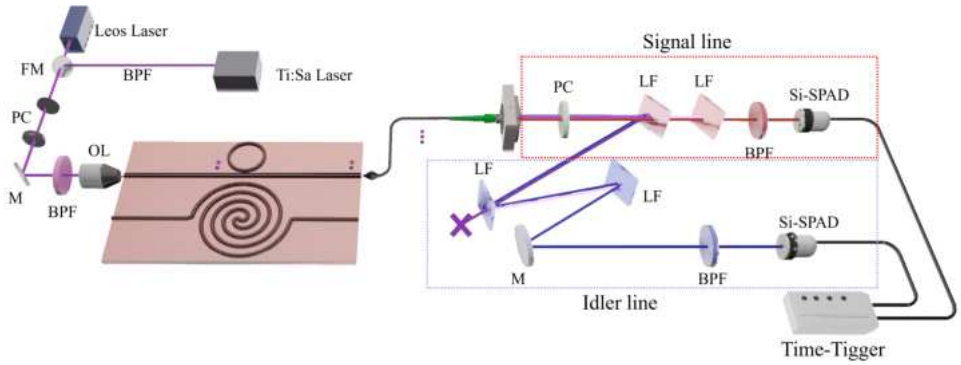

Figure 5.32: Experimental setup for nonlinear measurements. From left to right, two lasers were utilized for measurement, with the tunable CW laser from LEOS-solutions targeting the microring resonator and the Ti:Sa laser for the spiral waveguide. The pump beam is filtered through a BPF, with TE polarization selected via a sequence of half-wave ($\lambda/2$) and quarter-wave ($\lambda/4$) plates before being coupled to the chip using an objective lens. Both the spiral source and microring are integrated into the chip. The output beam is collected by a fiber and brought into free-space detection via a fiber port. Inside the detection setup, a long-pass filter (LF) separates the signal and idler photons into two paths, where residual pump light is eliminated before routing the photons to two silicon single-photon avalanche diodes (Si-SPADs) following an additional bandpass filter (PBF). Coincidences are registered via a timing trigger.

The choice of the pump laser depends on the quantum source and can be facilitated by employing a flipping mirror. The laser is butt-coupled to the chip via an optical lens (OL) with an 80 mm focal length. To ensure signal cleanliness, a BPF with 150 dB attenuation over 3 nm is positioned before the optical objective lens. Objectives are used to avoid spurious signals from non-linearly excited pulses.

The input cross-section measures (3400 $\times$ 140) nm, which tapers down to (650 $\times$ 140) nm over a 200 µm distance. The positioning of the chip allows for coupling with either the spiral waveguide or the microring resonator. At the output, the signal is collected by a tapered fiber with an MFD of 2.5 µm. This fiber is connected to polarizer

controls and a fibered 99/1 beam splitter (BS), where 1% of the signal is routed to a power meter, and the remaining 99% is directed to a fiber port for conversion into a free-space beam.

At this stage, the free-space signal comprises residual pump photons along with the generated photons. Long-pass filters are employed to separate the pump and divert the idler and signal into distinct paths. Specifically, two filters with a transmission of 140 dB are utilized to allow the signal to pass while reflecting the idler and pump. Additionally, two more long-pass filters with 140 dB attenuation in the idler branch are utilized to eliminate the pump and ensure that only the idler is reflected in the path. In Fig. 5.32 the two paths are illustrated.

In both pathways, two bandpass filters are positioned before the two free-space Silicon Single-Photon Avalanche Diodes (Si-SPADs). These filters serve to further refine the selection of the generated photons and mitigate contributions from Raman scattering and photoluminescent light in the unfiltered spectral region.

Coincidence detection is orchestrated by a time trigger (Swabian Time Tagger 20) with a resolution of 50 ps. The entire detection apparatus is isolated from external light sources to prevent any interference from black-body photons.

CAR in Spiral waveguides

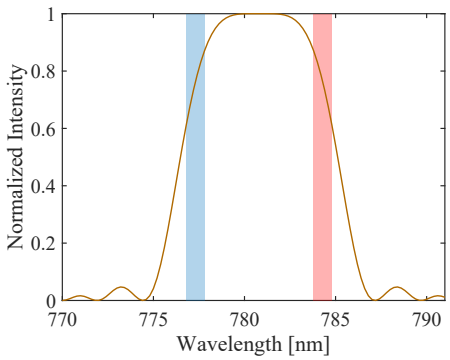

Figure 5.33: Generation band simulation of sFWM process in a waveguide long 1.5 cm. The two highlighted bands correspond to the selection of the idler (light blue band) and the signal (light red band).

The first CAR measurement was conducted on the 1.5 cm-long spiral waveguide. In this scenario, we opted for the Ti:Sa laser due to the absence of the need for a laser with high coherence time, as required in the case of microring resonators. The chosen pump wavelength was 781 nm, a selection driven by the peculiar behavior of LF-785 filters, which exhibit decreased efficiency when excessively angled.

With the intramodal process, we were able to proceed directly to the coincidence measurement, thanks to the continuous band around the pump. This facilitated understanding the extent to which we could deviate from the pump without compromising generation efficiency. Consequently, we strategically positioned the filters to maintain the idler and signal 3.6 nm away from the pump, ensuring effective residual pump filtration without sacrificing generation efficiency as shown in Fig. 5.33. We measured the CAR value in these configured settings changing the input power. Fig. 5.34(a) depicts the histogram of coincidences at an on-chip power of 17.5 mW within a 100 ns window, revealing the peak of coincidences and the plateau of the accidental coincidences.

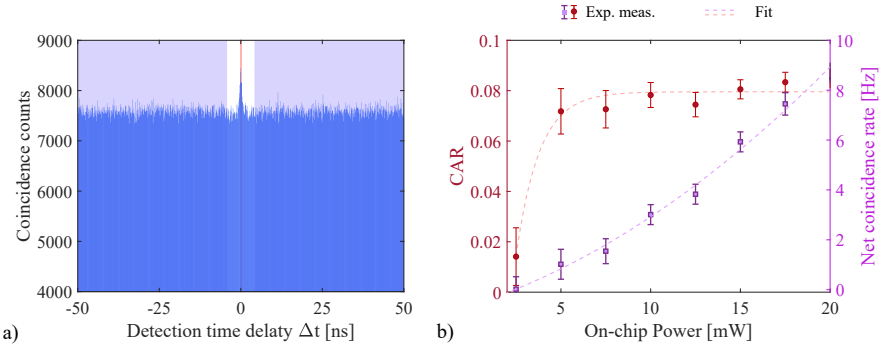

Figure 5.34: a) A histogram showing the coincidence measures at $\Delta t = 0$ (net coincidences + accidental coincidences) and $\Delta t \neq 0$ (accidental coincidences) for a spiral waveguide. A histogram with a bin of coincidences of 50 ps is displayed in dark blue. The zone containing the accidental coincidences is represented in light blue, while the used coincidence band of 550 ps is displayed in red. It is possible to observe the coincidence peak at $\Delta t = 0$. b) The CAR value (in dark red dots) and the net coincidence detection (in purple dots) as a function of the on-chip input power.

The resolution of the histogram matches the resolution of the electronic timing used, which is 50 ps. The light red region indicates the area designated as the window of coincidences (550 ps), while the light blue region is employed to account for accidental coincidences. Eq. (1.130), described in Chapter 1, was utilized to calculate the CAR value. Fig. 5.34(b) represents the CAR and net coincidence rate across varying on-chip power levels. We noted a CAR peak of (0.082 ± 0.001) with a net coincidence rate of 7 Hz and a coincidence window of 550 ps. Despite the low value influenced by prevalent photoluminescence and Raman noise, this result represents the first documented result of spiral entangled photon generation in the VIS-NIR region based on SiN.

CAR in Microring resonators

Generation measurements were also carried out on the microring resonator. For this particular application, a Leos laser with a spectral line width of less than 100 kHz was used (Fig. 5.32). In order to ensure that the produced photons and the pump photons were at the same wavelengths of the spiral case, a 20 µm microring resonator was used for the measurement, yielding a 1.6 nm FSR. As shown in Fig. 5.33, choosing its second resonance from the pump (3.2 nm from the pump) ensures a generation efficiency of 60-70%.
Fig. 5.35(a) displays the resonances illustrating the FSR of the microring. Using this microring resonator, we achieved the resonance shown in Fig. 5.35(b), allowing us to quantify the Q-factor value of $(18.3 \pm 1.6) \times 10^3$. The coupling length was determined at the point of maximum Extinction Ratio (ER), resulting in a length of 27.5 µm. Experimental values of the coupling length are depicted in Fig. 5.35(c), showing the variation compared to the Lumerical Simulation.

The Leos laser is precisely tuned to the microring resonator at a wavelength of 780.77 nm, yielding idler and signal wavelengths of 777.28 nm and 784.35 nm, respectively.

Coincidence measurement was carried out. The coincidence histogram at a resolution of 50 ps was shown in Fig. 5.36(a). The measurement is performed at an on-chip power of 9 mW, where the coincidence peak and the accidental coincidence plateau

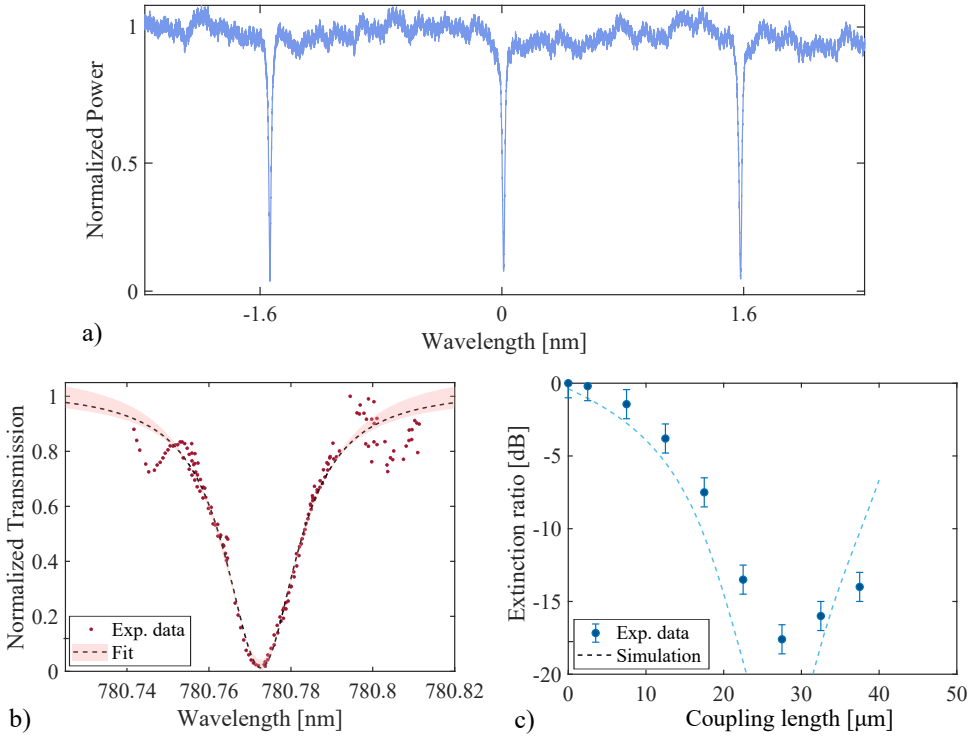

Figure 5.35: a) Microring resonator resonances spectrum with a radius of 20 µm and coupling length of 27.5 µm. b) Experimental data (dark red dots) and fit (dashed line) of the single resonance at 780.77 nm with a resolution of 0.5 pm. c) Experimental data (dark blue dots) and simulation (light blue line) of the extinction ratio as the coupling length changes.

may be easily identified. The light blue region shows the region where accidental coincidences were recorded, while the red region shows the 550 ps window where coincidences occurred. Again, the CAR value was determined using eq. (1.130).

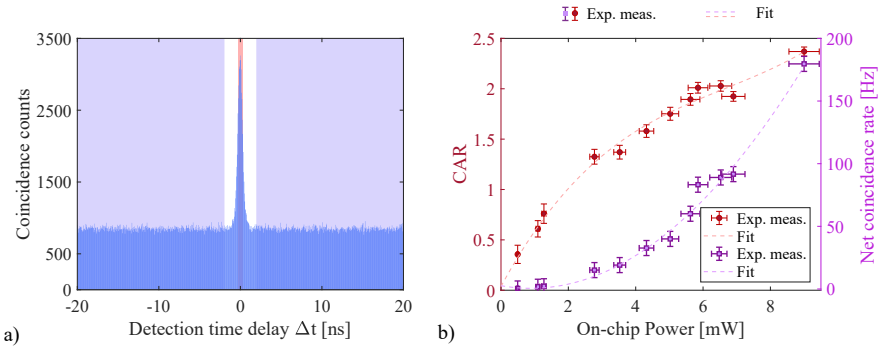

Figure 5.36: a) Histogram displaying coincidence measures at 9 mW on-chip input power in 135 s at $\Delta t = 0$ (net coincidences) and $\Delta t \neq 0$ (accidental coincidences) for a microring resonator. The histogram features bins of coincidences of 50 ps, depicted in dark blue. The region containing accidental coincidences is shaded in light blue, while the utilized coincidence band of 550 ps is highlighted in red. Notably, a coincidence peak is observable at $\Delta t = 0$. b) Plot illustrating the CAR value, denoted by dark red dots, alongside the net coincidence detection (represented by purple dots), plotted as a function of the on-chip input power.

The CAR value and net coincidences as a function of the on-chip power are shown in Fig. 5.36(b). The highest CAR value attained is 2.4, at a 190 Hz net coincidence rate. This result, while half compared to the state-of-the-art utilizing a microring resonator in the VIS-NIR range [86], surpasses the performance achieved with waveguides by several factors. This improvement can be attributed to the superior pump filtering capability of the microring resonator, as well as its higher generation efficiency and the enhancement derived from its Q-factor.

Evaluating the rate of pair generation within the chip takes into account the losses sustained in the signal and idler lines. Fig. 5.37 depicts the experimental rate of pair generation compared to simulations, which are represented by dashed lines. Potential improvements in the system are possible. First, by changing the waveguide's cross-section to increase the generation band, generation can be enabled farther by moving away from the pump, lessening the effect of noise. Second, raising the Q-factor has the potential to increase generation efficiency. Furthermore, photoluminescence and Raman scattering noise can be reduced through an optimized fabrication process.

5.4 Toward a quantum simulator in SiN platform

5.4.1 Variational Quantum Eigensolver algorithm

The field of quantum computing has witnessed rapid advancement in recent decades, transitioning from its conceptualization in the 1980s [170] to the realization of hardware proofs of principle in the 2000s [216, 217]. At the core of quantum computing lies the qubit [2], the fundamental unit of quantum information, capable of existing in a superposition of states:

$$\alpha \left|0\right\rangle + \beta \left|1\right\rangle , \tag{5.1}$$

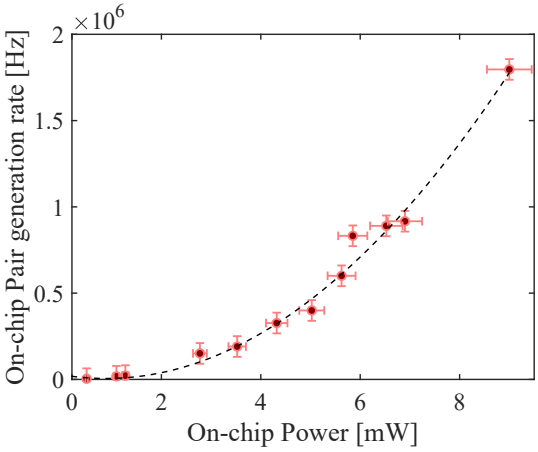

Figure 5.37: Pair generation rate on-chip considering the losses on the signal and idler lines of 20 dB respectively.

where $|\alpha|^2 + |\beta|^2 = 1$[3]. This stands in stark contrast to classical bits, which are confined to states 0 or 1. This unique property empowers quantum computers to explore vast solution spaces concurrently, offering exponential acceleration over classical algorithms for certain problems.

Although quantum technology is still in its early stages, fast advancements in quantum hardware and significant global investment have generated speculation that in the near future, Noisy-Intermediate Scale Quantum (NISQ) devices may outperform conventional computers [218]. NISQ devices represent short-term quantum computers with a restricted number of qubits and insufficient physical qubits to support robust error correction schemes. Despite their limitations, NISQ computers have exhibited superior performance compared to classical computers on specific problems tailored to their capabilities. Notably, current state-of-the-art devices typically have 50 to 100 qubits, enabling them to achieve "quantum supremacy"—outperforming the best classical supercomputer for certain mathematical tasks [180, 181]. However, the true potential of quantum computers—acceleration for practical applications, often referred to as quantum advantage—remains largely unrealized. Thus, a crucial technological challenge lies in harnessing current NISQ devices to realize quantum advantage. One promising approach is the adoption of shallow quantum circuits, comprising a modest number of quantum gates operating on a limited set of qubits.

Variational quantum algorithms (VQAs) [219–221] are examples of shallow circuits. VQAs leverage classical optimization techniques by employing parameterized quantum circuits to run on quantum computers, with parameter optimization delegated to classical optimizers. This approach not only maintains a low depth of the quantum circuit but also aids in noise mitigation. An example of a variational algorithm introduced by Peruzzo in 2014 is the Variational Quantum Eigensolver (VQE) [118, 222, 223]. Utilizing VQE entails a compromise, sacrificing the prolonged coherence times usually required for quantum phase estimation. Instead, it opts for a polynomial overhead, facilitated by iterative measurements and classical processing. The foundation of VQE lies in the Rayleigh-Ritz variational principle, which aims to optimize an upper bound for the lowest possible expectation value of an observable by using a trial wave function. This principle, when applied to a Hamiltonian $\hat{H}$ and a

[3]In appendix D, a description of the qubit, qudit, and quantum gates is reported

trial wave function $|\Psi(\vec{\theta})\rangle$, bounds the energy associated with the ground state (E_0) by [118, 224]:

$$E_0 \leq \frac{\langle\Psi(\vec{\theta})|\hat{H}|\Psi(\vec{\theta})\rangle}{\langle\Psi(\vec{\theta})|\Psi(\vec{\theta})\rangle}. \tag{5.2}$$

Here, E_0 denotes the lowest energy eigenvalue of the Hamiltonian $\hat{H}$, and $\vec{\theta}$ represents a vector of independent parameters $\vec{\theta} = (\theta_1, \ldots, \theta_n)^T$.

The core objective of VQE is to identify a parameterization of $|\Psi(\vec{\theta})\rangle$ that minimizes the expectation value of the Hamiltonian. A scheme is shown in Fig. 5.38. The

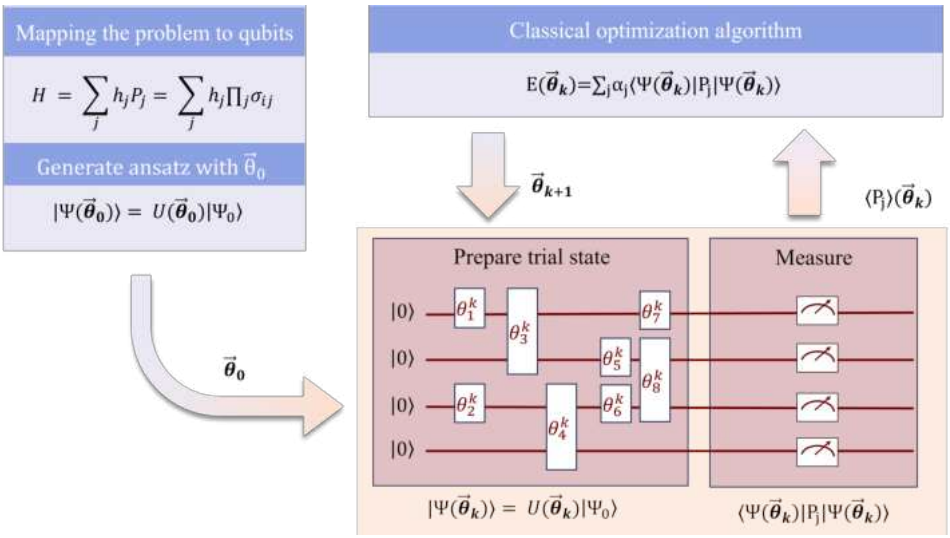

Figure 5.38: Scheme illustrating the VQE method, aiming to minimize the energy of the Hamiltonian by adjusting variational parameters θ. The process utilizes classical computing resources (depicted in blue) and quantum computing resources (depicted in red). The simulation commences with the construction of a fermionic Hamiltonian and subsequently, transformation into a qubit Hamiltonian, represented as a sum of Pauli operators. An ansatz is then selected to represent the wave function, initialized with an initial set of parameters. The trial state is prepared on a quantum computer as a quantum circuit comprising parametrized gates. The ensuing procedure iterates until the convergence criterion is met. At each iteration k, the energy of the Hamiltonian is computed by measuring every Hamiltonian term on a quantum computer and aggregating them on a classical computer. The computed energy is input into the classical algorithm, which updates parameters for the subsequent optimization step based on the chosen optimization algorithm.

ground state energy serves as a lower limit for the expectation value and ideally closely approximates it to the desired level of accuracy. Mathematically, the goal is to find an approximation to the eigenvector $|\Psi(\vec{\theta})\rangle$ of the Hermitian operator $\hat{H}$ corresponding to the lowest eigenvalue E_0.

Given the inefficiency of classical computers in preparing, storing, and measuring wave functions, quantum computers are leveraged for this task, followed by parameter updates using classical optimization algorithms. This workflow, as illustrated in Fig. 5.38, involves initializing the qubit register in the zero state.

To execute the minimization task on a quantum computer, an "ansatz" wave function is initially defined, which can be realized on a quantum device through a series of quantum gates. This wave function $|\Psi(\vec{\theta})\rangle$ is represented as the application of a generic parameterized unitary operation $U(\vec{\theta})$ to an initial state for N qubits, with $\vec{\theta}$ representing a set of parameters within the interval $(-\pi, \pi]$. This circuit generates the trial wave function:

$$|\Psi(\vec{\theta})\rangle = U(\vec{\theta})|\Psi_{\text{ref}}\rangle\,, \tag{5.3}$$

where $|\Psi_{\text{ref}}\rangle$ represents a reference state.

The term $|\Psi(\vec{\theta})\rangle$ is referred to as the "trial state", and $U(\vec{\theta})$ as the "Ansatz circuit". It's important to note that $|\Psi(\vec{\theta})\rangle$ (and any $U(\vec{\theta})$)) must be a normalized wave function. Subsequently, the VQE optimization problem is formulated as:

$$E_{\text{VQE}} = \min_{\vec{\theta}} \langle 0|U^{\dagger}(\vec{\theta})\hat{H}U(\vec{\theta})|\Psi_{\text{ref}}\rangle\,. \tag{5.4}$$

This equation, also known as the cost function of the VQE optimization problem, borrows terminology from the machine learning and optimization literature. Once the wave function is prepared, the next step is to measure the expectation value of the Hamiltonian.

In the second quantized basis set approach, chemical Hamiltonians can be represented as a linear combination of products of local Pauli operators using the Jordan-Wigner encoding [225]. This is expressed as:

$$H = \sum_j h_j P_j = \sum_j h_j \prod_i \sigma_{ji}\,. \tag{5.5}$$

Here, h_j represents a real scalar coefficient, σ_{ji} denotes one of the Pauli operators (I, X, Y, or Z)[4] acting on a specific qubit denoted by i, and j.

Using the linearity of expectation values, we can then express the energy $E(\vec{\theta}_k)$ as:

$$E(\vec{\theta}_k) = \sum_{j=1}^{N} h_j \langle \Psi(\vec{\theta}_k)| \prod_i \sigma_{ji} |\Psi(\vec{\theta}_k)\rangle\,. \tag{5.6}$$

To achieve the desired precision in determining the expectation value of each term in the Hamiltonian, the process of state preparation and measurement must be iterated multiple times. Unlike quantum phase estimation, where prolonged coherence times are necessary, the quantum computer is reset for each iteration, reducing the required coherence time. This strategy, termed the Hamiltonian averaging method for energy computation, requires a number of measurements of the order $O(1/\epsilon^2)$ to upload energies with a precision ϵ [226].

VQE in integrated Photonics

Within the EPIQUS project, VQE circuit was designed, specifically targeting four qubits. This approach is based on the entanglement of two photons across four dimensions (representing qubits), enabling the preparation of an arbitrary four-qubit fully parameterized state. The encoding method, termed path encoding, characterizes each qubit by the position of the photon within one of the four waveguides. Further details on this

[4] Here are the matrix representations of the identity and Pauli operators:
$I = \begin{pmatrix} 1 & 0 \\ 0 & 1 \end{pmatrix}$; $X = \begin{pmatrix} 0 & 1 \\ 1 & 0 \end{pmatrix}$; $Y = \begin{pmatrix} 0 & -i \\ i & 0 \end{pmatrix}$; $Z = \begin{pmatrix} 1 & 0 \\ 0 & -1 \end{pmatrix}$.

encoding are provided in Appendix D. Local measurements performed on each qubit facilitate the calculation of the expectation energy for any four-level Hamiltonian.

The integrated photonic circuit, as illustrated in Fig. 5.39(a), was conceptualized by Dr. Massimo Borghi. Before entering into details, it is important to introduce the equivalent circuit illustrated in Fig. 5.39(b). The state of a quartet of qubits, delineated

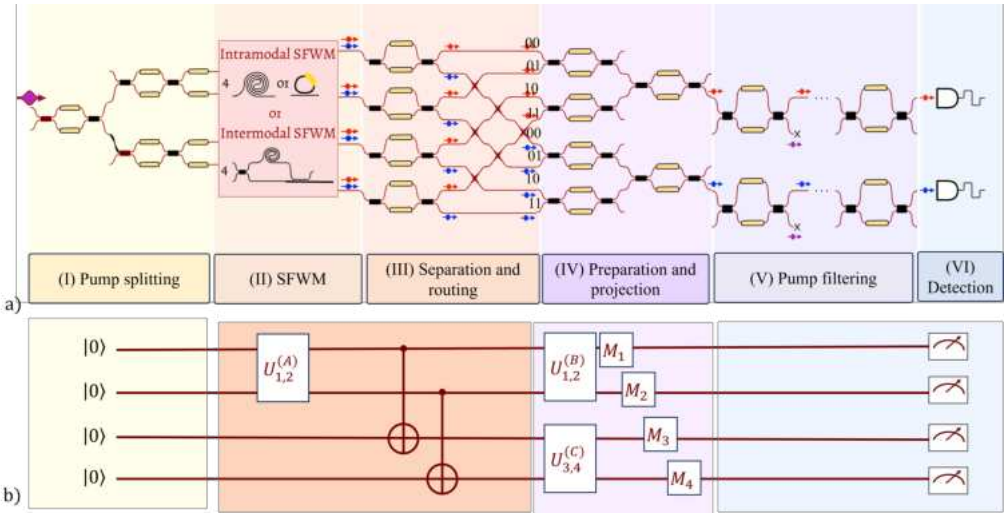

Figure 5.39: a) Implementation of the four-qubit VQE using a photonic circuit. In stage I, the pump laser is coherently divided to pump four-photon pair sources. One of the four sources emits a signal (red)/idler (blue) pair. Each photon is independently directed into one of the four waveguides of the corresponding ququart. In stage II, the generation of the biphoton state is performed. At the output of stage III, the four-qubit state is $\lambda_0|0000\rangle + \lambda_1|0101\rangle + \lambda_2|1010\rangle + \lambda_3|1111\rangle$. Stage IV completes the state preparation and measurement by applying an SU(4) operation to each ququart. In stage V, the pump filtering is reported as a series of aMZIs. The final stage, VI, performs the detection using only two SPADs. b) Equivalent circuit enabling the preparation of an arbitrary four-qubit state starting from the initial state $|0000\rangle$. The evolution from the beginning to the rightmost CNOT gate is executed through stages I, II, and III in the circuit of the panel (a).

within the computational basis, can be mathematically written as:

$$|\psi\rangle = \sum_{ijkl} f_{ijkl} \, |ijkl\rangle \ , \tag{5.7}$$

wherein the summation extends over the entire binary index permutations i, j, k, and l. The notation $|ijkl\rangle$ refers to a state of four qubits corresponding to the indices i, j, k, and l. For the sake of notational brevity, we introduce labels m and n, representing the binary index pairs i, j and k, l respectively, with both m and n spanning from 0 to 3. This reformulation permits the substitution of f_{ijkl} with f_{mn}, and correspondingly, $|ijkl\rangle$ with $|mn\rangle$, where $|mn\rangle$ denotes the canonical bipartite qubit states within the computational basis.

Upon expressing the matrix F as $F = UDV$, through its singular value decomposition—where U and V are unitary matrices of the fourth order and D is a diagonal

matrix—we can write the state as:

$$|\psi\rangle = \sum_{mnq} u_{mq} d_{qq} v_{qn} |mn\rangle \ . \tag{5.8}$$

Subsequently, we define the states $|\psi_q\rangle = \sum_m u_{mq} |m\rangle$ and $|\phi_q\rangle = \sum_n v_{qn} |n\rangle$, which culminates in the Schmidt decomposition:

$$|\psi\rangle = \sum_q \lambda_q |\psi_q\rangle |\phi_q\rangle \ , \tag{5.9}$$

where $\lambda_q = d_{qq}$. This universal scheme for state construction is described in reference [227], as illustrated in Fig. 5.39(b). A sequence of operations on the qubits is executed to actualize the target state starting from $|0000\rangle$. An SU(4) operation ($U_{1;2}^{(A)}$) is performed to obtain the transformation:

$$|0000\rangle \rightarrow (\lambda_0|00\rangle + \lambda_1|01\rangle + \lambda_2|10\rangle + \lambda_3|11\rangle)|00\rangle \ . \tag{5.10}$$

Given that the transformation is restricted to $|00\rangle$, the gate $U_{1;2}^{(A)}$ is not totally defined. It could be completed, for example, through Gram-Schmidt orthogonalization. In the second step, it is executed a pair of CNOT operations, one on qubits (1; 3) and the other on qubits (2; 4), thereby duplicating the states of the previous qubits onto the subsequent pair, yielding:

$$\lambda_1|0000\rangle + \lambda_2|0101\rangle + \lambda_3|1010\rangle + \lambda_4|1111\rangle \ . \tag{5.11}$$

Finally, it is used an SU(4) gate $U_{1;2}^{(B)}$ to qubits (1; 2) to effectuate the basis transformation $|00\rangle \rightarrow |\psi_0'\rangle$, $|01\rangle \rightarrow |\psi_1'\rangle$, $|10\rangle \rightarrow |\psi_2'\rangle$, and $|11\rangle \rightarrow |\psi_3'\rangle$. Concurrently, we apply a unitary operation $U_{3;4}^{(C)}$ to qubits (3; 4) to tranform $|00\rangle \rightarrow |\phi'{}_0\rangle$, $|01\rangle \rightarrow |\phi'{}_1\rangle$, $|10\rangle \rightarrow |\phi'{}_2\rangle$, and $|11\rangle \rightarrow |\phi'{}_3\rangle$. The resultant sets $|\psi_i'\rangle$ and $|\phi'{}_i\rangle$ are individually orthogonal, due to the unitary nature of $U_{1;2}^{(B)}$ and $U_{3;4}^{(C)}$.

The equivalent integrated photonic scheme is reported in Fig. 5.39(a) and can be divided into five distinct sections, enumerated by Roman numerals I through VI.

Section I comprises a triangular arrangement of three MZIs to coherently divide the pump laser and, thus, excite four integrated sources located in Section II. Here, the four sources can generate either through intermodal sFWM or intramodal processes. Notably, for the implementation of the VQE, purity is not a critical factor; rather, a high degree of indistinguishability among the four sources is needed. Consequently, waveguide spirals are favored over microrings.

Through the MZI network in Section I, adjustments in amplitudes and phases among photons emitted from distinct sources can be made. Operating within a regime where only one source emits a pair, post-selection is achieved by performing a coincidence measurement between any of the signal and idler modes.

Section III contains the routing stage, where the generated photons if produced through an intramodal process, are separated. For photons generated via the intermodal process, separation is achieved by the ADC located at the source's end. Subsequently, photons from the signal and idler are directed into four waveguides via a network of crossing, thereby creating two entangled ququarts. The first quartet is designated qubits (1, 2), while the second quartet is assigned qubits (3, 4). Here we obtain the same state described in eq. (5.11).

In Section IV, arbitrary SU(4) operations are applied to each ququart, which are performed through a square mesh of MZIs formed by thermal phase shifters. These operations enable arbitrary operations between the qubit pairs (1, 2) and (3, 4). The sequential execution of Sections I through IV collectively enables the synthesis of an arbitrary four-qubit state[5]. This section allows for the simultaneous preparation and measurement of the state.

In section V pump photons are removed through a sequence of aMIZs. In Section VI the detection is performed.

Fig. 5.40 depicts two implemented layouts, showcasing the outlined scheme in (a), alongside Perruzzo's original VQE scheme in (b) (red rectangle). Dr. Alessio Baldazzi and I designed these layouts, with a selection of spiral waveguides as the primary sources. The six distinct sections of the VQE are indicated by colored contours. In

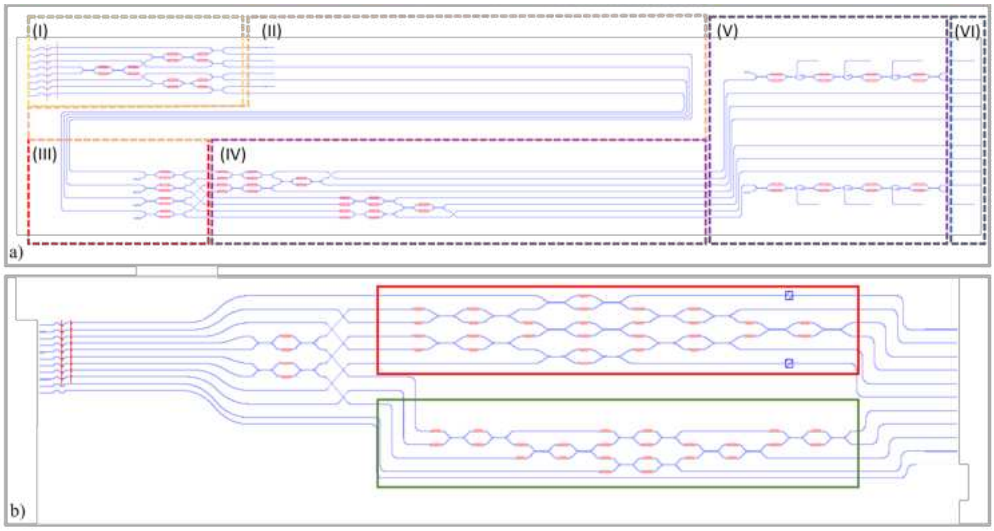

Figure 5.40: a) Design of the VQE as shown in Fig. 5.39. b) Proposed design of Peruzzo's VQE with the inclusion of two MZIs to expand the possibilities of quantum applications.

Fig. 5.40(b), Perruzzo's scheme is presented as a Clements scheme[6] improved by two auxiliary MZIs. This configuration serves as a versatile network capable of facilitating Bell state preparation.

Additionally, the green part illustrates Reck's scheme, which, together with Clements' scheme enclosed in the red box, has other applications such as boson sampling [228]. Further discussion of this topic will be provided in the next section. These configurations are designed without the integrated sources. In this case, one has to use an external SPDC source.

5.4.2 Boson sampling

One problem where quantum supremacy has been demonstrated is the Boson sampling problem. Scott Aaronson and Alex Arkhipov (AA) in 2011 introduced a problem known as boson sampling (BS) [228]. They argued that classical computers are incapable of accurately simulating the behavior of a linear passive optical system with Fock

[5]Details regarding the representation of qudit can be found in Appendix D.
[6]In the App.D the Clements and the Reck schemes are reported.

state inputs. In particular, predicting the results of sampling the output distribution of indistinguishable bosons undergoing interference on a randomly chosen linear network involves an exponential overhead in terms of time or resources. This problem is associated with the difficult #P-hard complexity class problem of evaluating the permanents of matrices with complex elements, making it unsolvable for classical computers. Photonic systems, with their integrated sources, linear propagation and detectors, offer promising platforms for its implementation. As AA themselves stated "it is like watching a dolphin in its natural habitat then we might see it displays equal intelligence with no special training at all"[228].

In response to theoretical advancements, significant experiments have been undertaken to conduct increasingly large boson sampling experiments [181, 192, 229, 230]. This has spurred a competitive race to achieve quantum advantage in photonic platforms, where the experiment surpasses classical computers. In the context of the EPIQUS project, the decision was made to implement boson sampling in the monolithic SiN platform.

Let's focus on how BS operates [231]. It is possible to develop two types of BS: the Scattershot BS [229], and the Gaussian BS [117]. Let us consider the case of the Scattershot BS (SBS). Imagine a set of m modes characterized by creation operators $a_i^\dagger$, where $i = 1, \ldots, m$, complying with bosonic commutation relations. A Fock state representing n photons spread across these modes, is denoted as:

$$|S\rangle = |s_1 s_2 \ldots s_m\rangle = \prod_{i=1}^{m} \frac{(a_i^\dagger)^{s_i}}{\sqrt{s_i!}} |0\rangle \,, \tag{5.12}$$

where s_i are non-negative integers indicating photon counts in each mode, and $\sum_i s_i = n$. When $s_i \leq 1$ for all i, the state indicates a scenario without photon collisions, which means that no mode has more than one photon.

Now, let's consider a linear-optical mode transformation U in $SU(m)$, also known as a linear interferometer. The input state undergoes evolution through a passive linear optical network, which applies a unitary transformation to the creation operators as follows:

$$\hat{U} \hat{a}_i^\dagger \hat{U}^\dagger = \sum_{j=1}^{m} U_{ij} \hat{a}_j^\dagger \,, \tag{5.13}$$

where $\hat{U}$ represents a unitary matrix describing the linear optics network. Consequently, the transition probability from an input state $|S\rangle = |s_1 s_2 \ldots s_m\rangle$ to an output state $|T\rangle = |t_1 t_2 \ldots t_m\rangle$ is given by:

$$P[S \to T] = \frac{|\mathrm{Perm}(U_{S,T})|^2}{\sqrt{s_1! \ldots s_m! t_1! \ldots t_m!}} \,, \tag{5.14}$$

where Perm is the permanent, $U_{S,T}$ is an $n \times n$ submatrix of U, built by replicating the i-th row of U t_i times and the j-th column of U s_j times.

If we consider a scenario where we insert a photon into each input, then the probability of finding a photon in each output is equal to Perm^2. A fascinating example of this is the HOM interference, where we can observe that the Perm(MMI matrix) = 0.

Due to the complexity of computing the permanent, this transition probability shows the computational challenge associated with a specific class of linear optical experiments. Specifically, the permanent is #P-hard, and the best-known classical algorithm for its computation requires exponential time.

The Boson Sampling system involves preparing an input state with n photons distributed across m modes, followed by a multimode interferometer described by a random unitary operator U. Photon detectors are then employed to measure the output states. The system does not compute the determinant of the matrix each time; rather, it leverages interference among photons within it to obtain their probability distribution at the output. Typically, the number of modes, m, scales as n^2 to prevent outputs with more than one photon.

Boson sampling in integrated photonics

The implementation of BS according to the approach outlined by AA involves three fundamental steps:

- **Input Preparation**: This step involves the initialization of the input states, which can include vacuum states and single-photon Fock states.
- **Evolution**: The initialized states undergo evolution through a passive linear interferometer, which implements a unitary transformation on the creation operators of the photons.
- **Measurement**: The output states resulting from the evolution process are then measured using on-off photodetectors to record the photon counts in each output mode.

Within the EPIQUS project, these three steps can be seamlessly executed on a monolithic SiN platform. Specifically, heralded single photons can be generated through the non-degenerate sFWM process, with the flexibility to use intermodal and intramodal sources interchangeably. The implementation of interferometric networks involves an ensemble of MZIs, while the detection stage utilizes integrated Si-SPADs. Let us divide the developed scheme of the PIC into five distinct parts, as depicted in Fig. 5.41. The

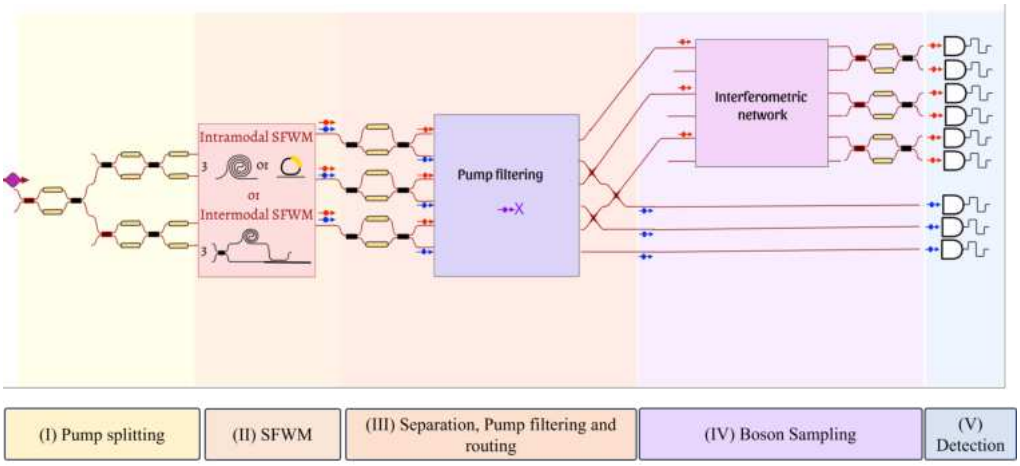

Figure 5.41: Circuit sketch illustrating the implementation of a scattering boson sampler. The circuit is divided into five parts. Part I: the injection of the pump into the sources. In Part II: the sFWM process. Part III: the separation of the generated photons by an aMZI, followed by a cascade of aMZIs to remove the residual pump. In Part IV, the network of 6×6 matrix of MZIs is present in the signal branch to perform the SBS. Part V: the detection process.

initial three blocks of the process are similar to the ones described in VQE, where multiple integrated sources can be excited. In this case, we consider 3 integrated sources.

In block IV, the idler and signal photons follow separate paths, which characterizes the SBS approach. In SBS, idler photons traverse their designated waveguides and are subsequently detected, while signal photons enter the interferometric 6×6 system.

The interferometric system, comprising an ensemble of MZIs, is configured based on either the Reck or Clements scheme, with an additional phase element. Details of these schemes are provided in Appendix D. At the output of this system, photons are detected by integrated Si-SPADs, and their measurements are synchronized with the detection of idler photons to establish coincidences.

In collaboration with Dr. Alessio Baldazzi, several layouts for SBS were developed. Fig. 5.42 illustrates one of these layouts, featuring three spiral sources followed by a photon generation separation and pump filtration process. Notably, this layout demonstrates how signal photons are directed to specific inputs of an interferometer system configured in the Reck scheme (block IV), while idler photons are directed towards readout on integrated Si-SPADs in block V.

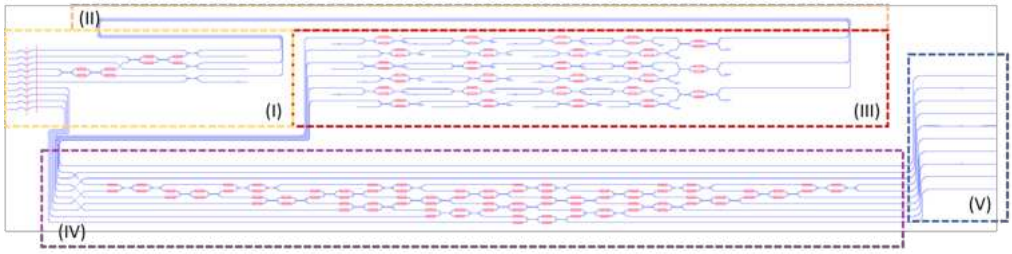

Figure 5.42: Layout of the SBS system. The blocks correspond to the blocks shown in Fig. 5.41.

In addition, different Reck and Clements 4×4 (Fig. 5.40(b)) and 7×7 (Fig. 5.43(a)-(b)) configurations were designed. These configurations were intended for use with an external SPDC source. It is worth mentioning that in the case of the interferometric system configured in a 7×7 Clements configuration (Fig. 5.43(a)), additional MZIs were incorporated. This simplifies the characterization of the interferometric system and enables the ensemble to be utilized for diverse applications, such as the implementation of probabilistic Controlled-NOT (CNOT) gates [232].

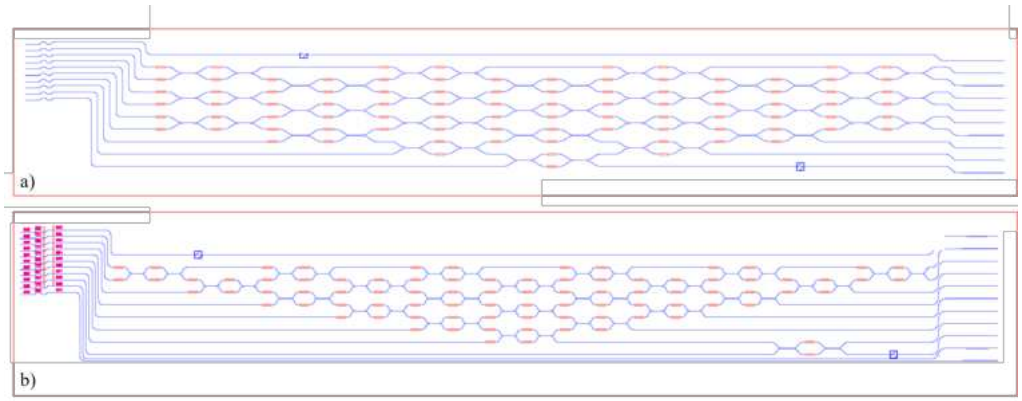

Figure 5.43: Integrated photonic design of MZIs network in Clements configuration (a) and Reck configuration (b). In (a), an additional MZI is inserted to perform CNOT operation. In blue, the waveguides, and in orange, the phase shifters.

5.4.3 Challenges and issues of the integrated platform

It is useful to introduce some aspects regarding the minimum specifications for realizing an integrated simulator. These specifications are closely related to the type of application (Boson sampling or VQE), configuration (Reck or Clements), and circuit depth. Different types of non-ideality affect the scalability of the PIC: error setting in phase shifters, the unbalance of the MMIs, the insertion loss of the different devices, and the coupling and propagation losses. In our case, the last two parameters constrain the scalability of the quantum simulator. Therefore, significant efforts are being made in the fabrication process to reduce them.
Regarding fidelity, the type of PIC configuration has a strong impact on it. Unbalanced losses, i.e., different paths through the interferometer suffer different losses, bring to poor fidelity in the desired operation. In the Clements configuration, this issue is mitigated because of the uniform structure among all the paths. Another important aspect concerns the rejection of integrated filters useful for residual pump removal [233]. Initial estimations suggest that 6-8 aMZIs need to be inserted in the cascade to achieve active filtering of about 120-150 dB.

5.5 Conclusions and future prospectives

This chapter presents my contribution to the European project EPIQUS, which aims to develop a fully integrated QS in a photonics platform with quantum light generation, manipulation, and detection. Through an investigation of two materials, SiON and SiN, in their linear and nonlinear regimes, SiN emerged as the preferred material for implementation in the VIS-NIR region. Numerous components were designated and tested within this platform, demonstrating their high performance.

Chapter 6

Swap test algorithm on a linear Photonic integrated Circuit

6.1 Quantum machine learning

Quantum Machine Learning (QML) [234–237] is an emerging interdisciplinary field that merges QC [238, 239] with Machine Learning (ML) [240, 241]. The primary goal of QML is to exploit quantum mechanical principles to devise more efficient algorithms for various ML tasks [242–244].

Among the different ML models, there are the Support Vector Machines (SVMs) [236, 245]. SVMs are well-known for their ability to cluster data, and they share conceptual similarities with quantum wave functions. As supervised learning models, SVMs demonstrate robustness in categorizing data clusters.[246].

Central to SVM functionality is the kernel function [247, 248], pivotal for quantifying dissimilarities between datasets in feature spaces. SVMs excel at classifying data clusters by assigning elements of the dataset to specific categories based on property definitions in a feature space, with kernel functions evaluating the distances between data points. The efficacy of SVM training and classification depends on the quality of these kernel functions, often expressed as scalar products [249, 250]. However, constructing kernel functions requires non-linear computational complexity, particularly challenging for classical computing systems, especially with large datasets.

On this front, speed-up can be achieved through quantum algorithms. Leveraging the large configuration spaces inherent in quantum systems, these algorithms hold promise for accelerating computations when executed on quantum hardware. The hybrid architecture seeks to integrate quantum-enhanced SVMs, thereby enhancing efficiency and providing input for the machine learning program.

The swap test [251] stands out as a quantum algorithm capable of computing the scalar product of two arbitrary quantum states by sampling an auxiliary qubit. Leveraging qubit encoding, this test offers the potential to accelerate the estimation of kernel function entries. Traditional classification algorithms for purely classical machines exhibit a scaling behavior of $O(\log(\epsilon^{-1})\text{poly}(M,N))$, where N represents the feature space dimension, M denotes the number of training data points, and ϵ signifies the desired accuracy [252]. Specifically, computing each kernel entry requires a time complexity of $O(\log(\epsilon^{-1})N)$, and this operation must be repeated $M(M-1)/2$ times. However, leveraging hybrid classical-quantum hardware and employing qubit-based encoding along with the implementation of the swap test, the linear scaling with N can be reduced to a logarithmic one, achieving a complexity of $O(\log(N)\epsilon^{-2})$ [253].

Present implementations of the swap test (SWT) have predominantly utilized superconducting qubits and trapped ions [254, 255]. These realizations often involve a higher number of gates and qubits compared to the gate-based representation proposed in previous works [254].

Quantum optics is a promising approach for implementing swap tests, although it currently exists only as a theoretical proposal [256]. Key among the challenges in the photonic platform is the realization of controlled-SWAP (CSWAP) or Fredkin gates [257]. Theoretical propositions and experimental demonstrations of CSWAP gates have explored diverse strategies including linear optics with probabilistic methodologies [258–260], cross-Kerr nonlinearities [261, 262], entangled photon pair sources [263–265], continuous variable versions with compressed two-mode states [266], single photons coupled with quantum dots in single-sided cavities [267], and combinations of coherent states, threshold photon detectors, and classical post-processing [268, 269]. Notably, innovative approaches encode three qubits within a single photon, exploiting its polarization state and orbital angular momentum [270]. It should be noted that this encoding is not scalable and results in a number of modes that increases exponentially with the number of qubits.

In this chapter, we explore an alternative photon-integrated circuit implemented on the SiN platform. The primary objective is to perform the swap test at room temperature. We achieve this by employing path encoding, which translates the presence of photons within specific waveguides to corresponding qubits. We present a proof-of-concept approach for the two-qubit swap test algorithm using only linear optical components—such as MMIs, waveguide crossings, and thermal phase shifters. We used photons from a weak coherent state (WCS) generated by an attenuated laser to validate our system. Detailed information about WCS can be found in Section 1.1.4.

6.2 Swap test algorithm

The estimation of the superposition of unknown quantum states constitutes a cornerstone in quantum information processing, serving as a fundamental primitive with broad applicability across diverse domains. These applications include quantum fingerprinting [271, 272], entanglement estimation [273], quantum information [274, 275], and quantum machine learning [246, 276]. In the majority of applications, the estimation of the overlap between quantum states is achieved through the use of the SWT [251]. Fig. 6.1 shows the gate notation of the SWT. The initial configuration of the circuit

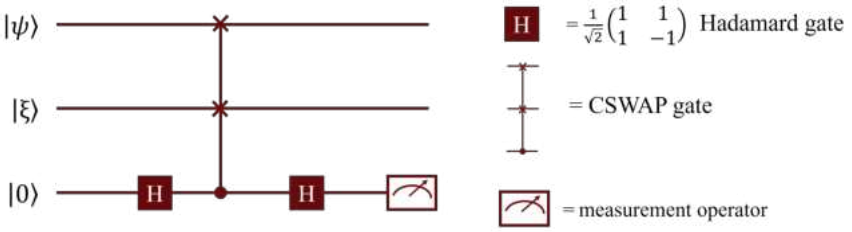

Figure 6.1: Gate representation of the swap test algorithm.

is characterized by the tensor product of three states:

$$|\psi\rangle \otimes |\xi\rangle \otimes |0\rangle \,. \tag{6.1}$$

Here, $|\psi\rangle$ and $|\xi\rangle$ represent the quantum states of interest, while $|0\rangle$ denotes the initial state of the ancillary qubit, also known as the ancilla.

Subsequently, the circuit initializes the two qubits $|\psi\rangle$ and $|\xi\rangle$ alongside the ancillary qubit $|0\rangle$. A Hadamard gate (H) is then applied to the ancillary qubit, inducing a superposition of $|0\rangle$ and $|1\rangle$. The resulting state is expressed as:

$$\frac{1}{\sqrt{2}}(|\psi\rangle \otimes |\xi\rangle \otimes |0\rangle + |\psi\rangle \otimes |\xi\rangle \otimes |1\rangle)\,. \tag{6.2}$$

Following this, a controlled-swap gate (CSWAP) is applied to the composite state, employing the ancillary qubit as the control qubit. The CSWAP operation swaps the states of the target qubits ($|\psi\rangle$ and $|\xi\rangle$) if the ancillary qubit is in the state $|1\rangle$. Consequently, the resulting state becomes:

$$\frac{1}{\sqrt{2}}(|\psi\rangle \otimes |\xi\rangle \otimes |0\rangle + |\xi\rangle \otimes |\psi\rangle \otimes |1\rangle)\,. \tag{6.3}$$

Subsequent to the CSWAP operation, another Hadamard gate (H) is applied to the ancillary qubit, resulting in the following state:

$$\frac{1}{2}(|\psi\rangle \otimes |\xi\rangle + |\xi\rangle \otimes |\psi\rangle) \otimes |0\rangle + \frac{1}{2}(|\psi\rangle \otimes |\xi\rangle - |\xi\rangle \otimes |\psi\rangle) \otimes |1\rangle\,. \tag{6.4}$$

Finally, a measurement is performed on the ancillary qubit, yielding the outcome probabilities $\mathbb{P}(0)$ and $\mathbb{P}(1)$, which are directly related to the scalar product of the two unknown states, as expressed by:

$$\mathbb{P}(0) = \frac{1}{2}(1 + |\langle\psi|\xi\rangle|^2) \quad \text{and} \quad \mathbb{P}(1) = \frac{1}{2}(1 - |\langle\psi|\xi\rangle|^2)\,. \tag{6.5}$$

These relationships can be readily inverted. Specifically, we can express the scalar product $|\langle\psi|\xi\rangle|^2$ in terms of the measured probabilities $\mathbb{P}(0)$ and $\mathbb{P}(1)$ as follows:

$$|\langle\psi|\xi\rangle|^2 = 2\,\mathbb{P}(0) - 1 = 1 - 2\,\mathbb{P}(1)\,. \tag{6.6}$$

These relationships show that the scalar product calculation can be turned into a sampling problem, with the statistics of the auxiliary qubit outcomes evaluating the qubit overlap. Notably, the swap test algorithm is often characterized as non-destructive, as the measurement is confined solely to the ancilla, allowing for continued use of the remaining qubits for subsequent operations. Consider equations (6.5), if the two qubit states $|\psi\rangle$ and $|\xi\rangle$ are equal i.e., $|\langle\psi|\xi\rangle|^2 = 1$, the auxiliary qubit has a zero probability of being in the state $|1\rangle$ and a certainty of being in the state $|0\rangle$. Conversely, if the two qubits are orthogonal, i.e., $|\langle\psi|\xi\rangle|^2 = 0$, the auxiliary qubit has an equal chance of being in either the $|0\rangle$ or $|1\rangle$ state. Intermediate scenarios lie between these extremes: as evident from equations (6.5)-(6.6), in all cases, it holds that $0.5 \leq \mathbb{P}(0) \leq 1$ and $0 \leq \mathbb{P}(1) \leq 0.5$.

As previously introduced, one application of the SWT is in implementing a quantum fingerprinting routine. Suppose two users, *Alice* and *Bob*, possess secret keys x and y, respectively, and wish to compare them. They can transmit their keys to a trusted node, which, utilizing the swap test circuit, can quantify the similarity between the keys. This approach significantly reduces the encoding length for the equality problem, where the objective is to determine:

$$f(x,y) = \begin{cases} 1 & \text{if } x = y \\ 0 & \text{if } x \neq y \end{cases}\,. \tag{6.7}$$

This problem, which typically requires exponentially longer encoding in classical scenarios, benefits from the use of qubits, where only $O(\log n)$ qubits are needed if both users possess n bits. The solution can be achieved with a probability dependent on the number of quantum hardware cycles.

The number of samples required to achieve an error η in the evaluation of the overlap with a probability $\mathbb{P}(0) = 1 - \delta$ scales as $O\left((1-\delta)\delta\,\eta^{-2}\right)$ [252, 253]. This scaling relation provides insight into the trade-off between the precision of the overlap evaluation and the number of samples needed to achieve it.

The swap test can be transformed into the SWITCH-test [277], aimed at discriminating between two quantum evolutions U_1 and U_2. This involves setting the two unknown qubits $|\psi\rangle$ and $|\xi\rangle$ to $U_1|\chi\rangle$ and $U_2|\chi\rangle$, respectively, where $|\chi\rangle$ is a reference state. The resulting algorithm yields:

$$\mathbb{P}(0) = \frac{1}{2}\left(1 + |\langle\chi|U_1^\dagger U_2|\chi\rangle|^2\right), \tag{6.8}$$

$$\mathbb{P}(1) = \frac{1}{2}\left(1 - |\langle\chi|U_1^\dagger U_2|\chi\rangle|^2\right). \tag{6.9}$$

Thus, the sampling outcomes provide insights into the proximity between the transformations U_1 and U_2. However, if our objective extends beyond mere discrimination criteria to include detailed knowledge of a specific transformation, quantum Hamiltonian learning, as proposed in [278, 279] and implemented in [280], allows for the estimation of salient Hamiltonian parameters.

Entangled state

The discussion outlined above applies specifically when the two qubits are prepared in the separable state $|\psi\rangle \otimes |\xi\rangle$. Now, let's consider the scenario where a generic entangled state is prepared in the first two entries of the circuit. In the computational basis, this can be expressed as:

$$\left(A_{00}|00\rangle + A_{01}|01\rangle + A_{10}|10\rangle + A_{11}|11\rangle\right) \otimes |0\rangle, \tag{6.10}$$

where $|A_{00}|^2 + |A_{01}|^2 + |A_{10}|^2 + |A_{11}|^2 = 1$. Again, the third qubit serves as the ancilla, initialized in the state $|0\rangle$.

Applying the swap test circuit to this entangled state yields the following output:

$$\begin{aligned}&\left[A_{00}|00\rangle + \frac{A_{01}+A_{10}}{2}\left(|01\rangle + |10\rangle\right) + A_{11}|11\rangle\right] \otimes |0\rangle \\ &+ \frac{A_{01}-A_{10}}{2}\left(|01\rangle - |10\rangle\right) \otimes |1\rangle.\end{aligned} \tag{6.11}$$

In this case, the probabilities are given by:

$$\mathbb{P}(0) = |A_{00}|^2 + |A_{11}|^2 + \frac{1}{2}|A_{01} + A_{10}|^2, \tag{6.12}$$

and

$$\mathbb{P}(1) = \frac{1}{2}|A_{01} - A_{10}|^2. \tag{6.13}$$

This result illustrates that in the presence of entanglement, $\mathbb{P}(1)$ can exceed 0.5, which is impossible when the two unknown qubits are in a separable state. For instance, choosing $A_{00} = A_{11} = 0$ and $A_{01} = -A_{10} = \frac{1}{\sqrt{2}}$ results in $\mathbb{P}(0) = 0$ and $\mathbb{P}(1) = 1$,

corresponding to the Bell state $\frac{1}{\sqrt{2}}(|01\rangle - |10\rangle)$. Other Bell states yield $\mathbb{P}(0) = 1$ and $\mathbb{P}(1) = 0$, as the overall state remains unchanged after the CSWAP gate.

This condition provides a sufficient criterion for identifying entanglement: if the swap test algorithm yields an outcome with $\mathbb{P}(1) > 0.5$, the state is entangled. However, it is not a necessary condition, as an entangled state can still yield $\mathbb{P}(1) \leq 0.5$.

An interpretation of this result can be offered by considering the states $|\pm\rangle \equiv \frac{1}{\sqrt{2}}(|0\rangle \pm |1\rangle)$ and observing that the two two-qubit states:

$$|+\rangle \otimes |\pm\rangle = \frac{1}{2}\{|00\rangle \pm |01\rangle + |10\rangle \pm |11\rangle\} \tag{6.14}$$

have overlap equal to one and zero, or equivalently, they result in $\mathbb{P}(1) = 0$ and $\mathbb{P}(1) = 0.5$, respectively. By applying a post-selection procedure, focusing only on cases where the two qubits are equal or different in the computational basis (i.e., they have the same or opposite parity), we can isolate events corresponding to Bell states. The same-parity condition selects $\frac{1}{\sqrt{2}}(|00\rangle \pm |11\rangle)$, while the opposite-parity condition selects $\frac{1}{\sqrt{2}}(|01\rangle \pm |10\rangle)$. For initial states $|+\rangle \otimes |\pm\rangle$, the conditional probability of the ancilla being in the state $|1\rangle$, given the same or opposite parity, remains zero after the swap test. When the initial state is $|+\rangle \otimes |-\rangle$, the conditional probability remains zero even if the two qubits are orthogonal because the events contributing to $\mathbb{P}(1)$ do not satisfy the chosen parity condition. However, for the initial state $|+\rangle \otimes |-\rangle$ and the opposite-parity condition, the conditional probability increases to 100%, as events where the ancilla outcome is different from one are neglected, and normalization is performed with respect to the opposite-parity event probability[1].

6.3 The swap test in a Photonic integrated circuit

6.3.1 Analytical description

We undertake a direct translation of the gates depicted in the standard schematic illustrated in Fig. 6.1 into the corresponding photonic operations, as depicted in Fig. 6.2(a). Subsequently, Fig. 6.2(b) presents a schematic of the PIC, respectively. The design of the PIC is also performed by the contribution of Dr. Nicolo Leone and Dr. Alessio Baldazzi. They additionally contributed to the experimental measurements. Before delving into the individual blocks, it is useful to introduce the type of encoding utilized to define the qubits.

Path encoding

To encode states within the PIC, we adopt a method employing path-encoded single photons, where the state is determined by the waveguide through which a single photon travels [19, 281, 282]. This qu*d*it representation is described in the App. D.

In our proof-of-concept experiment, we utilize photons from WCS to prepare the two qubits $|\psi\rangle$ and $|\xi\rangle$ as inputs for the swap test, with one qubit set to $|0\rangle$ for the ancilla. Hence, eight paths, i.e., 2^3, are necessary. The encoding is achieved by simply

[1] More rigorously, if we define A as the event when the ancilla is in the state $|1\rangle$ and B/C as the event when the two qubits have the same/opposite parity, the conditional probabilities $\mathbb{P}(A|B)$ and $\mathbb{P}(A|C)$ are defined by the ratio of $\mathbb{P}(A \cap B)/\mathbb{P}(B)$ and $\mathbb{P}(A \cap C)/\mathbb{P}(C)$ respectively. $\mathbb{P}(A \cap B) = 0$ for the initial states $|+\rangle \otimes |\pm\rangle$ and $\mathbb{P}(A \cap C) = 0$ only for $|+\rangle \otimes |+\rangle$. For the state $|+\rangle \otimes |-\rangle$, $\mathbb{P}(A|C)$ is 100% since $\mathbb{P}(A \cap C) = 0.5$ and $\mathbb{P}(C) = 0.5$.

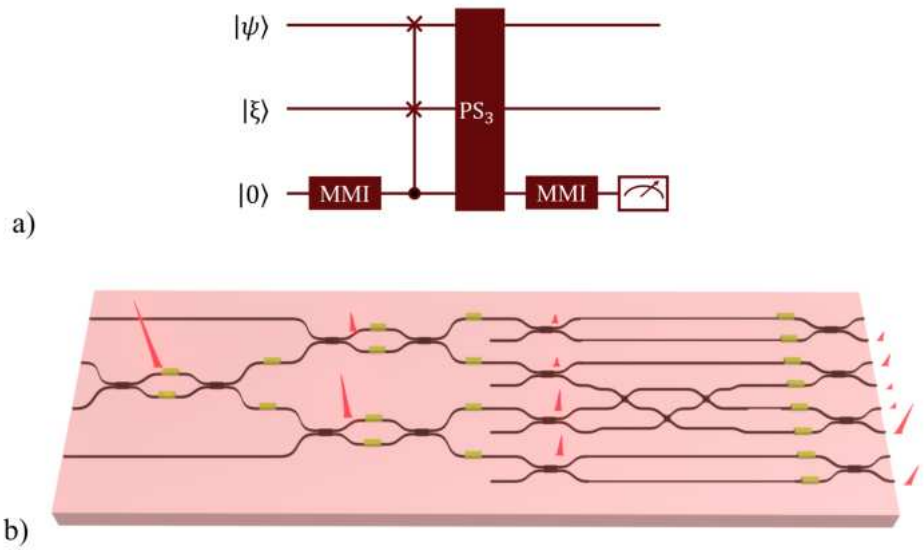

Figure 6.2: a) Gate Representation of our Linear Photonic Swap Test Circuit. In our linear photonic swap test circuit, the Hadamard (H) gate is realized using MMIs, while the PS_3 gate symbolizes the phase shifters necessary to equalize the optical paths. b) Schematic representation of the swap test PIC. In dark red the waveguides, in gold the thermal-phase shifter and in pink the cladding. The red pulses represent the photon statistics inside the platform.

representing the waveguide number and converting it to binary numbers:

$$\begin{aligned}
|0\rangle &\to |000\rangle \equiv |0\rangle \otimes |0\rangle \otimes |0\rangle\,, & |1\rangle &\to |001\rangle \equiv |0\rangle \otimes |0\rangle \otimes |1\rangle\,,\\
|2\rangle &\to |010\rangle \equiv |0\rangle \otimes |1\rangle \otimes |0\rangle\,, & |3\rangle &\to |011\rangle \equiv |0\rangle \otimes |1\rangle \otimes |1\rangle\,,\\
|4\rangle &\to |100\rangle \equiv |1\rangle \otimes |0\rangle \otimes |0\rangle\,, & |5\rangle &\to |101\rangle \equiv |1\rangle \otimes |0\rangle \otimes |1\rangle\,,\\
|6\rangle &\to |110\rangle \equiv |1\rangle \otimes |1\rangle \otimes |0\rangle\,, & |7\rangle &\to |111\rangle \equiv |1\rangle \otimes |1\rangle \otimes |1\rangle\,,
\end{aligned} \tag{6.15}$$

where the state on the left-hand side of the arrow represents the qudit state, while the first two positions on the right-hand side refer to the qubits, whose scalar product is of interest, and the third position refers to the ancilla. Thus, when a photon is in the top waveguide, or equivalently, the qudit is in the state $|0\rangle$, the corresponding prepared three-qubit state is $|000\rangle$. This principle extends to the remaining states.

Preparation Stage

The PIC comprises two primary stages. To simplify the Fig. 6.2(b) is split into this two parts: the preparation stage (Fig. 6.3) and the swap test stage (Fig. 6.4), corresponding to the setup of the state $|\psi\rangle \otimes |\xi\rangle$ and the execution of the swap test algorithm, respectively.

Fig. 6.3 the preparation stage is illustrated. This stage has three Mach-Zehnder interferometers (MZI) and six phase shifters (PS). Each MZI consists of two sequential blocks, each comprising a balanced MMI followed by phase shifters on each waveguide. As expressed in eq. (2.25), the transfer matrix $U_{MZI}(\theta)$ associated with the MZI is given by:

$$U_{\mathrm{MZI}}(\boldsymbol{\theta}) \equiv U_{\mathrm{MMI}} \cdot U_{\mathrm{PS}}(2\,\boldsymbol{\theta}) \cdot U_{\mathrm{MMI}} = \mathrm{i}\,\mathrm{e}^{-\mathrm{i}(\theta(1)+\theta(2))} \begin{pmatrix} \sin\Delta\theta & \cos\Delta\theta \\ \cos\Delta\theta & -\sin\Delta\theta \end{pmatrix}, \tag{6.16}$$

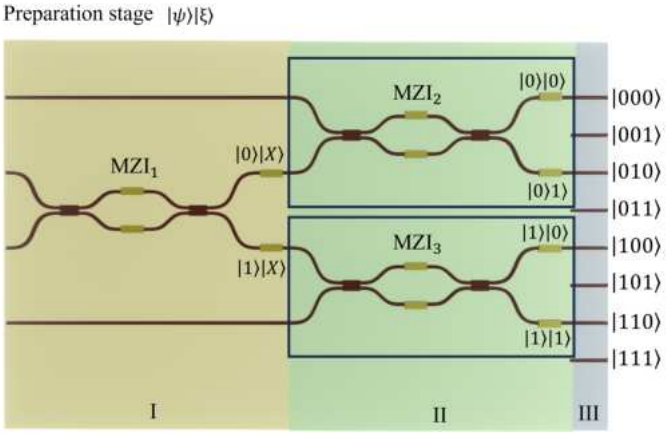

Figure 6.3: Scheme for the preparation stage circuitry for the two quantum states $|\psi\rangle$ and $|\xi\rangle$. Block I (yellow) includes one MZI and two thermal phase shifters dedicated to the identification of the first state $|\psi\rangle$. Block II (green) encompasses the circuitry for the second state $|\xi\rangle$, comprising two MZIs and the corresponding phase shifters. Block III (grey) features the incorporation of four additional waveguides to facilitate the generation of various configurations of input states, including the ancillary qubit.

where $\Delta\theta = \theta_1 - \theta_2$. Here, the top and bottom positions or states $|0\rangle$ and $|1\rangle$ are respectively represented by the vectors $\begin{pmatrix}1 & 0\end{pmatrix}^T$ and $\begin{pmatrix}0 & 1\end{pmatrix}^T$.

For ease of description, I divide the preparation stage into 3 different blocks. The first MZI and two PSs in block I establish the state of the first qubit by applying the phases $(\Delta\theta_1, \Delta\phi_1)$. Subsequently, in block II, the second and third MZIs along with the last four PSs (MZI_2, MZI_3, and PS_2 in the two rectangular regions) prepare the second qubit by setting the phases $(\Delta\theta_2, \Delta\phi_2)$.

Starting from the initial state $|0\rangle$ and applying the transformation defined as

$$U_{rot}(\boldsymbol{\theta}, \boldsymbol{\phi}) \equiv U_{PS}(\boldsymbol{\phi}) \cdot U_{MZI}(\boldsymbol{\theta}), \tag{6.17}$$

any point in the Bloch sphere associated with the single qubit can be reached. These transformations can be incorporated into the qubit structure, leading to the matrix representation of an MZI followed by PS operating on the k-th and $(k+1)$-th waveguides:

$$U^{(k)}_{\text{rot}}(\boldsymbol{\theta}, \boldsymbol{\phi}) \equiv \begin{pmatrix} 1 & 0 & \dots & \dots & \dots & 0 \\ 0 & \ddots & & & & \vdots \\ \vdots & & (U_{\text{rot}})_{11} & (U_{\text{rot}})_{12} & & \vdots \\ \vdots & & (U_{\text{rot}})_{21} & (U_{\text{rot}})_{22} & & \vdots \\ \vdots & & & & \ddots & 0 \\ 0 & \dots & \dots & \dots & 0 & 1 \end{pmatrix}, \tag{6.18}$$

Here, the entries of the matrix U_{rot} are determined by eq. (6.17), and the mapping from Dirac notation to vector notation, e.g., in the qu-quart case, is given by:

$$\begin{aligned} |00\rangle &\iff \begin{pmatrix}1 & 0 & 0 & 0\end{pmatrix}^T, \\ |01\rangle &\iff \begin{pmatrix}0 & 1 & 0 & 0\end{pmatrix}^T, \\ |10\rangle &\iff \begin{pmatrix}0 & 0 & 1 & 0\end{pmatrix}^T, \\ |11\rangle &\iff \begin{pmatrix}0 & 0 & 0 & 1\end{pmatrix}^T. \end{aligned} \tag{6.19}$$

For a setup with four waveguides, only three positions are available for a MZI followed by a PS, corresponding to $k = 1, 2, 3$. These choices correspond to the cases where this device operates on the first and second waveguides, second and third waveguides, and third and fourth waveguides, respectively.

The two states, considering the action of the triangular arrangement of U_{rot}s on the input photon states $|01\rangle$ can be described as:

$$\begin{aligned} |\psi\rangle \otimes |\xi\rangle &= U^{(2)}_{\text{rot}}(\boldsymbol{\theta_{22}}, \boldsymbol{\phi_{22}}) \cdot U^{(0)}_{\text{rot}}(\boldsymbol{\theta_{21}}, \boldsymbol{\phi_{21}}) \cdot U^{(1)}_{\text{rot}}(\boldsymbol{\theta_1}, \boldsymbol{\phi_1}) \cdot \begin{pmatrix}0\\1\\0\\0\end{pmatrix} \\ &= -e^{i\sum_{j=1,2}(\theta_1(j)+\theta_{21}(j)+\theta_{22}(j))} \begin{pmatrix} e^{i(\phi_1(1)+\phi_{21}(1))}\sin\Delta\theta_1\cos\Delta\theta_{21} \\ -e^{i(\phi_1(1)+\phi_{21}(2))}\sin\Delta\theta_1\sin\Delta\theta_{21} \\ e^{i(\phi_1(2)+\phi_{22}(1))}\cos\Delta\theta_1\sin\Delta\theta_{22} \\ e^{i(\phi_1(2)+\phi_{22}(2))}\cos\Delta\theta_1\cos\Delta\theta_{22} \end{pmatrix}, \end{aligned} \tag{6.20}$$

which can also be expressed in Dirac notation as:

$$\begin{aligned} |\psi\rangle \otimes |\xi\rangle &= U^{(2)}_{\text{rot}}(\boldsymbol{\theta_{22}}, \boldsymbol{\phi_{22}}) \cdot U^{(0)}_{\text{rot}}(\boldsymbol{\theta_{21}}, \boldsymbol{\phi_{21}}) \cdot U^{(1)}_{\text{rot}}(\boldsymbol{\theta_1}, \boldsymbol{\phi_1}) \cdot |01\rangle \\ &= -e^{i\sum_{j=1,2}(\theta_1(j)+\theta_{21}(j)+\theta_{22}(j))} \\ &\quad \Big\{ e^{i(\phi_1(1)+\phi_{21}(1))}\sin\Delta\theta_1 \left(\cos\Delta\theta_{21}|00\rangle - e^{-i\Delta\phi_{21}}\sin\Delta\theta_{21}|01\rangle\right) \\ &\quad + e^{i(\phi_1(2)+\phi_{22}(1))}\cos\Delta\theta_1 \left(\sin\Delta\theta_{22}|10\rangle + e^{-i\Delta\phi_{22}}\cos\Delta\theta_{22}|11\rangle\right)\Big\}, \end{aligned} \tag{6.21}$$

where $\Delta\phi_J \equiv \phi_J(1) - \phi_J(2)$, and an abuse of notation is used to denote the $U^{(k)}_{\text{rot}}$ matrix and corresponding unitary transformation.

These equations illustrate that the preparation step enables the parameterization of any two-qubit state, including entangled states. Specifically, any state of the form $A_{00}|00\rangle + A_{01}|01\rangle + A_{10}|10\rangle + A_{11}|11\rangle$ with $|A_{00}|^2 + |A_{01}|^2 + |A_{10}|^2 + |A_{11}|^2 = 1$ can be expressed. The state is separable if $\boldsymbol{\theta_2} \equiv \boldsymbol{\theta_{21}} - \frac{\pi}{2} = \boldsymbol{\theta_{22}}$ and $\boldsymbol{\phi_2} \equiv \boldsymbol{\phi_{21}} = \boldsymbol{\phi_{22}}$, and, modulo a global phase, it reads

$$\begin{aligned} |\psi\rangle \otimes |\xi\rangle &= \left(\sin\Delta\theta_1|0\rangle + e^{-i\Delta\phi_1}\cos\Delta\theta_1|1\rangle\right) \otimes \left(\sin\Delta\theta_2|0\rangle + e^{-i\Delta\phi_2}\cos\Delta\theta_2|1\rangle\right) \\ &= \begin{pmatrix} \sin\Delta\theta_1\sin\Delta\theta_2 \\ e^{-i\Delta\phi_2}\sin\Delta\theta_1\cos\Delta\theta_2 \\ e^{-i\Delta\phi_1}\cos\Delta\theta_1\sin\Delta\theta_2 \\ e^{-i(\Delta\phi_1+\Delta\phi_2)}\cos\Delta\theta_1\cos\Delta\theta_2 \end{pmatrix}, \end{aligned} \tag{6.22}$$

which is the generic form of a separable state of two qubits. Therefore, the first MZI sets the first qubit, while the second and the third ones set the second qubit: the setting of the second qubit implies a defined relationship between the phases of the second and third MZIs. This point has important practical implications since, for a generic state, it is required to compensate for the spurious global phase of the second and third MZIs due to fabrication imperfections.

At block III of the preparation stage, four additional waveguides are introduced, as depicted in Fig. 6.3. The arrangement of these additional waveguides follows the encoding scheme established during the preparation stage for the two qubits. Considering that, this state becomes:

$$|\Psi\rangle = |\psi\rangle \otimes |\xi\rangle \otimes |0\rangle = \begin{pmatrix} \sin\Delta\theta_1 \sin\Delta\theta_2 \\ 0 \\ e^{-i\Delta\phi_2} \sin\Delta\theta_1 \cos\Delta\theta_2 \\ 0 \\ e^{-i\Delta\phi_1} \cos\Delta\theta_1 \sin\Delta\theta_2 \\ 0 \\ e^{-i(\Delta\phi_1+\Delta\phi_2)} \cos\Delta\theta_1 \cos\Delta\theta_2 \\ 0 \end{pmatrix}. \tag{6.23}$$

Swap test stage

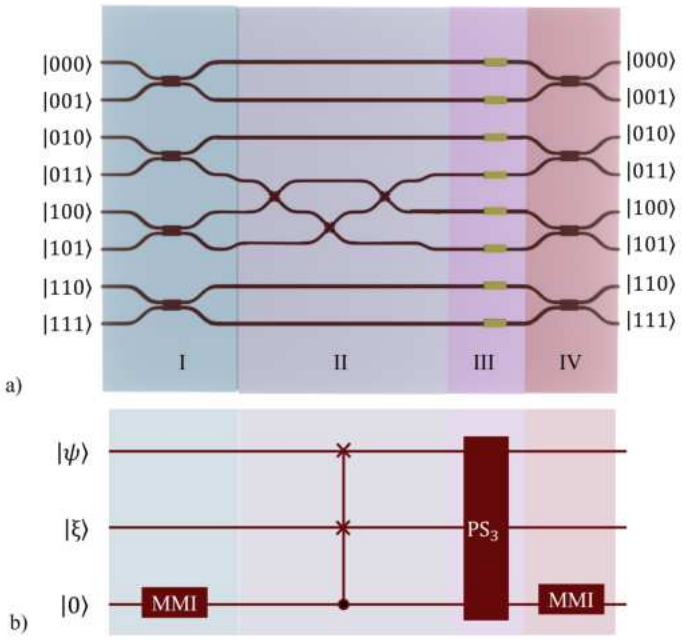

Figure 6.4: a) Our implementation of the swap test utilizing path encoding. The stage is segmented into four blocks labeled from I to IV, distinguished by different colors. Each block comprises MMIs, crossings, and heaters. b) Gate Representation of our Linear Photonic Swap Test Circuit divided into the same blocks.

Following the preparation stage, we enter the swap test stage. This stage too, for ease, is divided into blocks I to IV as shown in Fig. 6.4(a). For a direct understanding, Fig. 6.4(b) shows the gate representation of the swap circuit. In block I, the stage begins with a series of MMIs connecting every even and odd waveguide. This operation is

equivalent to applying the transformation $\mathbb{1} \otimes \mathbb{1} \otimes U_{\text{MMI}}$ to the state $|\psi\rangle \otimes |\xi\rangle \otimes |0\rangle$. In our implementation, instead of employing an H gate, we utilize the transformation U_{MMI}. The effect of this initial step, governed by the transformation $\mathbb{1} \otimes \mathbb{1} \otimes U_{\text{MMI}}$, can be expressed in matrix notation as:

$$\mathbb{1} \otimes \mathbb{1} \otimes U_{\text{MMI}} = \frac{1}{\sqrt{2}} \begin{pmatrix} 1 & i & 0 & 0 & 0 & 0 & 0 & 0 \\ i & 1 & 0 & 0 & 0 & 0 & 0 & 0 \\ 0 & 0 & 1 & i & 0 & 0 & 0 & 0 \\ 0 & 0 & i & 1 & 0 & 0 & 0 & 0 \\ 0 & 0 & 0 & 0 & 1 & i & 0 & 0 \\ 0 & 0 & 0 & 0 & i & 1 & 0 & 0 \\ 0 & 0 & 0 & 0 & 0 & 0 & 1 & i \\ 0 & 0 & 0 & 0 & 0 & 0 & i & 1 \end{pmatrix}. \tag{6.24}$$

This matrix representation shows the mapping from Dirac notation to vectorial notation, where each basis vector corresponds to a specific state. In block II, a central network of crossing waveguides is established to implement U_{CSWAP}, represented by the matrix:

$$U_{\text{CSWAP}} = \begin{pmatrix} 1 & 0 & 0 & 0 & 0 & 0 & 0 & 0 \\ 0 & 1 & 0 & 0 & 0 & 0 & 0 & 0 \\ 0 & 0 & 1 & 0 & 0 & 0 & 0 & 0 \\ 0 & 0 & 0 & 0 & 0 & 1 & 0 & 0 \\ 0 & 0 & 0 & 0 & 1 & 0 & 0 & 0 \\ 0 & 0 & 0 & 1 & 0 & 0 & 0 & 0 \\ 0 & 0 & 0 & 0 & 0 & 0 & 1 & 0 \\ 0 & 0 & 0 & 0 & 0 & 0 & 0 & 1 \end{pmatrix}. \tag{6.25}$$

Examining the eight basis vectors reveals that the CSWAP operation primarily involves swapping the states $|011\rangle$ and $|101\rangle$, the non-diagonal terms in the matrix. Indeed, it's remarkable that this operation occurs within a passive circuit, contrasting with the complexity of other photonic approaches reported in the literature [256, 261, 262]. However, the price to be paid for the realization of this passive device is the non-scalability of the encoding used. Phase shifters are introduced on all eight waveguides to compensate for spurious phases (block III). Another layer of MMIs implements the final transformation $\mathbb{1} \otimes \mathbb{1} \otimes U_{\text{MMI}}$ before detection (block IV).

The overall manipulation stage for the swap test can be represented as

$$U_{\text{swaptest}} = (\mathbb{1} \otimes \mathbb{1} \otimes U_{\text{MMI}}) \cdot U_{\text{PS}_8}(\boldsymbol{\theta_s}) \cdot U_{\text{CSWAP}} \cdot (\mathbb{1} \otimes \mathbb{1} \otimes U_{\text{MMI}}) \,. \tag{6.26}$$

The matrix describing the SWT stage can be factorized in three mutually commuting contributions:

$$\mathbf{MZI}^{(0)}\left(\theta_s(1), \theta_s(2)\right) \cdot \mathbf{MZI}^{(6)}\left(\theta_s(7), \theta_s(8)\right) \cdot U_{\textbf{swap-core}}\left(\theta_s(3), \theta_s(4), \theta_s(5), \theta_s(6)\right) \,. \tag{6.27}$$

Upon setting all phases $\boldsymbol{\theta_s}$ to zero and applying it to the generic state prepared earlier, the U_{swaptest} is:

$$U_{\text{swaptest}}\,|\Psi\rangle = \begin{pmatrix} 0 & \mathrm{i} & 0 & 0 & 0 & 0 & 0 & 0 \\ \mathrm{i} & 0 & 0 & 0 & 0 & 0 & 0 & 0 \\ 0 & 0 & \frac{1}{2} & \frac{\mathrm{i}}{2} & -\frac{1}{2} & \frac{\mathrm{i}}{2} & 0 & 0 \\ 0 & 0 & \frac{\mathrm{i}}{2} & -\frac{1}{2} & \frac{\mathrm{i}}{2} & \frac{1}{2} & 0 & 0 \\ 0 & 0 & -\frac{1}{2} & \frac{\mathrm{i}}{2} & \frac{1}{2} & \frac{\mathrm{i}}{2} & 0 & 0 \\ 0 & 0 & \frac{\mathrm{i}}{2} & \frac{1}{2} & \frac{\mathrm{i}}{2} & -\frac{1}{2} & 0 & 0 \\ 0 & 0 & 0 & 0 & 0 & 0 & 0 & \mathrm{i} \\ 0 & 0 & 0 & 0 & 0 & 0 & \mathrm{i} & 0 \end{pmatrix} \cdot \begin{pmatrix} \sin\Delta\theta_1 \sin\Delta\theta_2 \\ 0 \\ \mathrm{e}^{-\mathrm{i}\Delta\phi_2} \sin\Delta\theta_1 \cos\Delta\theta_2 \\ 0 \\ \mathrm{e}^{-\mathrm{i}\Delta\phi_1} \cos\Delta\theta_1 \sin\Delta\theta_2 \\ 0 \\ \mathrm{e}^{-\mathrm{i}(\Delta\phi_1+\Delta\phi_2)} \cos\Delta\theta_1 \cos\Delta\theta_2 \\ 0 \end{pmatrix}$$

$$= \frac{1}{2} \begin{pmatrix} 0 \\ 2\mathrm{i}\,\sin\Delta\theta_1 \sin\Delta\theta_2 \\ \mathrm{e}^{-\mathrm{i}\Delta\phi_2} \sin\Delta\theta_1 \cos\Delta\theta_2 - \mathrm{e}^{-\mathrm{i}\Delta\phi_1} \cos\Delta\theta_1 \sin\Delta\theta_2 \\ \mathrm{i}\,\mathrm{e}^{-\mathrm{i}\Delta\phi_2} \sin\Delta\theta_1 \cos\Delta\theta_2 + \mathrm{i}\,\mathrm{e}^{-\mathrm{i}\Delta\phi_1} \cos\Delta\theta_1 \sin\Delta\theta_2 \\ -\mathrm{e}^{-\mathrm{i}\Delta\phi_2} \sin\Delta\theta_1 \cos\Delta\theta_2 + \mathrm{e}^{-\mathrm{i}\Delta\phi_1} \cos\Delta\theta_1 \sin\Delta\theta_2 \\ \mathrm{i}\,\mathrm{e}^{-\mathrm{i}\Delta\phi_2} \sin\Delta\theta_1 \cos\Delta\theta_2 + \mathrm{i}\,\mathrm{e}^{-\mathrm{i}\Delta\phi_1} \cos\Delta\theta_1 \sin\Delta\theta_2 \\ 0 \\ 2\mathrm{i}\,\mathrm{e}^{-\mathrm{i}(\Delta\phi_1+\Delta\phi_2)} \cos\Delta\theta_1 \cos\Delta\theta_2 \end{pmatrix}. \tag{6.28}$$

Finally, $\{\mathbb{P}(x)\}_{x=0,1}$ represents the probability that the ancilla qubit is found in state x. It can be expressed as

$$\mathbb{P}(x) = \mathrm{Tr}[U_{\text{swaptest}}|\Psi\rangle\langle\Psi|U^{\dagger}_{\text{swaptest}} \cdot (\mathbb{1}\otimes\mathbb{1}\otimes P_x)] = \frac{1}{2}\left(1-(-)^x|\langle\psi|\xi\rangle|^2\right), \tag{6.29}$$

where P_x is the projector onto the state $|x\rangle$ for the ancilla qubit, and $|\psi\rangle$ and $|\xi\rangle$ are as given in eq. (6.20). The resulting probabilities for outcomes $\{\mathbb{P}(x)\}_{x=0,1}$ are given by:

$$\begin{aligned} \mathbb{P}(0) &= \frac{1}{2}\left(1-\cos^2(\Delta\theta_1-\Delta\theta_2)\cos^2\left(\frac{\Delta\phi_1-\Delta\phi_2}{2}\right)-\cos^2(\Delta\theta_1+\Delta\theta_2)\sin^2\left(\frac{\Delta\phi_1-\Delta\phi_2}{2}\right)\right), \\ \mathbb{P}(1) &= \frac{1}{2}\left(1+\cos^2(\Delta\theta_1-\Delta\theta_2)\cos^2\left(\frac{\Delta\phi_1-\Delta\phi_2}{2}\right)+\cos^2(\Delta\theta_1+\Delta\theta_2)\sin^2\left(\frac{\Delta\phi_1-\Delta\phi_2}{2}\right)\right). \end{aligned} \tag{6.30}$$

The scalar product of $|\psi\rangle$ and $|\xi\rangle$ reads

$$|\langle\psi|\xi\rangle|^2 = \cos^2(\Delta\theta_1-\Delta\theta_2)\cos^2\left(\frac{\Delta\phi_1-\Delta\phi_2}{2}\right)+\cos^2(\Delta\theta_1+\Delta\theta_2)\sin^2\left(\frac{\Delta\phi_1-\Delta\phi_2}{2}\right). \tag{6.31}$$

Indeed, it's worth noting that our derived result, eq. (6.29), obtained from the sampling of even and odd outputs ($x = 0$ and $x = 1$, respectively), matches the outcome of the standard swap test algorithm described before, with the exception of the exchange between the $\mathbb{P}(0)$ and $\mathbb{P}(1)$ for the ancilla, as demonstrated in eq. (6.5). This is due to the fact that, in this case, we are using MMI as Hadarmard.

Experimentally, the probabilities $\{\mathbb{P}(x)\}_{x=0,1}$ are determined by sampling the counts at the even and odd outputs of the ancilla qubit. This is expressed as:

$$\mathbb{P}(x) = \frac{N_x}{N_0+N_1}, \tag{6.32}$$

where N_0 and N_1 represent the photon counts detected from the even and odd waveguides, respectively. To acquire these counts, the phases of the operation U_{PS_3} in the

swap test stage III are adjusted, and only the even outputs are sampled using four detectors. A π shift of the phases in stage III, allows to detect at the same outputs the odd outputs with the same four detectors at the cost of doubling the overall acquisition time. Despite being based on the non-destructive swap test scheme, the implemented scheme becomes destructive due to the nature of the detection stage, where the total state (6.1) is written in single photon path encoding during each run.

Swapping of the outputs

To facilitate understanding, let's illustrate how the outputs corresponding to the ancillary qubit state $|0\rangle$ can be interchanged with those corresponding to $|1\rangle$ using the phase shifters within the swap test setup. This simplifies the sampling process, necessitating only four detectors across two runs.

Swapping states $|000\rangle \iff |001\rangle$ and $|110\rangle \iff |111\rangle$ is straightforward, facilitated by direct connections via a Mach-Zehnder interferometer, as detailed in eq. (6.27). By appropriately adjusting two phases, this swap can be executed.

Now, let's delve into the central segment of the swap test circuit, encompassing the waveguides associated with states $|010\rangle$, $|011\rangle$, $|100\rangle$, and $|101\rangle$. This segment is represented by the following matrix:

$$\begin{aligned}
&\frac{1}{2}\begin{pmatrix} 1 & \mathrm{i} & 0 & 0 \\ \mathrm{i} & 1 & 0 & 0 \\ 0 & 0 & 1 & \mathrm{i} \\ 0 & 0 & \mathrm{i} & 1 \end{pmatrix}\begin{pmatrix} \mathrm{e}^{\mathrm{i}\theta_s(3)} & 0 & 0 & 0 \\ 0 & \mathrm{e}^{\mathrm{i}\theta_s(4)} & 0 & 0 \\ 0 & 0 & \mathrm{e}^{\mathrm{i}\theta_s(5)} & 0 \\ 0 & 0 & 0 & \mathrm{e}^{\mathrm{i}\theta_s(6)} \end{pmatrix}\begin{pmatrix} 1 & 0 & 0 & 0 \\ 0 & 0 & 0 & 1 \\ 0 & 0 & 1 & 0 \\ 0 & 1 & 0 & 0 \end{pmatrix}\begin{pmatrix} 1 & \mathrm{i} & 0 & 0 \\ \mathrm{i} & 1 & 0 & 0 \\ 0 & 0 & 1 & \mathrm{i} \\ 0 & 0 & \mathrm{i} & 1 \end{pmatrix} \\
&= \frac{1}{2}\begin{pmatrix} \mathrm{e}^{\mathrm{i}\theta_s(3)} & \mathrm{i}\,\mathrm{e}^{\mathrm{i}\theta_s(3)} & -\mathrm{e}^{\mathrm{i}\theta_s(4)} & \mathrm{i}\,\mathrm{e}^{\mathrm{i}\theta_s(4)} \\ \mathrm{i}\,\mathrm{e}^{\mathrm{i}\theta_s(3)} & -\mathrm{e}^{\mathrm{i}\theta_s(3)} & \mathrm{i}\,\mathrm{e}^{\mathrm{i}\theta_s(4)} & \mathrm{e}^{\mathrm{i}\theta_s(4)} \\ -\mathrm{e}^{\mathrm{i}\theta_s(6)} & \mathrm{i}\,\mathrm{e}^{\mathrm{i}\theta_s(6)} & \mathrm{e}^{\mathrm{i}\theta_s(5)} & \mathrm{i}\,\mathrm{e}^{\mathrm{i}\theta_s(5)} \\ \mathrm{i}\,\mathrm{e}^{\mathrm{i}\theta_s(6)} & \mathrm{e}^{\mathrm{i}\theta_s(6)} & \mathrm{i}\,\mathrm{e}^{\mathrm{i}\theta_s(5)} & -\mathrm{e}^{\mathrm{i}\theta_s(5)} \end{pmatrix},
\end{aligned} \tag{6.33}$$

This matrix constitutes the central submatrix of $U_{\textbf{swap-core}}$.

The generic state injected into this central structure is $(A, 0, B, 0)$, assuming the ancillary qubit is always in the state $|0\rangle$. The resulting state is:

$$\frac{1}{2}\begin{pmatrix} A\mathrm{e}^{\mathrm{i}\theta_s(3)} - B\mathrm{e}^{\mathrm{i}\theta_s(4)} \\ \mathrm{i}\left(A\mathrm{e}^{\mathrm{i}\theta_s(3)} + B\mathrm{e}^{\mathrm{i}\theta_s(4)}\right) \\ -A\mathrm{e}^{\mathrm{i}\theta_s(6)} + B\mathrm{e}^{\mathrm{i}\theta_s(5)} \\ \mathrm{i}\left(A\mathrm{e}^{\mathrm{i}\theta_s(6)} + B\mathrm{e}^{\mathrm{i}\theta_s(5)}\right) \end{pmatrix}. \tag{6.34}$$

Inverting the computational-basis states $|0\rangle \iff |1\rangle$ for the ancillary qubit corresponds to swapping the first and second entries, as well as the third and fourth entries:

$$\frac{1}{2}\begin{pmatrix} \mathrm{i}\left(A\mathrm{e}^{\mathrm{i}\theta_s(3)} + B\mathrm{e}^{\mathrm{i}\theta_s(4)}\right) \\ A\mathrm{e}^{\mathrm{i}\theta_s(3)} - B\mathrm{e}^{\mathrm{i}\theta_s(4)} \\ \mathrm{i}\left(A\mathrm{e}^{\mathrm{i}\theta_s(6)} + B\mathrm{e}^{\mathrm{i}\theta_s(5)}\right) \\ -A\mathrm{e}^{\mathrm{i}\theta_s(6)} + B\mathrm{e}^{\mathrm{i}\theta_s(5)} \end{pmatrix}. \tag{6.35}$$

By adjusting $(\theta_s(3), \theta_s(4), \theta_s(5), \theta_s(6)) \rightarrow (\theta_s(3), \theta_s(4) + \pi, \theta_s(5), \theta_s(6) + \pi)$, we obtain:

$$\frac{1}{2}\begin{pmatrix} Ae^{i\theta_s(3)} + Be^{i\theta_s(4)} \\ i\left(Ae^{i\theta_s(3)} - Be^{i\theta_s(4)}\right) \\ Ae^{i\theta_s(6)} + Be^{i\theta_s(5)} \\ i\left(-Ae^{i\theta_s(6)} + Be^{i\theta_s(5)}\right) \end{pmatrix}. \tag{6.36}$$

Each entry modulus of the first state is equal to the modulus of each entry in the second state. Thus, we can confirm that swapping the computational-basis states of the ancillary qubit is equivalent to adjusting $(\theta_s(3), \theta_s(4), \theta_s(5), \theta_s(6)) \rightarrow (\theta_s(3), \theta_s(4) + \pi, \theta_s(5), \theta_s(6) + \pi)$. Consequently, we can confidently place detectors on just half of the outputs.

6.3.2 Experimental setup and calibration

The photonic chip was fabricated using a SiN material for applications in the visible-to-near infrared spectral range. This photonic chip employed a photolithography process on a multi-project wafer (MPW) platform supplied by the Ligentec SA foundry. The waveguide core dimensions measure (150×550) nm^2, carefully selected to ensure single-mode propagation at the operational wavelength of 750 nm, considering the chosen TE polarization. Fig. 6.5 illustrates the photo (a) of the PIC and the scheme of the

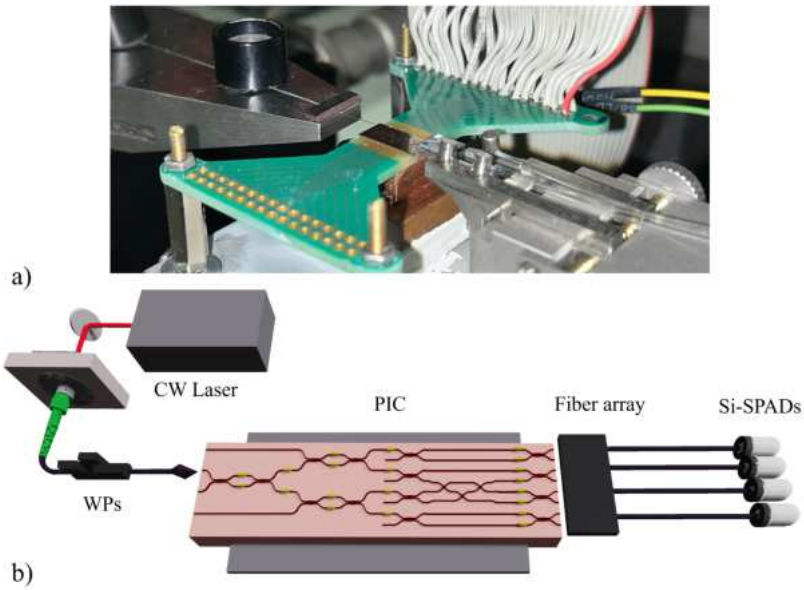

Figure 6.5: a) Photo of the PIC connected via wire bonding to the Printed Circuit Board (PCB), depicted in green. The PIC is placed on a copper pillar bonded to a Peltier cell. Visible in the image are the input fiber on the left and the fiber array on the right. Additionally, electronic wires are observed, used to manipulate the heaters of the PIC and control the temperature of the Peltier cell. b) The experimental setup consists of the Ti:Sapphire laser in CW configuration tuned to a wavelength of 750 nm. The beam is coupled to the chip through a lensed SM fiber, with polarization selected as TE polarization using a fiber wave plate. At the output, the signal from the four outputs is collected by a fiber array and directed to the fiber Si-SPADs.

setup (b). In our experimental setup, we utilized an attenuated CW Ti:Sapphire laser,

precisely tuned to 750 nm, as the light source. Prior to entering the chip, the laser light was attenuated using an optical variable attenuator, and its polarization was adjusted to TE configuration.

Optical coupling at the chip's input was facilitated by a lensed conical fiber, while output coupling was achieved using a standard fiber array. The currents required for controlling the MZIs and PSs on the PIC were supplied by a dedicated power supply (Qontrol systems - device model BP8).

Photon detection was performed using four fibered Si-SPADs from Excelitas, each exhibiting identical efficiencies. The output counts from these detectors were collected using time-tagging electronics from Swabian Instruments, interfaced with a PC.

During our experiments, we maintained a total photon flux of approximately 10^6 photons, with a time bin of 0.2 μs configured on the time tagger. Data acquisition was carried out for a duration of 30 ms, with each measurement consisting of ten separate acquisitions. Error estimates were obtained by analyzing the variance across these measurements.

To normalize the data, we selected the $|100\rangle$ output as a reference with an efficiency of 1. Consequently, the relative efficiencies of the other output states were determined as follows: 0.487 for $|000\rangle$, 0.975 for $|010\rangle$, and 0.958 for $|110\rangle$. To ensure accuracy, the mean dark counts of each SPAD were subtracted from the raw data. The discrepancies in the outputs can be attributed to losses occurring between the fibers of the fiber arrays and the chip outputs, stemming from defects on the faces of the outputs.

In our setup, no post-selection operation was necessary to discard time bins where more than one photon was detected. Additionally, a Peltier cell was employed to maintain thermal stability within the PIC, regulated by a proportional-integral-derivative (PID) controller. Between each set of ten acquisitions, the circuit was allowed to thermalize for a few seconds.

Phase calibration

The characterization of all on-chip MZIs was performed to establish the phase-power relation $\phi(W)$. This relation was determined by fitting the observed counts detected by a SPAD at the output ports of each MZI. The fitting equations employed, depending on the considered output port, are:

$$N_{\text{out1}} = a\cos^2(bW + d) + c\,, \tag{6.37a}$$

$$N_{\text{out2}} = a\sin^2(bW + d) + c\,, \tag{6.37b}$$

where a, b, c, and d are fitting parameters. Consequently, $\phi(W) = bW + d$. The collected data, along with the corresponding fits, are presented in Fig. 6.6. The waveguides of each arm of the MZIs are isolated from the surrounding substrate using trenches etched in the material. These trenches help reduce the heat diffusion coefficient, thereby mitigating thermal cross-talk between neighboring phase shifters.

The fit parameters for the different MZIs are summarized in Table 6.1.

	MZI_1	MZI_2	MZI_3
b [1/W]	11.74 ± 0.05	12.11 ± 0.03	11.70 ± 0.05
d	0.461 ± 0.004	0.106 ± 0.002	0.062 ± 0.004

Table 6.1: Fit parameters for different MZIs. Values of the parameters b and d were obtained from the fitting operations.

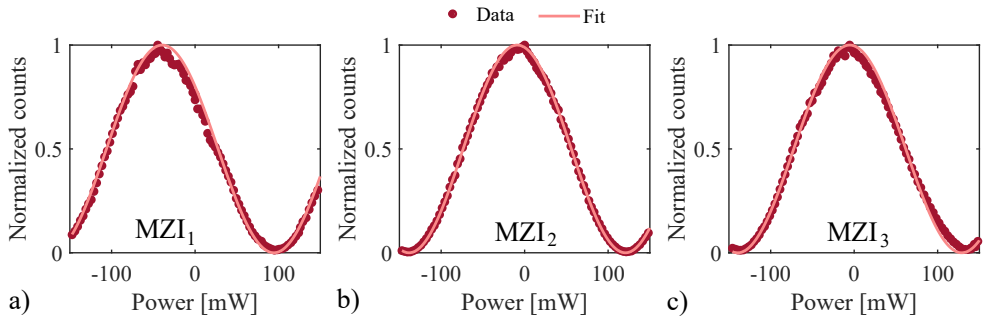

Figure 6.6: Characterization of different MZIs in the preparation stage. Characterization curves at 750 nm in TE polarization: **a)** MZI_1, **b)** MZI_2, **c)** MZI_3. The normalized counts are depicted in dark red, while the fits are represented in light red.

6.3.3 Swap test measurements

Separable state $|\psi\rangle \otimes |\xi\rangle$

The validation of our PIC involves comparing experimental results with theoretical predictions, as outlined by eq. (6.31). To account for the characteristics of our PIC, including MMI unbalance, CR insertion loss, and MZI phase calibration errors, we developed a comprehensive model detailed in Appendix E. This model enables us to establish a confidence interval of 2σ, within which experimental results must fall to be deemed comparable.

Initially, we conducted a preliminary validation using the computational basis states

$$|0\rangle \otimes |0\rangle\,, \qquad |0\rangle \otimes |1\rangle\,, \qquad |1\rangle \otimes |0\rangle\,, \qquad |1\rangle \otimes |1\rangle\,.$$

In table 6.2, the theoretical values of the corresponding squared scalar products, the model 2σ confident interval, and the experimental measurements with error bars derived from multiple runs on our PIC, are shown. We observed good agreement between theory and experiment for the orthogonal pairs of states $\{|0\rangle \otimes |1\rangle, |1\rangle \otimes |0\rangle\}$, while a slight deviation was noted for the parallel pairs $\{|0\rangle \otimes |0\rangle, |1\rangle \otimes |1\rangle\}$. This observed

	$\|0\rangle \otimes \|0\rangle$	$\|0\rangle \otimes \|1\rangle$	$\|1\rangle \otimes \|0\rangle$	$\|1\rangle \otimes \|1\rangle$
Theor. $\|\langle\psi\|\xi\rangle\|^2$	1	0	0	1
2σ	[0.960, 1.000]	[-0.001, 0.002]	[0.000, 0.039]	[0.970, 1.000]
Exp. $\|\langle\psi\|\xi\rangle\|^2$	(0.991 ± 0.003)	(0.01 ± 0.01)	(0.01 ± 0.02)	(0.990 ± 0.003)

Table 6.2: Theoretical, experimental, and confidence interval values of the squared scalar product of the computational basis states of the two qubits. Theoretical values are computed according to eq. (6.31), experimental results are obtained from measurements run on the PIC, while the 2σ confidence interval is calculated from the model taking into account PIC non-idealities.

deviation is attributed to actual manufacturing imperfections in our PIC. However, the experimental data falls within the 2σ confidence interval. Consequently, our PIC effectively estimates the quadratic scalar product of the computational basis states, validating its functionality.

In the second part of our validation process, we explore a specific family of states defined as follows:

$$|\psi\rangle = \frac{1}{\sqrt{2}}\left(|0\rangle + |1\rangle\right), \tag{6.38a}$$

$$|\xi(\omega)\rangle = \frac{1}{\sqrt{2}}\left(|0\rangle + e^{i\omega}|1\rangle\right), \tag{6.38b}$$

The state $|\xi\rangle$ has a parameter ω. We can manipulate the current of the phase shifter that determines ω by adjusting the second phase shifter from the top in PS_2 (as shown in Fig. 6.3) to study the behavior of the PIC. This approach enables us to examine scenarios ranging from the initial pair of parallel states ($\omega = 0$) to the orthogonal case ($\omega = \pm\pi$).

The collected data are depicted in Fig. 6.7 as dark red dots accompanied by their respective error bars in blue. Notably, the experimental observations closely match the theoretical predictions represented by light red squares, yielding a root mean square error (RMSE) of 0.026. Furthermore, all data points fall within the 2σ confidence interval (blue lines) derived from our realistic model. Thus, we confirm that our PIC adeptly estimates the squared scalar product of state pairs belonging to the family described in eq. (6.38).

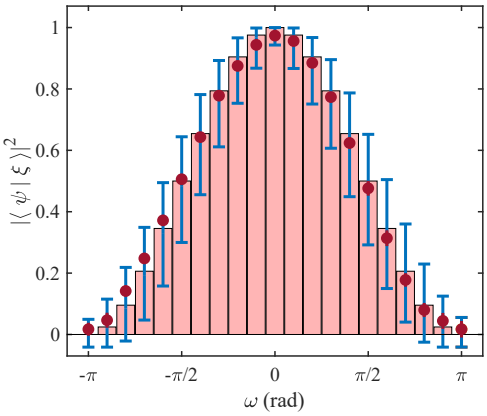

Figure 6.7: Experimental results for the family of state pairs described by eq. (6.38). Theoretical squared scalar products are depicted in light red, while experimentally obtained data from repeated measurements are shown in dark red, followed by error bars. The 2σ confidence interval is highlighted in blue.

Finally, the validation process of our PIC's functionality ends with the random selection of 3342 pairs of states $|\psi\rangle$ and $|\xi\rangle$, followed by the calculation of their squared scalar product using the PIC. A subset of 50 pairs of states, randomly chosen from the 3342 pairs, is illustrated in Fig. 6.8(a).
Our PIC demonstrates accurate computation of the squared scalar products for the majority of randomly selected state pairs, with deviations from theory typically falling within the confidence interval of our model. The histogram in Fig. 6.8(b) shows the discrepancy between the squared scalar product obtained by our PIC and the theoretical value, $|\langle\psi|\xi\rangle|^2_{Ex} - |\langle\psi|\xi\rangle|^2_{Th}$, for all 3342 randomly selected state pairs. The histogram's bin width is 0.02, centered around multiple values of 0.01. All distance values between theory and experiments range between -0.191 and 0.144, with a mean value of -0.012 ± 0.001.

The histogram's asymmetry with respect to zero primarily arises from the characteristics of the PIC, which tend to diminish the calculated squared scalar product, especially for values near 1. Fig. 6.8(c) presents the histogram of the absolute value $||\langle\psi|\xi\rangle|^2_{Ex} - |\langle\psi|\xi\rangle|^2_{Th}|$, showing both the mean and the median of the distribution. The mean distance measures 0.039 ± 0.001, and the squared scalar product of half of the

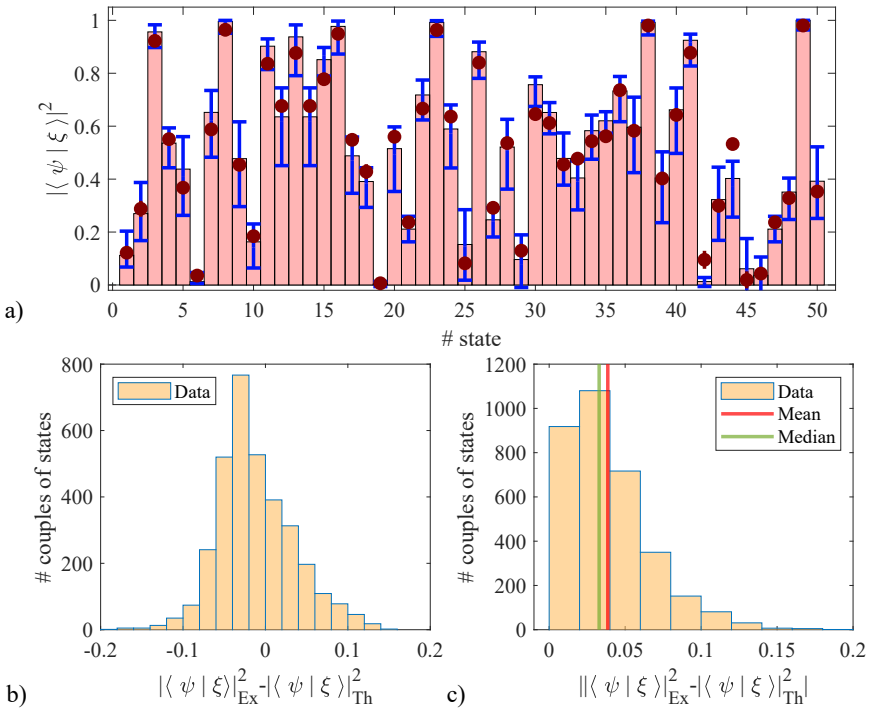

Figure 6.8: a) The panel of a subset of 50 pairs was randomly selected from the 3342 pairs measured. The expected theoretical value for the squared scalar product is represented by the light red bar, while the blue interval denotes the 2σ confidence interval provided by the model. Additionally, the experimental data, along with their error bars, are depicted as dark red dots. b) The histogram displays the difference between the experimental and theoretical squared scalar products, denoted as $|\langle\psi|\xi\rangle|^2_{\text{Ex}} - |\langle\psi|\xi\rangle|^2_{\text{Th}}$. c) This histogram shows the absolute distance between the experimental and theoretical squared scalar products, denoted as $||\langle\psi|\xi\rangle|^2_{\text{Ex}} - |\langle\psi|\xi\rangle|^2_{\text{Th}}|$. The median is illustrated by the green line, while the mean is represented by the red line. Each histogram bin has a width of 0.02 and is centered around multiple values of 0.01.

considered states is estimated with an error lower than 0.033. The observed RMSE slightly increases to 0.048 compared to the previous test on a much smaller set of states.

Our PIC yields squared scalar products within the 2σ confidence interval for approximately 88% of state pairs within the random ensemble. Our realistic model captures the systematic non-zero mean value of the distance $|\langle\psi|\xi\rangle|^2_{\text{Ex}} - |\langle\psi|\xi\rangle|^2_{\text{Th}}$ and describes the spread of the data around the corresponding expected theoretical values. Results outside the 2σ confidence interval are attributed to thermal crosstalk among the MZIs and PSs present in the preparation stage for high applied electrical power, phenomena not captured by our modeling.

Entangled state

Up to this point, our focus has been solely on separable states. In the validation process of our scheme, we examine the probability $\mathbb{P}(0)$ of finding the ancilla in the state $|0\rangle$ when the two unknown qubits are prepared in a Bell state. In our standard case, described in section 6.2, this corresponds to the probability of finding the ancilla in state

$|1\rangle$. We denote the probabilities for different Bell states in Table 6.3.
As anticipated by theory, the state $\frac{1}{\sqrt{2}}(|01\rangle - |10\rangle)$ yields a probability close to 100%,

	$\frac{1}{\sqrt{2}}(\|00\rangle \pm \|11\rangle)$	$\frac{1}{\sqrt{2}}(\|01\rangle + \|10\rangle)$	$\frac{1}{\sqrt{2}}(\|01\rangle - \|10\rangle)$
Theoretical $\mathbb{P}(0)$	0%	0%	100%
Experimental $\mathbb{P}(0)$	$(1.3 \pm 0.4)\%$	$(2 \pm 1)\%$	$(95 \pm 2)\%$
Model 2σ C.I. $\mathbb{P}(0)$	$[0, 1.38]\%$	$[0, 5.14]\%$	$[95.49, 100]\%$

Table 6.3: theoretical, experimental, and confidence interval values of $\mathbb{P}(0)$ for the Bell states of the two qubits. Theoretical values are derived from the theory detailed in Section 6.2. Experimental values are acquired via measurements on the PIC, while the 2σ confidence interval for $\mathbb{P}(0)$ accounts for PIC non-idealities.

while the other three states approach 0%. Our experimental results align well with these expectations and support the predictions of our non-idealities model. Notably, measurements on the input state $\frac{1}{\sqrt{2}}(|01\rangle + |10\rangle)$ yield a higher $\mathbb{P}(0)$ compared to the input state $\frac{1}{\sqrt{2}}(|00\rangle \pm |11\rangle)$, as anticipated by our model.

As done in the case with separable states, in the subsequent phase of our validation procedure, we investigate a specific category of states defined as follows:

$$|\Psi(\omega)\rangle = \frac{1}{\sqrt{2}}(|01\rangle + e^{i\omega}|10\rangle)\,. \tag{6.39}$$

Considering the state $|\Psi(\omega)\rangle$, it is possible to obtain the probability $\mathbb{P}(0)$ and $\mathbb{P}(1)$ from the eq. (6.12) and eq. (6.13). As in the previous case, due to MMIs instead of the H gate, the $\mathbb{P}(0)$ and $\mathbb{P}(1)$ are reversed. For the $\mathbb{P}(1)$ we obtain:

$$\mathbb{P}(1) = \left(\cos\frac{\omega}{2}\right)^2. \tag{6.40}$$

This approach enables us to explore scenarios ranging from the initial pair of parallel states ($\omega = 0$) to the orthogonal case ($\omega = \pm\pi$). From the experimental point of

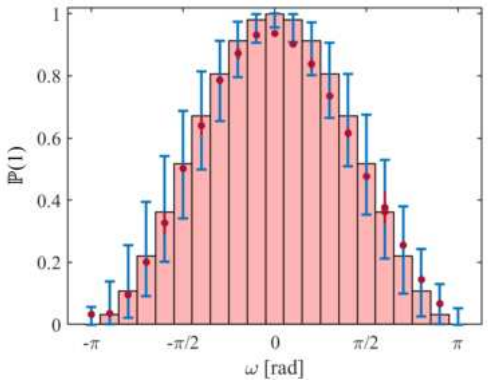

Figure 6.9: Experimental results for the family of state pairs described by eq. (6.39). Theoretical squared scalar products are depicted in light red, while experimentally obtained data from repeated measurements are shown in dark red, accompanied by error bars. The 2σ confidence interval is highlighted in blue.

view, we report the $\mathbb{P}(1)$. The experimental data, depicted in Fig. 6.9, are denoted

by dark red dots, each accompanied by its corresponding error bars. Remarkably, these experimental observations closely align with the theoretical predictions, represented by light red squares. Additionally, all data points fall within the 2σ confidence interval, illustrated by the blue lines, derived from our realistic model. This alignment confirms the ability of our PIC to estimate the quadratic scalar product of Bell's pairs of states.

Comparison

These observations validate the use of our PIC in calculating the squared scalar product across a broad ensemble of state pairs. Principal performance indicators are a mean absolute deviation of 0.039 and an RMSE of 0.048 in comparison to theoretical predictions. Additionally, the model of the PIC's imperfections not only helps to understand its operational mechanisms, which is crucial for creating improved versions, but also establishes confidence intervals for the PIC's readouts in kernel approximation.

As a benchmark, Table 6.4 provides a comparison of data for state overlap estimation obtained on superconducting quantum circuits using swap test or other algorithms such as ABA and BBA [254], which involve a higher number of qubits and resources. Notably, experimental proofs with other platforms, such as trapped ions [283], only demonstrate qualitative results, making quantitative comparisons challenging.

Table 6.4 highlights that our room temperature PIC estimates the squared scalar product with a root mean square error two times lower than the best results reported in the literature for the superconducting platform, which requires cryogenic temperatures. It is important to note that, compared to other approaches, our device demonstrates an exponential growth in resource requirements as the number of qubits increases.

platform	# qubits	root mean square error swap test	ABA	BBA	Ref.
integrated photonic	3	0.05	-	-	our work
superconducting IBM	5	0.31	0.11	0.12	[254]
superconducting Rigetti	19	0.54	0.43	0.16	[254]
trapped ion	5	not reported	-	-	[255]

Table 6.4: Comparison of performances of quantum circuits for states overlap estimation. Our results are compared with those obtained from quantum circuits in various quantum platforms, considering the number of qubits and RMSE across different algorithms. The symbol '-' is used to denote cases where no experiments have been carried out.

Furthermore, our proof-of-concept PIC demonstrates an average power consumption of 1.2 watts per single evaluation. This power allocation is distributed as follows: 0.25 watts for the preparation stage and 0.3 watts and 0.4 watts for the swap test stage, dedicated to sampling the ancilla states $|0\rangle$ and $|1\rangle$, respectively. The sampling duration is set at 60 milliseconds, with ten repetitions to enhance statistical accuracy. These power consumption figures are subject to optimization through improvements in design and fabrication, potentially at the expense of statistical robustness or by employing advanced single-photon detectors with reduced dead times.

6.4 Conclusions and future prospective

This study introduces a PIC engineered to compute the scalar product between any pair of qubits using the swap test algorithm. To our knowledge, this marks the first successful implementation of this quantum algorithm within an integrated photonic framework. Our design stands out for its simplicity and robustness, achieved by directly translating the gate-based swap test into our photonic system. Leveraging established integrated components such as multimode interference devices, beam splitters, and phase modulators, our PIC efficiently computes the quadratic scalar product for 3342 arbitrarily chosen pairs of states. The average deviation is 0.039, with a mean square deviation of 0.048, indicating competitive performance with superconducting circuits, while offering distinct advantages in simplicity and operation at room temperature.

Our quantum circuit promises to be a fundamental building block in quantum machine learning applications. However, it faces the limitation of resource non-scalability as the number of qubits increases. One potential solution for linearly improving the number of qubits relative to the resources needed is to use two swap test circuits in parallel, employing pairs of correlated photons as input sources and measuring output coincidences. Another potential application is to use our scheme to build two-layer feedforward neural networks or execute swap tests on any number of qubits, with linear growth of CSWAP gates and logarithmic growth of auxiliary qubits.

Chapter 7

Conclusions

This Thesis offers an investigation of the sources of quantum light, with a specific focus on biphoton states, generated by the parametric nonlinear sFWM process on an integrated photonics platform. The research delves into the fundamental principles of quantum optics, the role of silicon and silicon nitride materials in integrated optics, and a comparative analysis of various sFWM sources. Each of these sources possesses unique characteristics and limitations, rendering them more suitable for certain applications than others. Numerous experiments employing these sources have been conducted.

Utilizing the intermodal sFWM process, the generation of heralded single photons in the mid-infrared range has been observed, exhibiting exceptional characteristics and functioning at room temperature. The intermodal source facilitated the employment of silicon-based entangled photons in Ghost spectroscopy under conditions of high noise. This enabled the reconstruction of the CO_2 spectrum in scenarios where traditional measurement methodologies are unsuccessful.

The fabrication of a quantum simulator on a single platform was discussed as part of the EPIQUS project. This included the development of a silicon nitride-based platform optimized for operation in the visible to near-infrared spectrum. The generation of biphoton states and the examination of various integrated structures, instrumental in enabling the generation of entangled photon pairs, were described in detail. These results provide the basis for future experiments in integrated optics, which can be integrated into a single platform in a competitive manner.

The concluding chapter explored the implementation of the Quantum Swap Test algorithm on a silicon nitride platform, utilizing path encoding for qubit representation. The potential of SWT for efficient kernel function estimation was examined, introducing a novel approach to quantum algorithms.

In conclusion, this dissertation is my contribution to the field of quantum optics, offering valuable insights and paving the path for future research in this rapidly evolving and exciting field. The findings and methodologies presented in this work will serve as a robust foundation for further advancements in the generation and application of quantum light.

Appendix A

Quantum description of sFWM in photonic waveguides

Here, we report the analytical description of sFWM, starting the relation in eq. (1.112). I follow the review [28] for this theoretical part.

$$\mathcal{H}_{NL} = \frac{1}{4\varepsilon_0}\int \left[\Gamma^{(3)}_{ijkl}(\mathbf{r})\mathbf{D}_i(\mathbf{r},t)\mathbf{D}_j(\mathbf{r},t)\mathbf{D}_k(\mathbf{r},t)\mathbf{D}_l(\mathbf{r},t)\right] d\mathbf{r}\,. \tag{A.1}$$

Let's consider the eqs. (1.18), (1.19), (1.24) and (1.108). The displacement field operator expansion for a waveguide is:

$$\mathbf{D}_i(\mathbf{r},t) = \mathbf{D}_i^+(\mathbf{r},t) + \mathbf{D}_i^-(\mathbf{r},t)\,, \tag{A.2}$$

where

$$\mathbf{D}^- = (\mathbf{D}^+)^\dagger\,, \tag{A.3a}$$

$$\mathbf{D}^+ = \sum_j \mathbf{D}_j^+ = \sum_j \int \sqrt{\frac{\hbar\omega_{jk}}{4\pi}} a_j(k,t) d_{Jk}(y,z) e^{ikx} dk + \text{h.c.}\,. \tag{A.3b}$$

The eq. (A.1) becomes:

$$\begin{aligned}\mathcal{H}_{NL} = \frac{1}{4\varepsilon_0}\int d\mathbf{r}\Gamma^{(3)}_{ijkl}(\mathbf{r})(\mathbf{D}_i^+(\mathbf{r},t)+\mathbf{D}_i^-(\mathbf{r},t))(\mathbf{D}_j^+(\mathbf{r},t)+\mathbf{D}_j^-(\mathbf{r},t))\times \\ \times(\mathbf{D}_k^+(\mathbf{r},t)+\mathbf{D}_k^-(\mathbf{r},t))(\mathbf{D}_l^+(\mathbf{r},t)+\mathbf{D}_l^-(\mathbf{r},t))\,.\end{aligned} \tag{A.3c}$$

Expanding all terms will result in different effects, as described in section 1.3.4. The expression for the sFWM process can be written as:

$$H_{sFWM} = \frac{3}{\epsilon_0}\int \Gamma^{(3)}_{ijkl}(\mathbf{r})\mathbf{D}_s^-(\mathbf{r},t)\mathbf{D}_i^-(\mathbf{r},t)\mathbf{D}_p^+(\mathbf{r},t)\mathbf{D}_p^+(\mathbf{r},t)d\mathbf{r} + \text{h.c.}\,, \tag{A.4}$$

where p, s and i refer to the pumps, signal and idler photons. Considering the eq. (A.3a) and (A.3b) the Hamiltonian of the sFWM becomes:

$$\begin{aligned}H_{sFWM} = &\frac{3\hbar^2}{\epsilon_0 16\pi^2}\iint \Gamma_3\sqrt{\omega_{Pk}\omega_{Pk}\omega_{ik}\omega_{sk}}a_i^\dagger(k,t)a_s^\dagger(k,t)a_P(k,t)a_P(k,t) \\ &\times e^{i(k_p+k_p-k_i-k_s)x} d_{Pk}d_{Pk}d_{ik}^*d_{sk}^* dk_P dk_P dk_i dk_s + \text{h.c.}\,.\end{aligned} \tag{A.5}$$

After transitioning into the frequency domain and moving in the interaction picture, the Hamiltonian H_{sFWM} is transformed as:

$$\begin{aligned} H_{sFWM} =& \frac{3\hbar^2\omega^2_{ISP_1P_2}}{\epsilon_0 16\pi^2}\iint \Gamma_3 a_i^\dagger(\omega_i)a_s^\dagger(\omega_s)a_P(\omega_P)a_P(\omega_P) \\ &\times e^{i(k_p+k_p-k_i-k_s)x}e^{i(\omega_p+\omega_p-\omega_i-\omega_s)t}d\omega_P d\omega_P d\omega_i d\omega_s + \text{h.c.}\,, \end{aligned} \tag{A.6}$$

with

$$\omega_{SIP_1P_2} = \sqrt[4]{\omega_i\omega_s\omega_{P_1}\omega_{P_2}}\,, \tag{A.7}$$

and

$$n_2 = \frac{3\chi_3^{ijkl}}{4\epsilon_0 c n_P^2}\,. \tag{A.8}$$

We can introduce the coupling coefficient described by:

$$\gamma_{SiP_1P_2} = \frac{n_2\omega_{SIP_1P_2}}{cA^{eff}_{SIP_1P_2}}\,. \tag{A.9}$$

It is possible to rewrite the Hamiltonian as:

$$\begin{aligned} H_{sFWM} =& \frac{\gamma_{SiP_1P_2}\hbar^2\omega_{ISP_1P_2}}{4\pi^2}\int d\omega_P d\omega_P d\omega_i d\omega_s a_i^\dagger(\omega_i)a_s^\dagger(\omega_s)a_P(\omega_P)a_P(\omega_P) \\ &\times e^{i\Delta k x}e^{i(\omega_p+\omega_p-\omega_i-\omega_s)t} + \text{h.c.}\,, \end{aligned} \tag{A.10}$$

where $\Delta k = k_p + k_p - k_i - k_s$ is the phase mismatch parameter. $\mathcal{A}^{\text{eff}}$ is the effective area of the process, k is the wavevector of the four photons, and γ is the parameter that characterizes the strength of the FWM process [28].
We are ready to examine how a quantum state evolves under the influence of the this Hamiltonian. If the initial state is in the vacuum state, the state's evolution is characterized by:

$$|\Psi\rangle = \hat{\mathcal{U}}\,|0,0\rangle_{i,s} = \exp\left[\frac{-i}{\hbar}\int_{-\infty}^{\infty} dt\hat{H}_{sFWM}(t)\right]|0,0\rangle_{i,s}\,, \tag{A.11}$$

where $|0,0\rangle_{i,s} = |vac\rangle$. Upon conducting the time integral, a Dirac delta function is acquired through the relationship $2\pi\delta(\omega-\omega_0) = \int_{-\infty}^{\infty} dt\, e^{i(\omega-\omega_0)t}$. Let's consider the case of coherent laser pumps. The resulting integral in its expansion is described as:

$$\begin{aligned} \frac{-i}{\hbar}\int_{-\infty}^{\infty} dt\hat{H}_{sFWM}(t) =& \frac{i\gamma_{SiP_1P_2}\hbar\omega_{ISP_1P_2}}{2\pi}\int_0^L dx \iiiint d\omega_p 1\, d\omega_p 2\, d\omega_i\, d\omega_s \\ &\times \alpha_p(\omega_{p1})\alpha_p(\omega_{p2})\hat{a}_i^\dagger(\omega_i)\hat{a}_s^\dagger(\omega_s) \\ &\times e^{i\Delta\beta x}\delta(\omega_{p1}+\omega_{p2}-\omega_i-\omega_s) + \text{h.c.}\,. \end{aligned} \tag{A.12}$$

This allows us to eliminate the integral involving ω_{p2}. Ultimately, we can proceed with the integration over x. Integrating on the L path the exponential part will give:

$$\begin{aligned} &\frac{\gamma_{SiP_1P_2}\hbar\omega_{ISP_1P_2}L}{2\pi}\int d\omega_P d\omega_i d\omega_s a_i^\dagger(\omega_i)a_s^\dagger(\omega_s) \\ &\qquad\times \alpha_P(\omega_{P1})\alpha_P(\omega_i+\omega_s-\omega_{P1})\phi(\omega_s,\omega_i,\omega) + \text{h.c.}\,, \end{aligned} \tag{A.13}$$

where the function ϕ is the phase matching function, given by the following relation:

$$\phi(\omega_s, \omega_i, \omega) = e^{i\Delta k(\omega_s,\omega_i,\omega)L/2}\text{sinc}\left(\frac{\Delta k(\omega_s, \omega_i, \omega)L}{2}\right). \tag{A.14}$$

L is the waveguide length and Δk is the phase mismatch parameter [284].

Since our primary focus is on the weak interactions, we can expand the unitary evolution operator from eq. (A.11) using a first-order Taylor series, resulting in:

$$\begin{aligned}
|\Psi\rangle &= \hat{\mathcal{U}}\,|0,0\rangle_{i,s} = \\
&= \left[\mathcal{I} + \frac{\gamma_{SiP_1P_2}\hbar\omega_{ISP_1P_2}L}{2\pi}\int d\omega_P d\omega_i d\omega_s a_i^\dagger(\omega_i)a_s^\dagger(\omega_s)\right. \\
&\left.\times\, \alpha_P(\omega_{P1})\alpha_P(\omega_i+\omega_s-\omega_{P1})\phi(\omega_s,\omega_i,\omega) + \text{h.c.}\right]|0,0\rangle_{i,s} \\
&= |0,0\rangle_{i,s} + |II\rangle_{i,s}\,.
\end{aligned} \tag{A.15}$$

The biphoton wavefunction, denoted as $|II\rangle_{i,s}$, can be expressed in a general form using a two-dimensional complex function $F(\omega_i, \omega_s)$, referred to as the JSA. The JSA can be written as

$$F(\omega_s, \omega_i) = \int \mathrm{d}\omega\, \alpha_P(\omega)\alpha_P(\omega_s+\omega_i-\omega)\phi(\omega_s,\omega_i,\omega)\,, \tag{A.16}$$

where $\alpha(\omega)$, which is typically thought of as having a Gaussian profile, is the complex amplitudes of the pump beams. As we can see from eq. (A.16), the JSA receives two contributions: one from the shape of the pump beams and one that contains the kinematic parameter Δk. The JSA quantifies the probability density for the creation of the pair's first photon in the ω_s mode and the second photon in the ω_i mode. The $|II\rangle_{i,s}$ can be write:

$$|II\rangle_{i,s} = \iint d\omega_i\, d\omega_s\, F(\omega_i,\omega_s)\hat{a}_i^\dagger(\omega_i)\hat{a}_s^\dagger(\omega_s)\,|0,0\rangle_{i,s}\,. \tag{A.17}$$

Let's follow the backward Heisenberg picture approach and the approach in the reference [26]. The mean power linked to a single photon from each pair generated through CW sFWM in a channel waveguide pumped at ω_P is:

$$P_I = \frac{\hbar\omega_p}{\mathcal{T}}(\gamma_{SIP1P2}P_P L)^2\,, \tag{A.18}$$

where

$$\mathcal{T} = \frac{2\pi}{\int_0^{\omega_P} d\Omega(1-\Omega/\omega_P)^2\text{sinc}^2\left[(2k(\omega_P)-k(\omega_P+\Omega)-k(\omega_P-\Omega))\,L/2\right]}\,, \tag{A.19}$$

where $\Omega = \omega_1 - \omega_P$ representing positive detuning from ω_P. If, instead of considering the entire sFWM spectrum, we opt to concentrate on a limited spectral range with a bandwidth of $2\pi B$, we discover that

$$\mathcal{T}(\Omega) \approx \left[B\text{sinc}^2\left[(2k(\omega_P)-k(\omega_P+\Omega)-k(\omega_P-\Omega))L/2\right]\right]^{-1}. \tag{A.20}$$

From this, we can write the generated power of idler (signal) photons through the sFWM process in the waveguide as

$$P_{i(s)} = B\hbar\omega_p(\gamma_{SIP1P2}P_P L)^2\text{sinc}^2\left[(2k(\omega_P)-k(\omega_P+\Omega)-k(\omega_P-\Omega))L/2\right]. \tag{A.21}$$

In the case of the micro-ring resonator, this relation becomes:

$$P_{i(s)} = \frac{\hbar\omega_{\mu_P}}{\mathcal{T}}(\gamma P_P)^2 \frac{16\nu_{\mu_P}^2}{\pi^2\omega_{\mu_P}^2} Q_{\mu_P}^2 \,, \tag{A.22}$$

where Q_{μ_P} is the quality factor of the ring, R is the radius, and ν_{μ_P} is the group velocity. Considering a limited spectral range with a bandwidth of $2\pi B$, the relation will be:

$$P_{i(s)} = \hbar B(\gamma P_P)^2 \frac{64\nu_{\mu_P}^4}{\pi^2\omega_{\mu_P}^3} \frac{Q_{\mu_P}^4}{R^2} \,, \tag{A.23}$$

and for the unfiltered case:

$$P_{i(s)} = \hbar(\gamma P_P)^2 \frac{8\nu_{\mu_P}^4}{\pi^2\omega_{\mu_P}^2} \frac{Q_{\mu_P}^3}{R^2} \,. \tag{A.24}$$

There exists a distinction in describing $F(\omega_s, \omega_i)$ within the context of microring resonators. In this scenario, the enhancement effect attributed to the microring can be factored in. The expression for $F(\omega_s, \omega_i)$ is as follows:

$$F(\omega_s, \omega_i) = l_s(\omega_s) l_i(\omega_i) \int \mathrm{d}\omega\, \alpha_P(\omega) l_p(\omega) \alpha_P(\omega_s + \omega_i - \omega) l_p(\omega_s + \omega_i - \omega) \phi(\omega_s, \omega_i, \omega). \tag{A.25}$$

Here, $l_j(\omega)$ (where $j = i, s$) represents the Lorentzian function, depicting the linewidth of the microring resonance involved in the respective resonance process.

Appendix B

Modeling detection probabilities

The appendix outlines the methodology detailed in the supplementary of our work [130], aimed at modeling both linear and nonlinear losses involving pump, signal, and idler photons in photonic devices. The approach involves solving a system of differential equations governing pulse propagation, similar to the methodology reviewed in [57]. These equations account for phenomena such as TPA, XTPA, FCA, and propagation losses.

We assume an equal distribution of pump power between the TE0 and TE1 polarizations, leading to differential equations for the pump (P_p) and the signal/idler (P_j):

$$\frac{\partial P_p}{\partial z} = -\sigma_p N(P_p) P_p - 2\bar{\gamma}_{TPA} P_p^2 - \bar{\alpha}_p P_p \,, \tag{B.1a}$$

$$\frac{\partial P_j}{\partial z} = -\sigma_j N(P_p) P_j - 4\bar{\gamma}_{XTPA,j} P_p P_j - \alpha_j P_j \,, \tag{B.1b}$$

Here, $N(P_p) = \frac{\tau_c \bar{\gamma}_{TPA}}{\hbar\omega_p \mathcal{A}_0} P_p^2$ denotes the density of free carriers, where τ_c is the free carrier lifetime, ω_p is the pump frequency, and $\mathcal{A}_0$ is the waveguide area. The TPA parameter is computed as $\bar{\gamma}_{TPA} = \langle \gamma_{TPA,TE0}, \gamma_{TPA,TE1} \rangle$, where we average the nonlinear TPA parameters for the pump over the TE0 and TE1 modes. Similarly, the absorption coefficient for pump propagation, $\bar{\alpha}_p$, is calculated as the average of the absorption coefficients for the pump on the TE0 and TE1 modes. The XTPA parameter is determined as $\bar{\gamma}^j_{XTPA} = \langle \gamma^j_{XTPA,TE0}, \gamma^j_{XTPA,TE1} \rangle$, where $j = s, i$ refers to the signal and idler, respectively.

The expressions for $\gamma_{TPA,m}$ and $\gamma^j_{XTPA,m}$ depend on the mode of the pump waveguide m and are derived as follows [57]:

$$\gamma_{TPA,m} = \frac{1}{2} n_{g,m}^2 n_{Si}(\omega_p)^2 \beta_{TPA}(\omega_p) \frac{\int_{\mathcal{A}_0} |e_m(r)|^4 dA}{\left(\int_{\mathcal{A}_\infty} n_p(r)^2 |e_m(r)|^2 dA\right)^2} \,, \tag{B.2a}$$

$$\begin{aligned} \gamma^j_{XTPA,m} =& \frac{1}{2} \frac{\omega_j}{\bar{\omega}_{j,p}} n_{g,m} n_{g,j} n_{Si}(\bar{\omega}_{j,p})^2 \beta_{TPA}(\bar{\omega}_{j,p}) \times \\ & \times \frac{\int_{A_0} e_m(r) e_j(r) e_j^*(r) e_m^*(r) dA}{\int_{A_\infty} n_p(r)^2 |e_m(r)|^2 dA \int_{A_\infty} n_j^2(r) |e_j(r)|^2 dA} \,. \end{aligned} \tag{B.2b}$$

Here, $m = TE0, TE1$ refers to the pump mode and $j = i, s$. The mode for the idler and the signal is implied in the notation of eq. (B.2b), being TE1 for the signal and TE0 for the idler. $\bar{\omega}_{j,p} = (\omega_p + \omega_j)/2$ denotes the average frequency between ω_j and ω_p, $n_{g,m/j}$ represents the group index, $n_{Si}(\omega)$ is the bulk refractive index of silicon, $n_p(r)$

stands for the local distribution of the refractive index, $\beta_{TPA}(\omega)$ is the TPA coefficient of silicon, $e_m(r)$ denotes the optical field profile, and A_∞ represents the infinite orthogonal plane.

The coefficients and functions have been evaluated at the wavelength of the corresponding field: $\lambda = 1550$ nm for m or p, and $\lambda = 1260$ nm and $\lambda = 2015$ nm for i and s, respectively. Analogous to the TPA parameter for the XTPA, a non-trivial parameter needs to be measured, which, to date, cannot be found in the literature. However, it has been demonstrated that a good approximation is to use $\beta_{\mathrm{TPA}}(\bar{\omega}_j, p)$, calculated at the average frequency of the two photons involved in the XTPA process [151, 285]. With eq. (B.1), we model the linear and nonlinear losses for signal and idler channels as classical fields, using the optical power of the field instead of the single photon formalism [286]. The resulting transmission efficiency can be interpreted as the transmission probability through the waveguide experienced by signal and idler single photons.

By solving eqs. (B.1), we obtain the effective on-chip pump power $P_p(z)$ and the transmission efficiency of the signal and idler photons generated at z along the waveguide axis, denoted as $\eta_j(z)$. We calculate the total transmission as follows:

$$\eta_j(z) = \eta_j^{on}(z)\eta_j^{off}\,, \tag{B.3}$$

where we separate the effect of losses happening on the chip (such as propagation and nonlinear losses) from those happening off the chip (such as fiber-chip coupling, filtering, and detection losses). From eq. (B.1b), we calculate $\eta_j^{on}(z)$ as:

$$\eta_j^{on}(z) = e^{-\int_z^L \mathrm{A}_j(z')\,dz'} \tag{B.4a}$$

$$\mathrm{A}_j(z) = \sigma_j N(P_p) + 4\bar{\gamma}_{\mathrm{XTPA},j}P_p + \alpha_j\,, \tag{B.4b}$$

where L is the waveguide length. From this study, the average detection probability of singles and coincidences can be obtained as:

$$p_{\mathrm{si}} = \frac{\eta_{ND}}{L}\int_0^L \xi P_p^2(z)\eta_i(z)\eta_s(z)dz\,, \tag{B.5a}$$

$$p_i = \frac{\eta_{ND}}{L}\int_0^L \xi P_p^2(z)\eta_i(z)dz\,, \tag{B.5b}$$

$$p_s = \frac{1}{L}\int_0^L \xi P_p^2(z)\eta_s(z)dz\,, \tag{B.5c}$$

where we multiply the probability of generating a pair at z ($\xi P_p(z)^2$) with the probability that the photons are transmitted from z to the idler/signal detector ($\eta_i = s(z)$). We also consider the nonlinear response η_{ND} of the idler detector. In the low power range, we approximate eqs. (B.5) as the product between the average generation probability and the average transmission efficiency, yielding

$$p_{\mathrm{si}} \approx \frac{1}{L}\int_0^L \xi P_p^2(z)dz\frac{\eta_{ND}}{L}\int_0^L \eta_i(z)dz\frac{1}{L}\int_0^L \eta_s(z)dz \approx \xi\bar{P}_p^2\bar{\eta}_i\bar{\eta}_s\eta_{ND}\,, \tag{B.6a}$$

$$p_i \approx \frac{1}{L}\int_0^L \xi P_p^2(z)dz\frac{\eta_{ND}}{L}\int_0^L \eta_i(z)dz \approx \xi\bar{P}_p^2\bar{\eta}_i\eta_{ND}\,, \tag{B.6b}$$

$$p_s \approx \frac{1}{L}\int_0^L \xi P_p^2(z)dz\frac{1}{L}\int_0^L \eta_s(z)dz \approx \xi\bar{P}_p^2\bar{\eta}_s\,, \tag{B.6c}$$

where

$$\bar{P}_p = \sqrt{\frac{1}{L}\int_0^L P_p^2(z)dz}\,, \tag{B.7a}$$

$$\bar{\eta}_j = \bar{\eta}_j^{on}\bar{\eta}_j^{off}\,, \tag{B.7b}$$

$$\bar{\eta}_j^{on} = \frac{1}{L}\int_0^L \eta_j^{on}(z)dz\,. \tag{B.7c}$$

The reasoning behind this approximation stems from the congruence between the non-approximated and approximated probability values in the power range below 0.5 W, as illustrated in Fig. B.1.

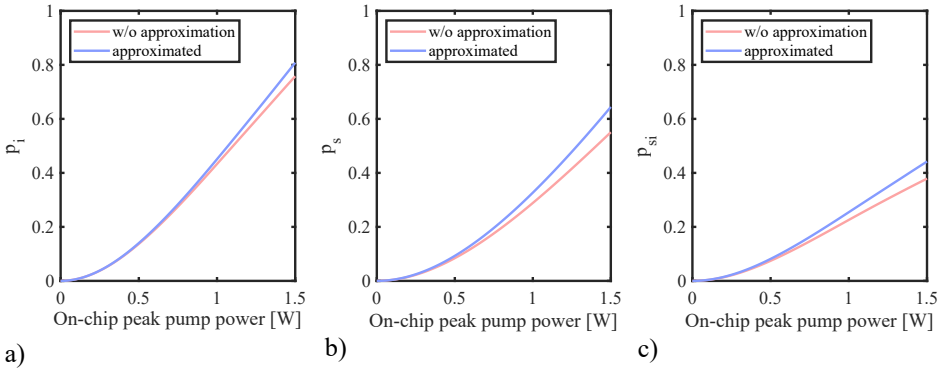

Figure B.1: Comparison of the p_i (a), p_s (b), and $p_s i$ (c) approximated and non-approximated values. Eq. (B.6) calculates the approximated values, and eq. (B.5) calculates the non-approximated values.

Parameter	Value	Reference
$\alpha_{p,TE0}$	$0.104\,\mathrm{cm}^{-1}$ ($0.45\,\mathrm{dB\,cm}^{-1}$)	Experimental
$\alpha_{p,TE1}$	$0.414\,\mathrm{cm}^{-1}$ ($1.80\,\mathrm{dB\,cm}^{-1}$)	Simulated
α_i	$0.067\,\mathrm{cm}^{-1}$ ($0.29\,\mathrm{dB\,cm}^{-1}$)	Simulated
α_s	$0.758\,\mathrm{cm}^{-1}$ ($3.29\,\mathrm{dB\,cm}^{-1}$)	Simulated
σ_p	$1.45\times10^{-21}\,\mathrm{m}^2$	[151]
σ_i	$0.96\times10^{-21}\,\mathrm{m}^2$	[151]
σ_s	$2.45\times10^{-21}\,\mathrm{m}^2$	[151]
$\beta_{TPA}(\omega_p)$	$7.5\times10^{-12}\,\mathrm{m\,W}^{-1}$	[57]
$\beta_{TPA}(\overline{\omega}_{i,p})$	$17.5\times10^{-12}\,\mathrm{m\,W}^{-1}$	[57]
$\beta_{TPA}(\overline{\omega}_{s,p})$	$7\times10^{-12}\,\mathrm{m\,W}^{-1}$	[57]
τ_c	50 ps	from fit
$n_{g,TE0}$	3.7369	Simulated
$n_{g,TE1}$	3.7911	Simulated
$n_{g,i}$	3.8177	Simulated
$n_{g,s}$	3.7714	Simulated
$n_{Si}(\omega_p)$	3.4757	[152]
$n_{Si}(\overline{\omega}_{i,p})$	3.4907	[152]
$n_{Si}(\overline{\omega}_{s,p})$	3.4624	[152]
$\mathcal{A}_0$	$1.95\times0.49\,\mathrm{mm}^2$	Experimental
$\gamma_{TPA,TE0}$	$7.00\,\mathrm{m}^{-1}\,\mathrm{W}^{-1}$	Calculated from eq. (B.2a)
$\gamma_{TPA,TE1}$	$6.81\,\mathrm{m}^{-1}\,\mathrm{W}^{-1}$	Calculated from eq. (B.2a)

$\gamma^{i}_{X,TPA,TE0}$	$5.38\,\mathrm{m}^{-1}\,\mathrm{W}^{-1}$	Calculated from eq. (B.2b)
$\gamma^{i}_{X,TPA,TE1}$	$3.44\,\mathrm{m}^{-1}\,\mathrm{W}^{-1}$	Calculated from eq. (B.2b)
$\gamma^{s}_{X,TPA,TE0}$	$0.97\,\mathrm{m}^{-1}\,\mathrm{W}^{-1}$	Calculated from eq. (B.2b)
$\gamma^{s}_{X,TPA,TE1}$	$1.50\,\mathrm{m}^{-1}\,\mathrm{W}^{-1}$	Calculated from eq. (B.2b)

Table B.1: Parameters used for TPA, XTPA, and FCA simulation.

In Table B.1, we present the values of the parameters used in the modeling. These values are reported also in the main text. The lifetime of free carriers, denoted by τ_c, is highly dependent on the waveguide's cross-section and the specific fabrication process. In the model, this value is estimated by matching the simulated pump transmission, obtained by solving eq. (B.1a), with the experimental one. The outcome of this fitting process is presented in Figure B.2(a). The transmission measurement has been conducted in the same waveguide used for the heralding experiment. In Fig. B.2(b) the transmission efficiency η_{ND} is reported.

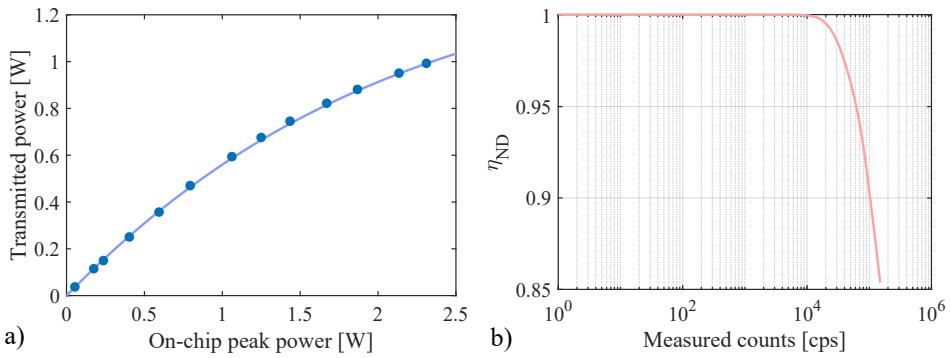

Figure B.2: a) Power transmitted compared to input power. The lines originate from the simulation, while the dots represent the experimental data. b) Transmission efficiency η_{ND}.

Appendix C

Simulation with thermal and poissonian statistics of $g^{(2)}$ and $g_H^{(2)}$

C.1 Heralded $g^{(2)}$

According to [50], the photons produced by the sFWM process can follow either a thermal or Poissonian distribution. The specific distribution depends on the degree of single-mode emission. When emission is single-mode, the statistics tend to be thermal. However, when there are multiple modes present, the statistics tend to be Poissonian. This difference also affects the behavior of the heralded second-order correlation function ($g_H^{(2)}$) [65]. As described in eq. (1.134), the $g_H^{(2)}$ is:

$$g_H^{(2)}(\Delta t) = \frac{R_{s_1 s_2 i}}{R_{s_1 i}(t) R_{s_2 i}(\Delta t)} R_i(t) = \frac{p_{s_1 s_2 i} p_i}{p_{s_1 i} p_{s_2 i}}, \tag{C.1}$$

where the idler photon is considered as herald and the signal photon is performed in the HBT interferometric measurement. The p_{s1s2i} is the probability of detecting the three-fold coincidences at the three detectors. p_{ij} (j = s1,s2) is the probability of having a two-fold coincidence between the j-detector and the idled one. p_i is the probability of having a click at the idler detector. The probabilities associated with different coincidence events involving signal and/or noise detections are evaluated per pulse or per coincidence window. By considering all possible events leading to three-fold coincidences, the expression for p_{s1s2i} is given by:

$$
\begin{aligned}
p_{s1s2i} = & \sum_{n=2} n^2(n-1)\mathcal{P}(n)\eta_{s1}\eta_{s2}\eta_i \quad \text{(2 signal photons, 1 idler photon)} \\
& + \sum_{n=1} n^2\mathcal{P}(n)(\eta_{s1}d_2 + d_1\eta_{s2})\eta_i \quad \text{(1 signal photon, 1 signal noise, 1 idler photon)} \\
& + \frac{1}{2}\sum_{n=2} n(n-1)\mathcal{P}(n)\eta_{s1}\eta_{s2}d_i \quad \text{(2 signal photons, 1 idler noise)} \\
& + \sum_{n=1} n\mathcal{P}(n)\eta_{s1}d_2d_i \quad \text{(1 signal photon, 1 signal noise, 1 idler noise)} \\
& + \sum_{n=1} n\mathcal{P}(n)d_1\eta_{s2}d_i \quad \text{(1 signal noise, 1 signal photon, 1 idler noise)} \\
& + \sum_{n=1} n\mathcal{P}(n)d_1d_2\eta_i \quad \text{(2 signal noise, 1 idler photon)} \\
& + d_1d_2d_i \quad \text{(2 signal noise, 1 idler noise)}\,.
\end{aligned}
\tag{C.2}
$$

This equation accounts for all possible events leading to three-fold coincidences involving signal and/or noise detections at the signal and idler detectors. $\mathcal{P}(n)$ is the photon number distribution, n is the number of pairs, d_j ($j = 1, 2$) and d_i are the noise detection probabilities at the signal and idler detectors respectively, η_j and η_i are the signal and idler channel transmissions respectively. The expression for p_{ji} is given by:

$$
\begin{aligned}
p_{ji} = & \sum_{n=1} n^2\mathcal{P}(n)\eta_j\eta_i\,(\text{1 signal photon, 1 idler photon}) \\
& + \sum_{n=1} n\mathcal{P}(n)\eta_j d_i\,(\text{1 signal photon, 1 idler noise}) \\
& + \sum_{n=1} n\mathcal{P}(n)d_j\eta_i\,(\text{1 signal noise, 1 idler photon}) \\
& + d_jd_i\,(\text{1 signal noise, 1 idler noise})\,.
\end{aligned}
\tag{C.3}
$$

The photon number distribution $\mathcal{P}(n)$ for Poissonian emission is given by:

$$
\mathcal{P}(n) = \frac{\bar{n}^n}{n!}e^{-\bar{n}}\,, \tag{C.4}
$$

where $\bar{n} = \xi P_p^2$ is the average number of pairs per pulse. In this situation, the probability for p_{12i} become:

$$
\begin{aligned}
p_{12i} = & \bar{n}^2(2+\bar{n})\eta_1\eta_2\eta_i \\
& + \bar{n}(2\bar{n}+1)(\eta_1 d_2 + d_1\eta_2)\eta_i \\
& + \bar{n}^2\eta_1\eta_2 d_i \\
& + \bar{n}\eta_1 d_2 d_i \\
& + \bar{n}d_1\eta_2 d_i \\
& + \bar{n}d_1 d_2\eta_i \\
& + d_1 d_2 d_i\,.
\end{aligned}
\tag{C.5}
$$

For p_{ji}:

$$\begin{aligned} p_{ji} &= \bar{n}(\bar{n}+1)\eta_j\eta_i \\ &+ \bar{n}\eta_j d_i \\ &+ \bar{n} d_j \eta_i \\ &+ d_j d_i \,. \end{aligned} \tag{C.6}$$

Similarly, for thermal photon number distribution, $\mathcal{P}(n)$ is given by:

$$\mathcal{P}(n) = \frac{\bar{n}^n}{(1+\bar{n})^{n+1}} \,. \tag{C.7}$$

For p_{12i}:

$$\begin{aligned} p_{12i} &= \frac{2(3\bar{n}^4 + 5\bar{n}^3 + 2\bar{n}^2)}{1+\bar{n}} \eta_1\eta_2\eta_i \\ &+ \bar{n}(2\bar{n}+1)\bar{n}(2\bar{n}+1)(\eta_1 d_2 + d_1\eta_2)\eta_i \\ &+ \bar{n}^2\eta_1\eta_2 d_i \\ &+ \bar{n}\eta_1 d_2 d_i \\ &+ \bar{n} d_1 \eta_2 d_i \\ &+ \bar{n} d_1 d_2 \eta_i \\ &+ d_1 d_2 d_i \,. \end{aligned} \tag{C.8}$$

For p_{ji}:

$$\begin{aligned} p_{ji} &= \bar{n}(2\bar{n}+1)\eta_j\eta_i \\ &+ \bar{n}\eta_j d_i \\ &+ \bar{n} d_j \eta_i \\ &+ d_j d_i \,. \end{aligned} \tag{C.9}$$

In both Poissonian and thermal distribution cases:

$$p_i = \bar{n}\eta_i + d_i \,. \tag{C.10}$$

This simulation approach allows us to model the behavior of the second-order correlation function under different emission statistics scenarios, which can be valuable for understanding and analyzing experimental results. This simulation approach was used to generate the values for $g_H^{(2)}$ in Fig. 4.9 reported in chapter 4.

C.2 Unheralded $g^{(2)}$

To simulate the second-order correlation function $g^{(2)}$, we employ a strategy similar to that used for the heralded case. The $g^{(2)}$ function is defined as eq. (1.131):

$$g^{(2)} = \frac{p_{12}}{p_1 p_2} \,. \tag{C.11}$$

where p_{12} represents the probability of coincidence between the two signal detectors, and p_1 and p_2 denote the probabilities of single detection for the two signal detectors. By considering all possible coincidence events, the coincidence probability p_{12} can be calculated as:

$$p_{12} = \sum_{n=2}^{n} n(n-1)\mathcal{P}(n)\eta_1\eta_2 + \sum_{n=1}^{n} n\mathcal{P}(n)(\eta_1 d_2 + d_1\eta_2) + d_1 d_2\,, \tag{C.12}$$

where $\mathcal{P}(n)$ represents the photon number distribution, η_j denotes the transmission probability for signal detector j, and d_j represents the noise detection probability at signal detector j ($j = 1, 2$).

The probabilities of single detection p_j are given by:

$$p_j = \sum_{n=1}^{n} n\mathcal{P}(n)\eta_j + d_j\,. \tag{C.13}$$

For a source with Poisson emission statistics, solving eq. (C.12) yields:

$$p_{12} = \bar{n}^2\eta_1\eta_2 + \bar{n}(\eta_1 d_2 + d_1\eta_2) + d_1 d_2\,, \tag{C.14}$$

where $\bar{n}$ is the average number of pairs per pulse. Similarly, for a source with thermal emission statistics:

$$p_{12} = 2\bar{n}^2\eta_1\eta_2 + \bar{n}(\eta_1 d_2 + d_1\eta_2) + d_1 d_2\,. \tag{C.15}$$

The single probabilities remain the same for both statistics:

$$p_j = \bar{n}\eta_j + d_j\,. \tag{C.16}$$

Theoretical values of $g^{(2)}$ can be calculated based on these equations. The thermal case represents an upper bound for $g^{(2)}$, while the Poissonian case represents a lower bound.

This simulation approach was used to generate the values for $g^{(2)}$ in Fig. 4.10 reported in chapter 4. It's worth noting that the simulation based on the JSI follows the methodology reported in Signorini et al. [115].

Appendix D

Quantum bits

D.1 Qubits

Quantum computing is based on the concept of quantum bits or qubits, which are similar to classical bits. However, unlike classical bits that can only be in a state of 0 or 1, qubits are two-level quantum systems with two basis states, usually represented as $|0\rangle$ and $|1\rangle$. In addition to these states, qubits can also exist in a linear combination of both, unlike classical bits. If a quantum system has n qubits, its Hilbert space will have 2^n dimensions, which means it can offer 2^n mutually orthogonal quantum states. This is a significant distinction when compared to classical bits, where n bits can only represent up to 2^n distinct entities.

The state of a qubit is described by complex probability amplitudes, enabling a combination of classical states to be represented. A general single-qubit can be represented as:

$$|\psi\rangle = \alpha|0\rangle + \beta|1\rangle\,, \tag{D.1}$$

where α and β are the complex numbers representing the probability amplitudes of $|0\rangle$ and $|1\rangle$ respectively. This state is normalized such that $|\alpha|^2 + |\beta|^2 = 1$, ensuring a total probability of 1. The outcome of a measurement on $|\psi\rangle$ cannot be predicted with certainty. This probabilistic nature of measurement outcomes is a fundamental aspect of quantum mechanics and distinguishes it from classical mechanics. The consideration of N qubits leads to work in the 2N-dimensional Hilbert space C^{2N}. As it is shown in Fig. D.1, the state $|\psi\rangle$ can be visualized as a point of the Bloch sphere S^2 in $\mathbb{R}^3$ and it is describe as:

$$|\psi\rangle = \cos\left(\frac{\theta}{2}\right)|0\rangle + e^{i\phi}\sin\left(\frac{\theta}{2}\right)|1\rangle\,. \tag{D.2}$$

Here, θ and ϕ are parameters that define the amplitudes and phases of the superposition. The angle θ lies between 0 and π, while ϕ lies between 0 and 2π.

A photonic qubit can be represented using a dual-rail encoding scheme illustrated in Fig. D.2. In this scheme, a photon in the upper waveguide represents the state $|0\rangle$, while a photon in the lower waveguide represents the state $|1\rangle$.
Unitary operations on qubits are called quantum *logic gates*. Quantum gates are represented by unitary operator U that describe how they transform the quantum state of the qubits on which they act. The general computational basis representation of U can be expressed as:

$$U = e^{\frac{i\theta}{2}} \begin{pmatrix} e^{i(\phi_1+\phi_2)/2}\cos\left(\frac{\theta}{2}\right) & e^{i(\phi_1-\phi_2)/2}\sin\left(\frac{\theta}{2}\right) \\ -e^{-i(\phi_1-\phi_2)/2}\sin\left(\frac{\theta}{2}\right) & e^{-i(\phi_1+\phi_2)/2}\cos\left(\frac{\theta}{2}\right) \end{pmatrix}, \tag{D.3}$$

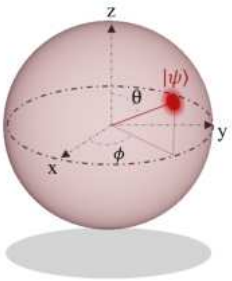

Figure D.1: Bloch sphere representation of the qubit $|\psi\rangle$. The angles θ and ϕ are shown.

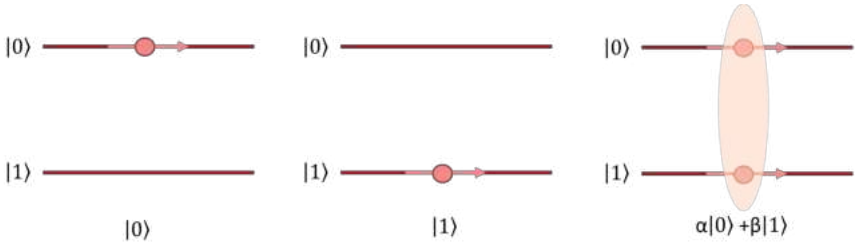

Figure D.2: The qubit representation in path encoding.

with $\theta \in \left(0, \frac{\pi}{2}\right)$ and $\phi_1, \phi_2 \in (0, 2\pi)$.

In integrated photonics it is possible to realize the unitary operator U with linear optical components: a MZI with two additional PSs positioned at the input and output. The unitary matrix U is:

$$U = R_z(\Phi)R_y(\theta)R_z(\Psi) = e^{i\phi/2}\begin{pmatrix} e^{i\Phi/2} & 0 \\ 0 & e^{-i\Phi/2} \end{pmatrix}\begin{pmatrix} \cos(\theta/2) & \sin(\theta/2) \\ -\sin(\theta/2) & \cos(\theta/2) \end{pmatrix}\begin{pmatrix} e^{i\Psi/2} & 0 \\ 0 & e^{-i\Psi/2} \end{pmatrix}. \tag{D.4}$$

Specifically, a PS inducing a relative phase ϕ between the qubit rails corresponds to a transfer matrix $R_z(\phi)$, while an MZI with phase difference θ is described by $R_y(\theta)$. The device illustrated in Fig. D.3 facilitates any rotation within the two-dimensional Hilbert space defined by the qubit's computational basis. Once a target transformation U is given, we can tune the phases Ψ, θ, and Φ by acting on three separate PS (e.g., by locally heating one of the rails). Using this integrated device is possible to obtain, for

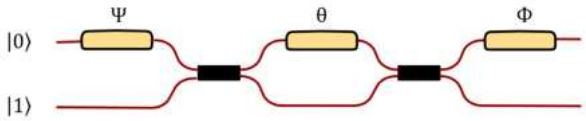

Figure D.3: The MZI with two additional phases Ψ and Φ.

instance, the single-qubit rotation gates and the Hadamard (H) gate expressed as:

$$R_x(\theta) = e^{-i\theta\sigma_x/2}; \quad R_y(\theta) = e^{-i\theta\sigma_y/2}; \quad R_z(\theta) = e^{-i\theta\sigma_z/2}; \quad H = \frac{1}{\sqrt{2}}\begin{pmatrix} 1 & 1 \\ 1 & -1 \end{pmatrix}. \tag{D.5}$$

where the σ_x, σ_y and σ_z are the Pauli gates described as:

$$\sigma_x = \begin{pmatrix} 0 & 1 \\ 1 & 0 \end{pmatrix}, \quad \sigma_y = \begin{pmatrix} 0 & -i \\ i & 0 \end{pmatrix}, \quad \sigma_z = \begin{pmatrix} 1 & 0 \\ 0 & -1 \end{pmatrix}. \tag{D.6}$$

Precisely considering the eq. (D.4) we observe the following:

- $R_z(\Phi)$: A PS corresponds to the rotation operator $R_z(\Phi)$. Setting $\Phi = \pi$ applies the σ_z operator, up to a global phase;
- $R_y(\theta)$: A MZI corresponds to the rotation operator $R_y(\theta)$ Setting $\theta = \pi$ applies the σ_y operator, up to a global phase.
- $R_x(\theta)$: The rotation operator $R_x(\theta)$ can be derived from eq. (D.4) as $R_x(\theta) = R_z(\pi/4)R_y(\theta)R_z(-\pi/4)$. Therefore, choosing $\theta = \pi/2$ applies σ_x, up to a global phase.
- H : The Hadamard $H = (\sigma_x + \sigma_z)/\sqrt{2}$, which has a matrix representation $\frac{1}{\sqrt{2}}\begin{bmatrix} 1 & 1 \\ 1 & -1 \end{bmatrix}$ in the computational basis, can be obtained by applying an MZI with $\theta = \pi/2$, up to an overall phase.

D.2 Qudits

A qu*d*it is used when more than two binaries are used to store a single photon, where d is the number of binaries. In Fig. D.4 is reported the integrated photonic qudit representation formed by d waveguides.

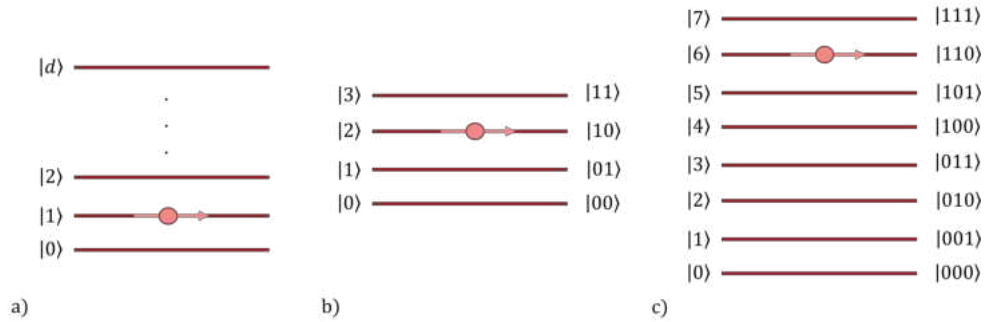

Figure D.4: General qu*d*it representation in path encoding in d waveguides (a). The case of 4 waveguides (b) and 8 waveguides (c) is illustrated.

This approach enhances the dimensionality of the Hilbert space while reducing the requisite number of photons. However, it entails managing additional spatial modes, leading to increased circuit depths for photon traversal. For instance, in Fig. D.4(b), with a binary $d = 4$, the following mapping is achieved:

$$|0\rangle \to |00\rangle, \quad |1\rangle \to |01\rangle, \quad |2\rangle \to |10\rangle, \quad |3\rangle \to |11\rangle,$$

where $|i\rangle$ $(i = 0, 1, 2, 3)$ denotes the binary storing the photon, and $|mk\rangle$ $(m, k = 0, 1)$ represents a two-qubit state. In this scenario, the four-dimensional qudit is referred to as a ququart. The computational capacity of a single photon confined within a ququart remains consistent within the Hilbert space H_4, which is equivalent to that of two photons in two dimensions (qubits). Generally, a system comprising n photons in $d = 2^k$ dimensions yields a $d^n = 2^{kn}$-dimensional Hilbert space, equivalent to kn qubits. For a three-qubit state, a $d = 8$ configuration is utilized, as depicted in Figure D.4(c).

The most general unitary transformation in the d-dimensional qudit space is governed by an SU(d), just as qubit manipulation requires an SU(2). Any operation U belonging to SU(d) can be systematically constructed by iteratively applying SU(2) operations, each acting on a subspace characterized by just two modes. This universal decomposition, called the Reck scheme [287], consists of a triangular lattice of $\frac{d(d-1)}{2}$ beamsplitters with different phase and reflectivity (called Givens rotations). By implementing PS and MZI for each rotation, an ensemble of $\frac{d(d-1)}{2}$ components becomes available for synthesizing any U within SU(d). Fig. D.5(a) illustrates a Reck scheme applicable for $d = 6$. In contrast, the Clements scheme [233] offers an alternative approach, leveraging a de-

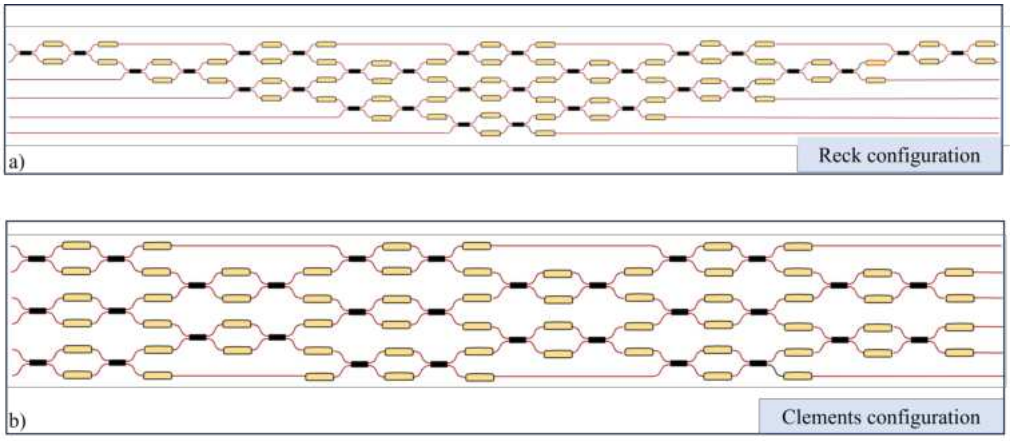

Figure D.5: The Reck (a) and the Clements (b) schemes are shown.

composition strategy that utilizes a square lattice of beamsplitters and phase shifters. As illustrated in Fig. D.5(b) for $d = 6$, this scheme provides a structured arrangement that ensures uniform optical depth along each path from input to output. Despite employing an equivalent number of tunable elements as the Reck scheme, the Clements scheme offers the advantage of maintaining consistent optical characteristics throughout the entire circuit.

It's important to recognize the multidimensional approach's limits, though. The dimensionality of the Hilbert space grows exponentially with the number of photons but scales polynomially with the number of modes. As the system size grows, this exponential escalation demands a matching rise in the resources needed, such as phase shifters and beamsplitters. Therefore, even though the multidimensional approach has some benefits, especially with regard to encoding efficiency, the exponential resource requirements that come with greater system sizes limit its scalability.

Appendix E

Model for non ideal characteristics of the PIC

This section discusses imperfections in the integrated photonic hardware used in the swap test demonstration described in Chapter 6. The actual performance of this hardware may diverge from theoretical predictions. In-depth examinations paralleling this study have been conducted in prior works, which offer additional insights into our methodologies [288–290]. Specifically, we address the following considerations:

1. MMIs do not precisely execute the matrix of a perfect beam splitter because of manufacturing discrepancies;
2. Couplers lack a perfect unitary transfer function;
3. Inaccuracies in calibration and power supply influence the precise current values set for each PS.

To account for the first point, the matrix description of an MMI is modified as follows:

$$U_{\mathrm{MMI}}(t,r) = \begin{pmatrix} t & \mathrm{i}r \\ \mathrm{i}r & t \end{pmatrix}, \tag{E.1}$$

where $t \neq r \neq \frac{1}{\sqrt{2}}$. It is important to recognize that typically, $t^2 + r^2 \leq 1$. To explicitly account for this, we reformulate the operator as:

$$U_{\mathrm{MMI}}(\alpha,\beta) = \beta \begin{pmatrix} \cos(\alpha) & \mathrm{i}\sin(\alpha) \\ \mathrm{i}\sin(\alpha) & \cos(\alpha) \end{pmatrix}, \tag{E.2}$$

$$\beta = \sqrt{t^2 + r^2}, \quad \cos(\alpha) = \frac{t}{\sqrt{t^2 + r^2}}, \quad \sin(\alpha) = \frac{r}{\sqrt{t^2 + r^2}}. \tag{E.3}$$

Regarding point 2, we conceptualize our intersection zone in the swap test as:

$$U_{\mathrm{CSWAP}}(T) = \sqrt{T} \begin{pmatrix} 1 & 0 & 0 & 0 & 0 & 0 & 0 & 0 \\ 0 & 1 & 0 & 0 & 0 & 0 & 0 & 0 \\ 0 & 0 & 1 & 0 & 0 & 0 & 0 & 0 \\ 0 & 0 & 0 & 0 & 0 & 1 & 0 & 0 \\ 0 & 0 & 0 & 0 & 1 & 0 & 0 & 0 \\ 0 & 0 & 0 & 1 & 0 & 0 & 0 & 0 \\ 0 & 0 & 0 & 0 & 0 & 0 & 1 & 0 \\ 0 & 0 & 0 & 0 & 0 & 0 & 0 & 1 \end{pmatrix}, \tag{E.4}$$

where $T < 1$ signifies the energy transmittance of an individual crossing element.

To address point 3, we incorporate error components in each matrix description of the PS. We denote $U_{\mathrm{PS}_n}(\boldsymbol{\theta}, \boldsymbol{\delta})$, defined as:

$$U_{\mathrm{PS}_n}(\boldsymbol{\theta}, \boldsymbol{\delta}) = \begin{pmatrix} e^{i(\theta(1)+\delta(1))} & \dots & 0 \\ \vdots & \ddots & \vdots \\ 0 & \dots & e^{i(\theta(n)+\delta(n))} \end{pmatrix}. \tag{E.5}$$

Observe that the variables $\boldsymbol{\delta}$ solely account for the power supply fluctuations and the inaccuracies introduced by the calibration fitting process for the various MZIs and PSs within the PIC. The thermal interference, which theoretically operates similarly by adding additional phase error components, is not considered here due to the challenge in quantifying its influence on the disparate PSs.

Before discussing the operations of the various stages of PIC, let us introduce the function of a solitary MZI, which alters the eq. (6.16) as:

$$U_{\mathrm{MZI}}(\boldsymbol{\theta}, \boldsymbol{\delta}) = U_{\mathrm{MMI}}(\alpha, \beta) \cdot U_{\mathrm{PS}_2}(2\boldsymbol{\theta}, 2\boldsymbol{\delta}) \cdot U_{\mathrm{MMI}}\,. \tag{E.6}$$

Note that in the aforementioned equation, we have omitted the explicit dependency on (α, β) for simplicity.

The matrix associated with the projection operation onto the state $|x\rangle$ with $x = 0, 1$ is given by:

$$P_x = \begin{pmatrix} 1-x & 0 \\ 0 & x \end{pmatrix}. \tag{E.7}$$

The operation of the preparation phase is delineated by:

$$\begin{aligned} &U_{\mathrm{preparation}}(\boldsymbol{\theta}_{\mathrm{Q1}}, \boldsymbol{\theta}_{\mathrm{Q2}}, \boldsymbol{\phi}_{\mathrm{Q1}}, \boldsymbol{\phi}_{\mathrm{Q2}}, \delta_{\mathrm{Q1}}, \delta_{\mathrm{Q2}_1}, \delta_{\mathrm{Q2}_2}, \delta_{\mathrm{Q2}_3}) \\ &\quad = U_{\mathrm{setQ2}}(\boldsymbol{\theta}_{\mathrm{Q2}}, \boldsymbol{\phi}_{\mathrm{Q2}}, \delta_{\mathrm{Q2}_1}, \delta_{\mathrm{Q2}_2}, \delta_{\mathrm{Q2}_3}) \cdot U_{\mathrm{setQ1}}(\boldsymbol{\theta}_{\mathrm{Q1}}, \boldsymbol{\phi}_{\mathrm{Q1}}, \delta_{\mathrm{Q1}})\,. \end{aligned} \tag{E.8}$$

The operators U_{setQ1} and U_{setQ2}, respectively, configure the first and second qubits of our state and are characterized as:

$$\begin{aligned} &U_{\mathrm{setQ1}}(\boldsymbol{\theta}_{\mathrm{Q1}}, \boldsymbol{\phi}_{\mathrm{Q1}}, \delta_{\mathrm{Q1}}) = \\ &(P_0 \otimes \sigma_x \otimes \mathbb{1} + P_1 \otimes \mathbb{1} \otimes \mathbb{1}) \cdot (U_{\mathrm{PS}_2}(\boldsymbol{\phi}_{\mathrm{Q1}}, \delta_{\mathrm{Q1}}) \otimes \mathbb{1} \otimes \mathbb{1}) \cdot (U_{\mathrm{MZI}}(\boldsymbol{\theta}_{\mathrm{Q1}}, \delta_{\mathrm{Q1}}) \otimes \mathbb{1} \otimes \mathbb{1})\,. \end{aligned} \tag{E.9}$$

and

$$\begin{aligned} &U_{\mathrm{setQ2}}(\boldsymbol{\theta}_{\mathrm{Q2}}, \boldsymbol{\phi}_{\mathrm{Q2}}, \delta_{\mathrm{Q2}_1}, \delta_{\mathrm{Q2}_2}, \delta_{\mathrm{Q2}_3}) = \\ &(U_{\mathrm{PS}_4}(\boldsymbol{\phi}_{\mathrm{Q2}}, \delta_{\mathrm{Q2}_3}) \otimes \mathbb{1}) \cdot \left(P_0 \otimes U_{\mathrm{MZI}}(\boldsymbol{\theta}_{\mathrm{Q2}} - \frac{\pi}{2}, \delta_{\mathrm{Q2}_2}) \otimes \mathbb{1} + P_1 \otimes U_{\mathrm{MZI}}(\boldsymbol{\theta}_{\mathrm{Q2}}, \delta_{\mathrm{Q2}_1}) \otimes \mathbb{1}\right), \end{aligned} \tag{E.10}$$

The operation of the swap examination is characterized as:

$$U_{\mathrm{swaptest}}(\boldsymbol{\phi_s}, \delta_s) = (\mathbb{1} \otimes \mathbb{1} \otimes U_{\mathrm{MMI}}) \cdot U_{\mathrm{PS}_8}(\boldsymbol{\phi_s}, \delta_s) \cdot U_{\mathrm{CSWAP}} \cdot (\mathbb{1} \otimes \mathbb{1} \otimes U_{\mathrm{MMI}})\,, \tag{E.11}$$

Subsequently, the entire operation of the PIC is articulated as:

$$\begin{aligned} &U(\boldsymbol{\theta}_{\mathrm{Q1}}, \boldsymbol{\theta}_{\mathrm{Q2}}, \boldsymbol{\phi}_{\mathrm{Q1}}, \boldsymbol{\phi}_{\mathrm{Q2}}, \boldsymbol{\phi_s}, \delta_{\mathrm{Q1}}, \delta_{\mathrm{Q2}_1}, \delta_{\mathrm{Q2}_2}, \delta_{\mathrm{Q2}_3}, \delta_s) = \\ &U_{\mathrm{swaptest}}(\boldsymbol{\phi_s}, \delta_s) \cdot U_{\mathrm{preparation}}(\boldsymbol{\theta}_{\mathrm{Q1}}, \boldsymbol{\theta}_{\mathrm{Q2}}, \boldsymbol{\phi}_{\mathrm{Q1}}, \boldsymbol{\phi}_{\mathrm{Q2}}, \delta_{\mathrm{Q1}}, \delta_{\mathrm{Q2}_1}, \delta_{\mathrm{Q2}_2}, \delta_{\mathrm{Q2}_3})\,. \end{aligned} \tag{E.12}$$

It should be noted that in the preceding equations, the dependence of the various operators on α and T has been excluded for simplicity. As a result, the output density

matrix at the conclusion of our PIC is denoted by:

$$\rho_{\text{out}} = U\rho_{\text{in}}U^{\dagger}\,, \tag{E.13}$$

where $\rho_{in} = |010\rangle\langle 010|$. The likelihood of detecting the outcome x in the third qubit at the PIC's output is then expressed as:

$$\mathbb{P}(x) = \frac{\text{Tr}[U\rho_{\text{in}}U^{\dagger}\cdot(\mathbb{1}\otimes\mathbb{1}\otimes P_x)]}{\text{Tr}[U\rho_{\text{in}}U^{\dagger}]}\,. \tag{E.14}$$

The normalization term $\text{Tr}[U\rho_{\text{in}}U^{\dagger}]$ is imperative due to the non-unitary nature of the operator $U_{\text{MMI}}(\alpha,\beta)$ and $U_{\text{CSWAP}}(T)$. This situation is managed as delineated in [289], since we are employing a linear system, which operates directly at the single-photon level. Furthermore, owing to this normalization, the values of β and T can be set to 1, as they are merely scalar factors that appear in both the numerator and denominator of eq. (E.14), thereby nullifying each other. Upon acquiring the probabilities $\{\mathbb{P}(x)\}_{x=0,1}$, the scalar product is then computed in accordance with eq. (6.29). The $n\sigma$ confidence intervals on the scalar product are determined by applying the error propagation algorithm mentioned in [291], taking into account $n\sigma$ deviations on the measured quantities (α, $1\sigma_\alpha = 0.02$, T, $1\sigma_T = 0.002$) and on the inferred ones (all the phase terms). It is noteworthy that we have adapted the solver to the Matlab pattern-search method as opposed to the algorithm cited in [291].

Bibliography

1. Slussarenko, S. & Pryde, G. J. Photonic quantum information processing: A concise review. *Applied Physics Reviews* **6** (2019).
2. Nielsen, M. A. & Chuang, I. L. *Quantum computation and quantum information* (Cambridge university press, 2010).
3. Ladd, T. D. *et al*. Quantum computers. *nature* **464,** 45–53 (2010).
4. Chugh, V., Basu, A., Kaushik, A. & Basu, A. K. Progression in quantum sensing/biosensing technologies for healthcare. *ECS Sensors Plus* **2,** 015001 (2023).
5. Gao, X., Cui, Y., Levenson, R. M., Chung, L. W. & Nie, S. In vivo cancer targeting and imaging with semiconductor quantum dots. *Nature biotechnology* **22,** 969–976 (2004).
6. Lawrie, B. J., Lett, P. D., Marino, A. M. & Pooser, R. C. Quantum sensing with squeezed light. *Acs Photonics* **6,** 1307–1318 (2019).
7. Degen, C. L., Reinhard, F. & Cappellaro, P. Quantum sensing. *Reviews of modern physics* **89,** 035002 (2017).
8. Dowling, J. P. Quantum optical metrology–the lowdown on high-N00N states. *Contemporary physics* **49,** 125–143 (2008).
9. Pirandola, S. *et al.* Advances in quantum cryptography. *Advances in optics and photonics* **12,** 1012–1236 (2020).
10. Bauer, B., Bravyi, S., Motta, M. & Chan, G. K.-L. Quantum algorithms for quantum chemistry and quantum materials science. *Chemical Reviews* **120,** 12685–12717 (2020).
11. Shields, A. J. Semiconductor quantum light sources. *Nature photonics* **1,** 215–223 (2007).
12. Gerry, C. C. & Knight, P. L. *Introductory quantum optics* (Cambridge university press, 2023).
13. Einstein, A., Podolsky, B. & Rosen, N. Can quantum-mechanical description of physical reality be considered complete? *Physical review* **47,** 777 (1935).
14. Loudon, R. & Knight, P. L. Squeezed light. *Journal of modern optics* **34,** 709–759 (1987).
15. Scheel, S. Single-photon sources–an introduction. *Journal of Modern Optics* **56,** 141–160 (2009).
16. Hanbury Brown, R. & Twiss, R. Q. in *A Source Book in Astronomy and Astrophysics, 1900–1975* 8–12 (Harvard University Press, 1979).
17. Mandel, L. Sub-Poissonian photon statistics in resonance fluorescence. *Optics letters* **4,** 205–207 (1979).
18. Kimble, H. J., Dagenais, M. & Mandel, L. Photon antibunching in resonance fluorescence. *Physical Review Letters* **39,** 691 (1977).
19. Knill, E., Laflamme, R. & Milburn, G. J. A scheme for efficient quantum computation with linear optics. *Nature* **409.** https://doi.org/10.1038/35051009 (2001).
20. MohammadNejad, S., Nosratkhah, P. & Arab, H. Recent advances in room temperature single-photon emitters. *Quantum Information Processing* **22,** 360 (2023).
21. Senellart, P., Solomon, G. & White, A. High-performance semiconductor quantum-dot single-photon sources. *Nature nanotechnology* **12,** 1026–1039 (2017).

22. McKeever, J. *et al.* Deterministic generation of single photons from one atom trapped in a cavity. *Science* **303,** 1992–1994 (2004).
23. Faraon, A., Barclay, P. E., Santori, C., Fu, K.-M. C. & Beausoleil, R. G. Resonant enhancement of the zero-phonon emission from a colour centre in a diamond cavity. *Nature Photonics* **5,** 301–305 (2011).
24. Trotta, R. *et al.* Wavelength-tunable sources of entangled photons interfaced with atomic vapours. *Nature communications* **7,** 10375 (2016).
25. Fasel, S. *et al.* High-quality asynchronous heralded single-photon source at telecom wavelength. *New Journal of Physics* **6,** 163 (2004).
26. Helt, L. G., Liscidini, M. & Sipe, J. E. How does it scale? Comparing quantum and classical nonlinear optical processes in integrated devices. *JOSA B* **29,** 2199–2212 (2012).
27. Azzini, S. *et al.* Ultra-low power generation of twin photons in a compact silicon ring resonator. *Optics Express* **20,** 23100–23107 (2012).
28. Quesada, N., Helt, L. G., Menotti, M., Liscidini, M. & Sipe, J. E. Beyond photon pairs—nonlinear quantum photonics in the high-gain regime: a tutorial. *Adv. Opt. Photon.* **14,** 291–403 (2022).
29. Wang, J., Sciarrino, F., Laing, A. & Thompson, M. G. Integrated photonic quantum technologies. *Nature Photonics* **14,** 273–284 (2020).
30. Acerbi, F. *et al.* Monolithically integrated SiON photonic circuit and silicon single-photon detectors for NIR-range operation. *Journal of Lightwave Technology* (2023).
31. Horodecki, R., Horodecki, P., Horodecki, M. & Horodecki, K. Quantum entanglement. *Reviews of modern physics* **81,** 865 (2009).
32. Luo, W. *et al.* Recent progress in quantum photonic chips for quantum communication and internet. *Light: Science & Applications* **12,** 175 (2023).
33. Gisin, N., Ribordy, G., Tittel, W. & Zbinden, H. Quantum cryptography. *Reviews of modern physics* **74,** 145 (2002).
34. Leone, N. *et al.* Generation of quantum-certified random numbers using on-chip path-entangled single photons from an LED (2023).
35. Loudon, R. *The quantum theory of light* (OUP Oxford, 2000).
36. Ekert, A. & Knight, P. L. Entangled quantum systems and the Schmidt decomposition. *American Journal of Physics* **63,** 415–423 (1995).
37. Mosley, P. J., Lundeen, J. S., Smith, B. J. & Walmsley, I. A. Conditional preparation of single photons using parametric downconversion: a recipe for purity. *New Journal of Physics* **10,** 093011 (2008).
38. Shih, Y. *An introduction to quantum optics: photon and biphoton physics* (CRC press, 2020).
39. Bagchi, B., Ghosh, R. & Khare, A. A pedestrian introduction to coherent and squeezed states. *International Journal of Modern Physics A* **35,** 2030011 (July 2020).
40. Glauber, R. J. Coherent and incoherent states of the radiation field. *Physical Review* **131,** 2766 (1963).
41. Yuen, H. P. Two-photon coherent states of the radiation field. *Physical Review A* **13,** 2226 (1976).
42. Grote, H. *et al.* First long-term application of squeezed states of light in a gravitational-wave observatory. *Physical review letters* **110,** 181101 (2013).
43. Al-Hilfy, A. & Loudon, R. Theory of photon correlations in two-photon cascade emission. *Journal of Physics B: Atomic and Molecular Physics* **18,** 3697 (1985).
44. Shih, Y. Entangled biphoton source-property and preparation. *Reports on Progress in Physics* **66,** 1009 (2003).
45. Magnitskiy, S. *et al.* A SPDC-based source of entangled photons and its characterization. *Journal of Russian Laser Research* **36,** 618–629 (2015).
46. Silverstone, J. W., Bonneau, D., O'Brien, J. L. & Thompson, M. G. Silicon quantum photonics. *IEEE Journal of Selected Topics in Quantum Electronics* **22,** 390–402 (2016).

47. Azzini, S. *et al.* Stimulated and spontaneous four-wave mixing in silicon-on-insulator coupled photonic wire nano-cavities. *Applied Physics Letters* **103** (2013).
48. Signorini, S. *et al.* Intermodal four-wave mixing in silicon waveguides. *Photonics Research* **6,** 805–814 (2018).
49. Barnett, S. & Radmore, P. M. *Methods in theoretical quantum optics* (Oxford University Press, 2002).
50. Takesue, H. & Shimizu, K. Effects of multiple pairs on visibility measurements of entangled photons generated by spontaneous parametric processes. *Optics Communications* **283,** 276–287 (2010).
51. Paul, H. Photon antibunching. *Reviews of Modern Physics* **54,** 1061 (1982).
52. Mandel, L. & Wolf, E. *Optical coherence and quantum optics* (Cambridge university press, 1995).
53. Migdall, A., Polyakov, S. V., Fan, J. & Bienfang, J. C. *Single-photon generation and detection: physics and applications* (Academic Press, 2013).
54. Christ, A. & Silberhorn, C. Limits on the deterministic creation of pure single-photon states using parametric down-conversion. *Physical Review A* **85,** 023829 (2012).
55. Christensen, J. B., Koefoed, J. G., Rottwitt, K. & McKinstrie, C. Engineering spectrally unentangled photon pairs from nonlinear microring resonators by pump manipulation. *Optics letters* **43,** 859–862 (2018).
56. Born, M. & Wolf, E. *Principles of optics: electromagnetic theory of propagation, interference and diffraction of light* (Elsevier, 2013).
57. Borghi, M., Castellan, C., Signorini, S., Trenti, A. & Pavesi, L. Nonlinear silicon photonics. *Journal of Optics* **19,** 093002 (2017).
58. Leuthold, J., Koos, C. & Freude, W. Nonlinear silicon photonics. *Nature photonics* **4,** 535–544 (2010).
59. Jalali, B., Raghunathan, V., Dimitropoulos, D. & Boyraz, O. Raman-based silicon photonics. *IEEE Journal of Selected Topics in Quantum Electronics* **12,** 412–421 (2006).
60. Müller, M. & Zumbusch, A. Coherent anti-Stokes Raman scattering microscopy. *ChemPhysChem* **8,** 2156–2170 (2007).
61. Li, S., Li, Y., Yi, R., Liu, L. & Qu, J. Coherent anti-Stokes Raman scattering microscopy and its applications. *Frontiers in Physics* **8,** 598420 (2020).
62. Inoue, K. Four-wave mixing in an optical fiber in the zero-dispersion wavelength region. *Journal of lightwave technology* **10,** 1553–1561 (1992).
63. Fukuda, H. *et al.* Four-wave mixing in silicon wire waveguides. *Optics express* **13,** 4629–4637 (2005).
64. Carman, R., Chiao, R. & Kelley, P. Observation of degenerate stimulated four-photon interaction and four-wave parametric amplification. *Physical Review Letters* **17,** 1281 (1966).
65. Signorini, S. & Pavesi, L. On-chip heralded single photon sources. *AVS Quantum Science* **2,** 041701 (2020).
66. Feng, L.-T., Guo, G.-C. & Ren, X.-F. Progress on integrated quantum photonic sources with silicon. *Advanced Quantum Technologies* **3,** 1900058 (2020).
67. Harada, K.-i. *et al.* Frequency and polarization characteristics of correlated photon-pair generation using a silicon wire waveguide. *IEEE Journal of Selected Topics in Quantum Electronics* **16,** 325–331 (2009).
68. Caspani, L. *et al.* Integrated sources of photon quantum states based on nonlinear optics. *Light: Science & Applications* **6,** e17100–e17100 (2017).
69. Meyer-Scott, E., Silberhorn, C. & Migdall, A. Single-photon sources: Approaching the ideal through multiplexing. *Review of Scientific Instruments* **91,** 041101 (2020).
70. Hadfield, R. H. Single-photon detectors for optical quantum information applications. *Nature photonics* **3,** 696–705 (2009).

71. Silberhorn, C. Detecting quantum light. *Contemporary Physics* **48,** 143–156 (2007).
72. Soref, R. The past, present, and future of silicon photonics. *IEEE Journal of selected topics in quantum electronics* **12,** 1678–1687 (2006).
73. Siew, S. Y. *et al.* Review of silicon photonics technology and platform development. *Journal of Lightwave Technology* **39,** 4374–4389 (2021).
74. Ye, W. N. & Xiong, Y. Review of silicon photonics: history and recent advances. *Journal of Modern Optics* **60,** 1299–1320 (2013).
75. Lockwood, D. J. & Pavesi, L. *Silicon photonics* (Berlin: Springer, 2004).
76. Pelucchi, E. *et al.* The potential and global outlook of integrated photonics for quantum technologies. *Nature Reviews Physics* **4,** 194–208 (2022).
77. Bogdanov, S., Shalaginov, M., Boltasseva, A. & Shalaev, V. M. Material platforms for integrated quantum photonics. *Optical Materials Express* **7,** 111–132 (2017).
78. Baets, R. *et al. Silicon photonics: Silicon nitride versus silicon-on-insulator* in *Optical Fiber Communication Conference* (2016), Th3J–1.
79. Blumenthal, D. J., Heideman, R., Geuzebroek, D., Leinse, A. & Roeloffzen, C. Silicon nitride in silicon photonics. *Proceedings of the IEEE* **106,** 2209–2231 (2018).
80. Xu, D.-X. *et al.* Silicon photonic integration platform—have we found the sweet spot? *IEEE Journal of Selected Topics in Quantum Electronics* **20,** 189–205 (2014).
81. Brès, C.-S. *et al.* Supercontinuum in integrated photonics: generation, applications, challenges, and perspectives. *Nanophotonics* **12,** 1199–1244 (2023).
82. Bernard, M. *et al.* Top-down convergence of near-infrared photonics with silicon substrate-integrated electronics. *Optica* **8,** 1363–1364 (2021).
83. Singh, V. N. & Kushvaha, S. S. *Nanomaterials for Energy and Sensor Applications* 2024.
84. Marder, A. A. *et al.* CdS/CdSe/CdS Spherical Quantum Wells with Near-Unity Biexciton Quantum Yield for Light-Emitting-Device Applications. *ACS Materials Letters* **5,** 1411–1419 (2023).
85. Lacava, C. *et al.* Si-rich silicon nitride for nonlinear signal processing applications. *Scientific reports* **7,** 22 (2017).
86. Cernansky, R., Martini, F. & Politi, A. Complementary metal-oxide semiconductor compatible source of single photons at near-visible wavelengths. *Optics Letters* **43,** 855–858 (2018).
87. Pedrotti, F. L., Pedrotti, L. M. & Pedrotti, L. S. *Introduction to optics* (Cambridge University Press, 2017).
88. Saleh, B. E. & Teich, M. C. *Fundamentals of photonics* (john Wiley & sons, 2019).
89. Agrawal, G. P. in *Nonlinear Science at the Dawn of the 21st Century* 195–211 (Springer, 2000).
90. Soldano, L. B. & Pennings, E. C. Optical multi-mode interference devices based on self-imaging: principles and applications. *Journal of lightwave technology* **13,** 615–627 (1995).
91. Saghaei, H., Elyasi, P. & Karimzadeh, R. Design, fabrication, and characterization of Mach–Zehnder interferometers. *Photonics and Nanostructures-Fundamentals and Applications* **37,** 100733 (2019).
92. Dong, P. Silicon photonic integrated circuits for wavelength-division multiplexing applications. *IEEE Journal of Selected Topics in Quantum Electronics* **22,** 370–378 (2016).
93. Yang, B.-K., Shin, S.-Y. & Zhang, D. Ultrashort polarization splitter using two-mode interference in silicon photonic wires. *IEEE Photonics Technology Letters* **21,** 432–434 (2009).
94. Fukuda, H. *et al.* Ultrasmall polarization splitter based on silicon wire waveguides. *Optics Express* **14,** 12401–12408 (2006).
95. Dai, D. & Bowers, J. E. Novel ultra-short and ultra-broadband polarization beam splitter based on a bent directional coupler. *Optics express* **19,** 18614–18620 (2011).

96. Trinh, P., Yegnanarayanan, S. & Jalali, B. Integrated optical directional couplers in silicon-on-insulator. *Electronics Letters* **31,** 2097–2098 (1995).
97. Chen, C.-L. *Foundations for guided-wave optics* (John Wiley & Sons, 2006).
98. Ulrich, R. Light-propagation and imaging in planar optical waveguides. *Nouvelle Revue d'Optique* **6,** 253 (1975).
99. Ulrich, R. & Ankele, G. Self-imaging in homogeneous planar optical waveguides. *Applied Physics Letters* **27,** 337–339 (1975).
100. Peruzzo, A., Laing, A., Politi, A., Rudolph, T. & O'brien, J. L. Multimode quantum interference of photons in multiport integrated devices. *Nature communications* **2,** 224 (2011).
101. Komma, J., Schwarz, C., Hofmann, G., Heinert, D. & Nawrodt, R. Thermo-optic coefficient of silicon at 1550 nm and cryogenic temperatures. *Applied Physics Letters* **101** (2012).
102. Rizal, C. & Niraula, B. Compact Si-based asymmetric MZI waveguide on SOI as a thermo-optical switch. *Optics Communications* **410,** 947–955. ISSN: 0030-4018. https://www.sciencedirect.com/science/article/pii/S0030401817308933 (2018).
103. Raghi S. El Shamy, e. a. Modelling, characterization, and applications of silicon on insulator loop terminated asymmetric Mach Zehnder interferometer. *Scientific Reports* **12** (2022).
104. Heebner, J., Grover, R. & Ibrahim, T. Optical microresonator theory. *Springer* (2008).
105. Ramiro-Manzano, F., Prtljaga, N., Pavesi, L., Pucker, G. & Ghulinyan, M. A fully integrated high-Q whispering-gallery wedge resonator. *Optics express* **20,** 22934–22942 (2012).
106. Feng, S. *et al.* Silicon photonics: from a microresonator perspective. *Laser & photonics reviews* **6,** 145–177 (2012).
107. Engin, E. *et al.* Photon pair generation in a silicon micro-ring resonator with reverse bias enhancement. *Optics express* **21,** 27826–27834 (2013).
108. Ghulinyan, M. *et al.* Whispering-gallery modes and light emission from a Si-nanocrystal-based single microdisk resonator. *Optics express* **16,** 13218–13224 (2008).
109. Landobasa, Y. M., Darmawan, S. & Chin, M.-K. Matrix analysis of 2-D microresonator lattice optical filters. *IEEE Journal of Quantum Electronics* **41,** 1410–1418 (2005).
110. Niehusmann, J. *et al.* Ultrahigh-quality-factor silicon-on-insulator microring resonator. *Optics letters* **29,** 2861–2863 (2004).
111. Lee, J.-M. *et al.* Do different kinds of photon-pair sources have the same indistinguishability in quantum silicon photonics? *Photonics Research* **11,** 1820–1837 (2023).
112. Hong, C.-K., Ou, Z.-Y. & Mandel, L. Measurement of subpicosecond time intervals between two photons by interference. *Physical review letters* **59,** 2044 (1987).
113. Silverstone, J. W. *et al.* On-chip quantum interference between silicon photon-pair sources. *Nature Photonics* **8,** 104–108 (2014).
114. Lee, J.-M. *et al.* Controlled-NOT operation of SiN-photonic circuit using photon pairs from silicon-photonic circuit. *Optic Communications* **509** (2022).
115. Signorini, S. & Pavesi, L. On-chip heralded single photon sources. *AVS Quantum Science* **2** (2020).
116. Gard, B. T., Motes, K. R., Olson, J. P., Rohde, P. P. & Dowling, J. P. in *From atomic to mesoscale: The role of quantum coherence in systems of various complexities* 167–192 (World Scientific, 2015).
117. Hamilton, C. S. *et al.* Gaussian boson sampling. *Physical review letters* **119,** 170501 (2017).
118. Peruzzo, A. *et al.* A variational eigenvalue solver on a photonic quantum processor. *Nature communications* **5,** 4213 (2014).

119. Brańczyk, A. M. Hong-ou-mandel interference. *arXiv preprint arXiv:1711.00080* (2017).
120. Adcock, J. C. *et al.* Advances in Silicon Quantum Photonics. *IEEE Journal of Selected Topics in Quantum Electronics* **27,** 1–24. https://doi.org/10.1109%2Fjstqe.2020.3025737 (Mar. 2021).
121. Francis-Jones, R. J. A., Wright, T. A., Gorbach, A. V. & Mosley, P. J. Engineered photon-pair generation by four-wave mixing in asymmetric coupled waveguides. *arXiv* (2018).
122. Anjum, O. F. *et al.* Bandwidth enhancement of inter-modal four wave mixing Bragg scattering by means of dispersion engineering. *APL Photonics* **4,** 022902. eprint: https://doi.org/10.1063/1.5048495. https://doi.org/10.1063/1.5048495 (2019).
123. Cordier, M. *et al.* Active engineering of four-wave mixing spectral correlations in multiband hollow-core fibers. *Opt. Express* **27,** 9803–9814 (Apr. 2019).
124. Lvovsky, A. I. in *Photonics: Scientific Foundations, Technology and Applications* (ed Andrews, D. L.) 121–163 (Wiley, 2015).
125. Lee, J.-M., Lee, W.-J., Kim, M.-S. & Ju, J. J. Noise Filtering for Highly Correlated Photon Pairs From Silicon Waveguides. *Journal of Lightwave Technology* **37,** 5428–5434 (2019).
126. Clemmen, S. *et al.* Continuous wave photon pair generation in silicon-on-insulator waveguides and ring resonators. *Opt. Express* **17,** 16558–16570. https://opg.optica.org/oe/abstract.cfm?URI=oe-17-19-16558 (Sept. 2009).
127. Ma, C. & Mookherjea, S. Prospects for photon-pair generation using silicon microring resonators with two photon absorption and free carrier absorption. *OSA Continuum* **3,** 1138–1153. https://opg.optica.org/osac/abstract.cfm?URI=osac-3-5-1138 (May 2020).
128. Faruque, I. I., Sinclair, G. F., Bonneau, D., Rarity, J. G. & Thompson, M. G. On-chip quantum interference with heralded photons from two independent micro-ring resonator sources in silicon photonics. *Optics express* **26,** 20379–20395 (2018).
129. Llewellyn, D. *et al.* Chip-to-chip quantum teleportation and multi-photon entanglement in silicon. *Nature Physics* **16,** 148–153 (2020).
130. Signorini, S. *et al.* A silicon source of heralded single photons at 2 μm. *APL Photonics* **6** (2021).
131. Sanna, M., Rizzotti, D., Signorini, S. & Pavesi, L. *An integrated entangled photons source for mid-infrared ghost spectroscopy* in *Quantum Sensing and Nano Electronics and Photonics XVIII* **12009** (2022), 143–151.
132. Sanna, M., Rizzotti, D., Signorini, S. & Pavesi, L. 2 μm Ghost Spectroscopy with an Integrated Silicon Quantum Photonics Source. *Advanced Quantum Technologies,* 2300159.
133. Aellen, T., Giovannini, M., Faist, J. & Von der Weid, J. P. Feasibility study of free-space quantum key distribution in the mid-infrared. *Quantum Information and Computation* **8,** 0001–0011 (2008).
134. Wang, Q. *et al.* Super-resolving quantum lidar: entangled coherent-state sources with binary-outcome photon counting measurement suffice to beat the shot-noise limit. *Optics express* **24,** 5045–5056 (2016).
135. Moreau, P.-A. *et al.* Demonstrating an absolute quantum advantage in direct absorption measurement. *Scientific reports* **7,** 6256 (2017).
136. Fernandez, D. C., Bhargava, R., Hewitt, S. M. & Levin, I. W. Infrared spectroscopic imaging for histopathologic recognition. *Nature biotechnology* **23,** 469–474 (2005).
137. Miller, L. M., Bourassa, M. W. & Smith, R. J. FTIR spectroscopic imaging of protein aggregation in living cells. *Biochimica et biophysica acta (BBA)-biomembranes* **1828,** 2339–2346 (2013).

138. Lambrecht, A. & Schmitt, K. in *Mid-infrared Optoelectronics* 661–715 (Elsevier, 2020).
139. Popa, D. & Udrea, F. Towards integrated mid-infrared gas sensors. *Sensors* **19,** 2076 (2019).
140. Marsili, F. *et al.* Efficient single photon detection from 500 nm to 5 μm wavelength. *Nano letters* **12,** 4799–4804 (2012).
141. Pittman, T. B., Shih, Y., Strekalov, D. & Sergienko, A. V. Optical imaging by means of two-photon quantum entanglement. *Physical Review A* **52,** R3429 (1995).
142. Vergyris, P. *et al.* Two-photon phase-sensing with single-photon detection. *Applied Physics Letters* **117** (2020).
143. Michelini, C., Signorini, S., Pruneri, V. & Pavesi, L. *Undetected photon interference measurements on a silicon chip* in *Quantum Communications and Quantum Imaging XXI* **12692** (2023), 93–100.
144. Kalashnikov, D. A., Paterova, A. V., Kulik, S. P. & Krivitsky, L. A. Infrared spectroscopy with visible light. *Nature Photonics* **10,** 98–101 (2016).
145. Prabhakar, S. *et al.* Two-photon quantum interference and entanglement at 2.1 μm. *Science advances* **6,** eaay5195 (2020).
146. Mancinelli, M. *et al.* Mid-infrared coincidence measurements on twin photons at room temperature. *Nature communications* **8,** 15184 (2017).
147. Holzman, I. & Ivry, Y. Superconducting nanowires for single-photon detection: progress, challenges, and opportunities. *Advanced Quantum Technologies* **2,** 1800058 (2019).
148. Verma, V. *et al.* Single-photon detection in the mid-infrared up to 10 μm wavelength using tungsten silicide superconducting nanowire detectors. *APL photonics* **6** (2021).
149. Rosenfeld, L. M. *et al.* Mid-infrared quantum optics in silicon. *Optics Express* **28,** 37092–37102 (2020).
150. Barh, A., Tidemand-Lichtenberg, P. & Pedersen, C. Thermal noise in mid-infrared broadband upconversion detectors. *Optics express* **26,** 3249–3259 (2018).
151. Lin, Q., Painter, O. J. & Agrawal, G. P. Nonlinear optical phenomena in silicon waveguides: modeling and applications. *Optics express* **15,** 16604–16644 (2007).
152. Li, H. Refractive index of silicon and germanium and its wavelength and temperature derivatives. *Journal of Physical and Chemical Reference Data* **9,** 561–658 (1980).
153. Kurtsiefer, C., Zarda, P., Mayer, S. & Weinfurter, H. The breakdown flash of silicon avalanche photodiodes-back door for eavesdropper attacks? *Journal of Modern Optics* **48,** 2039–2047 (2001).
154. Pearce, E., Phillips, C., Oulton, R. & Clark, A. Heralded spectroscopy with a fiber photon-pair source. *Applied Physics Letters* **117,** 054002 (2020).
155. Kalachev, A. *et al.* Biphoton spectroscopy of YAG: Er3+ crystal. *Laser Physics Letters* **4,** 722 (2007).
156. Whittaker, R. *et al.* Absorption spectroscopy at the ultimate quantum limit from single-photon states. *New Journal of Physics* **19,** 023013 (2017).
157. Jakeman, E. & Rarity, J. The use of pair production processes to reduce quantum noise in transmission measurements. *Optics communications* **59,** 219–223 (1986).
158. Gatti, A., Brambilla, E., Bache, M. & Lugiato, L. A. Ghost imaging with thermal light: comparing entanglement and classicalcorrelation. *Physical review letters* **93,** 093602 (2004).
159. Padgett, M. J. & Boyd, R. W. An introduction to ghost imaging: quantum and classical. *Philosophical Transactions of the Royal Society A: Mathematical, Physical and Engineering Sciences* **375,** 20160233 (2017).
160. Strekalov, D., Sergienko, A., Klyshko, D. & Shih, Y. Observation of two-photon "ghost" interference and diffraction. *Physical review letters* **74,** 3600 (1995).

161. Bahadori, M., Nikdast, M., Cheng, Q. & Bergman, K. Universal design of waveguide bends in silicon-on-insulator photonics platform. *Journal of Lightwave Technology* **37,** 3044–3054 (2019).
162. Ottonello-Briano, F. *et al.* Carbon dioxide absorption spectroscopy with a mid-infrared silicon photonic waveguide. *Optics Letters* **45,** 109–112 (2020).
163. HITRAN. *Hitran website main page,* https://hitran.org/
164. Shrivastava, A., Gupta, V. B., *et al.* Methods for the determination of limit of detection and limit of quantitation of the analytical methods. *Chron. Young Sci* **2,** 21–25 (2011).
165. Bucio, T. D. *et al.* Silicon nitride photonics for the near-infrared. *IEEE Journal of Selected Topics in Quantum Electronics* **26,** 1–13 (2019).
166. Sanna, M. *et al.* SiN integrated photonic components in the visible to near-infrared spectral region. *Opt. Express* **32,** 9081–9094. https://opg.optica.org/oe/abstract.cfm?URI=oe-32-6-9081 (Mar. 2024).
167. Piccoli, G., Sanna, M., Borghi, M., Pavesi, L. & Ghulinyan, M. Silicon oxynitride platform for linear and nonlinear photonics at NIR wavelengths. *Optical Materials Express* **12,** 3551–3562 (2022).
168. Penadés, J. S. *et al.* Suspended silicon waveguides for long-wave infrared wavelengths. *Optics letters* **43,** 795–798 (2018).
169. Manin, Y. Computable and uncomputable. *Sovetskoye Radio, Moscow* **128,** 28 (1980).
170. Feynman, R. P. *et al.* Simulating physics with computers. *Int. j. Theor. phys* **21** (2018).
171. Austin, B. M., Zubarev, D. Y. & Lester Jr, W. A. Quantum Monte Carlo and related approaches. *Chemical reviews* **112,** 263–288 (2012).
172. Orús, R. Tensor networks for complex quantum systems. *Nature Reviews Physics* **1,** 538–550 (2019).
173. Bishop, R. F. & Kümmel, H. G. The coupled cluster method. *Physics Today* **40,** 52–60 (1987).
174. Dreizler, R. M. & Gross, E. K. *Density functional theory: an approach to the quantum many-body problem* (Springer Science & Business Media, 2012).
175. Zgid, D. & Chan, G. K. Dynamical mean-field theory from a quantum chemical perspective. *The Journal of chemical physics* **134** (2011).
176. Schollwöck, U. The density-matrix renormalization group. *Reviews of modern physics* **77,** 259 (2005).
177. Cirac, J. I. & Zoller, P. Goals and opportunities in quantum simulation. *Nature physics* **8,** 264–266 (2012).
178. Georgescu, I. M., Ashhab, S. & Nori, F. Quantum simulation. *Reviews of Modern Physics* **86,** 153 (2014).
179. Johnson, T. H., Clark, S. R. & Jaksch, D. What is a quantum simulator? *EPJ Quantum Technology* **1,** 1–12 (2014).
180. Arute, F. *et al.* Quantum supremacy using a programmable superconducting processor. *Nature* **574,** 505–510 (2019).
181. Zhong, H.-S. *et al.* Quantum computational advantage using photons. *Science* **370,** 1460–1463 (2020).
182. Greiner, M., Mandel, O., Esslinger, T., Hänsch, T. W. & Bloch, I. Quantum phase transition from a superfluid to a Mott insulator in a gas of ultracold atoms. *nature* **415,** 39–44 (2002).
183. Lu, D. *et al.* Quantum chemistry simulation on quantum computers: theories and experiments. *Physical Chemistry Chemical Physics* **14,** 9411–9420 (2012).
184. Liu, J. & Xin, Y. Quantum simulation of quantum field theories as quantum chemistry. *Journal of High Energy Physics* **2020,** 1–48 (2020).

185. Zulehner, A. & Wille, R. Advanced simulation of quantum computations. *IEEE Transactions on Computer-Aided Design of Integrated Circuits and Systems* **38,** 848–859 (2018).
186. Brown, K. L., Munro, W. J. & Kendon, V. M. Using quantum computers for quantum simulation. *Entropy* **12,** 2268–2307 (2010).
187. Parrish, R. M., Hohenstein, E. G., McMahon, P. L. & Martínez, T. J. Quantum computation of electronic transitions using a variational quantum eigensolver. *Physical review letters* **122,** 230401 (2019).
188. Gross, C. & Bloch, I. Quantum simulations with ultracold atoms in optical lattices. *Science* **357,** 995–1001 (2017).
189. Blackmore, J. A. *et al.* Ultracold molecules for quantum simulation: rotational coherences in CaF and RbCs. *Quantum Science and Technology* **4,** 014010 (2018).
190. Blatt, R. & Roos, C. F. Quantum simulations with trapped ions. *Nature Physics* **8,** 277–284 (2012).
191. Barthelemy, P. & Vandersypen, L. M. Quantum dot systems: a versatile platform for quantum simulations. *Annalen der Physik* **525,** 808–826 (2013).
192. Spagnolo, N. *et al.* Experimental validation of photonic boson sampling. *Nature Photonics* **8,** 615–620 (2014).
193. Sansoni, L. *et al.* Two-particle bosonic-fermionic quantum walk via integrated photonics. *Physical review letters* **108,** 010502 (2012).
194. EPIQUS. *EPIQUS website main page,* https://epiqus.fbk.eu/home
195. Pfeiffer, M. H. *et al.* Photonic Damascene process for integrated high-Q microresonator based nonlinear photonics. *Optica* **3,** 20–25 (2016).
196. Roeloffzen, C. G. *et al.* Low-loss Si3N4 TriPleX optical waveguides: Technology and applications overview. *IEEE journal of selected topics in quantum electronics* **24,** 1–21 (2018).
197. Keck, D. & Tynes, A. Spectral response of low-loss optical waveguides. *Applied optics* **11,** 1502–1506 (1972).
198. Piekarek, M. *et al.* High-extinction ratio integrated photonic filters for silicon quantum photonics. *Optics letters* **42,** 815–818 (2017).
199. Stolen, R. H. & Lin, C. Self-phase-modulation in silica optical fibers. *Physical Review A* **17,** 1448 (1978).
200. Tzoar, N. & Jain, M. Self-phase modulation in long-geometry optical waveguides. *Physical Review A* **23,** 1266 (1981).
201. Sheik-Bahae, M., Hagan, D. J. & Van Stryland, E. W. Dispersion and band-gap scaling of the electronic Kerr effect in solids associated with two-photon absorption. *Physical review letters* **65,** 96 (1990).
202. Ikeda, K., Saperstein, R. E., Alic, N. & Fainman, Y. Thermal and Kerr nonlinear properties of plasma-deposited silicon nitride/silicon dioxide waveguides. *Optics express* **16,** 12987–12994 (2008).
203. Trenti, A. *et al.* Thermo-optic coefficient and nonlinear refractive index of silicon oxynitride waveguides. *AIP Advances* **8** (2018).
204. Blumenthal, D. J., Heideman, R., Geuzebroek, D., Leinse, A. & Roeloffzen, C. Silicon Nitride in Silicon Photonics. *Proceedings of the IEEE* **106,** 2209–2231 (2018).
205. Lacey, J. & Payne, F. Radiation loss from planar waveguides with random wall imperfections. *IEE Proceedings J (Optoelectronics)* **137,** 282–289 (1990).
206. Qiu, C. *et al.* Fabrication, Characterization and Loss Analysis of Silicon Nanowaveguides. *Journal of Lightwave Technology* **32,** 2303–2307 (2014).
207. Smith, J. A., Francis, H., Navickaite, G. & Strain, M. J. SiN foundry platform for high performance visible light integrated photonics. *Optical Materials Express* **13,** 458–468 (2023).
208. Buzaverov, K. A. *et al.* Low-loss silicon nitride photonic ICs for near-infrared wavelength bandwidth. *Optics Express* **31,** 16227–16242 (2023).

209. Sacher, W. D. *et al.* Visible-light silicon nitride waveguide devices and implantable neurophotonic probes on thinned 200 mm silicon wafers. *Optics express* **27,** 37400–37418 (2019).
210. Ruedas, J. F., Sabek, J., Bucio, T. D., Gardes, F. Y. & Horna, C. D. Basic building blocks development for a SiN platform in the visible range. *2021 IEEE 17th International Conference on Group IV Photonics (GFP),* 1–2 (2021).
211. Liu, D., Xu, H., Tan, Y., Shi, Y. & Dai, D. Silicon photonic filters. *Microwave and Optical Technology Letters* **63,** 2252–2268 (2021).
212. Nie, X., Turk, N., Li, Y., Liu, Z. & Baets, R. High extinction ratio on-chip pump-rejection filter based on cascaded grating-assisted contra-directional couplers in silicon nitride rib waveguides. *Optics letters* **44,** 2310–2313 (2019).
213. Schweikert, C. *et al.* Design of a Broadband Integrated Notch Filter in Silicon Nitride. *2020 International Conference on Numerical Simulation of Optoelectronic Devices (NUSOD),* 89–90 (2020).
214. Bogaerts, W. *et al.* Silicon microring resonators. *Laser & Photonics Reviews* **6,** 47–73 (2012).
215. Atvars, A. Analytical description of resonances in Fabry–Perot and whispering gallery mode resonators. *JOSA B* **38,** 3116–3129 (2021).
216. Chuang, I. L., Gershenfeld, N. & Kubinec, M. Experimental implementation of fast quantum searching. *Physical review letters* **80,** 3408 (1998).
217. Vandersypen, L. M. *et al.* Experimental realization of Shor's quantum factoring algorithm using nuclear magnetic resonance. *Nature* **414,** 883–887 (2001).
218. Preskill, J. Quantum computing in the NISQ era and beyond. *Quantum* **2,** 79 (2018).
219. Cerezo, M. *et al.* Variational quantum algorithms. *Nature Reviews Physics* **3,** 625–644 (2021).
220. Johnson, P. D., Romero, J., Olson, J., Cao, Y. & Aspuru-Guzik, A. QVECTOR: an algorithm for device-tailored quantum error correction. *arXiv preprint arXiv:1711.02249* (2017).
221. Yuan, X., Endo, S., Zhao, Q., Li, Y. & Benjamin, S. C. Theory of variational quantum simulation. *Quantum* **3,** 191 (2019).
222. McClean, J. R., Romero, J., Babbush, R. & Aspuru-Guzik, A. The theory of variational hybrid quantum-classical algorithms. *New Journal of Physics* **18,** 023023 (2016).
223. Fedorov, D. A., Peng, B., Govind, N. & Alexeev, Y. VQE method: a short survey and recent developments. *Materials Theory* **6,** 2 (2022).
224. Tilly, J. *et al.* The variational quantum eigensolver: a review of methods and best practices. *Physics Reports* **986,** 1–128 (2022).
225. Jordan, P. & Wigner, E. P. *Über das paulische äquivalenzverbot* (Springer, 1993).
226. McClean, J. R., Babbush, R., Love, P. J. & Aspuru-Guzik, A. Exploiting locality in quantum computation for quantum chemistry. *The journal of physical chemistry letters* **5,** 4368–4380 (2014).
227. Plesch, M. & Brukner, Č. Quantum-state preparation with universal gate decompositions. *Physical Review A* **83,** 032302 (2011).
228. Aaronson, S. & Arkhipov, A. *The computational complexity of linear optics* in *Proceedings of the forty-third annual ACM symposium on Theory of computing* (2011), 333–342.
229. Lund, A. P. *et al.* Boson sampling from a Gaussian state. *Physical review letters* **113,** 100502 (2014).
230. Brod, D. J. Complexity of simulating constant-depth BosonSampling. *Physical Review A* **91,** 042316 (2015).
231. Brod, D. J. *et al.* Photonic implementation of boson sampling: a review. *Advanced Photonics* **1,** 034001–034001 (2019).

232. Kwon, Y., Baldazzi, A., Pavesi, L. & Choi, B.-S. Quantum circuit mapping for universal and scalable computing in MZI-based integrated photonics. *Opt. Express* **32,** 12852–12881. https://opg.optica.org/oe/abstract.cfm?URI=oe-32-7-12852 (Mar. 2024).
233. Clements, W. R., Humphreys, P. C., Metcalf, B. J., Kolthammer, W. S. & Walmsley, I. A. Optimal design for universal multiport interferometers. *Optica* **3,** 1460–1465 (2016).
234. Wittek, P. Quantum Machine Learning: What Quantum Computing Means to Data Mining. *Academic Press, Cambridge, Massachusetts* (2014).
235. Rupp, M. Machine learning for quantum mechanics in a nutshell. *International Journal of Quantum Chemistry* **115,** 1058–1073. https://doi.org/10.1002/qua.24954 (2015).
236. Schuld, M., Sinayskiy, I. & Petruccione, F. An introduction to quantum machine learning. *Contemporary Physics* **56,** 172–185. https://doi.org/10.1080%2F00107514.2014.964942 (2015).
237. Biamonte, J. *et al.* Quantum machine learning. *Nature* **549,** 195–202. https://doi.org/10.1038%2Fnature23474 (2017).
238. Steane, A. Quantum computing. *Reports on Progress in Physics* **61,** 117 (1998).
239. Nielsen, M. A. & Chuang, I. L. Quantum Computation and Quantum Information: 10th Anniversary Edition. *Cambridge University Press* (2010).
240. Mitchell, T. M. Machine learning. *McGraw-hill, New York* (ed Munson, E. M.) (1997).
241. Langley, P. & Simon, H. A. Applications of Machine Learning and Rule Induction. *Commun. ACM* **38,** 54–64. ISSN: 0001-0782. https://doi.org/10.1145/219717.219768 (1995).
242. Niu, M. Y., Boixo, S., Smelyanskiy, V. N. & Neven, H. Universal quantum control through deep reinforcement learning. *npj Quantum Information* **5.** https://doi.org/10.1038/s41534-019-0141-3 (1 2019).
243. Li, J. & Kais, S. Quantum cluster algorithm for data classification. *Materials Theory* **5.** https://doi.org/10.1186/s41313-021-00029-1 (2021).
244. Moradi, S. *et al.* Clinical data classification with noisy intermediate scale quantum computers. *Scientific Reports* **12.** https://doi.org/10.1038/s41598-022-05971-9 (1 2022).
245. Cortes, C. & Vapnik, V. Support-vector networks. *Machine learning*, 273–297. https://doi.org/10.1023/A:1022627411411 (1995).
246. Rebentrost, P., Mohseni, M. & Lloyd, S. Quantum support vector machine for big data classification. *Physical review letters* **113,** 130503 (2014).
247. Cristianini, N. & Shawe-Taylor, J. *An introduction to support vector machines and other kernel-based learning methods* 93–124 (2000).
248. Patle, A. & Chouhan, D. S. *SVM kernel functions for classification* in *2013 International conference on advances in technology and engineering (ICATE)* (2013), 1–9.
249. Aizerman, M. A., Braverman, E. M. & Rozonoer, L. I. Theoretical foundations of the potential function method in pattern recognition learning. *Automation and Remote Control.* https://api.semanticscholar.org/CorpusID:92987925, 821–837 (2019).
250. Burges, C. J. A tutorial on support vector machines for pattern recognition. *Data mining and knowledge discovery* **2,** 121–167. https://doi.org/10.1023/A:1009715923555 (1998).
251. Barenco, A. *et al.* Stabilization of Quantum Computations by Symmetrization. *SIAM Journal on Computing* **26,** 1541–1557. https://doi.org/10.1137/S0097539796302452 (1997).

252. Rebentrost, P., Mohseni, M. & Lloyd, S. Quantum Support Vector Machine for Big Data Classification. *Phys. Rev. Lett.* **113,** 130503. https://link.aps.org/doi/10.1103/PhysRevLett.113.130503 (13 2014).
253. De Wolf, R. Quantum computing: Lecture notes. *arXiv preprint arXiv:1907.09415* (2019).
254. Cincio, L., Subaşı, Y., Sornborger, A. T. & Coles, P. J. Learning the quantum algorithm for state overlap. *New Journal of Physics* **20,** 113022. https://doi.org/10.1088%2F1367-2630%2Faae94a (2018).
255. Nguyen, C.-H., Tseng, K.-W., Maslennikov, G., Gan, H. & Matsukevich, D. Experimental swap test of infinite dimensional quantum states. *arXiv:2103.10219* (2021).
256. Kang, M.-S., Heo, J., Choi, S., Moon, S. & Han, S.-W. Implementation of SWAP test for two unknown states in photons via cross-Kerr nonlinearities under decoherence effect. *Scientific Reports* **9.** https://doi.org/10.1038/s41598-019-42662-4 (2019).
257. Fredkin, E. & Toffoli, T. Conservative logic. *International Journal of Theoretical Physics* **21.** https://doi.org/10.1007/BF01857727 (1982).
258. Milburn, G. J. Quantum optical Fredkin gate. *Physical Review Letters* **62,** 2124 (1989).
259. Fiurášek, J. Linear-optics quantum Toffoli and Fredkin gates. *Physical Review A* **73,** 062313 (2006).
260. Gong, Y.-X., Guo, G.-C. & Ralph, T. C. Methods for a linear optical quantum Fredkin gate. *Physical Review A* **78,** 012305 (2008).
261. Wu, Y.-x., Zhu, C.-h. & Pei, C.-x. Nearly deterministic quantum Fredkin gate based on weak cross-Kerr nonlinearity. *Optoelectronics Letters* **12.** https://doi.org/10.1007/s11801-016-6149-4 (5 2016).
262. Dong, L. *et al.* Nearly deterministic Fredkin gate based on weak cross-Kerr nonlinearities. *J. Opt. Soc. Am. B* **33,** 253–260. https://opg.optica.org/josab/abstract.cfm?URI=josab-33-2-253 (2016).
263. Patel, R. B., Ho, J., Ferreyrol, F., Ralph, T. C. & Pryde, G. J. A quantum Fredkin gate. *Science Advances* **2,** e1501531. eprint: https://www.science.org/doi/pdf/10.1126/sciadv.1501531. https://www.science.org/doi/abs/10.1126/sciadv.1501531 (2016).
264. Fiurášek, J. Linear optical Fredkin gate based on partial-SWAP gate. *Phys. Rev. A* **78,** 032317. https://link.aps.org/doi/10.1103/PhysRevA.78.032317 (3 Sept. 2008).
265. Ono, T., Okamoto, R., Tanida, M., Hofmann, H. F. & Takeuchi, S. Implementation of a quantum controlled-SWAP gate with photonic circuits. *Scientific Reports* **7.** https://doi.org/10.1038/srep45353 (1 2017).
266. Volkoff, T. J. & Subaşı, Y. Ancilla-free continuous-variable SWAP test. *Quantum* **6,** 800. ISSN: 2521-327X. http://dx.doi.org/10.22331/q-2022-09-08-800 (Sept. 2022).
267. Kang, M.-S., Heo, J., Choi, S.-G., Moon, S. & Han, S.-W. Optical Fredkin gate assisted by quantum dot within optical cavity under vacuum noise and sideband leakage. *Scientific Reports* **10.** https://doi.org/10.1038/s41598-020-61938-8 (1 2020).
268. Chabaud, U., Diamanti, E., Markham, D., Kashefi, E. & Joux, A. Optimal quantum-programmable projective measurement with linear optics. *Phys. Rev. A* **98,** 062318. https://link.aps.org/doi/10.1103/PhysRevA.98.062318 (6 Dec. 2018).
269. Kumar, N., Chabaud, U., Kashefi, E., Markham, D. & Diamanti, E. Optimal quantum-programmable projective measurements with coherent states. *Phys. Rev. Res.* **3,** 043035. https://link.aps.org/doi/10.1103/PhysRevResearch.3.043035 (4 Oct. 2021).

270. Wang, F. *et al.* Experimental demonstration of a quantum controlled-SWAP gate with multiple degrees of freedom of a single photon. *Quantum Science and Technology* **6,** 035005. https://doi.org/10.1088%2F2058-9565%2Fabf996 (June 2021).
271. Buhrman, H., Cleve, R., Watrous, J. & De Wolf, R. Quantum fingerprinting. *Physical Review Letters* **87,** 167902 (2001).
272. De Beaudrap, J. N. One-qubit fingerprinting schemes. *Physical Review A* **69,** 022307 (2004).
273. Ekert, A. K. *et al.* Direct estimations of linear and nonlinear functionals of a quantum state. *Physical review letters* **88,** 217901 (2002).
274. Bartlett, S. D., Rudolph, T. & Spekkens, R. W. Optimal measurements for relative quantum information. *Physical Review A* **70,** 032321 (2004).
275. Lindner, N. H., Scudo, P. F. & Bruß, D. Quantum estimation of relative information. *International Journal of Quantum Information* **4,** 131–149 (2006).
276. Havlíček, V. *et al.* Supervised learning with quantum-enhanced feature spaces. *Nature* **567,** 209–212 (2019).
277. Chamorro-Posada, P. & Garcia-Escartin, J. C. The SWITCH test for discriminating quantum evolutions. *J. Phys. A* **56,** 355301 (2023).
278. Wiebe, N., Granade, C., Ferrie, C. & Cory, D. Hamiltonian Learning and Certification Using Quantum Resources. *Physical Review Letters* **112.** https://doi.org/10.1103%2Fphysrevlett.112.190501 (May 2014).
279. Wiebe, N., Granade, C., Ferrie, C. & Cory, D. Quantum Hamiltonian learning using imperfect quantum resources. *Phys. Rev. A* **89,** 042314. https://link.aps.org/doi/10.1103/PhysRevA.89.042314 (4 Apr. 2014).
280. Wang, J. *et al.* Experimental quantum Hamiltonian learning. *Nature Physics* **13,** 551–555. https://doi.org/10.1038%2Fnphys4074 (Mar. 2017).
281. Adami, C. & Cerf, N. J. *Quantum Computation with Linear Optics* in *Quantum Computing and Quantum Communications* (ed Williams, C. P.) (1999), 391–401.
282. Kok, P. *et al.* Linear optical quantum computing with photonic qubits. *Reviews of Modern Physics* **79,** 135–174. https://doi.org/10.1103%2Frevmodphys.79.135 (Jan. 2007).
283. Linke, N. M. *et al.* Measuring the Rényi entropy of a two-site Fermi-Hubbard model on a trapped ion quantum computer. *Physical Review A* **98,** 052334. https://doi.org/10.1103%2Fphysreva.98.052334 (2018).
284. Garay-Palmett, K. *et al.* Photon pair-state preparation with tailored spectral properties by spontaneous four-wave mixing in photonic-crystal fiber. *Optics express* **15,** 14870–14886 (2007).
285. Poulvellarie, N., Ciret, C., Kuyken, B., Leo, F. & Gorza, S.-P. Highly nondegenerate two-photon absorption in silicon wire waveguides. *Physical Review Applied* **10,** 024033 (2018).
286. Husko, C. A. *et al.* Multi-photon absorption limits to heralded single photon sources. *Scientific reports* **3,** 3087 (2013).
287. Reck, M., Zeilinger, A., Bernstein, H. J. & Bertani, P. Experimental realization of any discrete unitary operator. *Physical review letters* **73,** 58 (1994).
288. Mazzucchi, S., Leone, N., Azzini, S., Pavesi, L. & Moretti, V. Entropy certification of a realistic quantum random-number generator based on single-particle entanglement. *Phys. Rev. A* **104,** 022416. https://link.aps.org/doi/10.1103/PhysRevA.104.022416 (2 Aug. 2021).
289. Leone, N., Azzini, S., Mazzucchi, S., Moretti, V. & Pavesi, L. Certified Quantum Random-Number Generator Based on Single-Photon Entanglement. *Phys. Rev. Applied* **17,** 034011. https://link.aps.org/doi/10.1103/PhysRevApplied.17.034011 (3 Mar. 2022).

290. Leone, N. *et al.* Generation of quantum-certified random numbers using on-chip path-entangled single photons from an LED. *Photon. Res.* **11,** 1484–1499. https://opg.optica.org/prj/abstract.cfm?URI=prj-11-9-1484 (Sept. 2023).
291. Brad Ridder. *Worst-Case Propagation of Uncertainty* version 1.2.0.0. Oct. 8, 2023. https://www.mathworks.com/matlabcentral/fileexchange/48139-worst-case-propagation-of-uncertainty.